CHARACTERIZATION OF CONCRETE MATERIAL FLOW DURING PROJECTILE PENETRATION

by

Robert Sobeski
A Dissertation
Submitted to the
Graduate Faculty
of
George Mason University
in Partial Fulfillment of
The Requirements for the Degree
of
Doctor of Philosophy
Civil and Infrastructure Engineering

Committee:

_______________ Dr. Girum Urgessa, Dissertation Director

_______________ Dr. Deborah Goodings, Committee Member

_______________ Dr. Mark Houck, Committee Member

_______________ Dr. Padmanabhan Seshaiyer, Committee Member

_______________ Dr. James Cargile, Committee Member

_______________ Dr. David Lattanzi, Committee Member

_______________ Dr. Deborah Goodings, Department Chair

_______________ Dr. Kenneth S. Ball, Dean, Volgenau School of Engineering

Date: 4/29/2014

Spring Semester 2014
George Mason University
Fairfax, VA

Characterization of Concrete Material Flow During Projectile Penetration

A Dissertation submitted in partial fulfillment of the requirements for the degree of Doctor of Philosophy at George Mason University

by

Robert Sobeski
Master of Science
Massachusetts Institute of Technology, 2001
Master of Science
Missouri University of Science and Technology, 1996
Bachelor of Science
United States Military Academy, 1992

Director: Girum Urgessa, Associate Professor
Sid and Reva Dewberry Department of Civil, Environmental, and Infrastructure Engineering

Spring Semester 2014
George Mason University
Fairfax, VA

DEDICATION

This dissertation is dedicated to Elizabeth Lefchak, Richard J. Longenhagen, and Daniel Gambal. “Life is eternal; and love is immortal; and death is only a horizon; and a horizon is nothing save the limit of our sight.” ~Rossiter W. Raymond

ACKNOWLEDGEMENTS

Firstly, I would like to thank my advisor, Dr. Girum Urgessa for his support, encouragement, and guidance during the dissertation process. I have been privileged to have such a talented engineer and researcher as my advisor. Secondly, I would like to acknowledge Dr. James Donald Cargile for his help, insights, and expertise related to concrete penetration. Without his mentoring, I never could have completed this dissertation. I also would like to thank the members of my committee, Dr. Deborah Goodings, Dr. Mark Houck, Dr. Padmanabhan Seshaiyer, and Dr. David Lattanzi for their support. I am very grateful to Ray Morale, Mark Adley, Stephen Akers, Phillip Bucci, and Alyson Armstrong of the U.S. Army Engineer Research and Development Center Waterways Experiment Station; Dr. Phillip Randels of the Defense Threat Reduction Agency; and Anthony Key of the Defense Intelligence Agency for their help. Finally, a special thanks to LTC (Ret.) Todd Hann of the Defense Threat Reduction Agency for sponsoring me and providing critically needed computer equipment and software.

TABLE OF CONTENTS

LIST OF TABLES

LIST OF FIGURES

LIST OF ABBREVIATIONS

Advanced Fundamental Concrete	AFC
Air Force Armament Laboratory	AFAL
Air Force Weapons Laboratory	AFWL
AUTODYN Finite Element Program	AUTODYN
Coupled Arbitrary Lagrangian-Eulerian	CALE
Caliber Radius Head	CRH
Chairman of the Joint Chiefs of Staff	CJCS
Data Sets	DS
Department of Defense	DoD
Depth of Penetration	DOP
DYNA Finite Element Program	DYNA
Elastic Plastic Impact Computation	EPIC
Federal Highway Administration	FHWA
Kilo-pounds per Square Inch	ksi
Holmquist-Johnson-Cook	HJC
Mega-Pascal	MPa
Normal (Ogive) Expansion Comparison Methodology	NECM
Naval Research and Development Command	NRDC
Root Mean Square	RMS
Sandia National Laboratory	SNL
Soils and Pavements Laboratory	SPL
Smoothed Particle Hydrodynamics	SPH
Spherical Expansion Comparison Methodology	SECM
Southwest Research Institute	SWRI
Ultra High Performance Concrete	UHPC
U.S. Army Armament Research Development and Engineering Center	USAARDEC
U.S. Army Ballistic Research Laboratory	USABRL
U.S. Army Engineer Research and Development Center	USAERDC
U.S. Army Engineer Waterways Experiment Station	USAEWES
U.S. Naval Weapons Laboratory	USNWL VHSC
Very High Strength Concrete	VHSC

ABSTRACT

CHARACTERIZATION OF CONCRETE MATERIAL FLOW DURING PROJECTILE PENETRATION

Robert Sobeski, Ph.D.

George Mason University, 2014

Dissertation Director: Dr. Girum Urgessa

The Department of Defense (DoD) has an operational requirement to predict, quickly and accurately, the depth of penetration that a projectile can achieve for a given target and impact scenario. Fast-running analytical models can provide reliable predictions, but they often require the use of one or more dimensionless parameters that are derived from experimental data. These analytical models are continually evolving, and the dimensionless parameters are often adjusted to obtain new analytical models without a true understanding of the change in characteristics of material flow across targets of varying strength and projectile impact velocities.

In this dissertation, the penetration of ogive-nose projectiles into concrete targets is investigated using finite element analyses. The Elastic-Plastic Impact Computation (EPIC) code is used to examine the velocity vector fields and their associated direction cosines for high and low-strength concrete target materials during projectile penetration. Two methodologies, referred as Normal Expansion Comparison Methodology (NECM)

and Spherical Expansion Comparison Methodology (SECM), are developed in MATLAB to quantify the change in concrete material flow during this short-duration dynamic event. Improved velocity profiles are proposed for better characterization of cavity expansion stresses based on the application of NECM and SECM to EPIC outputs. Structural engineers and model developers working on improving the accuracy of current analytical concrete penetration models and potentially reducing their reliance on fitting parameters will benefit from the findings of this research.

CHAPTER 1: INTRODUCTION

1.1 Motivation

The Department of Defense assesses weapons capabilities as part of its joint targeting cycle (OCJCS, 2007). These assessments provide important information to the commander so that necessary changes to tactics, protective systems, and/or weapon systems can be quickly identified. As part of this weapons assessment, the commander's staff will evaluate specific weapons' capabilities against identified target vulnerabilities to predict effects on the target. An important part of predicting effects is to determine the depth of penetration of a projectile into a target material with an acceptable accuracy. The commander's staff will often need to simulate numerous scenarios, each with multiple permutations. Because of the large number of simulations required, a quick run-time for penetration models is paramount.

Advances in concrete materials have led to continued evolutionary improvements in concrete strength and performance. Such advances have resulted in multiple classes of concrete, which are defined in numerous ways in the literature. Unfortunately, there is no authoritative source for classifying concrete by strength. Therefore, for the purpose of this dissertation, two broad categories of concrete are defined based on unconfined compressive strength: conventional-strength concrete (≤ 69 MPa (10 ksi)) and enhanced-strength concrete (> 69 MPa (10 ksi)). Table 1 shows further classifications of enhanced-strength concrete.

Table 1. Categories of Enhanced-Strength Concrete

Concrete Class	Concrete Strength
High Strength	69 to 130 MPa (10 to 19 ksi)
Very High Strength	130 to 190 MPa (19 to 28 ksi)
Ultra-High Performance	> 190 MPa (28 ksi)

Current quasi-analytical and analytical models that were originally developed for determining depth of penetration of projectiles into conventional-strength concrete targets give less accurate results when applied to enhanced-strength concrete targets. For example, Hansson (2003) reported penetration models with an upper strength limitation of about 65 MPa (9.4 ksi). New methods, therefore, need to be developed to improve the prediction of penetration depth into enhanced-strength concretes, especially in light of the relatively recent development of ultra-high performance concrete.

The ability to model accurately projectile penetration into enhanced-strength concrete has industrial implications as well. For example, the design and assessment of protective structures for high-speed machinery, critical nuclear systems, or facility protective barriers depend on accurate modeling techniques. High-speed machinery can include generator turbine blades, centrifuges, or fly wheels. Protective structures for this type of machinery must be capable of containing failed components and of protecting against outside intrusions. Some examples of critical nuclear systems include reactor vessels, spent fuel pools, and spent fuel casks. Containment structures for these types of systems must be robust enough to withstand accidental or deliberate impact. Finally, facility protective barriers often provide a first layer of defense against blast and fragmentation. Understanding how these barriers perform during penetration events is important to government and industry alike.

1.2 Statement of the Problem and Purpose of the Research

Need: The Department of Defense has an operational requirement for fast and accurate concrete penetration models. These models must be capable of predicting depth of penetration over a wide range of concrete strengths. Over the past decade, advances in concrete technology have resulted in new mixes that provide up to an order-of-magnitude improvement in compressive strength over conventional types of concrete. In response, researchers have a need to develop numerical methods for predicting enhanced-strength concrete penetration.

Gap: These methods, however, are often complex, unique to a given situation, and can take years to develop. Currently, there are no fast-running physics-based analytical models that accurately and reliably predict projectile penetration into enhanced-strength concrete targets. The current approach is to make incremental adjustments to existing algorithms as data becomes available. These adjustments are often made without a true understanding of the cause of the discrepancies.

Proposed approach for addressing the gap: The purpose of this research is to simulate existing concrete penetration data in order to observe and quantify the flow of concrete target material around the nose of the projectile during penetration. The material flow observations are assessed in order to make recommendations that characterize the behavior for improved physics-based analytical models capable of predicting penetration depth into enhanced-strength concrete.

Originality of approach and significance: This research is original because there has been little to no attempt thus far to investigate how parameters such as concrete strength, projectile velocity, and projectile nose geometry impact the flow of material during concrete penetration. The results from this research are significant because they provide a physical rationale for making analytical model improvements. This rationale can be used to improve and guide the development of fast-running analytical and physics-based computer codes used by the DoD. Improvements in these codes will provide analysts the ability to predict the penetration depth of rigid projectiles into enhanced-strength concrete targets.

1.3 Dissertation Organization

A state-of-the art literature review on the development of quasi-analytical and analytical methods that are used to determine projectile penetration of targets is presented in Chapter 2. The review also includes summaries of published work related to numerical methods that are directly applicable to the finite element code selected in this research or closely related codes, associated material models, concrete penetration and treatment of distorted elements.

Chapter three presents the experimental data available in the literature, the development of finite element models for analyzing the projectile penetration of concrete, and the validation of the models based on comparisons to the published experimental penetration data. Geometry developments of the projectiles and targets are presented in detail. In addition, two material models suitable for penetration mechanics of concrete targets are discussed.

Chapter four presents the development of two quantitative methodologies that can be used to determine the material flow response of a given target using outputs from a numerical computation. These methodologies referred to as the Normal Expansion Comparison Methodology (NECM) and the Spherical Expansion Comparison Methodology (SECM) provide a means of assessing how material flow deviates from either ogive-normal or spherical expansion quantitatively as a function of time, depth, velocity, or material strength. Chapter four also presents a method for determining the normal velocity profile for ogive projectiles based on the average velocities of the meshless particles trapped between the intact mesh and the advancing projectile nose.

Chapter five presents results and discussions of concrete material flow based on the application of NECM and SECM methodologies to the finite element model outputs of projectiles entering into concrete targets. The effects of varying concrete strength, striking velocity, and projectile nose geometry on particle movement are discussed. In addition, the effects of varying concrete strength and striking velocity on target nodes are included. Chapter five also presents a normal velocity profile for ogive projectiles derived from finite element computations. The finite element normal velocity profile is useful for comparison to velocity profiles used in existing analytical methods.

Chapter six presents conclusions, recommendations, limitations of the study and future work. The appendices contain data that is too large to be included in the main dissertation but is important to carry out future research or for reproducibility purposes. The appendices contain summaries of mesh geometry, the study of the effects of soakers, MATLAB codes developed for NECM and SECM, NECM and SECM output files, mesh geometry outputs, MATLAB code developed for normal velocity profiles, and normal velocity profiles for nodes and particles.

CHAPTER 2: LITERATURE REVIEW

2.1 Overview of Concrete Penetration

Concrete is a preferred construction material in protective structures. Extensive research in the last twenty years has resulted in the range of concrete strength five to six times greater than the typical range of conventional-strength concrete (Cargile, O'Neal and Neely, 2003 and FHWA, 2011). In light of this fact, there is a need to assess existing quasi-analytical and analytical approaches that are used to predict the impact resistance of concrete targets subjected to projectiles. Specifically, the assumptions used in existing quasi-analytical or analytical methods that are developed for penetrations of conventional concrete targets do not necessarily work for enhanced-strength concrete.

When a projectile enters the front side of a target and exits out the back side, the process is referred to as perforation. When the projectile enters the target but does not exit nor cause any permanent damage to the back side of the target, the process is referred to as penetration. There are two phases of penetration: the cratering phase and the tunneling phase. The cratering phase is short, usually about two projectile diameters in length, and causes a conical crater on the face of the target (Forrestal, Altman, Cargile and Hanchak, 1993). The tunneling phase can be many projectile diameters in length and it leaves behind a tunnel that is slightly larger than the diameter of the projectile (Forrestal, Okajima, and Luk 1988). During the tunneling phase, the projectile slows down due to reaction forces at the target-projectile interface. The forces at this interface are due to a combination of inertial stresses (the stresses required to accelerate target material out of the path of the projectile) and the material stresses (the stresses required to deform the the target material surrounding the newly opened cavity). At extremely high velocities (above 1-km/s), the inertial stresses dominate and the material stresses can often be ignored. At lower velocities, such as those investigated in this research (200-800-m/s), the material stresses dominate; and the target resistance is heavily influenced by the material properties of the concrete (UASBRL, 1980).

To further complicate the penetration mechanics, the material properties of concrete under dynamic conditions are significantly different from what is observed under quasi-static conditions. Loading rates are initially dependent upon the striking velocity, but then later depend upon the instantaneous velocity as the projectile slows down during tunneling. As the projectile slows down the loading rate decreases and the material properties change, thereby influencing target resistance and potentially the direction of material flow. Confinement and hydrostatic pressure can also influence material behavior. As the projectile achieves increased depths, the target's confinement and hydrostatic pressure changes, which in turn, affects the target resistance.

When concrete undergoes dynamic loading of sufficient rate and magnitude, cavity expansion occurs. The cavity grows in size as the concrete undergoes an initial elastic reponse followed by platic flow, crack formation and fragmentation, comminution, and densification. Beyond the cavity, several response regions are formed. Forrestal and Tzou (1997) identified three regions of response: a plastic region, a cracked region, and an elastic region. At high velocities, however, the cracked region can be reduced or eliminated. To achieve good agreement with the data, Forrestal and Tzou treated the plastic region as a compressible material. Satapathy (IAT, 1997) proposed a pulverized region just outside of the cavity instead of a compressible plastic region. Satapathy treated the pulverized material as a Mohr-Coulomb material with a pressure dependent shear strength.

A state-of-the art literature review is included below on the development of quasi-analytical and analytical methods that are used to determine projectile penetration of targets, dating back to the middle of the 20th century. The review encompasses projectile penetration into a variety of target materials to include metals and soils. These early works provide motivation for the development of the equations used for projectile penetration of concrete targets. The review concludes by presenting summaries on numerical methods, which focused on published work that is directly applicable to selected finite element codes, associated material models, and the treatment of distorted elements in this research.

2.2 Methods of Predicting Projectile Penetration

There are three approaches for determining the impact mechanics of targets subjected to projectiles; quasi-analytical, analytical and numerical approaches (Zukas, 2004). The first category, quasi-analytical methods, is based on simplified algebraic equations developed with data points that are obtained through small-scale or large-scale physical tests. However, these methods do not provide insight into material behavior during projectile penetration.

The second category, analytical methods, is based on solving differential equations of continuum mechanics by introducing simplifying assumptions. However, analytical methods typically rely on assuming material properties, which are necessary to arrive at closed-form solutions. Both quasi-analytical and analytical methods are quite important in (i) characterizing small-scale or large-scale experimental data, (ii) developing a basic understanding of the penetration mechanics, and (iii) making faster predictions of global parameters such as penetration depth within the limits of applicability of the methods.

The third category, numerical methods, is based on arriving at numerical solutions of the governing differential equations of dynamic equilibrium through finite difference or finite element methods. The numerical method is a good choice for analyzing impact mechanics because there is virtually no limitation on the model size or geometric complexity that the method can handle. Numerical methods work well for problems involving a single material or numerous parts made of different materials. The applied loads can be static or dynamic, and the structural responses can be linear or non-linear. However, numerical methods also have their drawbacks, such as the need for detailed material models and geometries and the expertise needed for interpreting outputs. Numerical methods require a complete description of the material behavior in all loading regimes. The elastic behavior, the tensile, compressive, and shear yield strengths, the direction of material flow, and failure mechanisms must be well understood at various pressures, strains, temperatures, and strain rates.

2.3 Quasi-Analytical Methods

Quasi-analytical methods are employed when the physical phenomenon being described is highly complex and dependent upon variables that are difficult to isolate and control. These methods often have, at their core, fundamental basis in physics such as the work-energy equations or equations of motion. For example, Newton's second law of motion allows one to quickly relate the mass and deceleration of a projectile to the target's resistive force. Then, the resistive force can be determined by conducting tests or experiments and tabulating the results. The earliest work done on penetration mechanics by Euler, Poncelet, and Petry was empirical in nature (NRDC, 1950). Empirical equations can be extremely accurate, but they are only valid for the specific range of target-projectile parameters that were originally tested. Application of these equations outside the tested domain is not widely trusted. For example, the generalized Poncelet model achieved a very good fit with small caliber data previously analyzed by Stipe. When this model was extended to incorporate larger caliber penetrators, the results were unsatisfactory (NRDC, 1950).

Rahman, Zaidi, and Latif (2010) provided a summary of twenty quasi-analytical equations used for determining depth of penetration into concrete targets. The summary is extensive beginning with the Modified Petry Formula developed in 1910 until equations developed in early 2000s. These equations were developed with parallel research efforts in the US, United Kingdom and France. Stivaros and Philippacopoulos (2011) provided a list of some of the well-known empirical equations including: the Modified National Defense Research Council (NDRC), Bechtel, Modified Petry, Chang/DOE, Army Corps of Engineers (ACE), Ballistic Research Laboratory (BRL), Stone and Webster, Ammann and Whitney, CEA-EDF, CRIEPI, Sandia National Laboratories (SNL), and Haldar equations. They highlight that most of these equations were developed on the basis of small-scale ballistic tests and are not expected to provide good results for large size projectiles. Bangash (2009) documented quasi-analytical methods used to predict projectile penetration of non-deformable and deformable missiles into concrete targets. Of these methods, SNL has one of the most comprehensive empirical databases for penetration events. In 1967, SNL published empirical equations to predict projectile penetration into soil, rock, and concrete (SNL, 1997). These initial empirical equations were based on an extensive experimental database, and consequently have undergone only slight modifications over the years. In 1997, the empirical equations used for predicting penetration depth into a uniform target material are expanded to include penetration into layered targets. In addition, the penetration equations were used to improve the basic geometric scaling laws and to better understand scaled model experimental results (SNL, 1997). These equations have two forms as shown in eqn (1) and eqn (2) based on the velocity of the projectile.

$$D = 0.3K_h SN(W/A)^{0.7}\ln(1+2\times10^{-5}V^2) \quad for\ V \le 61\ m/s\, or\, 200\, ft/s \tag{1}$$

$$D = 0.00178K_h SN(W/A)^{0.7}(V-100) \quad for\ V \ge 61\ m/s\, or\, 200\, ft/s \tag{2}$$

where S represents the penetrability of the target and is given by eqn (3); K_h is a correction factor for lightweight projectiles and hard targets; N is the nose performance coefficient; W is the weight of the penetrator in pounds; A is the cross sectional area of the projectile shank in pounds per square inch; and V is the impact velocity of the projectile in feet per second.

$$S = 0.085 K_e (11 - P)(t_c T_c)^{-0.06} (5000 / f_c^{'})^{0.3} \tag{3}$$

where K_e is a correction factor for edge effects in the concrete target; t_c is the cure time of concrete in years; T_c is target layer thickness in feet; f'_c is the unconfined compressive strength of the concrete in pounds per square inch; and P is reinforcement percentage by volume. The SNL penetration equations are accurate within approximately 15%, except near the limits of applicability. The equation for the penetrability of the concrete target (S) is reported to be accurate within approximately 10% (SNL, 1997).

The SNL equations, however, are often criticized because of their use of the S-number and because of the difficulty of relating physical meaning to the equations. In the development of the equations, an assumed form of the depth prediction is fitted with sufficient experimental data without incorporating Newton's equation of motion. For example, USERDC (2006) noted that the S-number could not account for differences between cohesive and non-cohesive materials. Further, the equations cannot be used to accurately predict deceleration histories within targets.

2.4 Analytical Methods

Analytical methods attempt to provide a correlation between many of the variables in the phenomenon being modeled. They are typically based on solving differential equations of continuum mechanics. However, these methods typically rely on simplified material properties, which are necessary to arrive at closed-form solutions. Ideally, equations developed with these methods require only the initial conditions, and material properties of the target and projectile as input. Two well-established analytical methods for penetration of projectiles in concrete targets include the cavity expansion method and the differential area force law method. SPL (1975) noted that the differential force law method requires more computer effort than the cavity expansion method. It was indicated that the material constants were difficult to generate from material properties alone. It is further reported that the cavity expansion model required shorter computer computation times and that the parameters needed could be determined from laboratory tests of the target material. Therefore, the cavity expansion method is mostly used in later development of target-penetration mechanics in concrete.

Understanding the cavity expansion chronology is important for researchers who will develop analytical equation for target-penetration mechanics in concrete, specifically as technological innovation allows for the development of higher concrete strengths. Bishop, Hill and Mott (1945) presented a method of calculating the pressure (P_s) required to enlarge a cavity indefinitely by plastic flow at quasi-static velocities as shown in eqn (4).

$$P_S = \frac{2Y}{3}\left[1 + 3\ln\left(\frac{c}{a}\right)\right] + \frac{2\pi^2}{27}A \tag{4}$$

where Y is the yield strength of the target in tons per square inch; c is the radius of the plastic region in inches; a is the radius of the cavity in inches; and A is the cross-sectional area of the penetrator in square inches. The method assumed elastic and plastic incompressibility of the target material, but accounted for material strain hardening. The relationship between the plastic region-to-cavity radii ratio and the material properties of the target was given by eqn (5).

$$\frac{c}{a} = \left(\frac{E}{(1+\nu)Y}\right)^{1/3} \tag{5}$$

where E is the Young's modulus of the target material in tons per square inch; ν is the Poisson's ratio of the target material; and all other variables as defined earlier. Hill (1948) extended his quasi-static work by deriving an equation for the dynamic cavity expansion pressure of incompressible metals. Later on, he added compressibility of the target material to his quasi-static equations as shown in eqn (6).

$$P_S = \frac{2Y}{3}\left[1 + \ln\left(\frac{E}{3Y(1-\nu)}\right)\right] \tag{6}$$

Although Hill's equations accounted for compressibility of the target material, he did not develop an equation that accounted for both compressibility and strain hardening at the same time. For quasi-static expansion, Hill's compressible model predicted a slightly lower cavity pressure than the incompressible model. For dynamic expansion, the difference between these two models was further pronounced (Satapathy, 2001).

NRDC (1950) derived an equation for determining the target resistance force, R, during penetration. It was noted that for a given projectile and target, the penetration depth is not proportional to the striking kinetic energy, but rather given by eqn (7).

$$R = \frac{g(z)}{K\eta}\left(\frac{V}{d}\right)^{0.20} C \tag{7}$$

where g(z) is a depth dependent factor that accounts for the entry of the nose of a projectile; z is the depth of nose penetration measured in calibers; K is the penetrability of the concrete; η is the nose shape factor for the projectile; d is the caliber; V is the initial velocity of the projectile; and C is a constant. NRDC interpreted its findings as the resistance force is dependent on depth, velocity, or both during penetration. It was also stated that the resistance pressure may depend on the time rate of deformation of the target material. NRDC (1950) also noted that the legacy Poncelet's model (Johnson, 1972), which defines resistive force as a function of the penetration velocity plus a constant, worked well for some smaller-caliber projectiles, but it did not provide good results for larger-caliber projectiles.

Hopkins (1960) developed a method for calculating pressure for the dynamic expansion of a cavity in a large mass of ductile metal. He assumed that the elastic target material was incompressible, followed Hooke's law, and yielded in accordance with the Tresca yield criteria. Hence, his method accounted for both work-hardening and strain-rate effects. Building on the work of Bishop et al. (1945), Hopkins (1960) incorporated both the material strength and the inertial resistance of the target into his equations. For quasi-static expansion, he accounted for work hardening as a polynomial and arrived at the expression shown in eqn (8).

$$P_S = \frac{2Y}{3}\left[1 + \ln\left(\frac{2E}{3Y}\right)\right] + \frac{2\pi^2}{27}E_t \tag{8}$$

where E_t is the constant tangent modulus for linear strain hardening; and all other variables as defined earlier. Hopkins's equation was a special case of a similar expression first presented by Chadwick (1959). For dynamic expansion, Hopkins (1960) assumed an elastic-plastic deformation of a work-hardened material and developed eqn (9). The first two terms correspond to the quasi-static pressure result and the remaining term accounts for inertial effects.

$$P = \frac{2Y}{3}\left[1 + \ln\left(\frac{2E}{3Y}\right)\right] + \frac{2}{3}Y \ln\left(1 - a_o{}^3 / a^3\right) + \rho\left(a\ddot{a} + \frac{3}{2}\dot{a}^2\right) \tag{9}$$

where P is the pressure at any time t; ρ is the density of the target material; a_o is the initial radius of the cavity; a is the radius of the cavity at any time t; $\dot{a}$ is the rate of change of a; $\ddot{a}$ is the rate of change of $\dot{a}$; and all other variables as defined earlier.

AFWL (1965) developed the governing equations for dynamic cavity expansion by characterizing the properties of continua as compressible elasto-plastic and kinematically hardened. The governing equations include a system of equations that are applicable except at discontinuities (conservations of mass, momentum, energy) and a particular form of the equation of state that is applicable at discontinuities (Rankine-Hugoniot jump equation). It was concluded that the hydrostatic component of the stress state decreases much more rapidly than a decreasing cavity pressure as long as the cavity is expanding, and the presence of the deviatoric stress permits the radial transmission of a compressive stress despite the existence of hydrostatic tension.

Goodier (1965) presented the large expansion of a spherical cavity in a strain-hardened material. He assumed the target material to be elastically and plastically incompressible, and approximated the target response using the solution presented by Hill (1948). Following Hopkins' (1960) approach, Goodier divided his equation into static and dynamic terms for pressure as shown in eqn (10).

$$P = \frac{2Y}{3}\left[1 + \ln\left(\frac{2E}{3Y}\right)\right] + \frac{2\pi^2}{27}E_t + \rho\left(a\ddot{a} + \frac{3}{2}\dot{a}^2\right)\cos\theta \tag{10}$$

where θ is the angle which has a value of zero at the tip and π/2 at the shoulder of the projectile nose; and all other variables as defined earlier. He accounted for the curvature of spherical projectiles using a factor of cos θ. The equation of motion then reduced to eqn (11).

$$-\frac{1}{3}D(2\rho_p + \rho_T)\ddot{q} = \frac{2Y}{3}\left[1 + \ln\left(\frac{2E}{3Y}\right)\right] + \frac{2\pi^2}{27}E_t + \rho_T \dot{q}^2 \tag{11}$$

Where $\dot{q}$ is the velocity when 2q/D is 1; D is diameter of the projectile; ρ_P is the density of the projectile; ρ_T is the density of the target material; $\ddot{q}$ is the deceleration of the projectile; and all other variables as defined earlier.

SNL (1966) sought to develop equations that realistically describe the behavior of the target during the penetration event. 2-D and 3-D tests that led to a description of boundary conditions, and effects of target geometry and constraints were conducted. SNL provided a review of the works of Poncelet, Euler and several other earlier researchers. Since the Euler formula contained one parameter that was independent of velocity, SNL concluded that this was the quasi-static resistance. The quasi-static resistance, however, had already been shown to be a non-linear function of area and depth (Hopkins, 1960). This was not consistent with SNL's findings. SNL provided three important observations regarding the limitations of the technology for collecting data for penetration events in 1966. First, velocities, displacements and accelerations could not be measured during the penetration event. Second, constitutive equations for the target materials were not known. Third, knowledge of how the target was displaced in front of the projectile was not observable. However, current technologies allow for the direct measurement of motion during a penetration event, and the constitutive equations for many materials have now been published. Understanding how the target is displaced from the projectile's front is also possible through the use of computer simulation.

Hunter and Crozier (1968) solved compressibility by using a similarity transformation by assuming that the ratio of yield stress to density remained constant. This work is the basis for Forrestal and Longcope (1982) who later adapted the use of the similarity transformation for solving cavity expansion problems. Hanagud and Ross (1971) added target material compressibility to the dynamic cavity expansion problem through a locking approximation based on material behavior under hydrostatic stress, and with an elastic-plastic response in shear. Their governing equation is shown in eqn (12).

$$P(t) = P_S + \rho_{lP}(B_1 a\ddot{a} + B_2 \dot{a}^2) \tag{12}$$

where the pressure (P_S) is defined by eqn (13).

$$P_S = \frac{4}{9}E(1-e^{-3\beta}) - \frac{2}{3}Y\ln(\delta) + \frac{2\pi^2}{27}E_t - \frac{4}{9}E_t\eta \tag{13}$$

B_1 and B_2 are constants related to the dynamic pressure; β and δ are material constants defined by eqn (14).

$$\beta = \frac{Y}{2E};\ B_1 = 1-\delta^{1/3};\ B_2 = \frac{3}{2} - (1+\alpha_P)\delta^{1/3} + \frac{1}{2}\delta^{4/3} \tag{14}$$

The vertical resisting force (F) and the terminal depth of penetration (q_t) are given by eqn (15) and eqn (16) respectively.

$$F = \frac{2}{3}\rho_{lP}(B_1 a\ddot{a} + B_2\dot{a}^2)\pi a^2 \tag{15}$$

where ρ_{1P} is the locking density and all other variables as defined earlier.

$$q_t = q_o + \frac{3}{4}\frac{(M/A) + B_1(D/3)\rho_{lP}}{B_2\rho_{lP}}\ln\left(\frac{P_S + (2/3)B_2\rho_{lP}V_o^2}{P_S}\right) \tag{16}$$

where q_o is penetration depth; M is the mass of projectile; D is the diameter of projectile; A is the cross-sectional area of projectile; ρ_{IP}; α_P is $1-\rho_{le}/\rho_{lp}$; a; E_t is the tangent modulus for linear strain-hardening; V_o is velocity at start of tunneling phase; and all other variables as defined earlier.

Penetration depths calculated for compressible cases were determined to be lower than the incompressible cases at low velocities. Hanagud and Ross (1971) concluded that this was expected, since at lower projectile impact velocities, the material behind the advancing front is compressed over its initial stress-free value. At higher velocities, the compressibity effect increases due to high-pressure effects, but the target material also behaves more like a fluid and tends to lose its shear resistance to penetration.

SPL (1975) presented comparison of five different methods used to predict rigid body motion of a large penetrator normally impacting soil (Sandia Empirical Formula, Spherical Cavity Expansion theory, Cylindrical Cavity Expansion Theory, Viscoplastic Force Law, and Differential Area Force Law). It was found that no single analysis method was superior to the others as to warrant its exclusive use. In addition, the cavity expansion theories were the only methods that employed a description of the target that was expressed in terms of measurable engineering properties. The ability to define the target in measureable engineering properties is an important advantage to using cavity expansion theory in modeling penetration effects.

Bernard and Hanagud (USAEWES, 1975) as well as Bernard (USAEWES, 1976) developed a model using cavity expansion theory for concentrically layered media. They extended Goodier's theory (1965) so that it is applicable to deep as well as shallow penetration problems. They empirically determined a relationship between dynamic penetration resistance to the solid Reynolds number and the projectile geometry. The relationship was found to be the same for all targets and projectile combinations. As such, the model only required projectile characteristics and target constitutive properties as input. Their model was shown to be accurate within 20% when the target density and unconfined strength were known.

Tate (1977) categorized penetration events into three velocity regimes. He noted that at sufficiently low velocities, the stresses within the penetrator and target were both elastic. As the velocity increased, impact pressures also increased and eventually exceeded the yield strength of the projectile or target or both. At that point, larger plastic deformation occurred. At even higher velocities, past what is known as the hydrodynamic transition velocity, the projectile behaved more like a fluid jet. Tate concluded that the hydrodynamic transition velocity occurred because the rod erosion rate exceeded the rate of propagation of gross plastic deformation.

Forrestal, Norwood and Longcope (1981) solved for the axial resultant force on a conical and ogival projectile nose assuming a constant shear failure-pressure ratio (μ=0) as shown in eqn (17).

$$F_Z = \pi \rho_o V^2 C_1 + \pi \rho_o V^2 C_2 \frac{\ln \eta}{1-\eta} - \pi \tau_o C_3 \ln \eta \tag{17}$$

where C_1 is the length of the penetrator nose; C_2 is the axial position where the radial stress becomes tensile and the target is no longer in contact with the penetrator; C_3 is the radius of curvature of the nose; τ_o is the target shear strength; V is the velocity of the projectile; ρ_o is the density of the target; η is (1- ρ_0/ρ) and all other variables as defined earlier. The authors noted that the radial stress increased behind the wave front and was maximum at the penetrator surface for all values of μ and τ_0. The resultant force on a conical nose for a target described by a linear hydrostat was found to be proportional to V tan ϕ; whereas the resultant force on a conical nose for a target described as a locked hydrostat was found to be proportional to $(V \tan \phi)^2$, where ϕ is half the angle formed by the tip of the projectile.

Forrestal and Longcope (1982) published a closed form solution to the cavity expansion problem. Earlier cavity expansion solutions (Forrestal et al., 1981) idealized the target material as a locking solid hydrostat. Tri-axial tests, however, suggest that concrete materials are better represented as linear hydrostats. This work simplified cavity expansion equations to a 1-D wave propagation in the radial direction. The equations were reduced to nonlinear ordinary differential equations by means of a similarity transformation and then linearized and solved in closed form. Their material model included Tresca yield criterion and a tension cutoff. Forrestal (1986) developed a cylindrical cavity expansion model for penetration into dry porous rock and compared his results with projectile deceleration test data. He observed that the cylindrical cavity expansion approximation over-predicted the early time deceleration response and under-predicted the later deceleration response.

Tate (1986) stated that the modified Bernoulli equation had been used for about 20 years in engineering modeling of the quasi-steady-state phase of high-speed long rod penetration. However, a major drawback of the theory has been that the strength factors appeared merely as empirical constants unrelated to such properties as the dynamic yield strength of the material.

Luk and Forrestal (1987) developed a closed form solution for cavity expansion of concrete targets that was based on post-test target observations and tri-axial material tests as well as the impact velocity, geometry, and mass of the penetrator. Their model could be used for a rigid spherical or ogival nosed projectile. They determined the resistive force as shown in eqn (18).

$$F_z = \pi a^2 Y \left(A + \frac{8\psi - 1}{24\psi^2} B V_z^{\,2} \right) \tag{18}$$

where a is the radius of the projectile; Y is the yield stress of the target; ψ is the caliber-radius head; V_Z is the penetrating velocity; A and B are constants given by eqn (19) and eqn (20) respectively; η* is the locked volumetric strain; and all other parameters as defined earlier.

$$A = (2/3)[1 - \ln \eta^*] \tag{19}$$

$$B = \frac{\rho_o}{Y\gamma^2} \left[\frac{3Y}{E} + \eta^* \left(1 - \frac{3Y}{2E} \right)^2 + \frac{3\eta^{*2/3} - \eta^*(4 - \eta^*)}{2(1 - \eta^*)} \right] \tag{20}$$

where ρ_o is the initial density; and γ is a material constant defined by eqn (21).

$$\gamma = \left(\left(1 + \frac{Y}{2E} \right)^3 - (1 - \eta^*) \right)^{1/3} \tag{21}$$

The final depth of penetration was then determined from eqn (22).

$$P = P_t + \frac{m}{2\beta} \ln \left(1 + \frac{\beta V_t^{\,2}}{\alpha} \right) \tag{22}$$

where P_t is depth of penetration large enough to create a locked hydrostat and was given by eqn (23); V_t is the penetration velocity at P_t; V_o is the impact velocity; m is the projectile mass; α and β depend on nose shape and outputs from locked/linear solutions; and all other parameters as defined earlier.

$$P_t = \frac{m}{2\beta}\ln\left(\frac{\alpha + \beta V_o^2}{\alpha + \beta V_t^2}\right) \tag{23}$$

Forrestal et al. (1988) presented penetration mechanics based on rate independent, elastic-perfectly plastic targets. They used cavity expansion approximations to obtain closed form penetration equations in 6061-T651 aluminum. For the spherical cavity expansion approximation, they found that the axial force on the nose of a conical penetrator is given by eqn (24).

$$F_z = \pi a^2 \sigma_n(V_z)\left(1 + \mu/\tan(\varphi)\right) \tag{24}$$

where $\sigma_n(V_z)$ is determined from one-dimensional expansion analyses; μ is the sliding-friction coefficient;a is the radius of the projectile; and ϕ is the half angle of the conical nose of the projectile. A total of six force equations were derived (three nose shapes times two expansion shapes). Only one of the six equation is shown in eqn (24) for illustrative purposes. The final penetration depth is then determined using spherical cavity expansion and is given by eqn (25).

$$P = \frac{m}{2\beta_s}\ln\left(1 + \frac{\beta_s V_o^2}{\alpha_s}\right) \tag{25}$$

where α_s and β_s are constants dependent on the shape of the projectile nose that were given by eqns (25) - (31); and all other parameters as defined earlier. For spherical nosed penetrators,

$$\alpha_s = \pi a^2 K A_s (1 + \mu\pi / 2) \tag{26}$$

$$\beta_s = (\pi a^2 \rho / 2) B_s (1 + \mu\pi / 4) \tag{27}$$

For ogival nosed penetrators,

$$\alpha_s = \pi a^2 K A_s [1 + 4\mu\psi^2 (\pi / 2 - \theta_o) - \mu(2\psi - 1)(4\psi - 1)^{1/2}] \tag{28}$$

For conical nosed penetrators,

$$\beta_s = \pi a^2 \rho B_s [(8\psi - 1) / 24\psi^2 + \mu\psi^2 (\pi / 2 - \theta_o) - [\mu(2\psi - 1)(6\psi^2 + 4\psi - 1)(4\psi - 1)^{1/2}] / 24\psi^2] \tag{29}$$

$$\alpha_s = \pi a^2 K A_s (1 + \mu / \tan\phi) \tag{30}$$

$$\beta_s = \pi a^2 \rho B_s (1 + \mu / \tan\phi) \sin^2 \phi \tag{31}$$

where ρ is the density of the target material; and all other parameters as defined earlier.

Forrestal and Luk (1992) presented developed closed-form equations for the normal penetration of ogival nosed projectiles into soil targets. The equations required tri-axial material data for the constitutive models. Analyses were simplified by using the spherical cavity expansion approximation. The authors idealized pressure-volumetric strain as a locked hydrostat; and the shear strength-pressure behavior as Mohr-Coulomb yield criteria as well as Mohr-Coulomb Tresca-limit yield criteria. The equations were validated by comparing predicted rigid-body decelerations and final penetration depths to the results of field tests into soil targets using 23.1 kg, 95.25 mm diameter projectiles. They used eqn (24) and they formerly developed (Forrestal et al., 1988) with modified α_s and β_s to predict penetration depth of ogival nosed projectile into soil targets. The modified α_s and β_s for soil targets is given by eqn (32) and eqn (33).

$$\alpha_s = \pi a^2 \tau_o A[1 + 4\mu\psi^2(\pi/2 - \theta_o) - \mu(2\psi - 1)(4\psi - 1)^{1/2}] \quad (32)$$

$$\begin{aligned}\beta_s = \pi a^2 \rho_o B[(8\psi - 1)/24\psi^2 + \mu\psi^2(\pi/2 - \theta_o) \\ -[\mu(2\psi - 1)(6\psi^2 + 4\psi - 1)(4\psi - 1)^{1/2}]/24\psi^2]\end{aligned} \quad (33)$$

where τ_o is the target shear strength; ρ is the target density; A and B depend on material properties and cavity expansion velocity; and all other parameters as defined earlier.

Forrestal, Altman, Cargile and Hanchak (1993) developed an analytical equation for determining depth of penetration of concrete targets using spherical cavity approximations. Their equation contained a single dimensionless constant that depended only on the unconfined compressive strength of the target. The constant was derived from test data. Following post-test investigations, the authors argue that the cavity immediately after impact (crater region) is a conical region with the length of about four times the radius of the projectile (4*a*), followed by a circular cylinder region (tunnel region). The axial force (F) on the nose of the projectile was determined by eqn (34) and the depth of penetration (P) was given by eqn (35).

$$F = \begin{cases} cz & \text{for } 0 < z < 4a \\ \pi a^2 (Sf_c' + N\rho V^2) & \text{for } 4a < z < P \end{cases} \quad (34)$$

$$P = \frac{m}{2\pi a^2 \rho N} \ln\left(1 + \frac{N\rho V_1^2}{Sf_c'}\right) + 4a \quad \text{for } P > 4a \quad (35)$$

where P is the final depth of penetration; z is the penetration depth in the tunneling region; a is the projectile shank radius; m is projectile mass; ψ is caliber radius head; N is a function of the caliber radius head; V is rigid body projectile velocity; V_1 is rigid body projectile velocity when the crater phase starts at $z = 4a$; V_s is the striking velocity; ρ is the density of the target material; f'_c is the unconfined compressive strength of the target; and S is the dimensionless target strength parameter determined from experimental data in combination with eqn (36).

$$S = \frac{N\rho V_s^2}{f_c'}\left[\left(1+\frac{4\pi a^3\rho N}{m}\right)\exp\left(\frac{2\pi a^2(P-4a)N\rho}{m}\right)-1\right]^{-1} \tag{36}$$

The authors found that their deceleration and depth predictions from the spherical cavity expansion approximations were in good agreement with experimental results.

Forrestal, Cargile and Tzou (1993) derived penetration equations for ogive-nosed projectiles into concrete by modifying eqn (34) that was developed by Forrestal, Altman, Cargile and Hanchak, (1993). Their penetration equations predict axial force on the projectile nose, rigid-body motion and final penetration depth. The equations were verified by eleven penetration experiments in concrete strengths between 32-40 MPa. Their equation for predicting final depth of penetration is given by eqn (37).

$$P = \frac{m}{2\pi a^2\rho BN}\ln\left(1+\frac{BN\rho V_1^2}{\tau_o A}\right)+4a \quad for\ P>4a \tag{37}$$

where A and B are constants obtained from elastic-cracked-plastic spherically symmetric cavity expansion analysis; τ_o is the target shear strength; and all other parameters as defined earlier. The rigid body projectile velocity when the crater phase starts at $z = 4a$ is V_1 and given by eqn (38).

$$V_1^2 = \frac{mV_s^2 - 4\pi a^3\tau_o A}{m+4\pi a^3 BN\rho} \tag{38}$$

They compared their analytical models with existing test data and they showed that the two results were in good agreement.

Forrestal, Altman, Cargile and Hanchak (1994) compared the output of their previous models (Forrestal, Altman, Cargile and Hanchak, 1993) to data presented by Canfield and Clator (USNWL, 1966). The authors added penetration equations for position, velocity, and acceleration as a function of time as shown in eqns (39) - (41).

$$z = \frac{m}{\pi a^2 N\rho} \ln\left(\frac{\cos^2\left(\tan^{-1}\left(\frac{N\rho}{Sf_c'}\right)^{1/2} V_1 - \frac{\pi a^2 (Sf_c' N\rho)^{1/2}(t-t_1)}{m} \right)}{\cos\left(\tan^{-1}\left(\left(\frac{N\rho}{Sf_c'}\right)^{1/2} V_1 \right)\right)} \right) + 4a, \quad 4a < z < P \tag{39}$$

$$V = \left(\frac{Sf_c'}{N\rho}\right)^{1/2} \tan\left(\tan^{-1}\left(\left(\frac{N\rho}{Sf_c'}\right)^{1/2} V_1 \right) - \frac{\pi a^2 (Sf_c' N\rho)^{1/2}(t-t_1)}{m} \right), \quad 4a < z < P \tag{40}$$

$$a = \frac{dV}{dt} = \frac{-\pi a^2 Sf_c' / m}{\cos^2\left(\tan^{-1}\left(\left(\frac{N\rho}{Sf_c'}\right)^{1/2} V_1 \right) - \frac{\pi a^2 (Sf_c' N\rho)^{1/2}(t-t_1)}{m} \right)}, \quad 4a < z < P \tag{41}$$

Predictions from these models were shown to be in good agreement with the data for projectile velocities between 250 m/s and 800 m/s.

Forrestal, Tzou, Askar, and Longcope (1995) developed equations for penetration of rigid spherical-nosed projectiles into ductile targets. The authors generalized previously developed equations by using an elastic-perfectly plastic constitutive idealization of the target material. For an incompressible material, the penetration depth was given by eqn (42).

$$P = \frac{2}{3}\left(\frac{\rho_p}{\rho_t}\right)\ln\left(1 + \frac{3\rho_t {V_s}^2}{4A}\right)\left(L + \frac{2a}{3}\right) \tag{42}$$

where; ρpP is the projectile density; ρpt is the target density; V_s is the striking velocity; L is the length of the projectile shank; a is the radius of the projectile shank; Y is the yield strength of the target; E is the Young's modulus of the target; and A is a material constant given by eqn. (43).

$$A = \left(\frac{2Y}{3}\right)\left(1 + \ln\left(\frac{2E}{3Y}\right)\right) \tag{43}$$

For a compressible material, the penetration depth was given by eqn (44).

$$P = \left(\frac{\rho_p/\rho_t}{B_s}\right)\ln\left(1 + \frac{1}{2}\left(\frac{B_s}{A_s}\right)\left(\frac{\rho_t {V_s}^2}{Y}\right)\right)\left(L + \frac{2a}{3}\right) \tag{44}$$

where A_s depend only on the target material properties and is given by eqn (45); B_s is a constant adjusted to fit test data with cavity expansion results; and other parameters as defined earlier.

$$A = \left(\frac{2}{3}\right)\left(1 + \ln\left(\frac{E}{3(1-\nu)Y}\right)\right) \tag{45}$$

The compressible target model over-predicted penetration depth from test data especially at higher velocities. The authors concluded that the tangential stress on the projectile nose was not being properly addressed. They based this conclusion on the fact that photographs of tests showed a thin melted layer along the length of the target tunnel. To account for this, they offered a modified form of A_s and B_s which fit the test data well.

Forrestal and Tzou (1997) developed a spherical-cavity expansion model for concrete targets. In the model, the pressure-volumetric strain response of the target material was idealized as incompressible or linearly compressible, and the shear strength-pressure relationship was idealized with a Mohr–Coulomb failure criterion with a tension cutoff. They found that the cracked region disappeared as the expansion velocity increased and that compressibility had significant influence on target resistance.

Satapathy (1997) presented a review of the historical and theoretical backgrounds of cavity expansion. He considered the consequences of projectile erosion and offered a new method for modeling material behavior. The author quantitatively explored the effects of finite boundary on penetration resistance, thereby explaining observed degradation of the penetration resistance in small samples. He expanded on previous cavity expansion analyses to consider cracking due to tensile strain. Finally, he developed an equation for the quasi-static expansion of brittle materials by assuming spherical and cylindrical symmetries and Mohr-Coulomb-type behavior.

Gold (USAARDEC, 1997) conducted an analytical study of penetration of concrete by projectiles traveling at high velocities. He studied the effects of yield strength model on the depth of penetration, and found that constant yield-strength models did not agree with the experimental data, while the pressure-dependent yield-strength models were in good agreement. Gold determined that the increased target resistance to penetration was due to an increased rate of projectile erosion. He also noted that the target resistance depended on the projectile velocity and the relative strength of the projectile and the target. When the penetrator velocity was fixed, the radial and axial target material displacements determined the size of the resulting crater. Therefore, since the target flow field is controlled primarily by the yield-strength properties of the target, the constitutive behavior of the target material is a principle factor in target resistance.

Frew, Hanchak, Green and Forrestal (1998) presented depth of penetration experiments in concrete targets with limestone (soft) aggregates. They compared experimental results using the analytical penetration eqn (37) that described target resistance by density, caliber radius head, and strength parameters determined from depth of penetration versus striking velocity. The authors noted that the resistance parameter for the limestone aggregate concrete targets considerably decreased for large diameter projectiles. This phenomenon, however, was not observed in concrete targets with quartz-based (hard) aggregates. Specifically, for hard aggregate concrete targets with nearly equal unconfined compressive strengths, projectiles of varying diameters resulted in nearly the same value of target resistance. For limestone aggregate concrete targets, however, projectiles with varying diameters had varying target resistance values. The target resistance value decreased as the projectile shank diameter increased for soft aggregate concrete targets.

Satapathy (2001) proposed an elastic-cracked-comminuted model for other brittle targets (such as ceramic) where he assumed material compressibility in the elastic and cracked regions, and material incompressibility in the comminuted regions. He concluded that similar observations were made by Forrestal and Tzou's (1995) penetration models for concrete targets.

Warren (2002) described an extension of Forrestal, Altman, Cargile and Hanchak's (1993) penetration method to limestone aggregate concrete targets that accounted for pitch, yaw and projectile deformation. The depth of penetration was given by eqn (46). Note that eqn (46) is similar in nature to eqn (37).

$$P = \frac{m}{2\pi a^2 \rho_o N} \ln\left(1 + \frac{N\rho_o V_1^2}{R}\right) + 4a, \quad for\, P > 4a \tag{46}$$

where P is the final depth of penetration; a is the projectile shank radius; m is projectile mass; N is a function of the caliber radius head; V_1 is rigid body projectile velocity when the crater phase starts at a depth of 4*a* and is given by eqn (47); V_s is the striking velocity; ρ_o is the density of the target material; and R is the resistance determined from experimental data in combination with eqn (48).

$$V_1^2 = \frac{mV_s^2 - 4\pi a^3 R}{m + 4\pi a^3 N\rho_o} \tag{47}$$

$$R = \frac{N\rho_o V_s^2}{\left(1 + \frac{4\pi a^3 \rho_o N}{m}\right)\exp\left(\frac{2\pi a^2 (P - 4a) N\rho_o}{m}\right) - 1} \tag{48}$$

Warren treated the cratering region of the target by dividing it into 10 uniformly spaced layers with increasing strength. This was done in an effort to account for the target material that is ejected out during entry of the projectile to create a conical crater. Comparison with experimental results showed that Warren's method provides reasonably accurate prediction of both depth of penetration and projectile deformation.

Forrestal, Frew, Hickerson, and Rohwer (2003) presented the effects of projectile velocity, projectile head radius, and concrete compressive strength on rigid-body penetration depth into conventional and enhanced-strength concretes. This study differed from previous studies in that accelerometers were embedded in the projectiles allowing time dependent deceleration data to be collected during penetration experiments. They found that the cavity expansion model, modified by post-test observations, predicted the penetration depth very well for 23 MPa (3 ksi) concrete but under-predicted penetration depth for 39 MPa (6 ksi) concrete. In previous experiments using data from smaller projectiles, the target strength term model predicted R=360 and R=460 for 23 and 39 MPa (3 and 6 ksi) concrete targets respectively. In this experiment, values of R=165 and R=360 were determined. The new data suggested that a diameter scale effect was not currently taken into account in these concrete penetration equations. They also determined that the target strength term, and not the inertial term, dominates the penetration process for striking velocities less than 460 m/s. Measured and calculated values of penetration depth agreed within 15%.

Frew, Forrestal, and Cargile (2006) conducted experiments to investigate the effects of target diameter on penetration deceleration and depth. They fitted the projectiles with single-channel acceleration data recorders. The measured decelerations and penetration depths were analyzed using penetration models developed by Forrestal et al. (2003). Their analysis suggested that target diameter has a negligible effect on penetration depths and deceleration magnitudes for conventional-strength concretes. This conclusion was made irrespective of the measured front face target damage.

He, Wen, and Guo (2011) proposed a spherical cavity expansion model for penetration of ogival-nosed projectiles into concrete targets with shear-dilatancy. They used a dilatant-kinematic constant to account for the effects of shear dilatancy and compressibility in the comminuted region. They computed the radial stress at the cavity surface, and then calculated the results of penetration using a numerical method. They concluded that shear strength plays a dominant role in determining target resistance.

Schwer (2009) reviewed previous research on strain-rate induced dynamic increase factors (DIF). Schwer concluded that at high strain rates, target material exhibited non-homogeneous deformations that negated the utility of the associated dynamic increase factor. Cargile et al. (2003) conducted normal impact experiments studying striking velocity versus depth of penetration of rigid projectiles into very-high-strength-concrete (VHSC) targets. The authors reported that approximately a 50% reduction in penetration is expected by using the VHSC versus conventional concrete.

The inclusion of fibers in VHSC did not improve the penetration resistance of a given strength of concrete significantly, but does provide for greater resistance to visible damage surrounding the penetration crater. Predictions of depth of penetration using a spherical-cavity expansion model with elastic-cracked-plastic regions agreed well with the experimental results. In recent years, efforts in investigating the response of ultra-high performance concrete targets for impact loading are documented in Unosson and Nilsson (2006), Habel and Gauvreau (2008), Millard, Molyneauz, Barnett, and Goa (2010), and SNL (2010). However, the application of cavity based analytical models for penetration of ultra-high performance/strength concrete targets is still lacking.

2.5 Numerical Methods

Numerical methods are based on arriving at numerical solutions of the governing differential equations of equilibrium through finite difference or finite element methods. They are a good choice for analyzing impact mechanics because there is virtually no limitation on the model size or geometric complexity that cannot be handled by the methods. However, numerical methods also have their drawbacks, such as the need for detailed material models (requiring a complete description of the material behavior in all loading regimes), geometries and the expertise needed for interpreting outputs.

The literature review presented here on numerical methods is focused only on published work that is directly applicable to the selected or similar finite element codes, associated material models, and treatment of highly distorted elements that will be used in this research.

AFAL (1987) examined two and three-dimensional computational approaches for simulating a steel projectile impacting a concrete target using the Elastic Plastic Impact Computation (EPIC) code. The research showed that for the data being analyzed the 3-D results were in general agreement with the two-dimensional results. Examples of oblique and yawed impacts were presented to demonstrate the benefits of the three-dimensional capability of the code.

Holmquist, Johnson, and Cook (1993) presented a constitutive model for concrete subject to high pressures, strains, and strain rates. The model, often referred to as the HJC model, expresses equivalent strength as a function of volumetric strain, damage, pressure and cohesive strength. The model allows damage to accumulate thereby reducing the effect of cohesive strength. The model relates pressure to volumetric strain using three response regions: elastic, transition, and locked. The elastic region accounts for the behavior where the pressure volumetric strain is described by the results of uniaxial stress compression tests when pressure is below the crushing pressure. The transition region accounts for crushing and the removal of air voids as the material is compressed beyond the elastic region. Finally, the locked region accounts for the behavior of the fully dense material.

Gold, Vradis, and Pearson (1996) used the CALE (Coupled Arbitrary Lagrangian Eulerian) code to conduct numerical computations on concrete penetration. The research concluded that the structure of the flow field around the penetrator is the most important element that governs target resistance. The results supported the use of a porous equation of state that produced a realistic elasto-plastic flow in the concrete medium.

Johnson, Beissel, and Stryk (2000) presented a generalized particle algorithm that allows for the efficient handling of severe distortions of a mesh caused by high velocity impacts. The paper also discussed challenges and suggested improvements for an improved generalized particle algorithm.

SWRI (2000) conducted a sensitivity analysis of the penetration depth in concrete to changes in the parameters of the Holmquist-Johnson-Cook (HJC) material model. Results of the study showed that unconfined compressive strength had the most influence on the calculated penetration depth. The pressure hardening exponent, normalized pressure hardening coefficient, and the minimum strain parameter comprised a group of the second most depth-sensitive parameters. The study was performed using the EPIC code and data from conventional-strength concrete tests.

Warren (2002) conducted finite element simulations of the penetration of limestone targets by ogive-nosed projectiles. The finite element mesh that was used to model the ogive-nosed projectiles was constructed with 2816 eight-node, constant strain hexahedral continuum elements, and had a total of 3197 nodes. Warren, however, did not discretize the concrete target nor use a contact algorithm in his research; instead he used a combined analytical and computational technique to model target resistance (Warren, 2002).

Johnson et al. (2004) summarized the issues associated with numerical modeling of ballistic impact problems. They present developments that improve the accuracy of finite element applications to this problem. They discuss a conversion algorithm that automatically converts distorted elements into particles. Finally, they provide example computations that demonstrated agreement with test data.

Zukas (2004) provided an excellent overview of the use of hydrocodes for running computations of events involving high strain rates. Zukas covered methods of discretization, kinematics, material behavior, Langrangian methods, Euler methods, particle methods, and much more than can be summarized here. Of particular interest is his discussion of EPIC. Zukas (2004) states that EPIC was the first wave propagation code to use finite elements, preceding DYNA by a year. He also discussed the importance of sliding interfaces, rezoning, erosion, conversion, and viscosity.

Tham (2005) conducted AUTODYN-3D simulations on the perforation and penetration of reinforced concrete targets. Tham examined three constitutive models. The first constitutive model assumed a constant yield strength, the second assumed a pressure-dependent yield strength, and the third assumed a pressure-dependent yield strength, a damage function, and a strain-rate hardening function. He found improvements in the model predictions when the pressure-dependent yield was assumed and greater improvement was achieved when pressure-dependent yield strength, a damage function, and a strain-rate hardening function were assumed.

Tham (2006) conducted numerical simulations of 3-CRH steel ogival-nose projectile with a mass of 2.3 kg fired against cylindrical concrete target with a striking velocity of 315-m/s using AUTODYN 2-D. He assessed three numerical schemes, (Langrangian, Coupled Euler–Lagrangian, and Coupled Smooth Particles Hydrodynamics (SPH) – Lagrangian) for predicting the maximum depth of penetration into concrete targets. Simulations using the Coupled SPH - Lagrangian numerical scheme gave the best overall agreement with the experimental data.

Rosenberg and Dekel (2008) used AUTODYN to conduct three sets of numerical studies. The first set of computations involved the symmetric expansion of a cavity inside various metal spheres. The second set of computation involved the asymmetric expansion of a cavity inside various metal spheres, and finally the last set of computations involved the expansion of a cylindrical cavity inside of various metal targets.

Wang, Li, Shen, and Wang (2007) investigated the penetration of concrete targets by ogive-nose steel projectiles. They used LS-DYNA with a proposed erosion algorithm to study the maximum penetration depth as well as perforation of thin targets. The LS-DYNA results with the proposed erosion algorithm were found to provide better cratering and spalling results than those produced by material models Type 78 and Type 111 found inside the LS-DYNA material library.

Numerical methods for predicting projectile penetration into concrete (such as finite element methods) have been well established. The accuracy of these methods remains highly dependent upon the accuracy of the concrete material models chosen. Material models that incorporated pressure-dependent yield, damage, and strain-rate hardening typically provided the most accurate results. Finite element methods must be capable of handling highly distorted elements through the use of alogrithms such as erosion or conversion.

CHAPTER 3: NUMERICAL MODEL DEVELOPMENT AND VALIDATION BASED ON EXISTING EXPERIMENTAL PENETRATION DATA

3.1 Overview

The objective of this chapter is to present an overview of the published experimental penetration data used in this research, to present the development of the finite element models used for analyzing the material flow of concrete during penetrations, and to present the validation of the finite element models based upon comparison to the published experimental penetration data.

3.2 Description of Penetration Experiments and Data Sets from the Literature

Any approach for studying the material flow of concrete during projectile penetration is constrained by the lack of a dedicated, statistically significant, amount of test data. Test data exists, but it is very limited (especially in open literature) and often lacks the appropriate experiments needed to fully characterize the concrete's material properties. Figure 1 shows the extent of the published data with sufficient information for use in a detailed numerical simulation effort. The Elastic Plastic Impact Computation (EPIC) finite element code and its built-in concrete material models were used to carry out the in-depth investigation of this research. To capture the complexity of the problem, the effects of varying concrete compressive strength and projectile diameter, nose shape, and striking velocity on the target response to projectile penetration into concrete were analyzed.

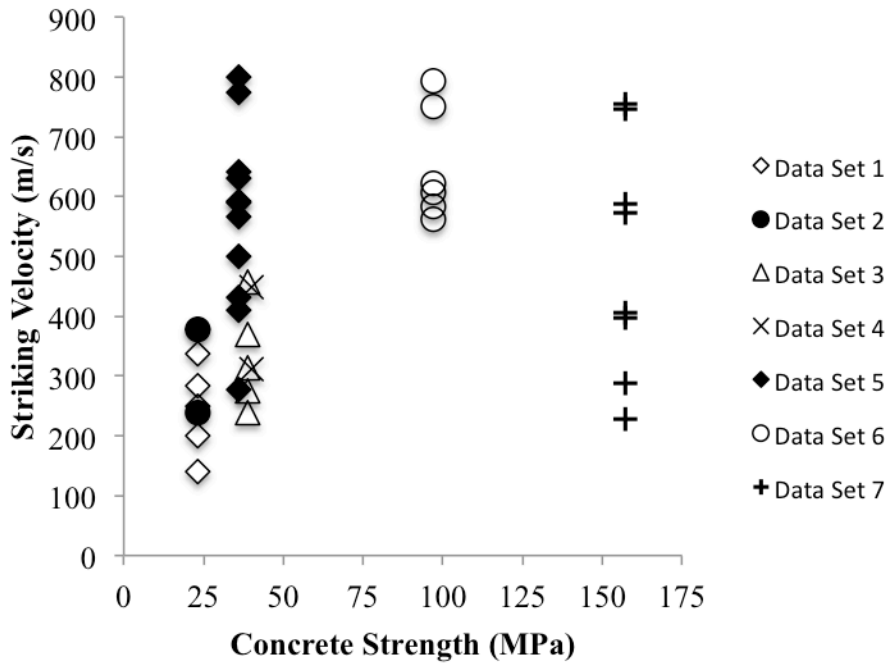

Figure 1. Research Domain for Concrete Strength and Striking Velocity Data from the Literature. (Forrestal et al., 2003, Forrestal et al., 1994 and USAERDC, 1999).

The projectile-striking velocities ranged from approximately 200 to 800-m/s. In this velocity range, projectiles have negligible deformation and can therefore be treated as rigid. Further, the target material parameters, such as strength, stiffness, hardness, and toughness govern the depth of the penetration within this velocity regime. Beyond this velocity range projectiles typically erode as they penetrate the target, and the depth of penetration becomes better governed by the Alekseevskii–Tate model (Chen and Li, 2004). The first four sets of data were based on experiments conducted using a 76.2-mm diameter projectile, while the remaining three sets of data were based on experiments using a 26.9-mm diameter projectile. For the purpose of this dissertation, it is convenient to refer to the 76.2-mm diameter as the large projectile and the 26.9-mm projectile as the small projectile. The large projectiles were about 13 times the mass of the small projectiles. All projectiles were made of 4340 R_c45 steel and had ogive-shaped noses. Some data existed at velocities below 200-m/s; but at these velocities, the projectiles did not penetrate the target (Forrestal et al., 2003).

Forrestal et al. (2003) published depth of penetration data for ogive-nosed projectiles impacting 23-MPa (3.3-ksi) and 39-MPa (5.7-ksi) concrete strengths. The 23-MPa (3.3-ksi) concrete was mixed using granite aggregate while the 39-MPa (5.7-ksi) concrete was mixed using limestone aggregate. The density of the granite mixture was 2040 kg/m^3 (0.074-lb/in^3) and the density of the limestone mixture was 2250 kg/m^3 (0.081-lb/in^3). Concrete compressive strength tests and penetration tests were conducted between 140 and 460 days after concrete placement. The projectiles were machined from 4340 Rc45 steel. The strength of 4340 Rc45 steel at high strain rates is well over 1500-MPa, which is well above the strengths of the concretes tested (LANL, 1994). The 76.2-mm projectiles were launched using an 83-mm powder gun. Striking velocities, which did not exceed 500-m/s because of the gun limitations, were measured using a Hall Intervalometer System. Each of the projectiles contained a void, which allowed for the insertion of a single-channel data recorder and accelerometer. Measurements of the projectile's deceleration in the target (up to 13,000 G) were available. Pitch and yaw angles were determined by evaluating pictures from a high-speed digital framing camera. Pitch and yaw did not exceed 4 degrees, and are therefore assumed to be normal for the purposes of this research. Tests showed that for each event a conical entry crater, about two projectile diameters deep, followed by a circular tunnel region, slightly wider than the projectile diameter, was formed. Little to no deformation or abrasion of the projectiles occurred during the experiments and consequently they were reused as needed. Hence, the projectiles in this study are assumed to be rigid. It is worth mentioning that abrasion models exist in literature such as the one presented by Silling & Forrestal (2007). However, these models typically only include the relationship between axial forces and velocities, and do not account for tangential tractions or friction.

Forrestal et al. (2003) found that the target resistive values determined from these tests suggested a projectile diameter scaling effect. Their analysis also showed that the strength properties of the concrete dominated the experimental results, and that target inertial effects were less important. Penetration depths for these experiments are shown in Table 2 through Table 5.

Table 2. Data Set 1, 23-MPa (3-ksi) 3 CRH, Concrete Penetration Data

Shot Number	Striking Velocity (m/s)	Penetration Depth (m)
06/2	139.3	0.24
03/1	200.0	0.42
02/2	250.0	0.62
01/1	283.7	0.76
05/3	336.6	0.93
04/4	378.6	1.18

Table 3. Data Set 2, 23-MPa (3-ksi) 6 CRH, Concrete Penetration Data

Shot Number	Striking Velocity (m/s)	Penetration Depth (m)
08/2	238.4	0.58
07/1	378.6	1.25

Table 4. Data Set 3, 39-MPa (6-ksi) 3 CRH, Concrete Penetration Data

Shot Number	Striking Velocity (m/s)	Penetration Depth (m)
11/3	238.1	0.30
12/4	275.7	0.38
09/1	314.0	0.45
10/2	369.5	0.53
14/5	456.4	0.94

Table 5. Data Set 4, 39-MPa (6-ksi) 6 CRH, Concrete Penetration Data

Shot Number	Striking Velocity (m/s)	Penetration Depth (m)
15/2	312.5	0.61
16/3	448.5	0.99

Forrestal et al., (1994) published depth of penetration data for ogive-nosed projectiles impacting 36-MPa (5-ksi) and 97-MPa (14-ksi) concrete in 1994. The density of the 36-MPa (5-ksi) and 97-MPa (14-ksi) concrete was 2370-kg/m^3 (0.086-lb/in^3) and 2340-kg/m^3 (0.085-lb/in^3) respectively. Concrete samples were taken at the time of target fabrication to test the unconfined compressive strength of the concrete, including compression tests that were performed at the time of the experiment. The projectiles were machined from 4340 steel and heat-treated to a hardness of R_c 43-45. The 26.9-mm projectiles were launched using an 83-mm powder gun. Projectiles were fitted with plastic sabots and obturators to achieve a proper fit in the gun tube. The sabot strips and obturators fell away from the projectile prior to target impact. Striking velocities with this projectile-gun combination reached as high as 800-m/s.

All penetration experiments were conducted between 30 and 60 days after concrete placement. For all trials, the projectiles impacted normal to the target with the pitch and yaw measurements less than one degree. Based on these experiments, Forrestal et al. (1994), proposed a dimensionless factor, S, linked to the resistive capabilities of the target. The S value for the 36-MPa (5-ksi) target was determined to be 12, while the S value for the 97-MPa (14-ksi) target was determined to be 7. The S value is worth mentioning here because the work done in this research may help reduce the reliance on the use of an empirical S value when seeking analytical solutions. Table 6 and Table 7 show the penetration data collected from these experiments.

Table 6. Data Set 5, 36-MPa (5-ksi) 2 CRH, Concrete Penetration Data

Shot Number	Striking Velocity (m/s)	Penetration Depth (m)
1	591	0.51
2	590	0.73
3	631	0.61
4	642	0.62
5	773	0.87
6	800	0.96
14	277	0.17
13	410	0.31
15	431	0.41
11	499	0.48
12	567	0.53

Table 7. Data Set 6, 97-MPa (14-ksi) 2 CRH, Concrete Penetration Data

Shot Number	Striking Velocity (m/s)	Penetration Depth (m)
2	561	0.35
1	584	0.38
3	608	0.42
4	622	0.44
6	750	0.63
5	793	0.61

USAERDC (1999) published depth of penetration data for ogive-nosed projectiles impacting Very High Strength Concrete (VHSC). Striking velocities were measured using a streak camera. Pitch and yaw were kept under 4 degrees and were measured using flash X-rays just prior to impact. Projectiles were fitted with plastic sabots and obturators to fit the 83-mm smooth bore gun. VHSC is made by carefully selecting aggregate material to improve gradation and increase strength and density. In the mix, reactive materials are maximized and water content is minimized. Pressure is applied prior to setting and then heat treatment is applied after setting. The result is concrete with strengths several times greater than conventional concrete. USAERDC (1999) reported that penetration into the 157-MPa concrete was about 50% of that into 36-MPa concrete (USAERDC, 1999). Table 8 lists the results for penetration tests into VHSC.

Table 8. Data Set 7, 157-MPa (23-ksi) 2 CRH, Concrete Penetration Data

Shot Number	Striking Velocity (m/s)	Penetration Depth (m)
1	406	0.18
2	587	0.30
3	287	0.13
4	747	0.44
5	573	0.29
6	754	0.46
7	397	0.16
8	229	0.08

3.3 Finite Element Analysis

The finite element procedures were completed on two computing systems running five computer software programs as shown in Figure 2. CUBIT, Tecplot, MATLAB and Excel were run on a local machine, while EPIC and Tecplot were run on a High Performance Computing System (HPCS) at the U.S. Army Engineer Reseach and Development Center (ERDC) in Vicksburg, Mississippi. The HPCS is a part of the DoD Supercomputing Resource Center. The computational framework for this research is shown in Figure 2.

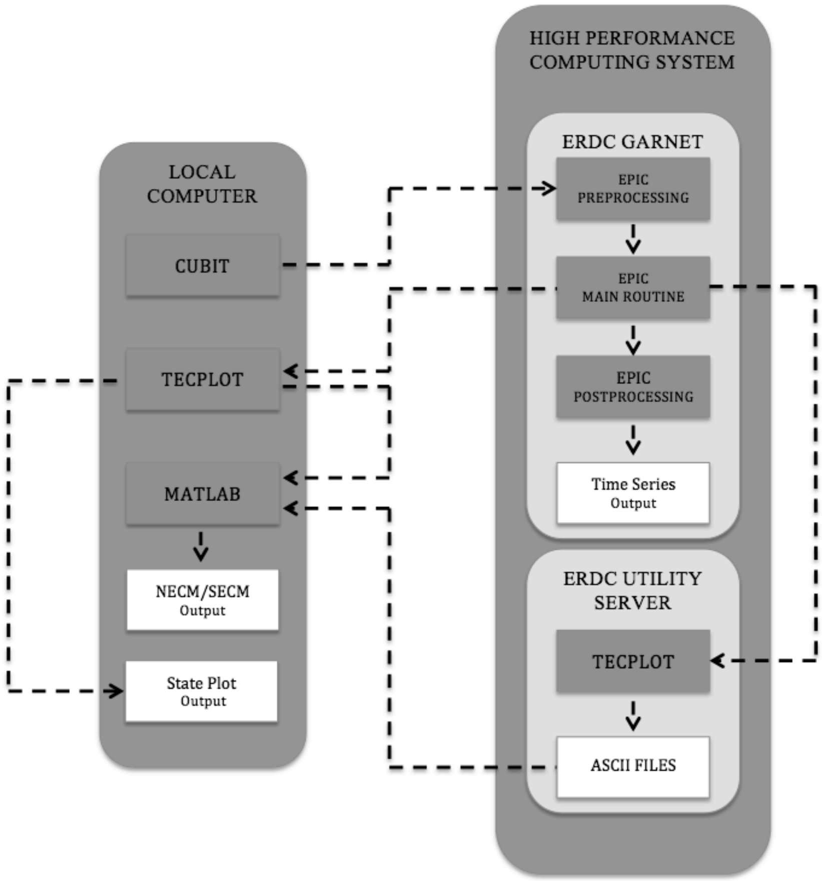

Figure 2. Computational Framework

The inputs to the system, which include the detailed geometry and material parameters, as well as the general impact variables defining the event are not shown, but are an integral part of the system. The finite element code EPIC is located on the Garnet machine as shown in Figure 2. Garnet is a Cray XE6 running a Linux operating system that can be accessed remotely through eight login nodes. EPIC jobs were submitted to and managed by a batch queuing system.

3.3.1 Geometry Development of Projectiles and Targets in CUBIT

The 3-D geometries and finite element meshes of the projectiles and targets were created using the CUBIT Automated Geometry and Mesh Generation Toolkit (SNL, 2014). CUBIT provides a graphical user interface for generating meshed geometries and several tool kits for verifying the quality of a finite element mesh. All geometries were developed as 3-dimensional half geometries that were symmetric about their X-Z plane and set at Y=0. Using the half-geometries resulted in the saving of computational time and provided improved visibility of the targets' velocity vectors without slicing the geometry through the center of the target.

At a top level, the steps in the CUBIT meshing process are as follows:

- Identify key coordinates of the quarter geometry
- Connect the coordinates with curves forming a 2-D surface
- Sweep the surface 90 degrees to create a quarter-geometry solid model
- Decompose the quarter-geometry by partitioning
- Imprint and merge the geometry
- Set interval sizes for each curve in the volume
- Set meshing schemes for surfaces and sub-volumes
- Mesh the geometry
- Copy/reflect the geometry to form a half geometry
- Merge and imprint geometry
- Specify the boundary conditions, and finally
- Export the mesh to a Genesis file.

The three variations of projectiles used in this study are shown in Table 9. Figure 3 and Figure 4 detail two variations of the large (76.2-mm) projectiles that were developed to resemble the projectiles used in Forrestal et al. (2003). The first variation of the large projectile had a caliber radius head (CRH) of 3, while the second variation had a CRH of 6. The CRH is a measure of nose pointiness. It is related to the radius of the ogive, S and the diameter of the projectile, $D_{projectile}$, as shown in eqn. (49).

$$S = CRH \times D_{projectile} \tag{49}$$

Table 9. Projectile Configurations

Type	Nominal Mass (kg)	Caliber Radius Head	Length (mm)	Shank Diameter (mm)	Tail Diameter (mm)	Center of Gravity (from tail) (mm)
1	13.0	3	530.73	76.2	80.01	251.46
2	13.0	6	528.47	76.2	80.01	239.34
3	0.91	2	242.4	26.9	26.9	113.9

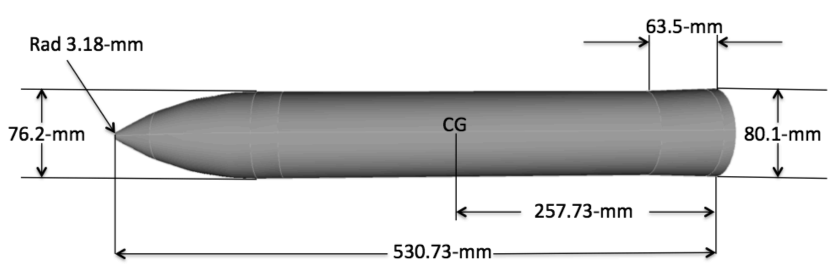

Figure 3. Large (76.2-mm) Projectile with 3-CRH Ogive Nose

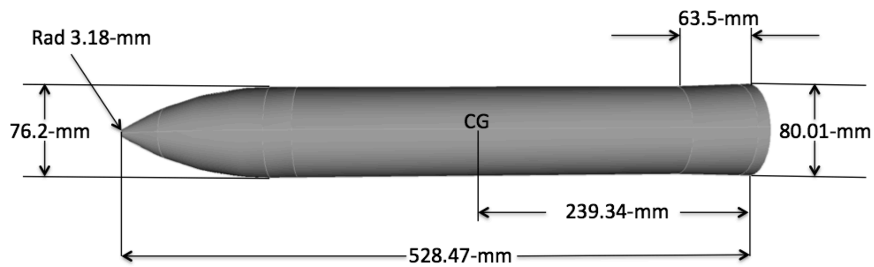

Figure 4. Large (76.2-mm) Projectile with 6-CRH Ogive Nose

Note that the tail of the projectile flares out to 80.01-mm and the nose of the projectile is blunted. The flattened nose has a radius of 3.18-mm.

Figure 5 details the 26.9-mm projectile that was developed to resemble the projectiles used in Forrestal et al. (1994) and USAERDC (1999). The projectile had a CRH of 2. The type of projectile used in these experiments was hollow containing an approximately 166-mm by 10-mm void along its longitudinal axes. Placement and exact size of the void was adjusted during geometry development to fit the mass and center-of-gravity of the projectile.

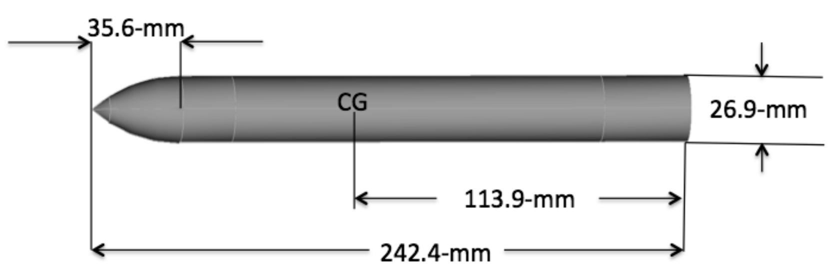

Figure 5. Small Projectile, 26.9-mm Diameter, 2-CRH, 0.91-kg

The geometries of the projectiles were developed by first plotting the key vertices in two dimensions (Figure 6). The coordinate system in CUBIT was dimensionless, but the vertices were plotted such that they could be imported into EPIC as metric units. The vertices were connected using lines and curves from the CUBIT geometry toolbox and then grouped to form a planar surface. The surface was then swept 90 degrees about the Z-axis to create a quarter-volume.

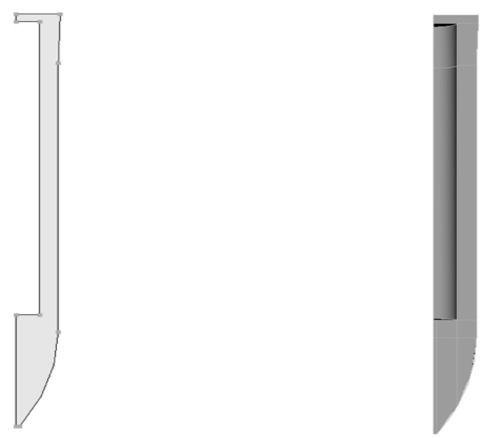

Figure 6. CUBIT Surface Geometry and Quarter Volume

The radius of curvature of the nose is defined by eqn (49). The quarter volume was then decomposed using planar and cylindrical cuts, such that the axial cross section of the geometry was uniform (sweepable) along each sub-volume as shown in Figure 7.

Figure 7. Decomposed Quarter Volume

The sub-volume that comprised the projectile nose was meshed first. As a representative example, the nose of the 0.906-kg projectile (referred to as the small projectile) is shown in Figure 8.

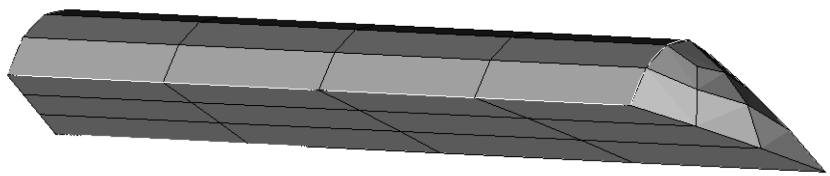

Figure 8. First Meshed Subvolume of the Projectile Nose

CUBIT's automatic meshing function could not determine a meshing solution on its own for this particular geometry. Therefore, to mesh the nose, each curve in the sub-volume was first assigned an interval ensuring that the intervals matched along opposite edges of the geometry. The surfaces of the wedge-shaped ends were then meshed using the pave meshing scheme. The pave scheme automatically meshes an arbitrary three-dimensional surface with quadrilateral elements. The paver allows for easy transitions between dissimilar sizes of elements and element size variations such as the curved pointy nose of the projectile. The generated mesh is well formed with nearly square elements that are perpendicular to the boundaries (Blacker and Stephenson, 1991). The three remaining surfaces on the volume were meshed using the map mesh scheme. The map mesh scheme automatically meshes a surface (or volume) with a mesh of quadrilaterals (or hexahedra) where each interior node on a surface (or volume) is connected to 4 (or 6) other nodes (SNL, 2014). Finally, the volume was meshed using the sweep meshing scheme in a direction from the curved nose-surface to the opposite planar end of the sub-volume. The sweep scheme can automatically mesh a volume by translating or rotating a topologically similar surface along a single axis from a source to target surface (SNL, 2014).

Next, the adjacent section of the projectile nose was added as shown in Figure 9. Again, the edge intervals were defined making sure that the interval matching criteria was met. The planar sides of the volume were paved and the curved surface was mapped. The mesh is swept starting from the first paved side and ending with the second paved side.

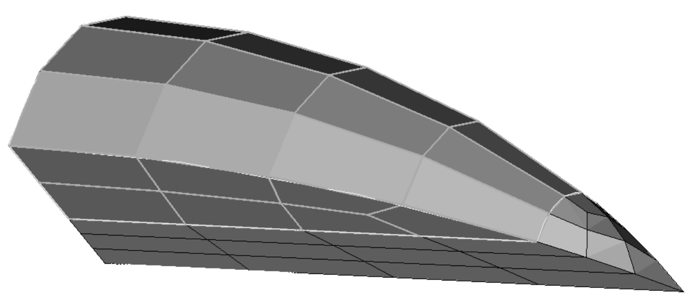

Figure 9. First and Second Meshed Subvolumes of the Projectile Nose

Subsequent sub-volumes of the projectile were meshed by setting the intervals on each of the undefined edges and then applying CUBIT's automatic meshing function to the unmeshed sub-volumes. The meshed quarter-volume (Figure 10) was then reflected axially upon itself to produce the 3-D meshed half-volume. Figure 11 depicts this volume. Note the formation of a void inside of the geometry. This void was left empty for the three projectile models used in this research, but it could easily be filled with a filler material if needed. The projectile shown in Figure 6 through Figure 11 is the 0.906-kg projectile, which is the smaller of the two projectiles, used in this research.

Figure 10. Fully Meshed Quarter Volume

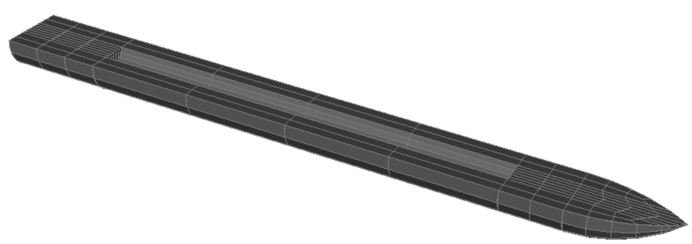

Figure 11. Fully Meshed Half Volume

The larger, 13-kg projectile, was created in a similar fashion as the smaller projectile, but required extra sub-volumes to account for the blunt nose of the projectile.

Care had been taken to start the meshing process at the nose of the projectile and proceeding towards the tail of the projectile in order to get the volume to mesh properly.

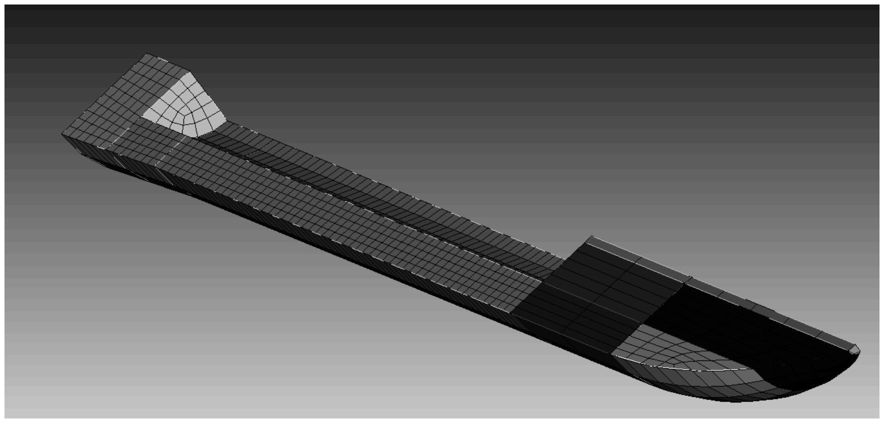

Figure 12. Fully Meshed Quarter Volume of the 13-kg Projectile

For all data sets, the targets were cast inside galvanized corrugated steel culverts. As such, each target had a cylindrical geometry, but the height and radius of the cylinder varied. A typical cylindrical target geometry is shown in Figure 13. There were a total of 10 target variations as shown in Table 10. The culvert diameters ranged from 0.76-m to 1.83-m. In all cases, the target-diameter to projectile-diameter ratio was at least 24. This ratio ensured that no large cracks would reach the outer edge of the concrete thereby causing misleading depth of penetration values. The culverts were not included in the finite element models of the targets. The projectile-diameter ratio was assumed to be sufficiently large such that the culvert's presence would not be noticed. This assumption was verified by running two finite element models with the culvert in place for data set 5 at 600-m/s. The results of these two finite element runs showed that the presence of the culvert had no effect on the depth of penetration. Appendix 10 has a similar analysis on the effects of using soakers on the outer surface of the target. Similarly, it was found that the target's side and bottom surface boundaries were too far from the penetration event to play a significant role in the penetration depth.

The target lengths varied from 0.76-m to 1.83-m. In all cases, the length of the target was at least twice the depth of penetration. Finally, concrete strengths varied from 23-MPa (3-ksi) to 157-MPa (23-ksi). For the purposes of this research, the 157-MPa concrete is considered enhanced-strength.

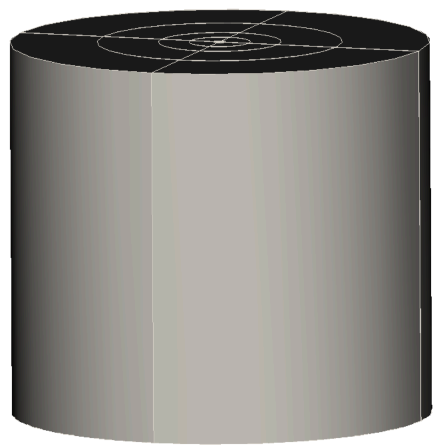

Figure 13. Typical Cylindrical Target Geometry

Table 10. Target Configurations

Type	Concrete Strength MPa (psi)	Diameter (m)	Length (m)
A	39 (5,656)	1.83	1.83
B	39 (5,656)	1.83	1.22
C	23 (3,335)	1.83	1.83
D	23 (3,335)	1.83	1.22
E	157 (22,771)	0.76	0.91
F	36 (5,000)	1.22	1.83
G	36 (5,000)	1.37	0.91
H	36 (5,000)	1.37	0.76
I	36 (5,000)	1.37	1.07
J	97 (14,000)	1.37	1.22

Target geometries were created using the same meshing process. Each of the targets was meshed using a finer-sized mesh along the center axis and a coarser mesh along the outer perimeter of the target. Because of this, the computational time was reduced considerably, but the mesh in the region of high pressure and strain contained adequate detail for the model to provide good results. Mesh dimensions for each of the models are shown in Appendix 5. As shown in Figure 14, the projectile and target were initially separated by 1 mm to keep the two geometries and materials separate.

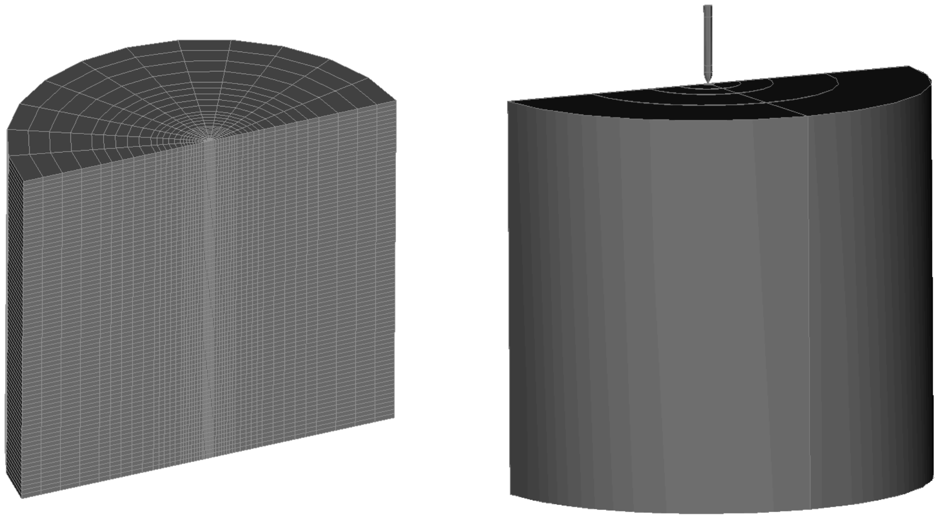

Figure 14. Meshed Target Half-Volume and Projectile-Target Pair

The 3-D half-geometries of the projectiles and targets were created using hexahedron elements, but were later converted to tetrahedrons using EPIC's pre-processor. EPIC converts each hexahedron element into 24 tetrahedrons. This two-step meshing process ensured that the tetrahedral elements were arranged in a symmetric manner, thereby, minimizing the potential for unwanted tetrahedral mesh locking. Table 11 shows the mesh sizes for a representative set of data. Mesh size information for the other data sets can be found in Appendix 5.

Table 11. Mesh Geometry for Data Set 5

Geometry Summary	Projectile	Target	Total
Number of Nodes	2,061	840,626	842,687
Number of Elements	8,256	3,964,160	3,972,416
Average Element Volume (m^3)	6.86E-09	2.69E-07	2.69E-07
Maximum Element Volume (m^3)	3.37E-08	1.68E-06	1.68E-06
Minimum Element Volume (m^3)	4.22E-10	4.48E-10	4.22E-10
Average Aspect Ratio	0.162182	0.231186	0.231042
Maximum Aspect Ratio	0.616392	0.49266	0.616392
Minimum Aspect Ratio	0.0238	0.031049	0.0238
Average Minimum Height (m)	0.0012	0.003674	0.003669
Maximum Minimum Height (m)	0.00216	0.009541	0.009541
Minimum Minimum Height (m)	0.000343	0.000299	0.000299

3.3.2 Numerical Computation in EPIC and Selected Material Models

Numerical modeling was performed using the 2011 Elastic Plastic Impact Computation (EPIC) code. EPIC is an explicit Lagrangian Finite Element Analysis (FEA) code designed to model short-duration high-velocity impacts. During short-duration high-velocity impacts, it is very difficult to measure stress, strain, pressure, and temperature with any degree of certainty. Consequently, a constitutive model of material behavior is needed. EPIC was chosen in this research because of its large library of concrete material models that are readily available to study short-duration dynamic events. The two concrete constitutive models used in this research are the HJC model developed and named after Holmquist, Johnson, and Cook (1993) and the Advanced Fundamental Concrete (AFC) model (USAERDC, 2010). The material model parameters are derived from quasi-static stress-strain tests and wave propagation experiments such as split-Hopkinson bar, plate impact tests, expanding ring tests, coplanar bar impacts and other sources.

The HJC concrete model is a computational constitutive model for concrete that includes the effects of material damage, high strain rate, and permanent crushing. The model relates the normalized equivalent stress in concrete to the normalized pressure by the relationship given in (50).

$$\sigma^* = \left[A\left(1-D\right)+BP^{*N}\right]\left[1+C\ln\dot{\varepsilon}^*\right] \tag{50}$$

where σ^* is the equivalent stress normalized by the unconfined compressive strength, D is the damage factor, P^* is the normalized pressure, ε^* is the dimensionless strain rate, A is the normalized cohesive strength, B is the normalized pressure hardening coefficient, N is the pressure hardening exponent, and C is the strain rate coefficient. If D = 0 the concrete is undamaged and if D = 1 the concrete is fractured. The model accumulates damage from equivalent plastic strain and plastic volumetric strain. The asterisks represent normalization by dividing the value by the unconfined compressive strength of the concrete.

Three pressure-volume response regions are considered. The first region is the linear elastic region, which occurs when the pressure is less than the crushing pressure. The second region is the transition region, which occurs between the crushing pressure and the locking pressure. The third region is the comminuted region, which occurs above the locking pressure and it is where the concrete is compressed into a fully dense material. Porous materials like concrete compact irreversibly under compression, crack and separate in tension, and yield under shear. As pressure increases, however, the shear strength increases as well. Pressure constants are obtained from shock Hugoniot data.

Two-dimensional tests using the HJC constitutive concrete model compared reasonably well to experimental data (Johnson, 2009).

In EPIC, the HJC model requires inputs for up to 30 model parameters, which can be grouped into six categories -- mass/thermal properties, strength properties, pressure properties, artificial viscosity, facture properties, and total failure strain. A complete description of each of these variables is presented in (Holmquist, Johnson, and Cook, 1993).

With knowledge of a few key parameters, however, reasonable results can be achieved by approximating the less sensitive parameters. Thacker (SWRI, 2000) conducted a probabilistic sensitivity analysis of the HJC concrete model parameters. In this study, Thacker developed an importance ranking of the parameters in a conventional-strength concrete and found that the unconfined compressive strength had the most influence on the computed penetration depth. In this research, existing HJC models were varied only by changing the unconfined compressive strength. All other material properties were left as defined by the original material model.

Adley et al. (USAERDC, 2010) provides an overview of the AFC model and states that the model simulates irreversible hydrostatic crushing, material yielding, plastic flow, and material damage. The report also states that the model has a nonlinear, pressure-volume relationship, a linear shear relationship, strain-rate hardening effects for the failure surface, and it separates the hydrostatic response from the deviatoric response. The compressive hydrostatic behavior in the AFC model is the same model used in the HJC. The shear behavior model, however, varies based upon the sign of the first invariant (tension vs compression) and by a factor that is a function of the third invariant of the deviatoric stress tensor. This allows the model to differentiate between the extension and compression failure surfaces due to the inclusion of the third invariant.

3.3.3 Numerical Model Validation Using Depth of Penetration Data Sets

To validate the models developed in EPIC, the results of the numerical computations were compared to the seven sets of test data published by Forrestal et al. (1994), Forrestal et al. (2003), and USAERDC (1999). For each experimental data set, simulations were run with both the HJC and AFC constitutive material models. The numerical models predicted depth of penetration reasonably well when compared to experimental Data Sets 3-7. However, the numerical models did not agree well with the results of the experimental Data Sets 1-2.

For data set 3, Figure 15, the HJC model predicts the depth of penetration with a Root Mean Square (RMS) error of 11%. The AFC had a RMS error of 12.6%. The HJC model, however, performed very well for striking velocities below 375-m/s. In this range, the RMS error was approximately 1.8%.

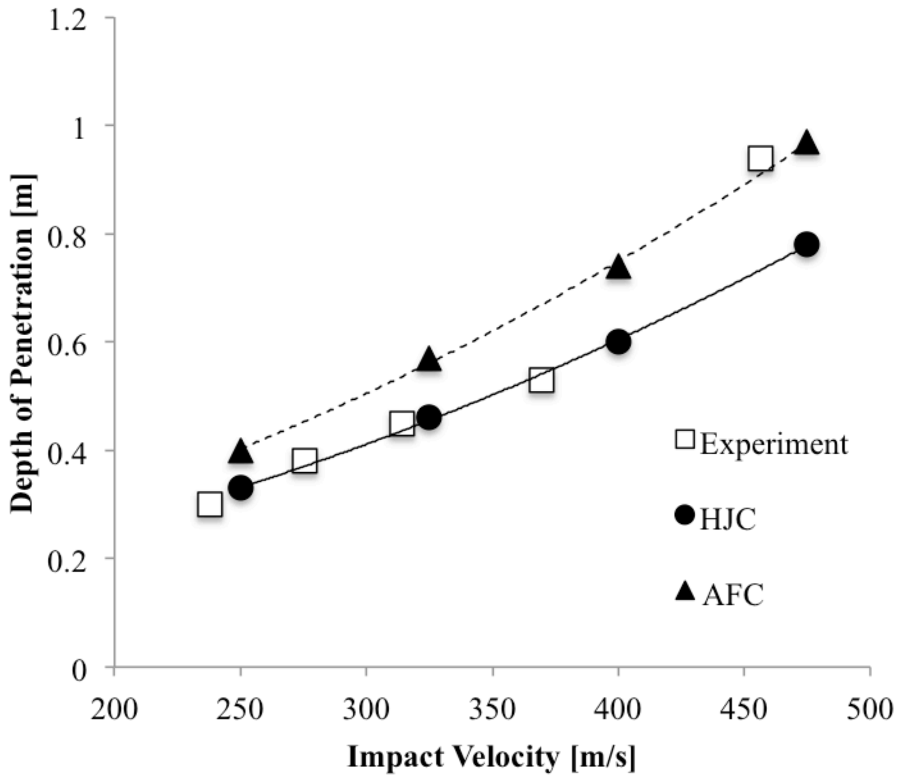

Figure 15. Comparison of EPIC Output to Test Data (Data Set 3)

Data Set 4 (Figure 16) shows the penetration results for the 6 CRH projectiles into 39-MPa concrete. The AFC model predicted the depth of penetration result better than the HJC model when compared to the experimental data. AFC predictions had a RMS error of 8.2% while HJC predictions had a RMS error of 12.2%.

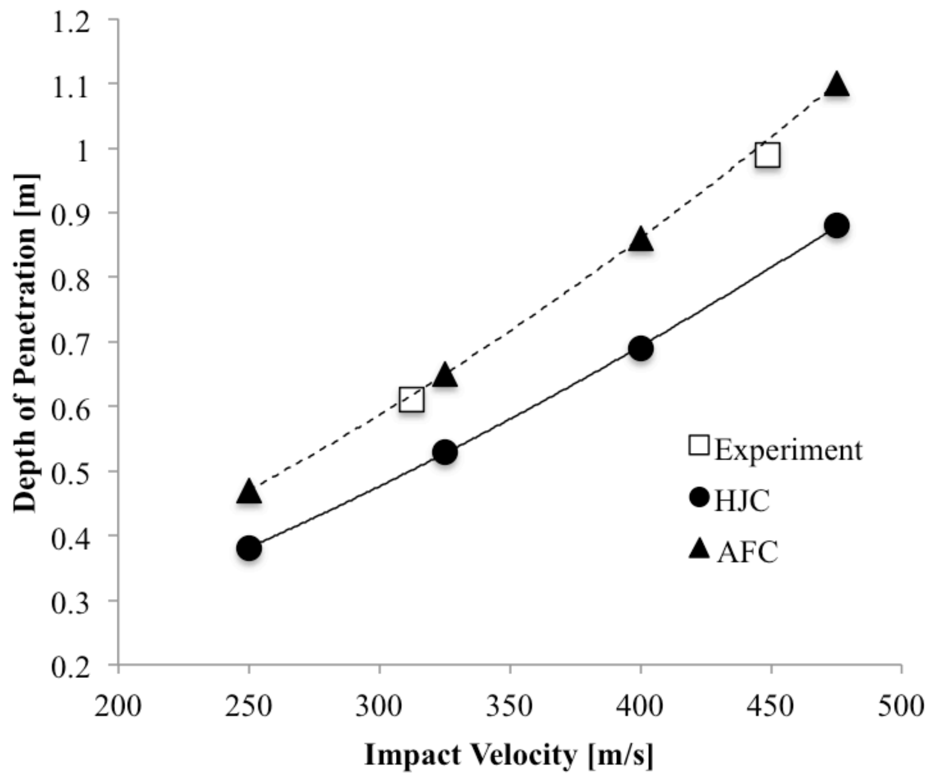

Figure 16. Comparison of EPIC Output to Test Data (Data Set 4)

The AFC and HJC models provide an upper and lower bound for Data Set 5 (Figure 17). The HJC model is consistently lower than the test values. HJC predictions had a RMS error of 9.6%. The AFC had a RMS error of 6%.

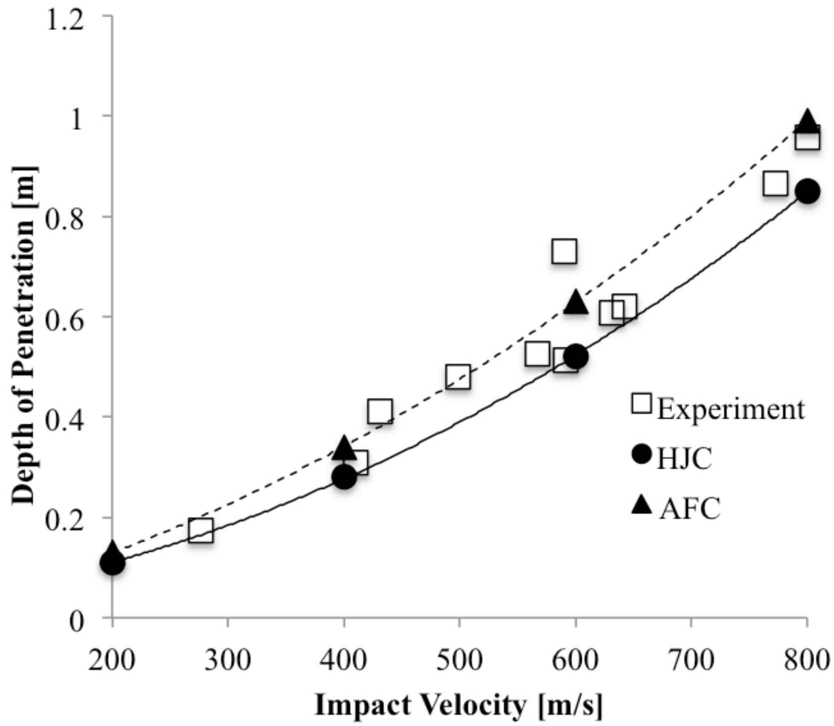

Figure 17. Comparison of EPIC Output to Test Data (Data Set 5)

Results from both the HJC and AFC models agree very well when compared to test values from Data Set 6 (Figure 18). The HJC RMS error is 8.7% and the AFC RMS error is 4.8%.

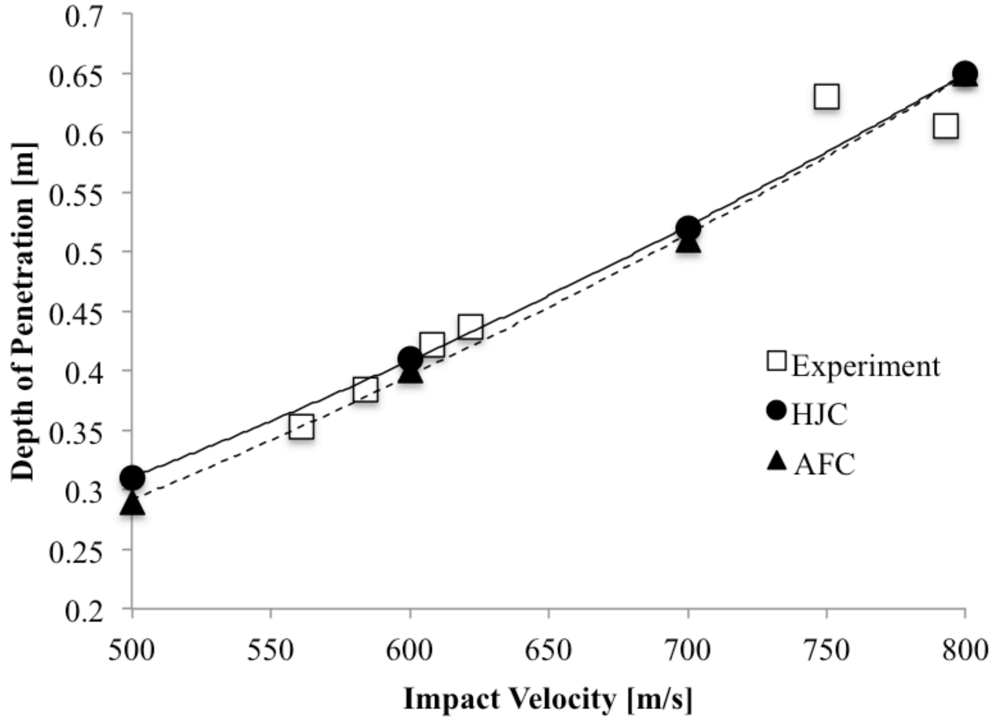

Figure 18. Comparison of EPIC Output to Test Data (Data Set 6)

Results from both the HJC and AFC models agree very well when compared to test values from Data Set 7 (Figure 19). The HJC model had a RMS error of 4.1%, while the AFC model had a RMS error of 3.5%. It is worth noting that in comparisons of the numerical results to experimental data for Data Sets 3-7, the AFC model performed better than the HJC model at high impact velocities.

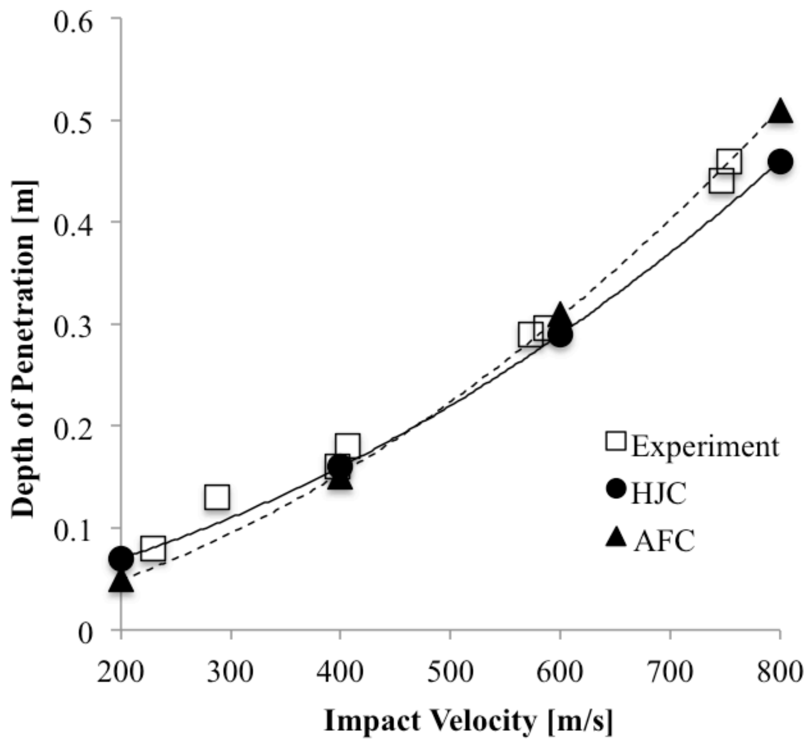

Figure 19. Comparison of EPIC Output to Test Data (Data Set 7)

Data Sets 1 and 2 contained data for penetration into 23-MPa concrete made with quartz aggregate. An adequate material model was not identified to characterize this aggregate. In the absence of a quartz aggregate-based concrete model, a limestone aggregate-based model, with a modified compressive strength of 23-MPa, was examined. The results did not adequately reflect the experimental data. As many different material models were examined, only a single representative example of the results are shown in Figure 20.

Therefore, the material flow studies in the upcoming chapters focused only on finite element models developed for Data Sets 3-7.

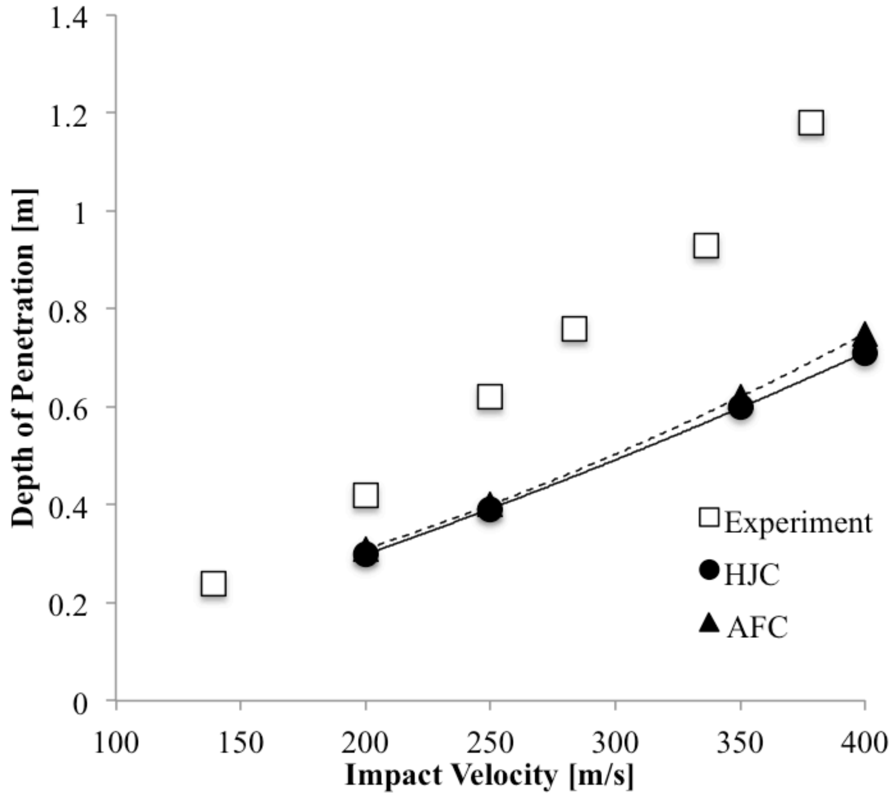

Figure 20. Comparison of EPIC Output to Test Data (Data Set 1)

The HJC model and the AFC model both predicted depth of penetration with similar accuracy for Data Sets 3 through 7. In this dissertation, the HJC model was selected because of its ability to accurately predict depth of penetration, because of its availability in finite element models such as EPIC and LS-DYNA, and because of the availability of a sensitivity study conducted by SWRI (2000).

CHAPTER 4: CAVITY EXPANSION COMPARISON METHODOLOGIES

4.1 Overview of the Cavity Expansion Comparison Methodologies

The objective of this chapter is to present the development of quantitative methodologies that can be used to determine the material flow response of a given target using outputs from a numerical computation. The approach taken here is to determine the material flow response by investigating the direction of particle and node velocities around the nose of projectiles at various times during a given penetration event. The vector field shown in Figure 21 provides a qualitative view of a nodal vector field during a projectile's tunneling phase.

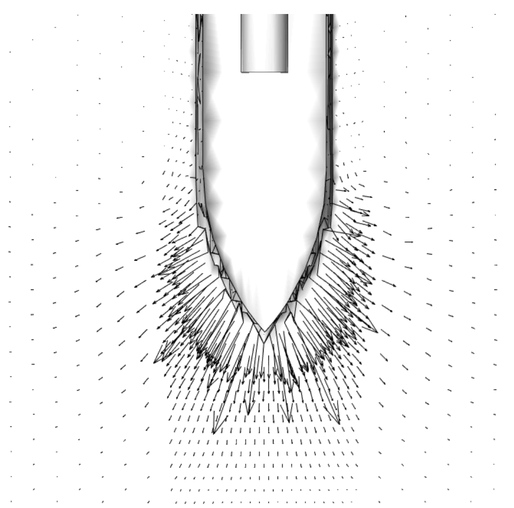

Figure 21. Cross-Sectional View of Projectile During Tunneling Phase

The arrows represent the magnitude and direction of the velocity of each node in the target mesh. Qualitatively, the material movement in Figure 21 has spherical characteristics, but quantitative methods of assessing the shape of this cavity expansion are needed.

Two methodologies were developed to address this need. They are referred to as the Normal Expansion Comparison Methodology (NECM) and the Spherical Expansion Comparison Methodology (SECM). Both these methodologies provide a means of assessing how material flow deviates from either ogive-normal or spherical expansion quantitatively as a function of time, depth, velocity, or material strength.

The procedure used to compare numerical analysis output from EPIC to ogive-normal or spherical expansion is summarized in Figure 22.

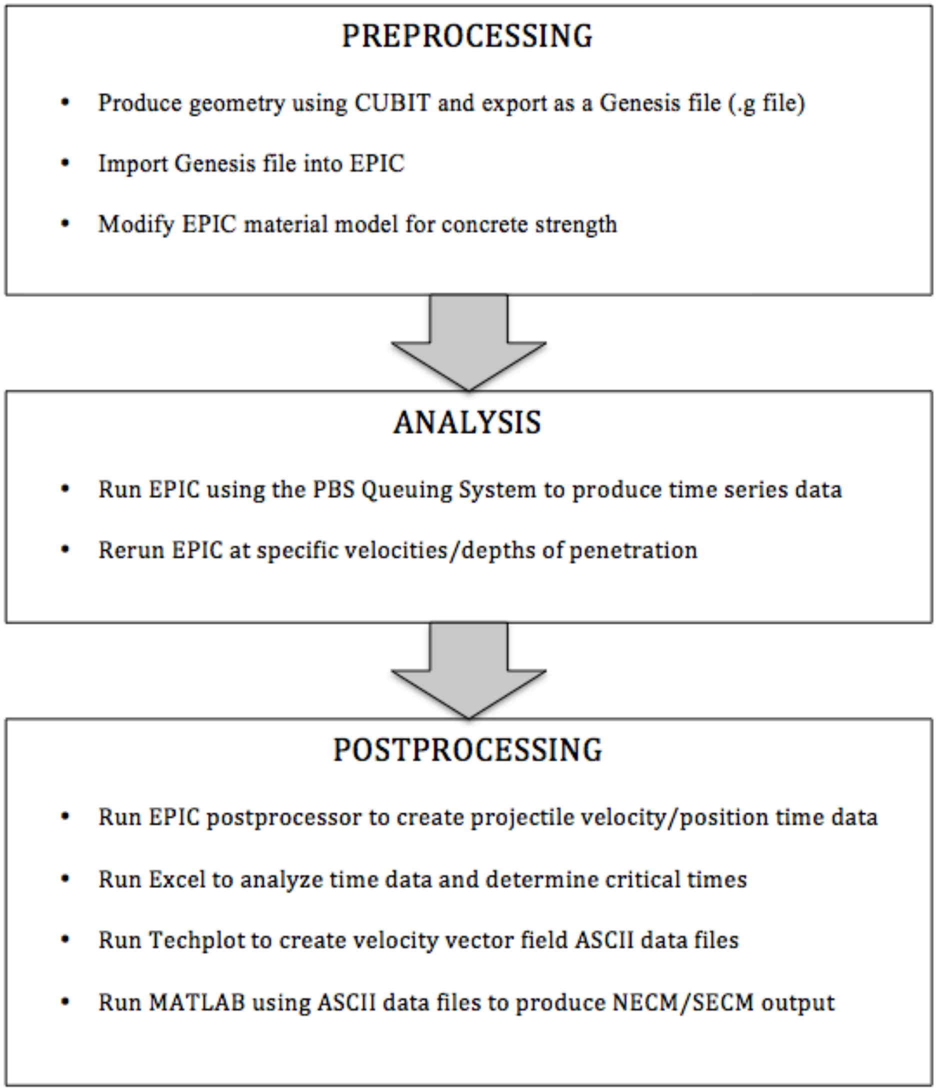

Figure 22. Finite Element Analysis Procedure

The data for each critical time step was examined individually. Once the data for a particular time step was imported into MATLAB the following steps were taken:

- Identify particles or nodes of interest
- Define position vector for each particle or node
- Determine the velocity vector for each particle or node

- Plot the velocity direction (angle the velocity vector makes with the negative z direction) vs. the particle/node location (angle the position vector makes with the negative z direction).
- Bin results into 1 degree bins
- Determine direction of the resultant vector for all velocities in each bin
- Plot the resultant velocity direction vs particle/node location

Appendices 7 and 8 show the MATLAB codes that were developed for the purpose of evaluating the concrete material expansion. Although the codes were not designed to be production codes, an effort was made to provide user-friendly options such as choosing the type of projectile to be used in a given run and turning on and off graphical outputs. As a research code, the MATLAB program allowed maximum flexibility for analyzing node and particle velocity data from different perspectives.

4.2 Expansion of Meshless Particles

As a projectile penetrates a concrete target at high velocity, the target mesh becomes severely distorted along the projectile-target interface. Severe grid distortions are a problem for Lagrangian codes because the time step is often coupled to the size of the smallest element in the mesh. Further, depending upon mesh geometry, large distortions can sometimes cause local stiffening and locking of the mesh. EPIC provides the user with an option to convert severely distorted elements into meshless particles. Both these particles and the surrounding mesh can be seen in Figure 23.

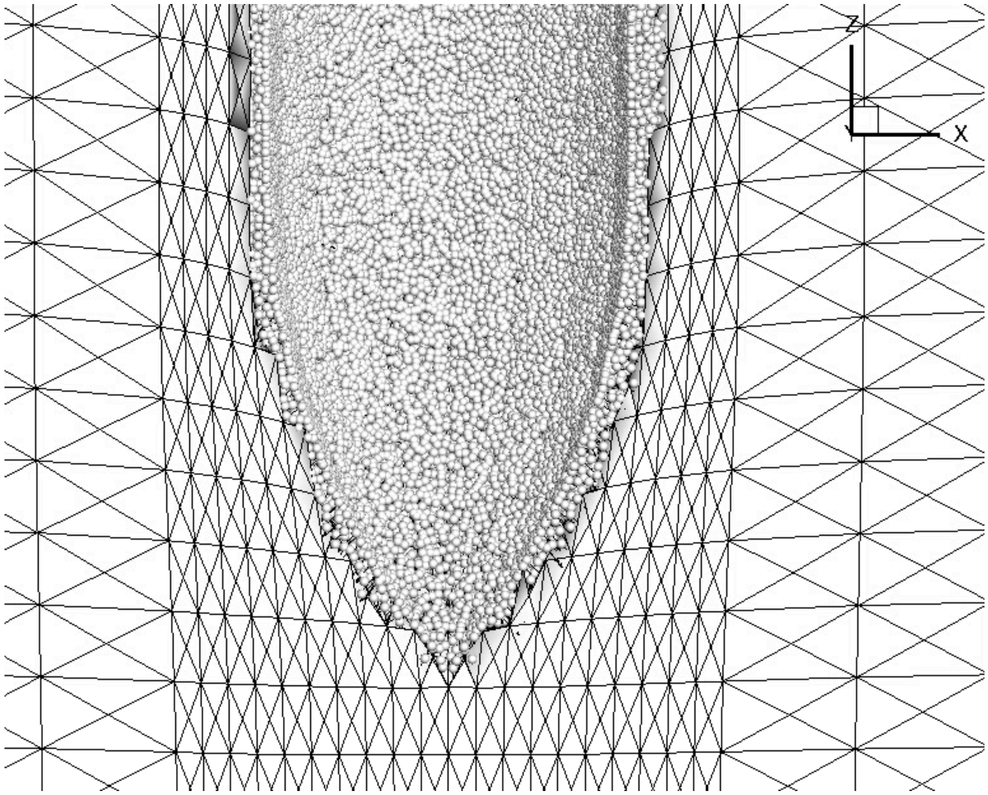

Figure 23. Concrete Mesh and Meshless Particles

Figure 24 demonstrates the upward movement of particles towards the projectile's entry point. The particles with velocity vectors forming an angle of less than 90 degrees with the negative z axis are shaded in dark while the particles with velocity vectors forming an angle greater than 90 degrees with the negative z axis are shown in white. Approximately one-third of the particles are moving downward. The remaining two-thirds of the particles are either moving outward or upward.

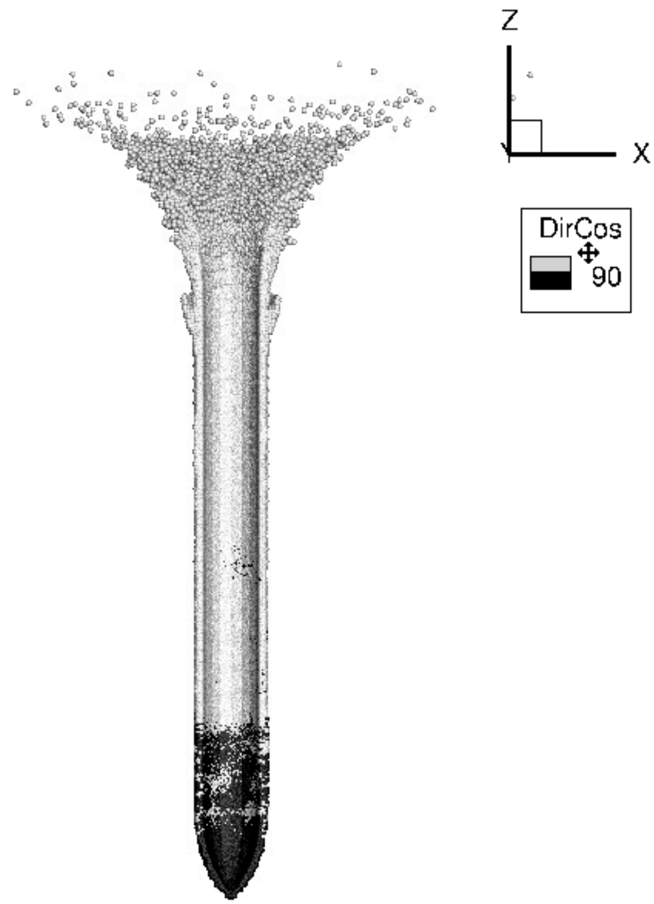

Figure 24. Meshless Particle Flow for Data Set 5
600-m/s DOP=0.3-m (Dark Particle's Velocity
Vector is Less than 90 Degrees with z-Axis)

Figure 25 depicts a converted target mesh during projectile penetration for 36-MPa concrete. In order to see the meshless particles more clearly, the projectile layers of the output were deactivated. The general shape of the projectile nose, however, is easily discernable since the meshless particles surround the projectile-target boundary. The conversion option works well on concrete penetration problems because physically, the concrete along the projectile-target boundary exceeds its failure point during the event. The comminuted concrete has no tensile stresses, but continues to have mass, volume, velocity and compressive strength similar to meshless particles. As the projectile moves forward, it continues to exert force on the meshless particles forcing them to interact with the intact concrete elements or to move up and out towards the entry point of the target. The predicted movement of comminuted concrete out of the projectile tunnel is consistent with observed material behavior during penetration experiments such as Tham (2005), and Frew et al. (2006).

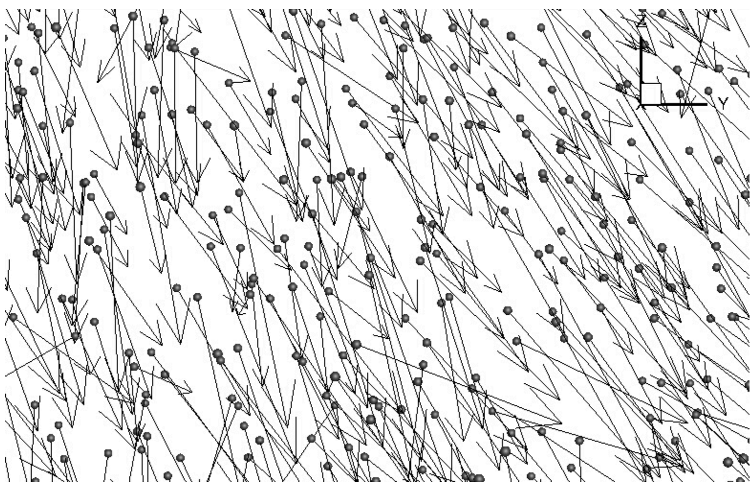

Figure 25. Meshless Particle Velocity Vectors

Individual meshless particles move in various directions as shown in Figure 25. The movement of an individual particle is quite complex and varies greatly from one particle to the next. The net-flow of material, however, is of greater interest than the seemingly random motion of individual particles. The direction of the net-flow through a surface can be estimated by determining the direction of the net particle velocity through that surface. This is true only when the particle sizes and densities are relatively constant.

If particles sizes and masses vary widely then momentum must be conserved and in effect heavier particles are weighted more strongly when determining the average velocity.

It is worth noting that EPIC has an alternative option for handling extremely distorted elements. This alternative option is known as erosion. In this option, the highly distorted elements are simply removed from the model leaving a void in the place of the distorted elements based a pre-defined limit such as element failure strain. Details of erosion algorithms are extensively covered in literature for example Zukas (2004), Belytschko and Lin (1987). However, this method typically results in over-prediction of penetration depths because the presence of voids allows the projectile to move forward and occupy the empty space without incurring the resistive forces afforded by meshless particles.

For penetration problems in the velocity regime of this study (200-800-m/s) conversion was only required for the target materials. The steel projectile remained intact, and little to no projectile material underwent distortions great enough to require conversion. This rigid-projectile model behavior is supported by the state of post-impact projectiles where little to no deformations were observed as reported in Forrestal et al. (1994), Forrestal et al. (2003) and O'Neil et al. (1994). The mesh size of the projectile and target had to be within an order of magnitude of each other in order to prevent unwanted erosion or conversion of the projectile nose.

If there are no forces other than those applied by the advancing nose of the projectile, the concrete particles at the nose of the projectile are imparted with a velocity that is downward and outward in a perfectly ogival-expansion pattern. Figure 26 depicts concrete particles in contact with the projectile nose. The location of these particles along the nose of the projectile can be identified using a variable angle θ_R that falls between θ_{R1} and θ_{R2}. If a particle moved outward and normal to the surface of the projectile, the velocity vector of that particle would be parallel to its ogival position vector ($\theta_V = \theta_R$). In this dissertation, the condition where $\theta_V = \theta_R$ for all particles is referred to as ogive-normal expansion.

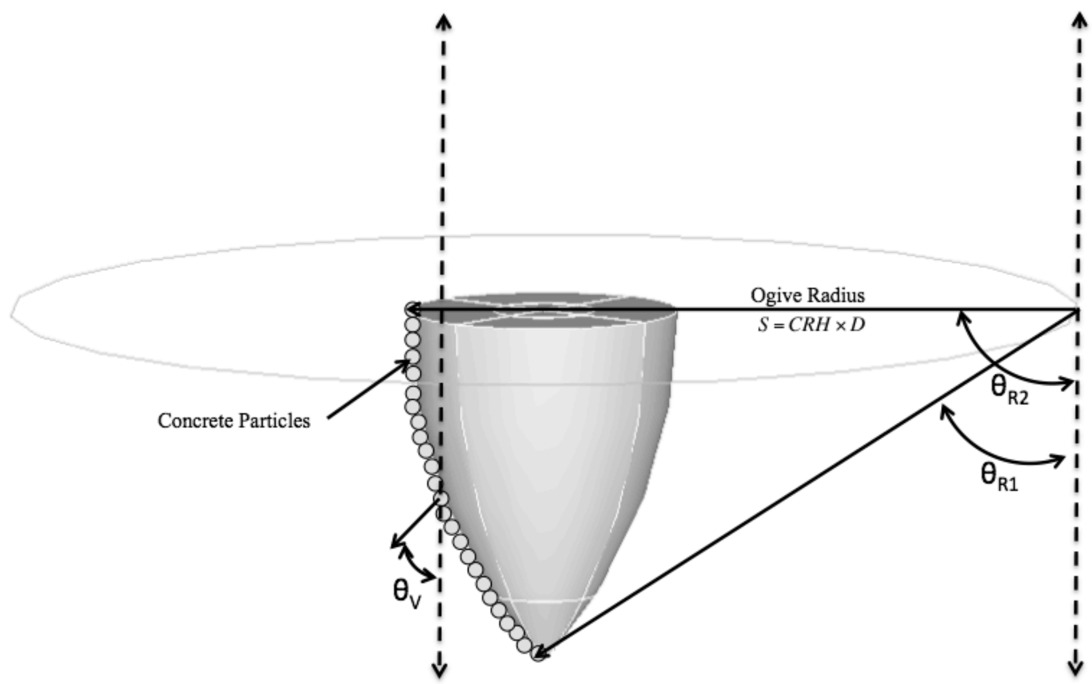

Figure 26. Ogival Expansion of Meshless Particles

NECM can be used to calculate the average θ_V as a function of θ_R. This is achieved through a series of MATLAB operations. The first step is to isolate the meshless particles surrounding the nose of the projectile at any particular time of interest.

Each particle is isolated by selecting only those particles below the shoulder of the projectile and within two concentric ogival shells: one at the radius of the ogive and the other at 4-mm beyond the radius of the ogive (See Figure 27). The 4-mm thickness was determined by trial and error, but was proven to capture over 99% of the particles for the projectile geometries studied. All the position, velocity, and pressure information is carried with the particles, as they are isolated.

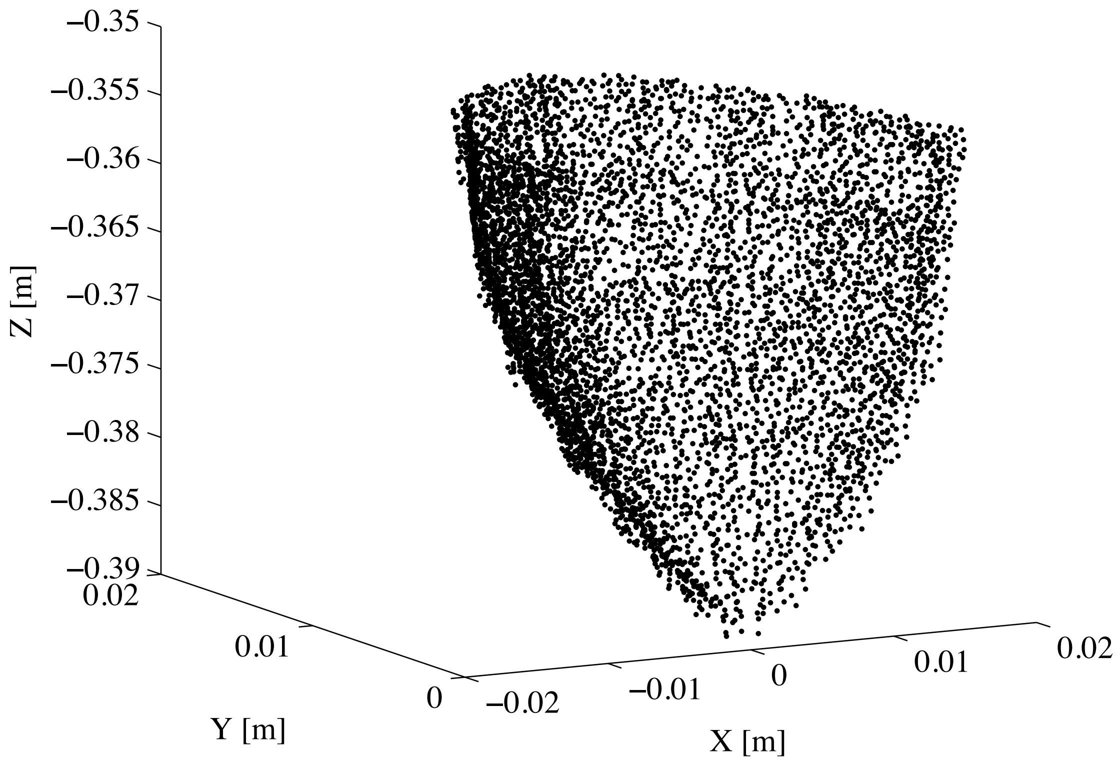

Figure 27. Plot of Meshless Particles DS5, 600-m/s at time 0.85-ms

The next MATLAB operation is to determine the values of θ_R and θ_V for each particle. A typical plot of θ_V vs. θ_R is shown in Figure 28. Each value of θ_R has several corresponding values of θ_V. This is because θ_R represents a ring of meshless particles encircling the outer surface of the projectile nose. Although the particle velocities vary, a clear linear trend is discernable from the scatter plot.

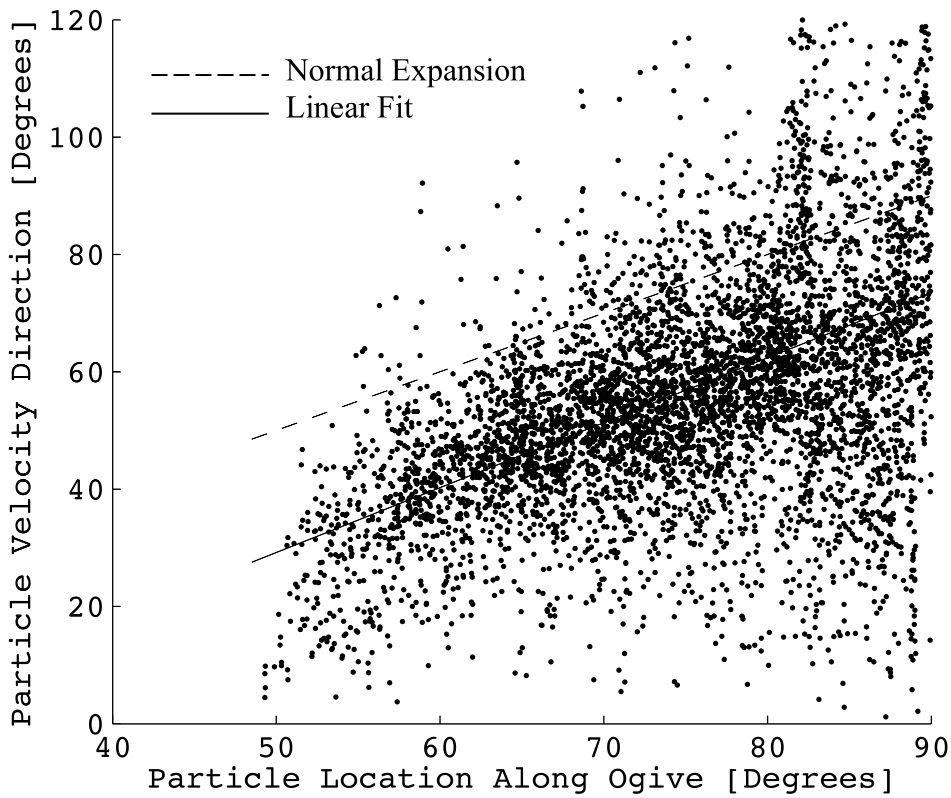

Figure 28. Meshless Particle Direction Versus Ogival Position for DS5, 600-m/s at 0.85-ms

Since each of the data points in Figure 28 represents a vector, a single net vector can be determined for each position along the ogive by binning the vectors into one-degree groups along θ_R. The direction the net vector makes with the z-axis can then be reported as an average value for that particular bin. The result of binning the data in Figure 28 is shown in Figure 29. It is worth noting that the linear fit of the binned data is slightly different than the linear fit for the un-binned data. Thought was given to identify which fit provides a better explanation of material flow. It was determined that the binned fit was a better representation because it is based on vector addition.

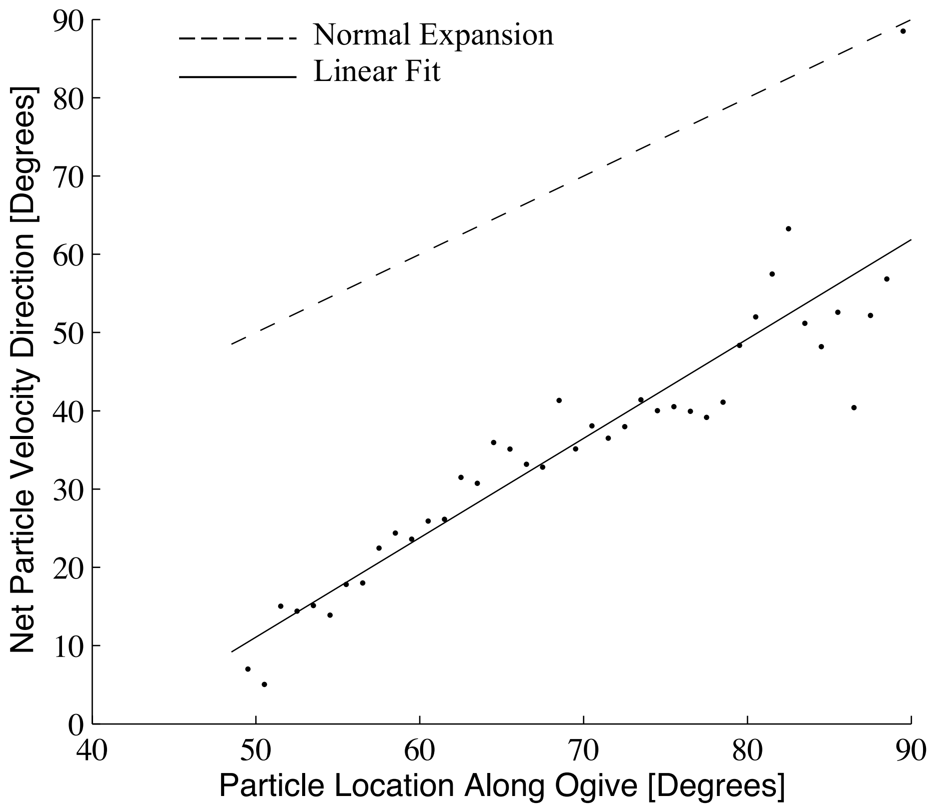

Figure 29. Average Particle Direction Versus Ogival Position for DS5, 600-m/s at 0.85-ms

Ogive-normal expansion is typically assumed in cavity expansion analysis. That is, the velocity direction of the concrete particles along the projectile-target interface are assumed to be normal to the outer surface of the projectile nose as shown in Figure 30a. The normal velocity at any point along the nose is then determined by multiplying the projectile velocity by $\cos(\theta_R)$. This practice is perfectly acceptable as ogive-normal is the direction of the applied force from the projectile surface.

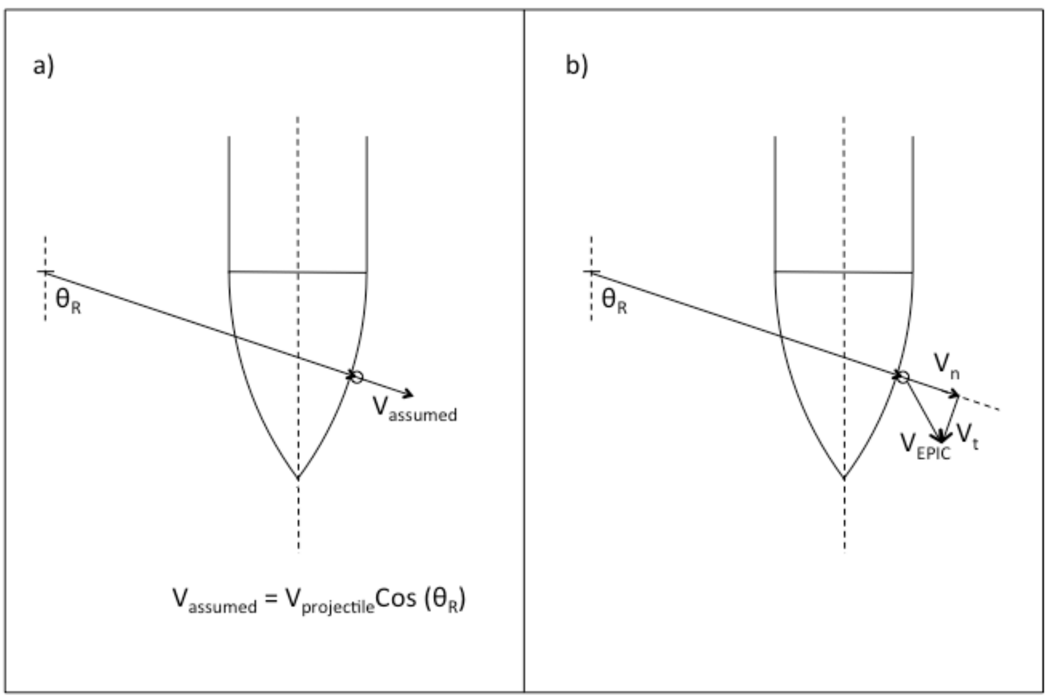

Figure 30. Typical Velocity Assumption vs EPIC Velocity
a) Assumed Normal Velocity b) EPIC Derived Velocity

In a real penetration event, however, the projectile force is not the only force acting on a particle. The forces exerted on the concrete at the projectile-target interface are very complex and dependent upon the material parameters of the target. The meshless particle velocities found in our EPIC computations, in fact, were not necessarily normal to the surface of the projectile. In this case, NECM can be used to determine the normal component of the EPIC velocity as shown in Figure 30b. NECM does this by calculating $\Delta\theta_V$ (the difference between the direction of the velocity vector and the ogival position vector) and then determining V_{normal} as

$$V_{normal} = V_{EPIC} \cos(\Delta\theta_V) \tag{51}$$

4.3 Expansion of Element Nodes

As the target material fails, EPIC converts the failed elements into meshless particles. These particles become trapped between the projectile and the concrete mesh as shown in Figure 31. The meshed elements adjacent to the projectile-target boundary experience significant pressure, and the concrete's failure limits change based on the material's constitutive properties.

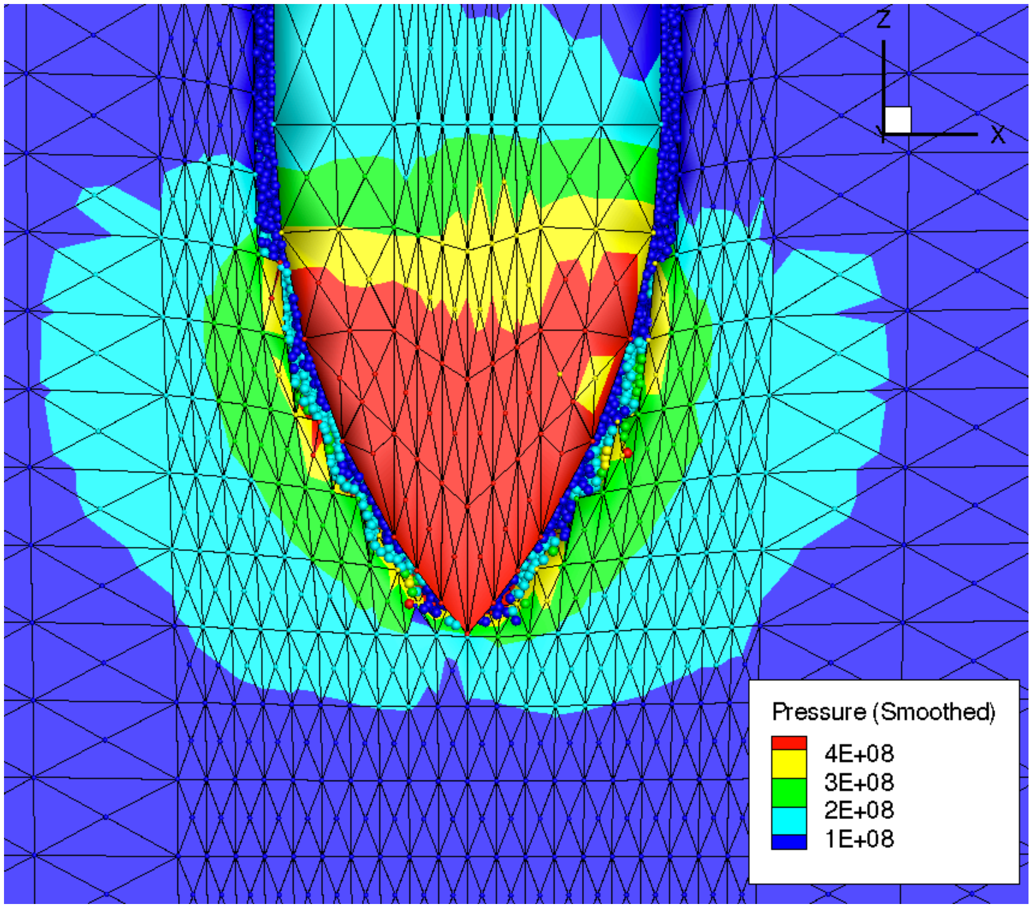

Figure 31. Projectile Penetration into Concrete

Figure 31 is a typical pressure distribution for 36-MPa concrete. Note that the highest pressures within the intact concrete mesh occur along the sides of the projectile nose and not in front of the nose. The steel nose of the projectile also reaches high pressures, but the pressures achieved in this velocity regime are not high enough to cause projectile material failure. The net force of the particles act on the intact concrete mesh causing material flow similar to that shown in Figure 32 where the velocity vectors have been attached to the nodes of the mesh.

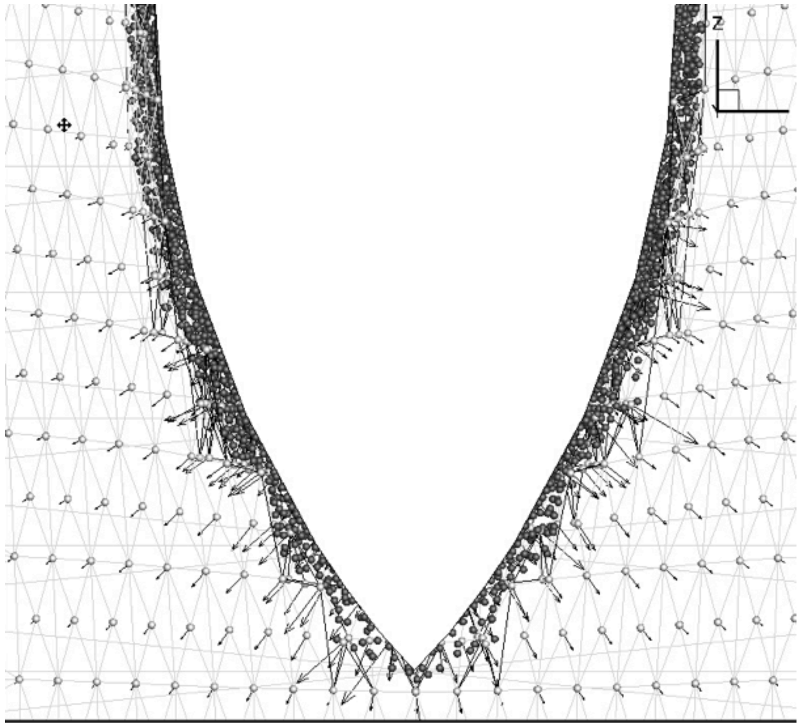

Figure 32. Nodal Velocity Vector Field

The flow of material in the intact concrete mesh can be assessed in a similar way to the meshless particles of the previous section. It is useful, however, to compare the nodal movement of the target material to spherical cavity expansion as shown in Figure 33.

In Figure 33, the bottom half of a spherical shell is shown surrounding the tip of the projectile. The shell has an inner radius equal to the radius of the projectile ($R_{projectile}$) and an outer radius 4-mm larger than the radius of the projectile ($R_{projectile} + 4mm$). The direction of motion for each node that lies within the spherical shell and is part of the intact target mesh can be assessed. The node shown in Figure 33 has a velocity vector v and a position vector r. The angle between v and r can be determined from $\theta_v - \theta_r$. If θ_v

and θ_r are equal for all nodes within the spherical shell, then the concrete is undergoing spherical cavity expansion.

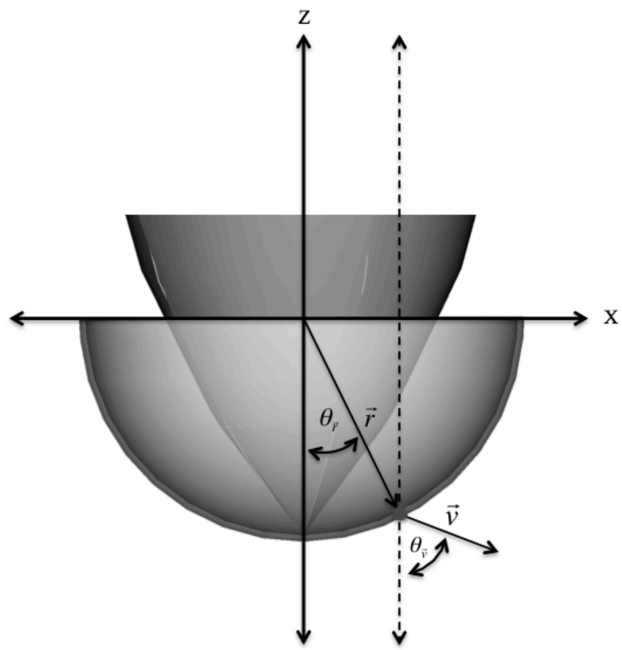

Figure 33. Position Vector and Velocity Vector of Spherical Shell of Radius (R_{proj})

As a representative example, the nodes forming a spherical shell around the projectile nose for Data Set 5 at a 600-m/s striking velocity are shown in Figure 34. The inner radius of the shell was selected to be one projectile radius (13.45-mm) and its thickness was set at 4-mm. The hemispherical shell was centered along the longitudinal axis of the projectile, one projectile radius (13.45-mm) above the tip of the projectile nose.

Using the center of the sphere as the origin, the angles the velocity vectors of each node made with the negative z-axis were plotted against the angle that the position vector of each node made with the negative z-axis. The result is shown in Figure 35.

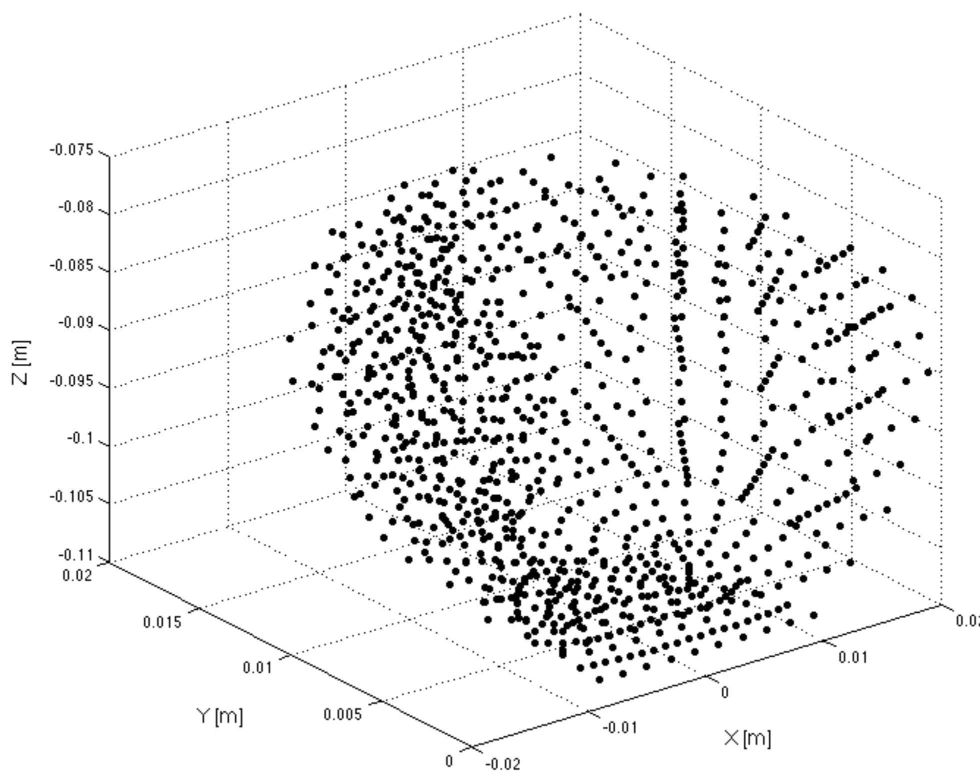

Figure 34. Spherical Quarter Shell Containing Target Nodes

The data in Figure 35 was sorted by node location into 1-degree bins along the independent axis. The velocity vectors for all nodes within a given bin were then summed together forming a single resultant vector. The angle this resultant vector made with the negative z-axis was then plotted as a single point representing all vectors inside the bin.

Figure 36 shows the scatter plot of the resultant value of the bin versus the location of the node along the sphere. The slope and offset of the linear fit to this scatter plot provided a quantitative measure for the direction of material flow. If the flow of material for a given run were spherical, the slope of the linear fit to the data in Figure 36 would be approximately 1 and the offset would be zero. This ideal case was plotted as a dashed line for reference purposes.

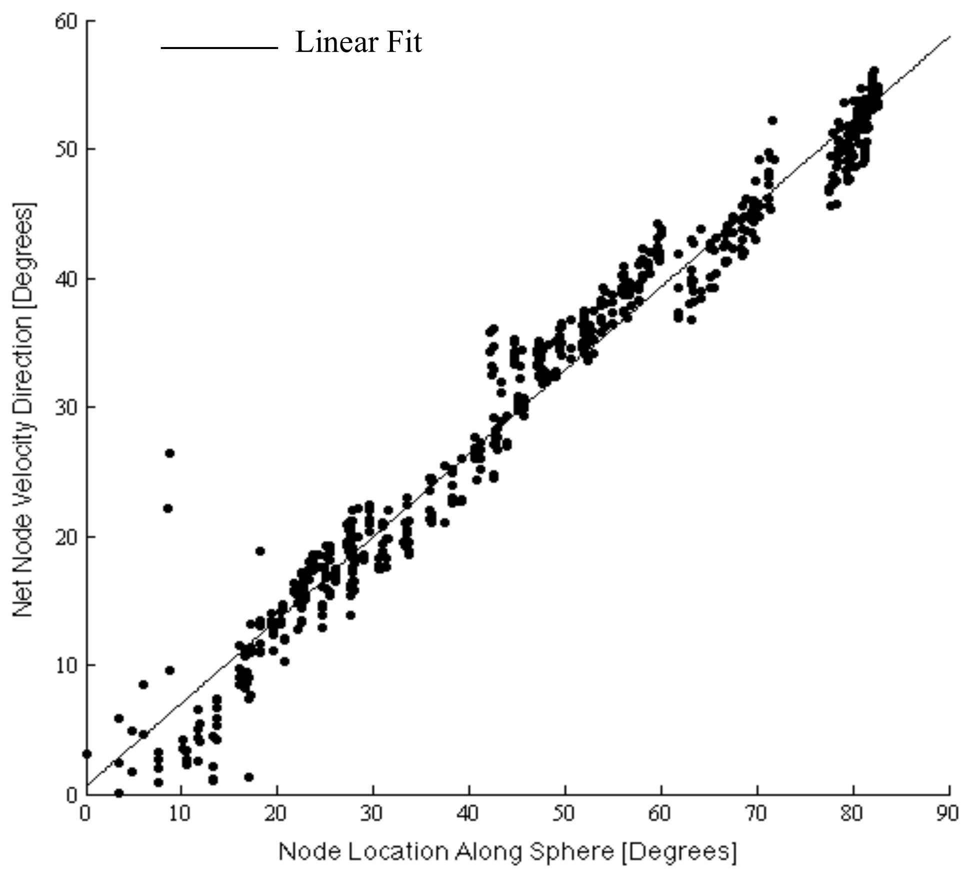

Figure 35. Velocity Direction vs. Spherical Position

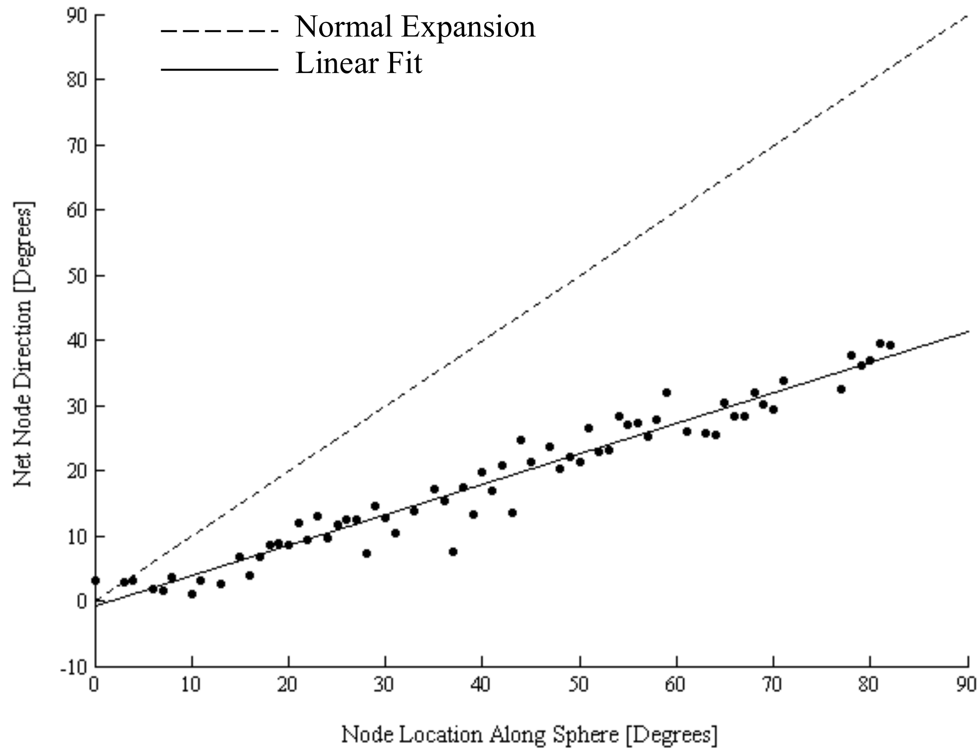

Figure 36. Net Velocity Direction vs. Spherical Position

The methodology developed above for quantifying the shape of material movement is referred to as the Spherical Expansion Comparison Methodology (SECM). The output of the SECM is the slope and intercept of the Net Node Direction vs. Node Location line in Figure 36. The closer this slope is to unity, the closer the movement of material is to spherical expansion.

CHAPTER 5: RESULTS AND DISCUSSIONS

5.1 Description of Material Flow

The objective of this chapter is to present the results and discussions of concrete material flow based on the application of NECM and SECM methodoliges on the finite element model outputs of projectiles entering into concrete targets.

Figure 37 shows a projectile as it passes through a depth of 0.1-m of concrete, 0.26-ms after striking the target at 400-m/s. The contour represents the direction of material flow. Specifically, the DirCos value in Figure 37 represents the angle a velocity vector of a node, at any given point in the target, makes with the negative z-axis. Blue signifies movement downward in a negative z-direction, and red signifies movement upwards in a positive z-direction. In Figure 37, a spherical compression wave is seen in blue moving outward and away from the point of impact. At the top of the target, in red, a distinct bulging region is seen, and the crater ejecta, represented by meshless particles, can be seen as they move up and out from the point of impact. The contour in Figure 37 is useful for a qualitative assessment, but it is difficult to compare two or more contours quantitatively from different penetration times or scenarios.

Vector streamtraces are also helpful for visualizing the direction of nodal material flow. Figure 38 is a close up of Figure 37 with streamtraces added. Streamtraces are a Tecplot feature that allows nodal velocity flows to be mapped very quickly. Appendix 9 contains a comparison of streamtraces at 400-m/s for various strength concretes. From Figure 38, the material near the surface, and within a few calibers of the axis of penetration, is moving upward. The material at the tip of the projectile moves in the negative z-direction. As the shoulder of the projectile is approached the radial component of velocity increases. The shoulder in Figure 38 is delineated with a horizontal line and is equivalent to $\theta_R = 90^\circ$ from Figure 26 in Chapter 4.

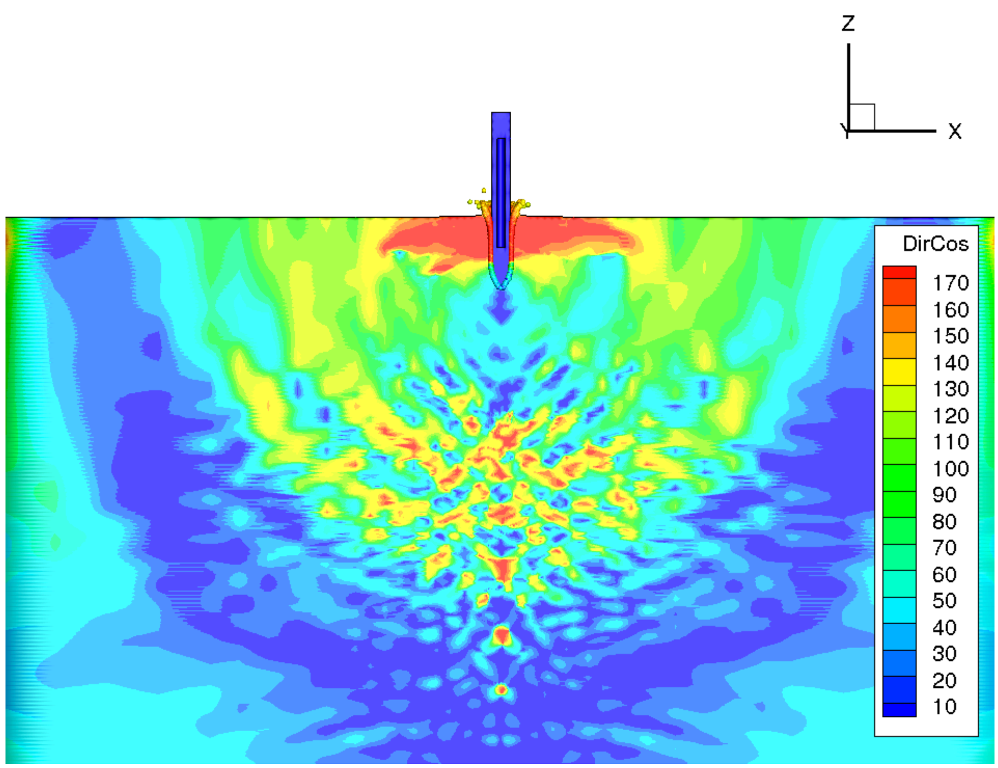

Figure 37. Data Set 5. 36-MPa Concrete, 26.9-mm Projectile Direction of Material Movement as Measured from Negative Z-axis at a Projectile Depth of 0.1-m

Qualitatively, the stream traces in Figure 38 suggest that the nodal flow is close to a spherical shape near the tip of the projectile. While this qualitative assessment is helpful, quantitative methods for comparing flow to spherical and normal expansion is needed.

In addition to nodal flow, Figure 38 shows the direction of movement of the meshless particles which are produced during the finite element computations. Clearly, at this depth, there is a distinct change in the direction of material movement at the shoulder of the projectile. Above the shoulder, particles are moving upward with little-to-no radial component of velocity. Below the shoulder, particles have their maximum radial velocity. Near the tip of the projectile the radial component of velocity again decreases to just about zero.

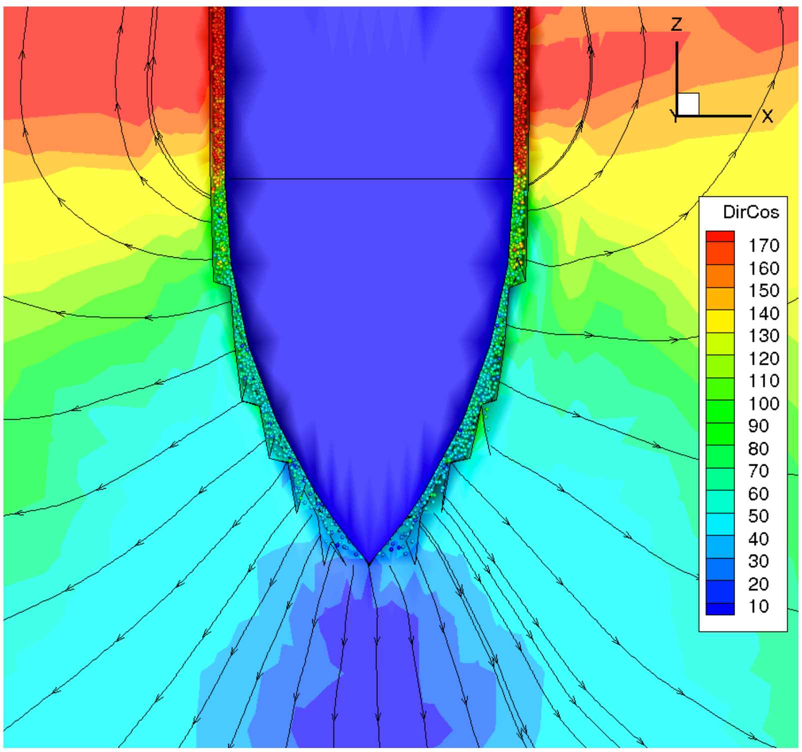

Figure 38. Data Set 5. 36-MPa Concrete, 26.9-mm Projectile
Direction of Particle and MaterialM at the Projectile Shoulder

The magnitudes of the particle and nodal velocities are depicted in Figure 39. The meshless particles, in general, achieve higher velocities than the nodes in the intact target mesh. The particle velocities just below the shoulder ($80^\circ < \theta_R < 90^\circ$) are much lower than the velocities near the tip of the projectile. The dashed horizontal line in Figure 39 is located about one caliber above the nose of the projectile ($\theta_R = 80.7^\circ$). Figure 39 shows that in general, the highest velocities are achieved within one caliber of the tip of the projectile or where $\theta_R < 80.7^\circ$ for the 26.9-mm projectile.

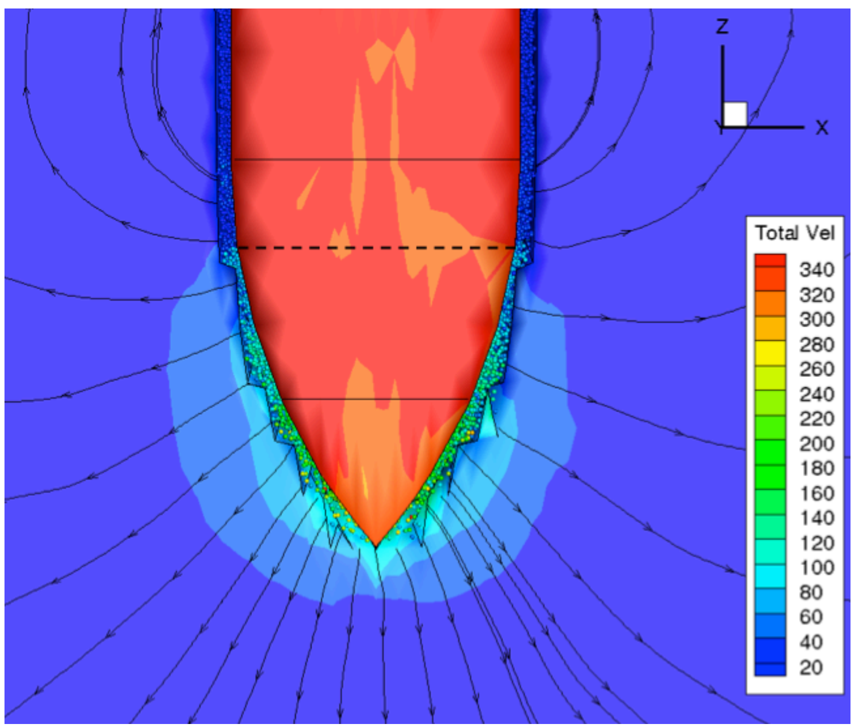

Figure 39. Data Set 5. 36-MPa Concrete, 26.9-mm Projectile, Total velocity contour

Tecplot allows the use of value blanking which is a convenient way to identify a region of interest based upon a specified threshold. The threshold used in Figure 40 is the total velocity; any concrete target nodes with a velocity lower than the threshold (in this case – 5-m/s) are blanked out. 5-m/s was chosen because it produces a region of interest that falls at the shoulder of the projectile ($\theta_R = 90^{\circ}$) with the exception of the crater region near the entry point of the projectile. There is movemet in this area but it is the ejecta coming out of the crater.

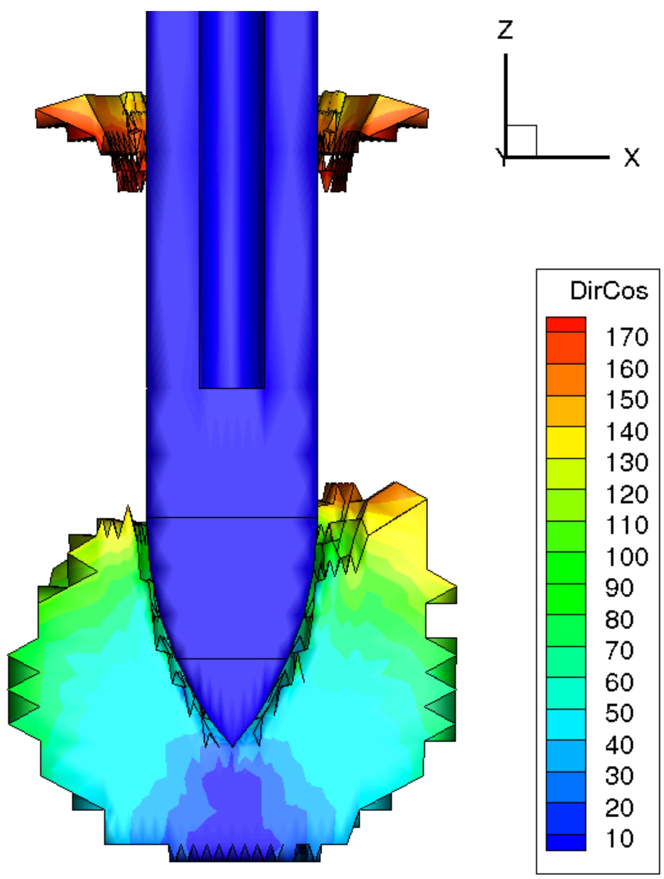

Figure 40. Data Set 5. 36-MPa Concrete, 26.9-mm Projectile, Total Velocity Contour

With the 5-m/s region established as a baseline, it is useful to consider an order of magnitude change in the velocity constraint on the region of interest. Specifically, at 50-m/s the region of interest is dramatically reduced as shown in Figure 41. In this representative case, the region of interest is now approximately at or below ½-caliber from the nose of the projectile ($\theta_R < 65.7^\circ$).

The circle superimposed on the nose of the projectile in Figure 41 has a ½-caliber radius. The concrete material nodes located between the circle and the nose of the projectile have the highest velocity, and will ultimately be radially displaced as the projectile continues to penetrate the target. This region of concrete (within the ½-caliber radius) is of particular importance when determining the target resistance; especially if it is calculated using the cavity expansion methodology where node velocity is used to determine the radial stress at that location. Forrestal et al. (1988) used a $V_Z \cos(\theta)$ assumption for the velocity profile along the nose of an ogival projectiles penetrating into aluminum targets. The $V_Z \cos(\theta)$ assumption is based purely on the geometry of the nose and the knowledge that the normal component of velocity approaches zero near the shoulder.

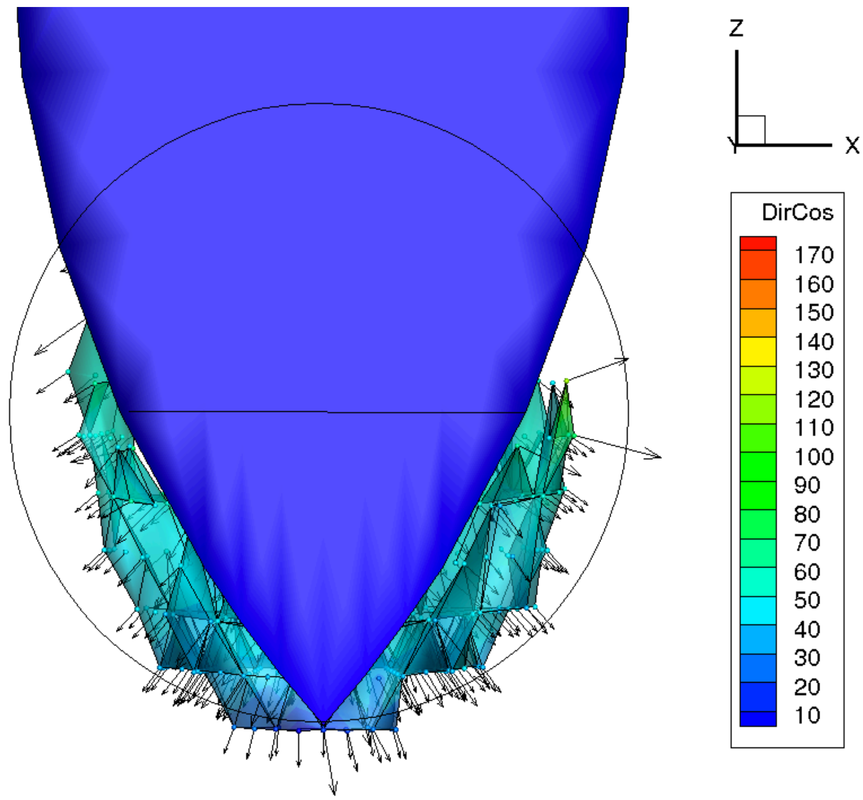

Figure 41. Data Set 5. 36-MPa Concrete, 26.9-mm Projectile.
Region of High Velocities and High Stresses.

Figure 42 shows the pressure countours generated from the finite element analysis of Data Sets 3, 5, 6 and 7. (Data set 4 is not shown for the aesthetics of the figure.) The units of pressure in the legend of the figures are in Pascals. The highest pressure regions are located along the sides of the projectile nose. As the distance between the projectile nose and target location increases, the pressure in the target quickly decreases. In Figure 42 the 100-MPa contours are roughly the same radius for all figures despite the change in concrete strength. This indicates that the far field concrete experiences the same pressure profile regardless of the concrete strength. The high-pressure contour (300-MPa) radii, however, increases as the strength of the concrete increases. Note that contours in Figure

42 are taken at the same penetration depth of two calibers which is twice the diameter of the projectile. For the large projectile, 2-calibers is 0.15-m while for the small projectile, 2-calibers is 0.06-m.

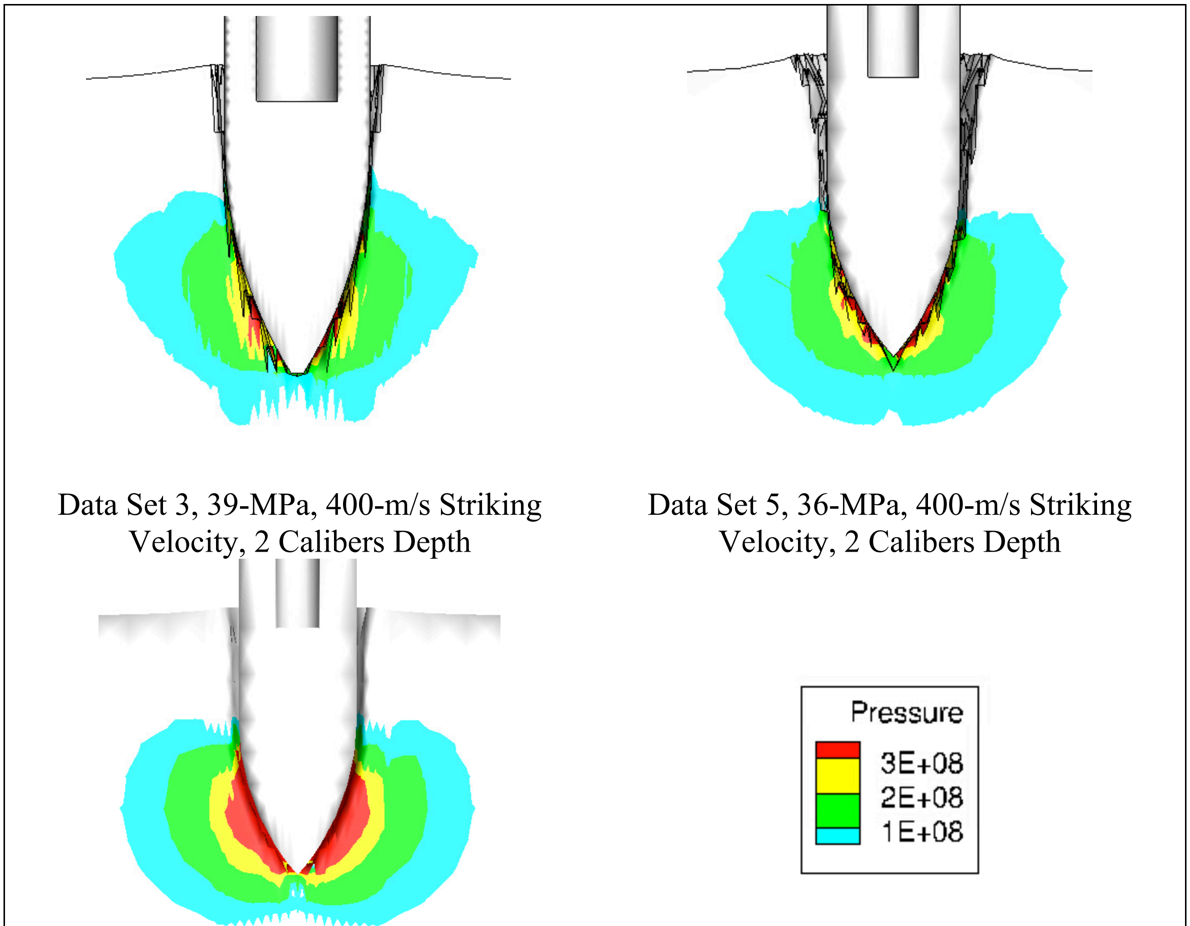

Data Set 3, 39-MPa, 400-m/s Striking Velocity, 2 Calibers Depth

Data Set 5, 36-MPa, 400-m/s Striking Velocity, 2 Calibers Depth

Data Set 7, 157-MPa, 400-m/s Striking Velocity, 2 Calibers Depth

Figure 42. Pressure Contours in Various Strength Concretes at a Depth of 2 Calibers

This is expected since the higher strength concrete does not fail as quickly as the lower strength concrete, and therefore cannot relieve the pressure as quickly. As a consquence, pressure builds up in a larger portion of the higher strength concrete surrounding the cavity.

Over the past several decades, a variety of analytical solutions using a cavity expansion model have been developed as described in chapter 2. Each of the expansion methods have been shown to have limited success in predicting penetration depth based upon the intial conditions of the problem. For example, Forrestal (1986) assumed that the shape of the cavity expansion was cylindrical; that is, the target material was restricted to move only in the radial direction. However, he determined that the cylindrical expansion overpredicted the early-time deceleration response and under-predicted the later-time deceleration response. Forrestal and Tzou (1997) developed a dynamic cavity expansion model for concrete by assuming a constant velocity of the cavity wall, a constant velocity of the plastic/elastic interface, and a spherically symmetric shape of expansion. Recently, Shiqiao, Lei, Haipeng, Xinjian and Li (2007) proposed a normal curve surface system that allows dynamic cavity expansion to be investigated assuming an ogive-normal expansion of the stress waves and target material. A key assumption in the work of Shiqiao et al. (2007) is that the responding medium of concrete expands in direction that is normal to the outer surface of the projectile nose. In all above cases, the assumed direction of expansion is an important aspect of the respective analytical model, yet little has been done to quantify the direction of material flow during penetration. This dissertation provides a plausible method for quantifying the direction of material flow.

5.2 Analysis of the Flow of Meshless Particles

This section will discuss the results from material flow analysis of five sets of penetration data. The material flow analysis was performed using the finite element method analysis described in Chapter 3, and the two methodologies, i.e. NECM and SECM discussed in Chapter 4. The finite element model converted highly distorted elements into meshless particles. The direction of movement of these particles as well as the direction of flow of the nodes of the target mesh were investigated. Movement of the meshless particles provides insight as to how comminuted material in the pulverized region may flow.

5.2.1 Effects of Varying Concrete Strength on Particle Movement

Data Sets 5, 6, and 7 were derived from experiments using the same size projectiles but different strength concrete targets. By comparing the material flow inside the targets at similar depths and striking velocities, the effects of varying concrete strength on the direction of particle movement can be assessed. Figure 43, Figure 44, and Figure 45 shows NECM plots for a striking velocity of 600-m/s, an instantaneous depth of 0.1-m, and increasing concrete strength (36-MPa, 97-MPa, and 157-MPa). The dashed lines in these figures represent ogive-normal expansion. For Data Set 5 (36-MPa), a linear fit of the NECM values results in a slope of approximately 1.7 and a y-intercept of -69.4 (note that the x-axes of the graphs start at 40 degrees).

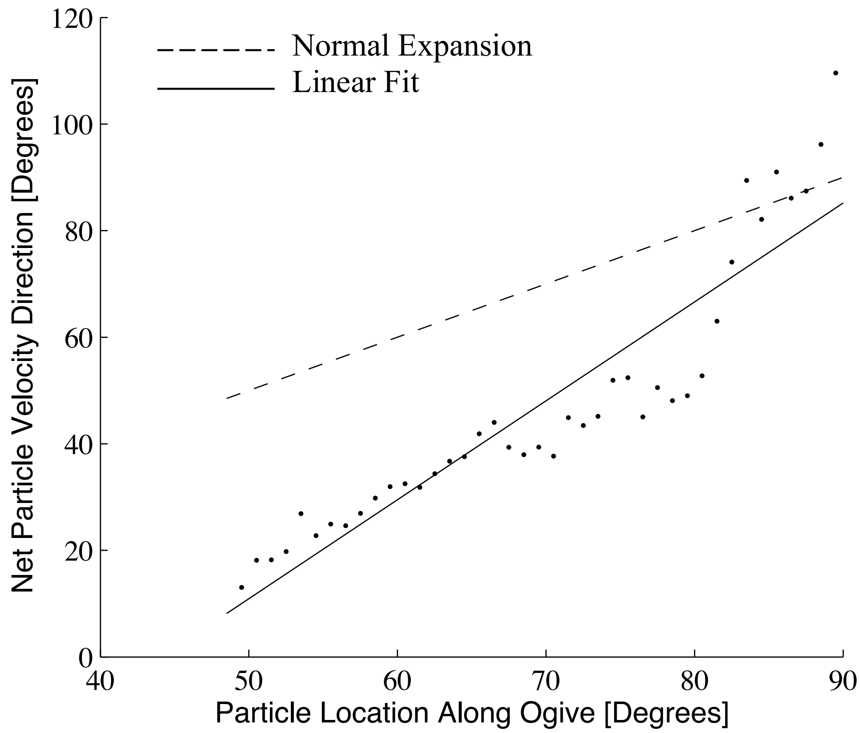

Figure 43. NECM Plot for Data Set 5, 36-MPa Concrete, Striking Velocity 600-m/s, Time Step: 0.169-ms, Zmin: -0.10-m, Slope: 1.9, Int: -81.9

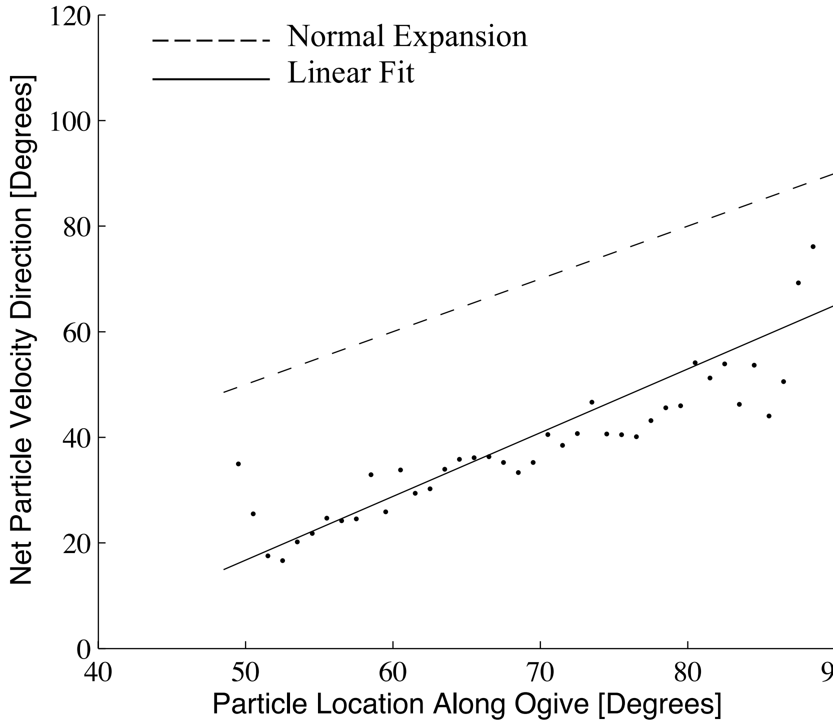

Figure 44. NECM Plot for Data Set 6, 97-MPa Concrete, Striking Velocity 600-m/s, Time Step: 0.174-ms, Zmin: -0.10-m, Slope: 1.2 Int: -43.6

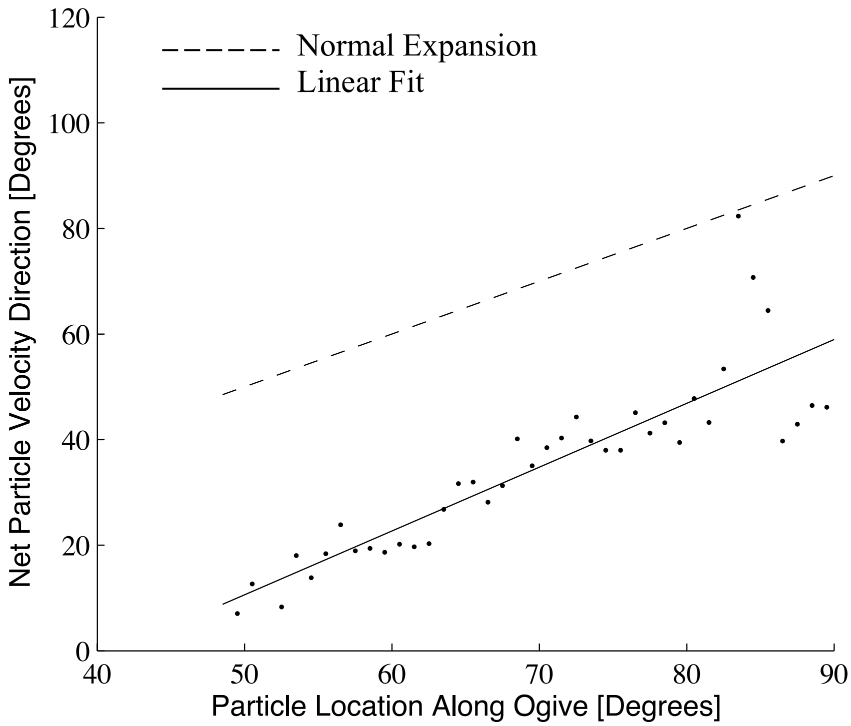

Figure 45. NECM Plot for Data Set 7, 157-MPa Concrete, Striking Velocity 600-m/s, Time Step: 0.177-ms, Zmin: -0.10-m, Slope: 1.2, Int: -49.9

The NECM slope, as described previously in Chapter 4, provides a first-order measurement for comparing the direction of material flow to that of ogive-normal expansion. From Figure 43, Figure 44, and, Figure 45 as the concrete strength is increased, the slopes of the NECM values approach unity. The linear fit in Figure 43, however, is only accurate to about $\theta_R = 65^\circ$. Beyond this position, the linear fit is skewed because of the high NECM values beyond $\theta_R = 80^\circ$ trend linearly upward with a slope that is greater than that of the original NECM fit.

Furthermore, this upward trend accounts for about 25% of the data. Because of the large amount of data trending linearly upward, a bilinear plot describes the NECM output more accurately. The first part of the bilinear fit had a slope close to unity, and the second part of the bilinear fit had a slope of approximately 6-degrees/degrees (Figure 46). The first part of the bilinear fit, however, is more important because as shown in Figure 39, the magnitude of the particle velocities above $\theta_R = 80^\circ$ is very low.

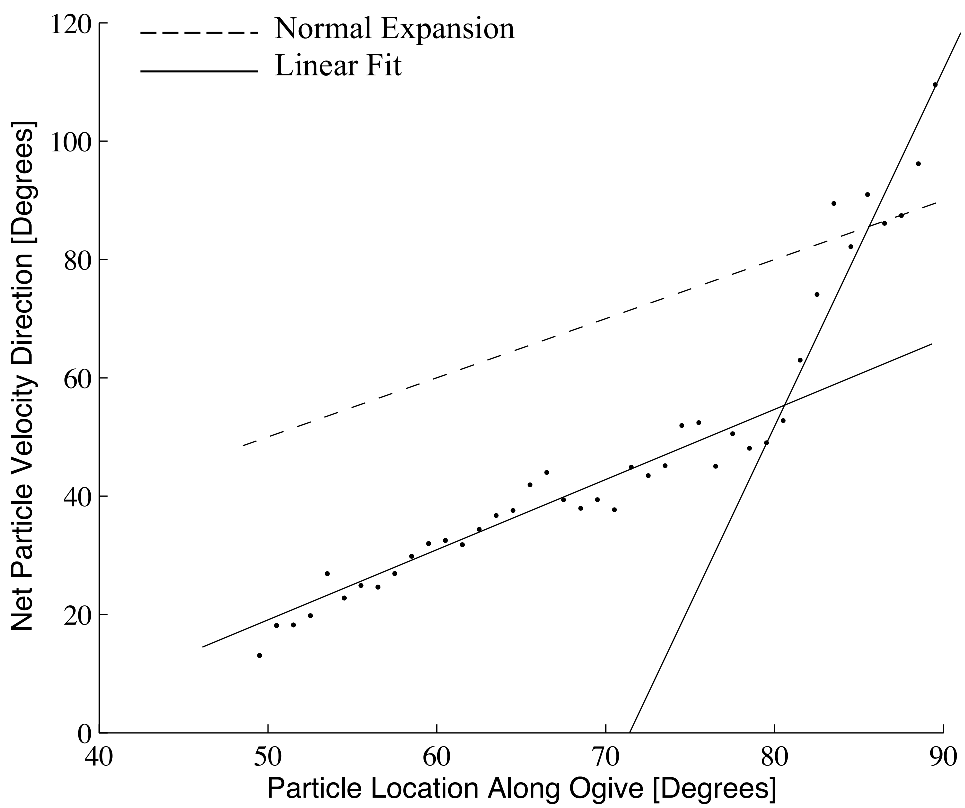

Figure 46. Bilinear NECM Plot for Data Set 5, Striking Velocity 600-m/s

Figure 47 shows the direction of particle flow around the nose of the projectile. To simplify the view, only two colors are shown indicating movement above and below 90 degrees. Only particles located below the shoulder of the projectile are shown. It is clear that the percentage of particles with a direction greater than 90 degrees is high. This supports the bilinear fit suggested for Figure 46 This sort of bilinear distribution for the NECM data is seen predominantly in the lower strength concretes (36-39MPa) at striking velocities below 500-m/s. Figure 44 shows the NECM plot for 97-MPa concrete. In this plot there are still a few NECM values out near the projectile's shoulder ($\theta_R = 90^\circ$) that are trending upward, but not enough to justify describing the data as a bilinear distribution.

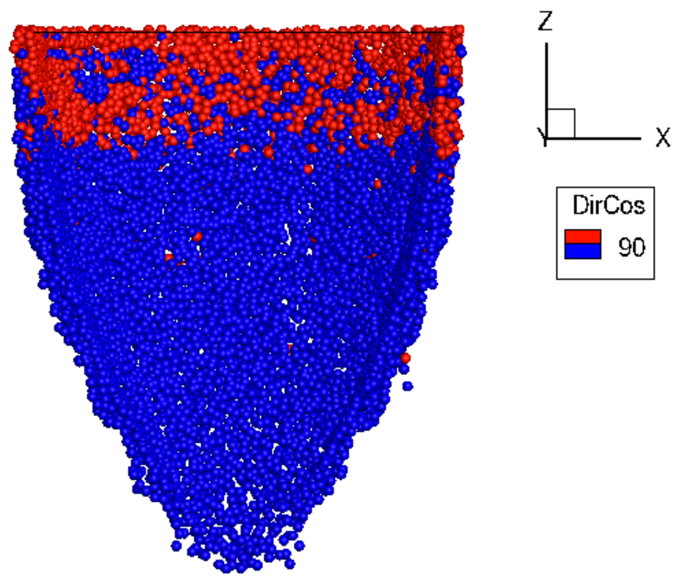

Figure 47. Particles Corresponding to Bilinear Plot in Figure 43
for Data Set 5, Striking Velocity 600-m/s

The NECM values for the 157-MPa concrete (Figure 45) are described well by the NECM linear fit. Figure 48 shows that the red band of particles seen in Figure 47 is no longer present. This indicates the absence of a bilinear distribution. Similar calculations were conducted for striking velocities of 800 m/s, and Table 12 through Table 15 summarize the NECM slope values as a function of concrete strength for both striking velocities of 800-m/s and 600-m/s. The data in Table 12 through Table 15 do not support a trend for changes in the flow of particles as a result of concrete strength. It is important to note that the NECM values in the tables are for a single linear fit. Bilinear slope data is not tabulated, but high slope values are typically an indication of a bilinear distribution.

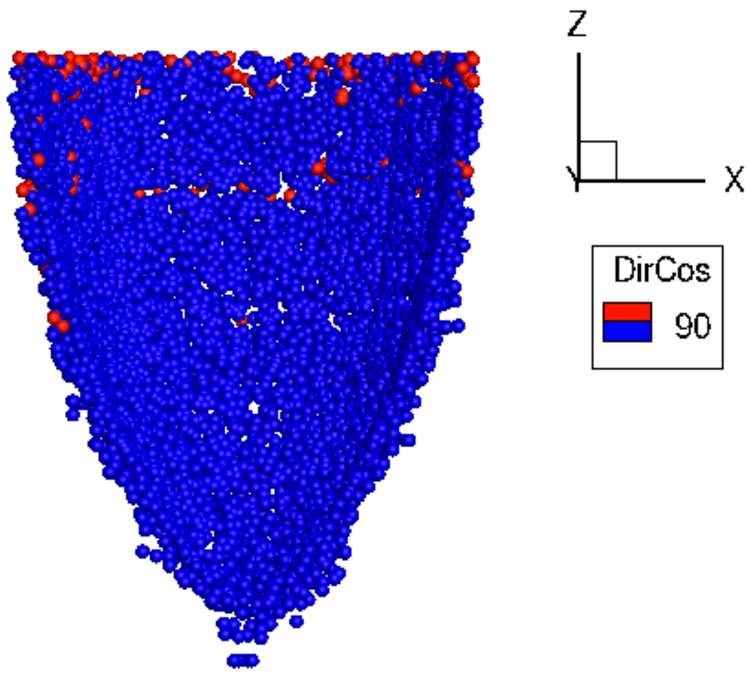

Figure 48. Particles Corresponding to NECM Plot in Figure 44
for Data Set 6, 97-MPa Concrete, Striking Velocity 600-m/s

Table 12. Ogive-Normal Flow Comparison: Increasing Concrete Strength/Increasing Depth for Data Sets 5, 6, and 7
26.9-mm, 2-CRH Projectile, 800-m/s Striking Velocity

Instantaneous Depth (m)	Concrete Strength (MPa)		
	36	97	157
0.1	0.8	0.9	0.9
0.2	0.3	0.6	0.8
0.3	04	1.0	1.1
0.4	0.4	1.2	1.2
0.5	0.8	1.4	
0.6	0.9	1.8	
0.7	1.0		
0.8	1.2		

Table 13. Ogive-Normal Flow Comparison: Increasing Concrete Strength/Decreasing Velocity for Data Sets 5, 6, and 7
26.9-mm, 2-CRH Projectile, 800-m/s Striking Velocity

Instantaneous Velocity (m/s)	Concrete Strength (MPa)		
	36	97	157
700	0.6	0.5	0.9
600	0.4	1.0	0.9
500	0.5	1.2	1.1
400	0.6	1.5	1.1
300	0.6	1.2	1.0
200	1.3	1.8	1.3
100	1.2	1.2	1.2

Table 14. Ogive-Normal Flow Comparison: Increasing Concrete Strength/Increasing Depth for Data Sets 5, 6, and 7
26.9-mm, 2-CRH Projectile, 600-m/s Striking Velocity

Instantaneous Depth (m)	Concrete Strength (MPa)		
	36	97	157
0.1	1.9	1.2	1.2
0.2	1.0	0.8	1.1
0.3	1.0	1.2	
0.4	1.1	1.2	
0.5	0.9		

Table 15. Ogive-Normal Flow Comparison: Increasing Concrete Strength/Decreasing Velocity for Data Sets 5, 6, and 7 26.9-mm, 2-CRH Projectile, 600-m/s Striking Velocity

Instantaneous Velocity (m/s)	Concrete Strength (MPa) 36	97	157
500	0.9	1.0	0.9
400	1.1	1.1	1.2
300	1.3	1.2	0.9
200	1.3	1.4	1.2
100	1.1	1.4	1.4

5.2.2 Effects of Varying Striking Velocity on Particle Movement

Figure 49, Figure 50, Figure 51, and Figure 52 show the net direction of motion of target particles as a function of particle location along the nose of the projectile when the instantaneous depth of the projectile is 0.1-m into a 36-MPa (5-ksi) concrete target. The plots show that particles near the tip of the projectiles moved at angles that were approximately 40 degrees below ogive-normal expansion. For the 200, 400 and 600-m/s projectiles, particles closer to the shoulder of the projectile ($\theta_R \geq 80^\circ$), moved in a direction linearly upward when compared to ogive-normal expansion. Since the number of NECM values above 80 degrees is approximately 25% of the data, a bilinear distribution is assumed. For the 800-m/s striking velocity the particles moved in a direction approximately 40 degrees below that of ogive-normal motion along the entire length of the projectile nose. Thus a bilinear distribution is not required to describe the 800-m/s data. For the 200, 400, and 600-m/s NECM plots, the slopes of the first part of the bilinear fit decreases as the striking velocity increases. At the same time, the slope of the second part of the bilinear fit also decreases. For all striking velocities analyzed in

Data Set 5, there appears to be both an ogive-normal component and an ogive-tangent component to material flow.

In Figure 50, the ogive-tangent component is believed to be the cause of the gap between the linear fit of the data and the dashed line indicating ogive-normal expansion. For the projectiles with striking velocities of 200, 400 and 600-m/s, the ogive-tangent component decreases from the tip of the projectile $\theta_R = 48^\circ$ to the shoulder of the projectile $\theta_R = 90^\circ$. For the 800-m/s striking velocity, the ogive-tangent component of material flow remained proportionally constant along the entire nose of the projectile.

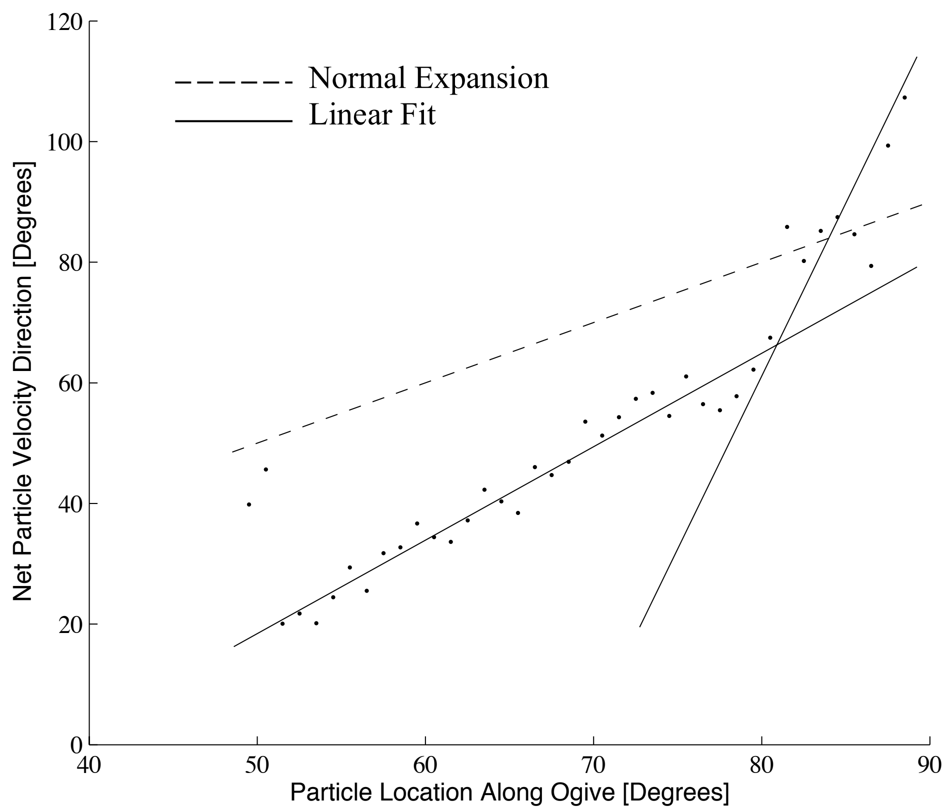

Figure 49. Net Particle Direction vs Ogival Location. DS-5, 200-m/s, DOP = 0.1-m

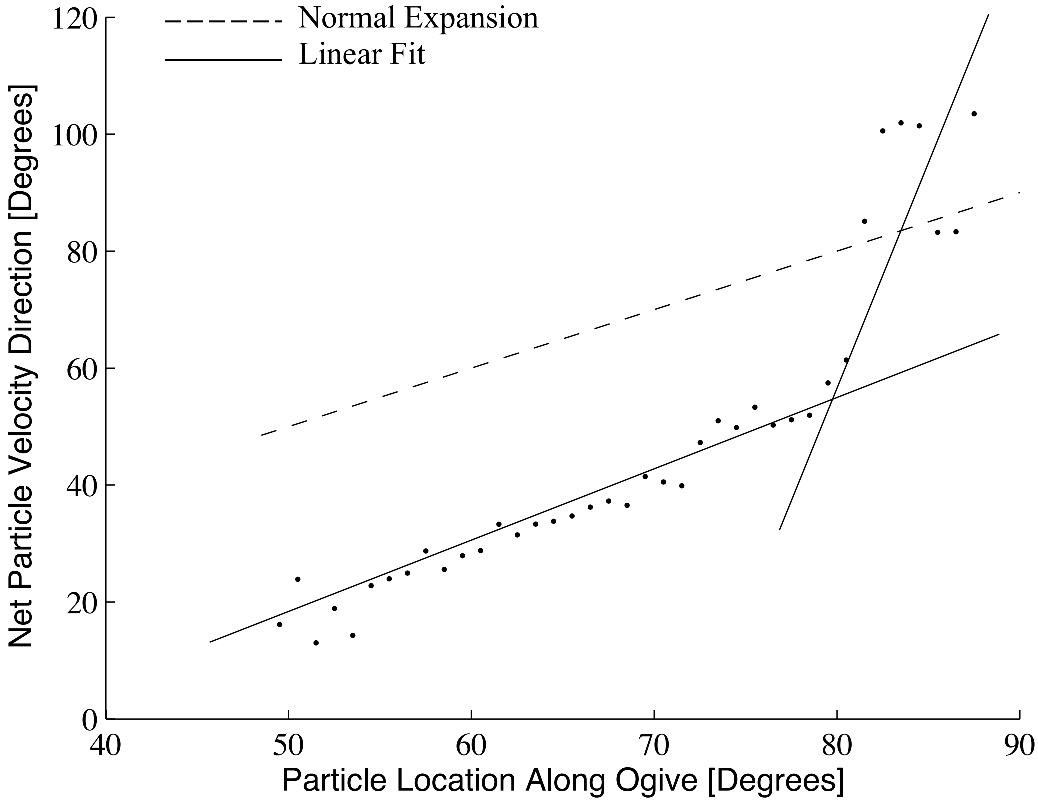

Figure 50. Net Particle Direction vs Ogival Location. DS-5, 400-m/s, DOP = 0.1-m

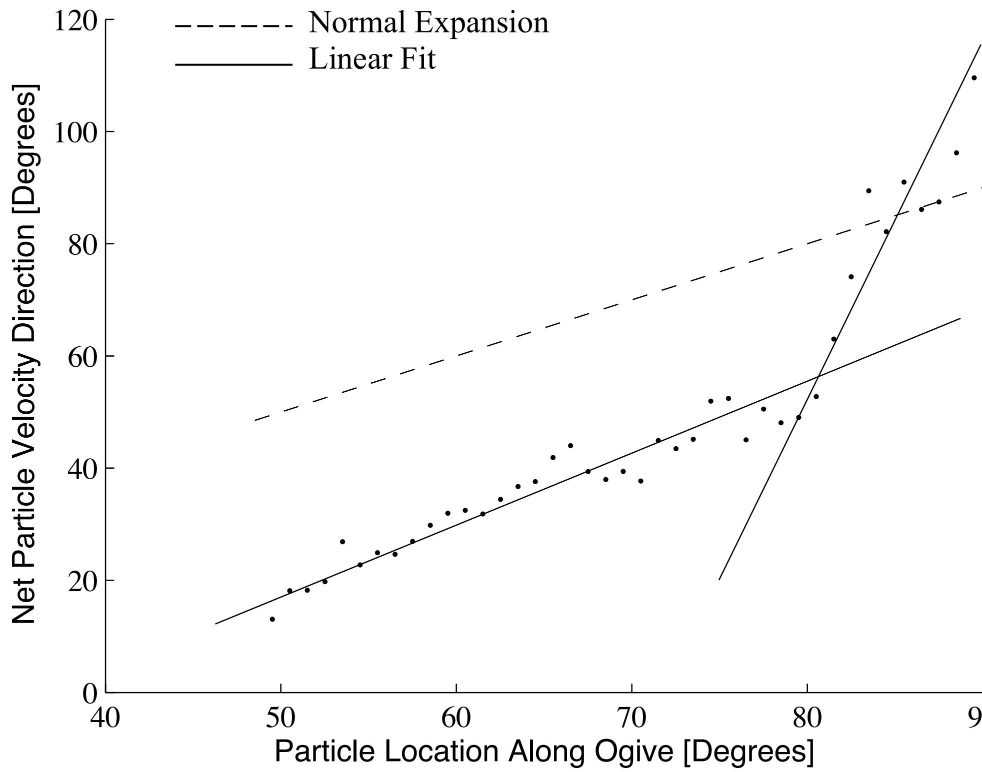

Figure 51. Net Particle Direction vs Ogival Location. DS-5, 600-m/s, DOP = 0.1-m

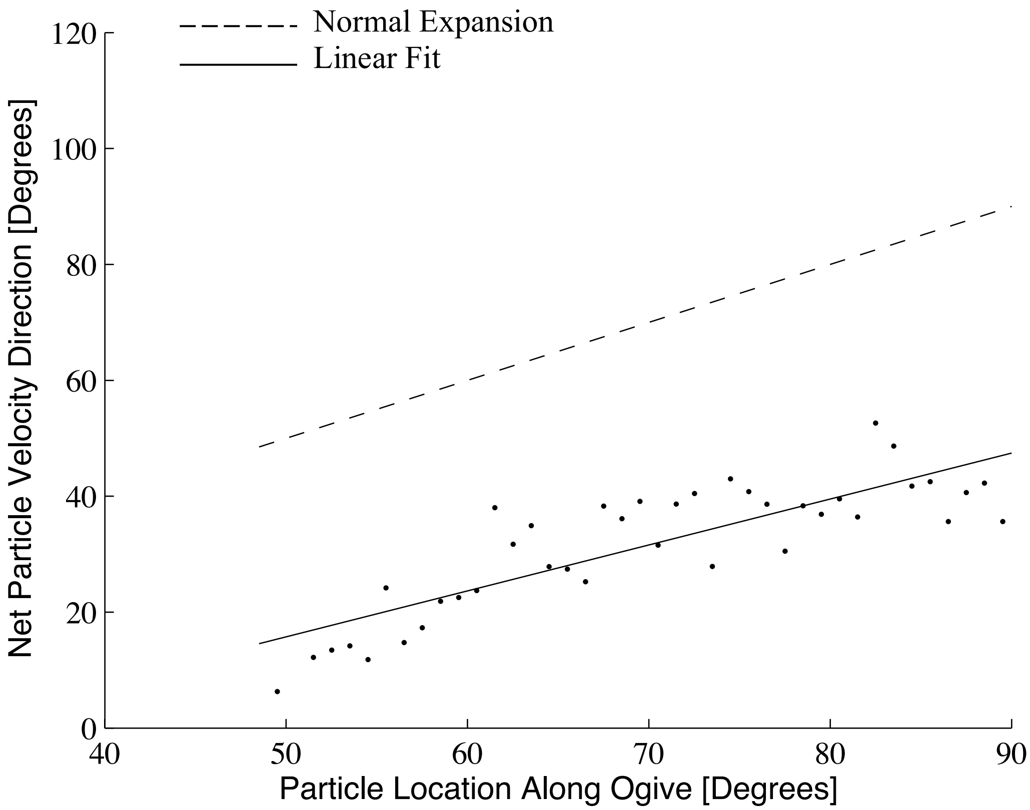

Figure 52. Net Particle Direction vs Ogival Location. DS-5, 800-m/s, DOP = 0.1-m

Table 16 contains the results obtained by applying the Normal Expansion Comparison Methodology (NECM) to the finite element output from Data Set 5. The values represent the slope of a single linear fit to the data. As the striking velocity increased, the NECM values generally decreased which corresponded to the flattening of the linear fit to the data as seen in Figure 49 through Figure 52. Although the data trended downward as striking velocity increased, it also fluctuated due to the bilinear nature of the data. The fluctuation for Data Set 5 is reduced considerably when only the slopes from the bilinear fits are considered. NECM values greater than 1.5, however, provide a quick indication that a bilinear distribution exists.

Average values were derived from the reported NECM values for Striking Velocity vs Instantaneous Velocity, and Striking Velocity vs Instantaneous Depth. As a general rule, the average NECM slope values decreased rapidly and then leveled off as the projectile's striking velocity on the target increased. This was true for all data sets. NECM values in Data Set 6 are essentially level, but the velocity regime for that data set is 500-m/s and above. As a result, higher NECM values at lower penetration velocities cannot be seen. The data in Table 17 through Table 21 suggests that NECM values for lower strength concrete do not level off at the same rate as NECM values for higher strength concrete.

Table 16. Ogive-Normal Flow Comparison: Increasing Striking Velocity/Increasing Instantaneous Depth for Data Set 5, 26.9-mm, 2-CRH Projectile into 36-MPa Target

Instantaneous Depth (m)	Striking Velocity (m/s)			
	200	400	600	800
0.1	2.0	2.4	1.9	0.8
0.2		0.9	1.0	0.3
0.3			1.0	0.4
0.4			1.1	0.4
0.5			0.9	0.8
0.6				0.9
0.7				1.0
0.8				1.2

Table 17. Average NECM Values for Data Set 3
76.2-mm, 3CRH, Projectile into 39-MPa Target

Data Set	Striking Velocity (m/s)			
	250	325	400	475
3	3.9	3.5	2.7	2.6

Table 18. Average NECM Values for Data Set 4
76.2-mm, 6CRH Projectile into 39-MPa Target

Data Set	Striking Velocity (m/s)			
	250	325	400	475
4	7.2	6.0	4.9	4.9

Table 19. Average NECM Values for Data Set 5
26.9-mm, 2-CRH Projectile into 36-MPa Target

Data Set	Striking Velocity (m/s)			
	200	400	600	800
5	1.9	1.6	1.2	0.7

Table 20. Average NECM Values for Data Set 6
26.9-mm, 2-CRH Projectile into 97-MPa Target

Data Set	Striking Velocity (m/s)			
	500	600	700	800
6	1.0	1.2	0.9	1.2

Table 21. Average NECM Values for Data Set 7
26.9-mm, 2-CRH Projectile into 157-MPa Target

Data Set	Striking Velocity (m/s)			
	200	400	600	800
7	2.0	1.0	1.1	1.0

5.2.3 Effects of Varying Projectile Diameter on Particle Movement

Table 22 contains the average NECM values for Data Set 3, which used the larger (76.2-mm) projectiles. The average NECM values remained well above unity even at higher striking velocities. It is useful to compare Data Sets 3 and 5 since they had nearly the same concrete strength, but very different projectile diameters. In particular, for a 400-m/s striking velocity, the NECM value for the large projectile was 3.8 while the NECM value in Table 23 for the small projectile was 1.8. At a depth of 4 calibers (0.3-m), the NECM curve for the large projectile is shown in Figure 54. The NECM value (slope of the linear fit) at this point was 3.0. By visually inspecting the data, however, it can be seen that up to a position of 80-degrees along the ogive nose of the projectile, the data had a slope of approximately unity. Beyond the 80-degree position, the data quickly rose in a bilinear fashion to a slope of about 10. For the small projectile, at a depth of 4 calibers (0.1-m) a similar trend is seen (Figure 53). Note that the x-axis changes scale.

Table 22. Average NECM Values for Data Set 3
76.2-mm, 3CRH, Projectile into 39-MPa Target

Data Set	Striking Velocity (m/s)			
	250	325	400	475
3	3.9	3.5	2.7	2.6

Table 23. Average NECM Values for Data Set 5
26.9-mm, 2-CRH Projectile into 36-MPa Target

Data Set	Striking Velocity (m/s)			
	200	400	600	800
5	1.9	1.6	1.2	0.7

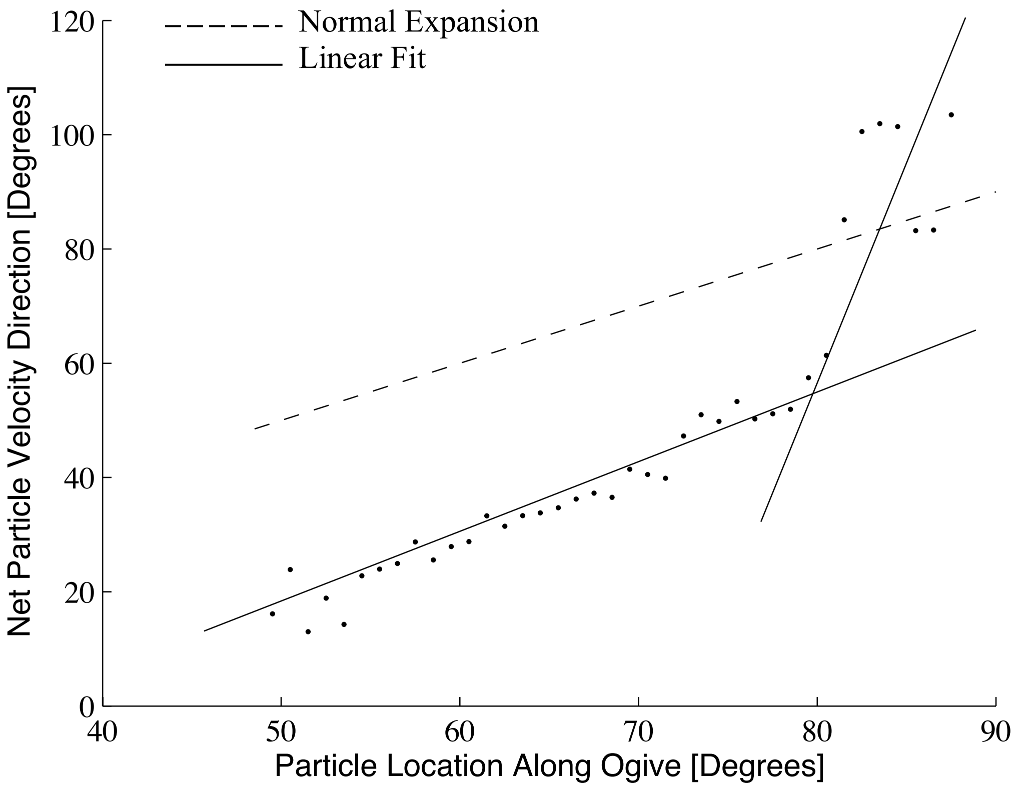

Figure 53. NECM Plot for Data Set 5, Striking Velocity 400-m/s

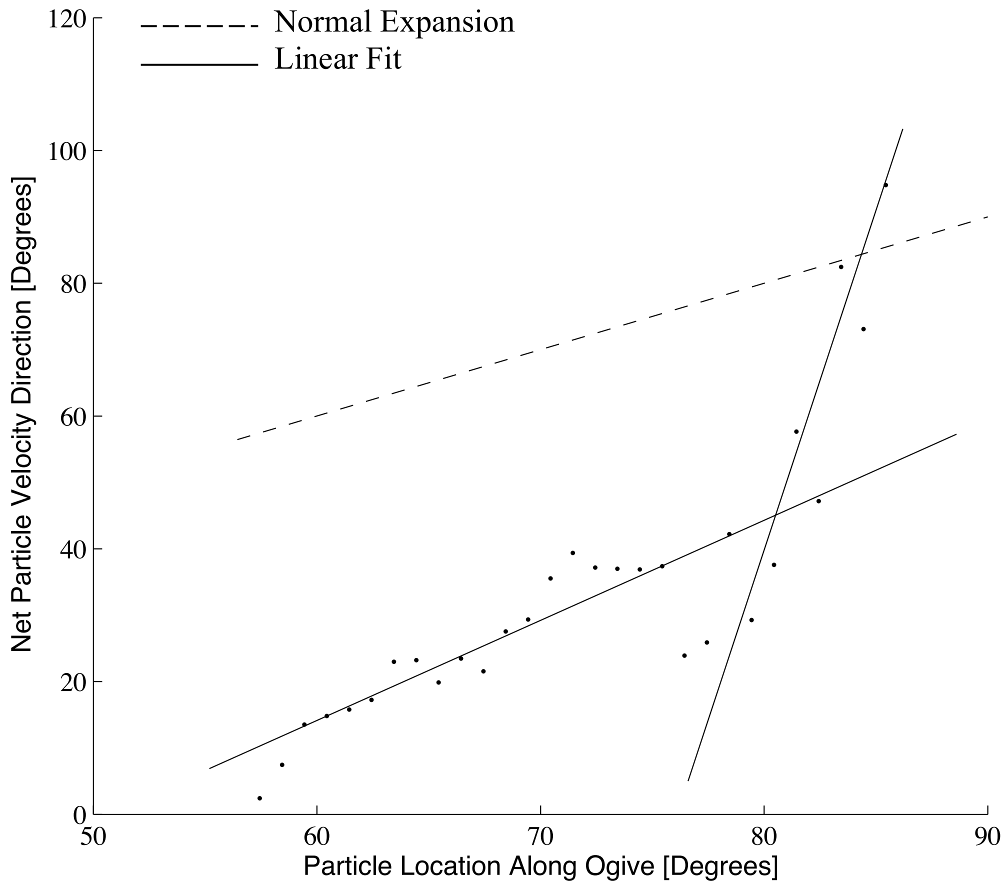

Figure 54. NECM Plot for Data Set 3, Striking Velocity 400-m/s

The slope of the first linear fit is slightly above unity. In both cases, the actual direction of material flow is approximately 40 degrees downward from ogive-normal expansion. The particles with a θ_R above 80 degrees quickly approach ogive-normal expansion. The flow of material for the larger diameter projectile behaves similar to the smaller projectile as long as it is at the same caliber depth. By the time the projectiles slow down to an instantaneous velocity of 200-m/s, the bilinear distribution is no longer visible. At an instantaneous velocity of 200-m/s the larger projectile has a NECM slope of 2.0 while the smaller projectile has a NECM slope of 1.4. Hence, the NECM values for the smaller projectile level off at a faster rate than the NECM values for the larger projectile. Appendices 1 and 3 contain a complete listing of the NECM plots and tables for Data Sets 3 through 7.

5.2.4 Normal Particle Velocity Magnitude

The previous sections on particle movement discussed methods of quantifying and comparing the direction of concrete flow. Results have shown that there is an approximately 40-degree difference between the flow of particles in EPIC and what is expected from ogive-normal expansion. It is often assumed in cavity expansion analysis, however, that the particles at the projectile-target interface move normal to the surface of the projectile. The results in this research indicate that this is not the case. The normal velocity can be determined by NECM from the EPIC output as discussed in Chapter 4 and depicted again for reference in Figure 55.

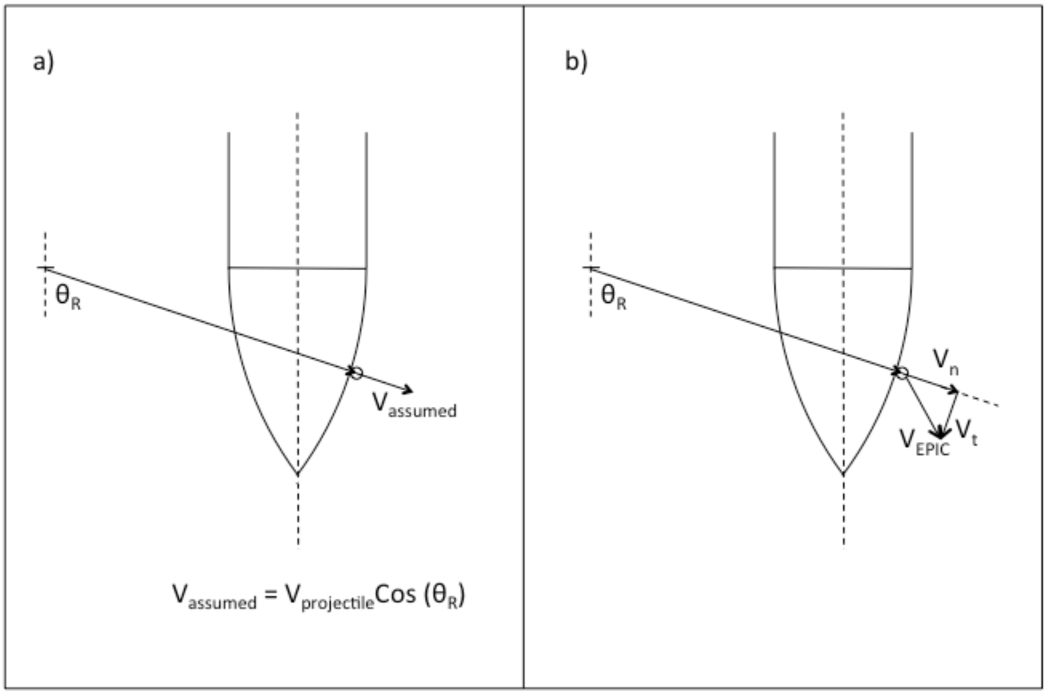

Figure 55. Typical Velocity Assumption vs EPIC Velocity
a) Assumed Normal Velocity b) EPIC Derived Velocity

Appendix 11 contains plots of the magnitude of the normal component of the total velocity along the surface of the ogive for all data sets. Figure 56 is a representative plot. At any given location along the ogive, the actual magnitude of the normal vector on that ring varies quite a bit. The data, however, trends linearly, and the linear fit of the data provides a good average of the normal vector magnitude.

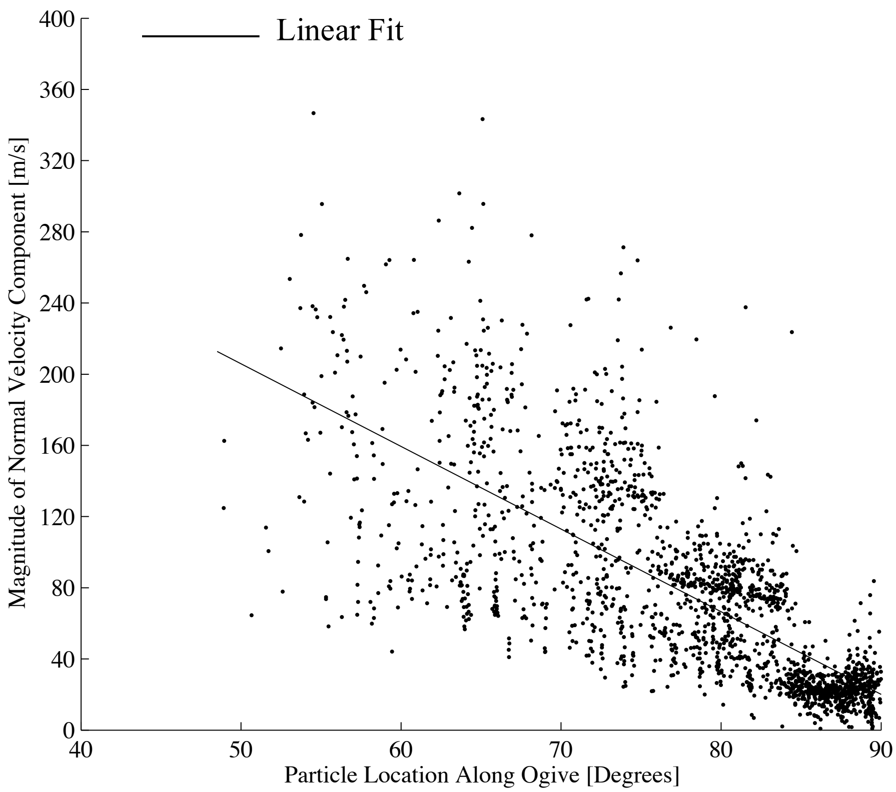

Figure 56. EPIC Normal Velocity Profile Along Ogive Nose for 157-MPa Concrete and 600-m/s Striking Velocity/400-ms Inst. Velocity

Figure 57 shows the normal velocity profiles for Data Set 7 with a striking velocity of 400-m/s. The slope of the normal profile decreases as the depth of penetration increases. This trend can be seen for all data sets. As the projectile slows down, the velocity profile shifts downward because there is less energy remaining in the system. As a projectile comes to a stop, the velocity profile becomes completely flat.

Figure 58 through Figure 63 show plots of the EPIC normal velocity profile compared with the $V_z\cos(\theta)$ assumption. Figure 58, Figure 59, and Figure 60 are the small projectile at the same striking velocity with varied concrete strength. At 500-m/s there is a gap between the assumption used in current analytical equations and the normal values determined using NECM. As the projectile slows down, the gap diminishes, and the $V_z \cos(\theta)$ assumption agrees well with the EPIC output at 100 m/s. The higher strength concrete loses energy at a faster rate than the lower strength concrete.

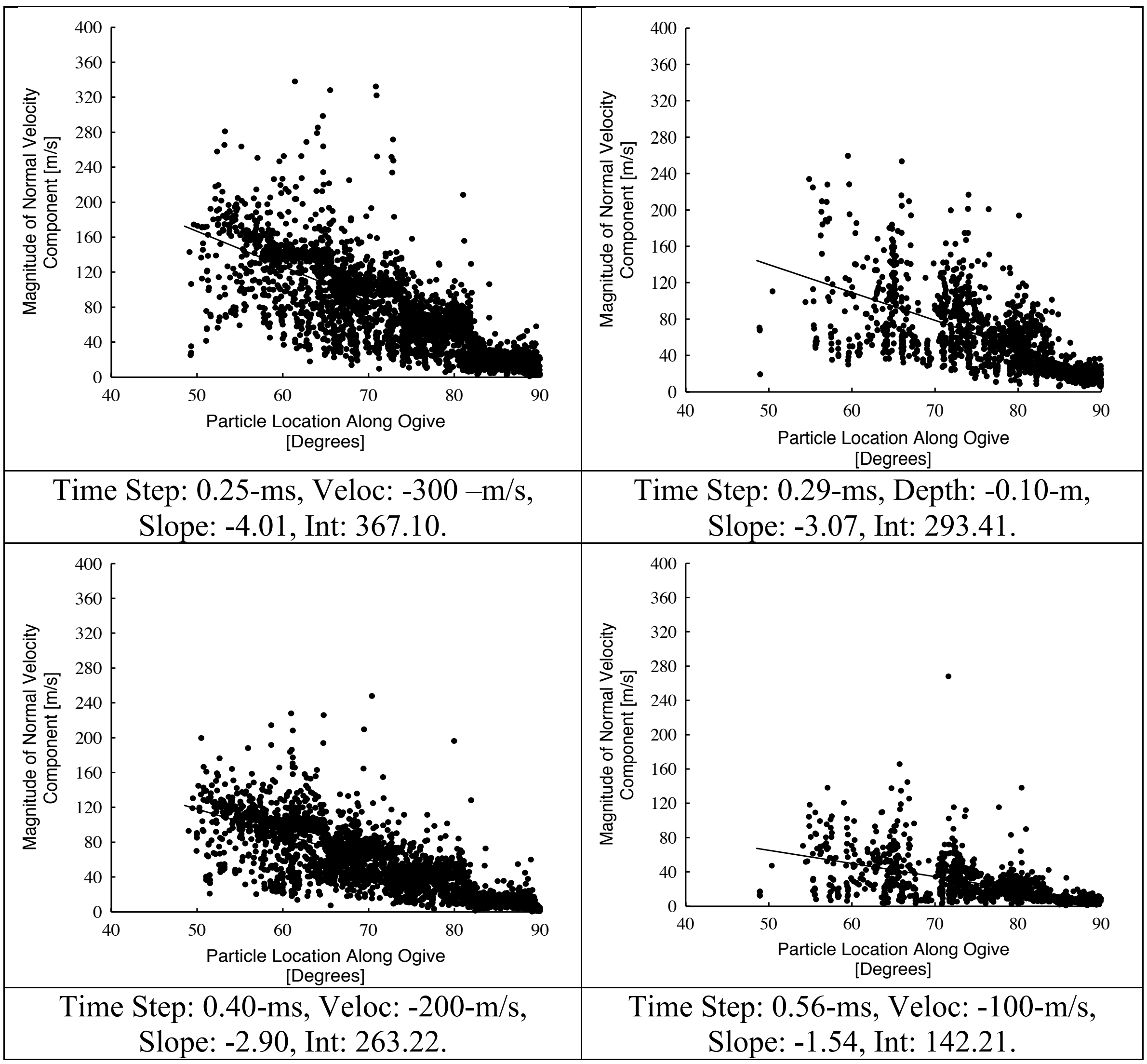

Time Step: 0.25-ms, Veloc: -300 –m/s, Slope: -4.01, Int: 367.10.

Time Step: 0.29-ms, Depth: -0.10-m, Slope: -3.07, Int: 293.41.

Time Step: 0.40-ms, Veloc: -200-m/s, Slope: -2.90, Int: 263.22.

Time Step: 0.56-ms, Veloc: -100-m/s, Slope: -1.54, Int: 142.21.

Figure 57. Normal Velocity Profile, Data Set 7, 157-MPa Concrete, 26.9-mm, 2-CRH Projectile, 400-m/s Striking Velocity

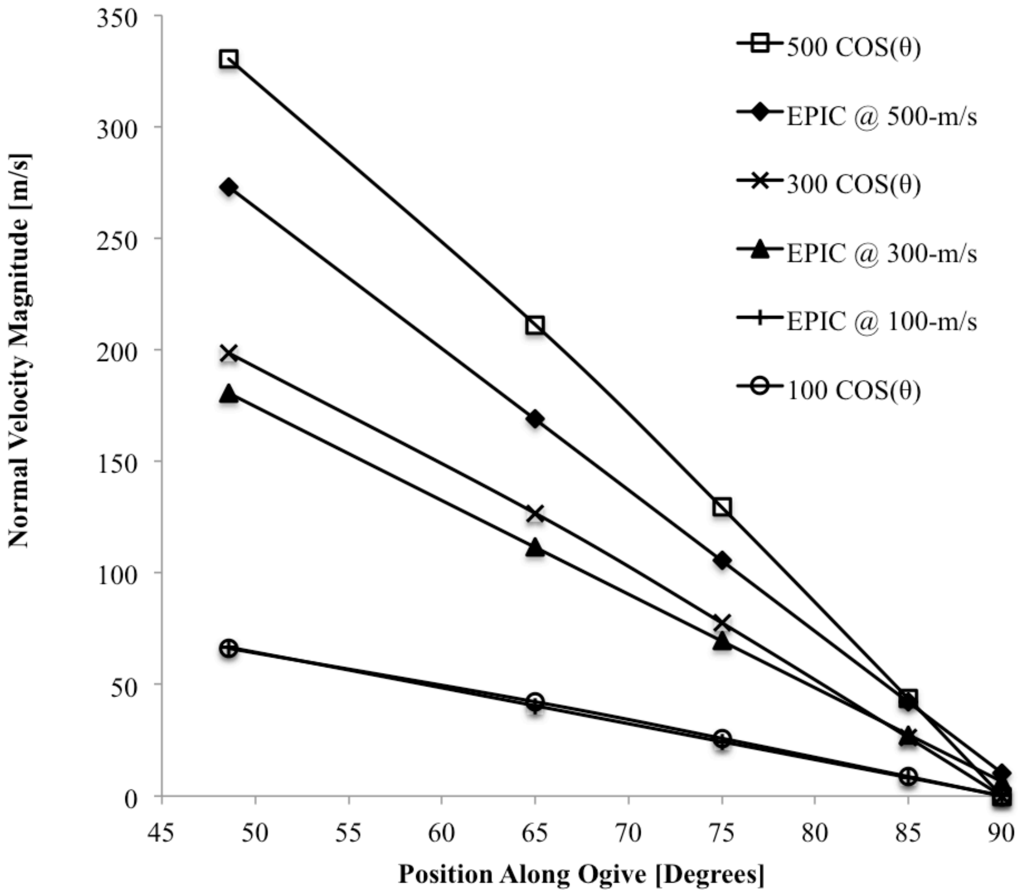

Figure 58. EPIC and $V_z \cos(\theta)$ Output for Data Set 5
36-MPa, 600-m/s Striking Velocity

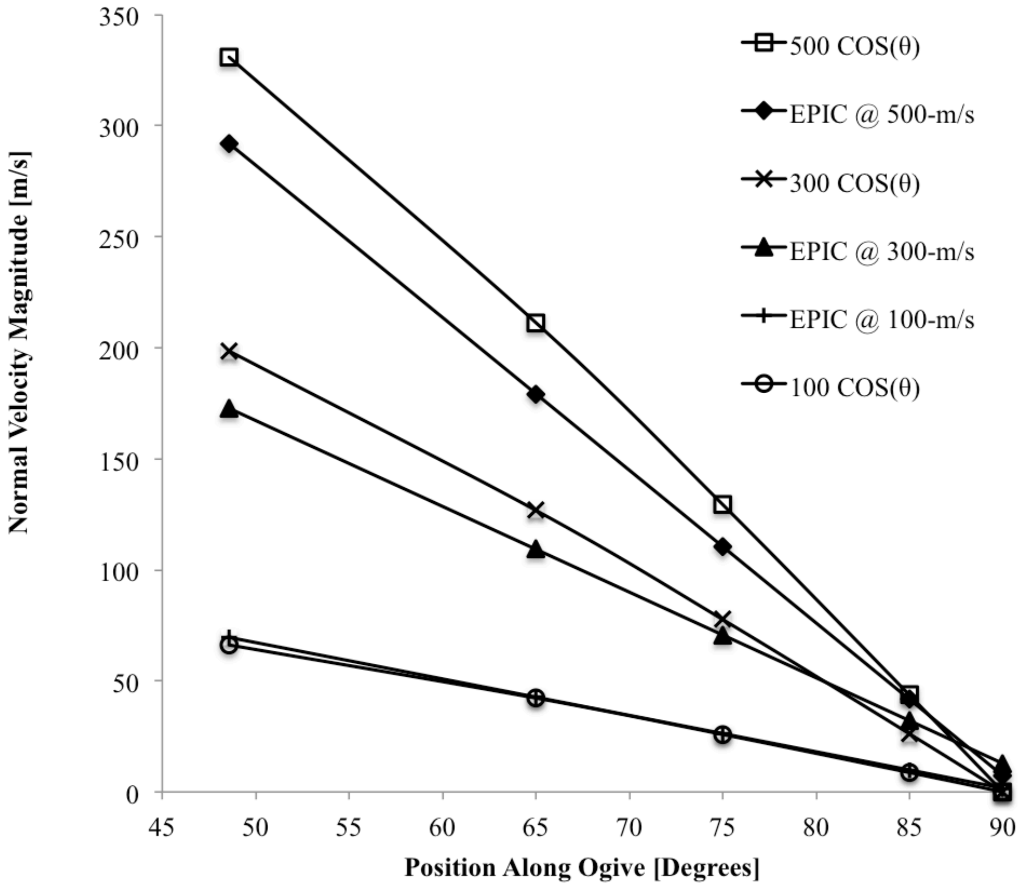

Figure 59. EPIC and $V_z \cos(\theta)$ Output for Data Set 6
97-MPa, 600-m/s Striking Velocity

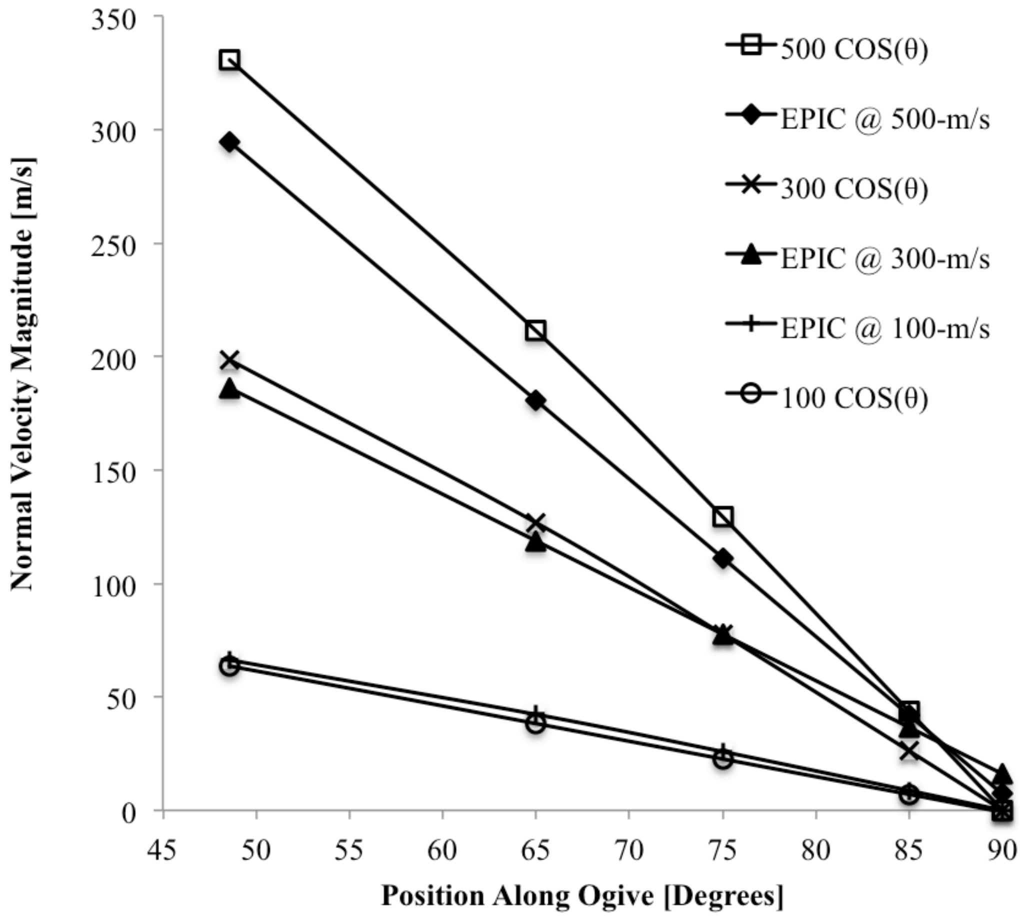

Figure 60. EPIC and $V_z \cos(\theta)$ Output for Data Set 7
157-MPa, 600-m/s Striking Velocity

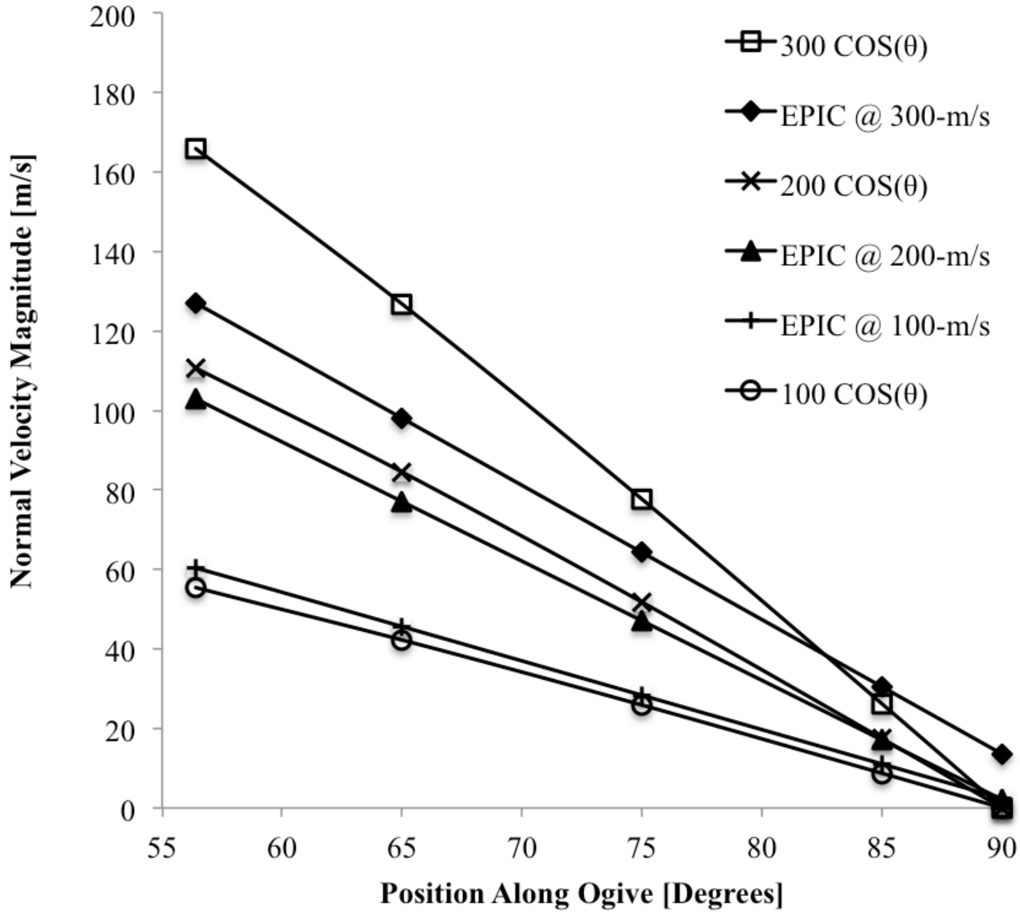

Figure 61. EPIC and $V_z \cos(\theta)$ Output for Data Set 3
39-MPa, 400-m/s Striking Velocity

Figure 61, Figure 62, and Figure 63 show plots of the EPIC normal velocity profiles for Data Sets 3, 5, and 7 and a striking velocity of 400-m/s. These profiles are compared with the $\cos(\theta)$ assumption. The larger projectile in Data Set 3 produces a much larger gap (between the velocity profiles of EPIC and that of the analytical assumption) than the smaller projectiles. As before, the projectile entering the high strength concrete dissipated energy faster than the ones entering lower strength concrete.

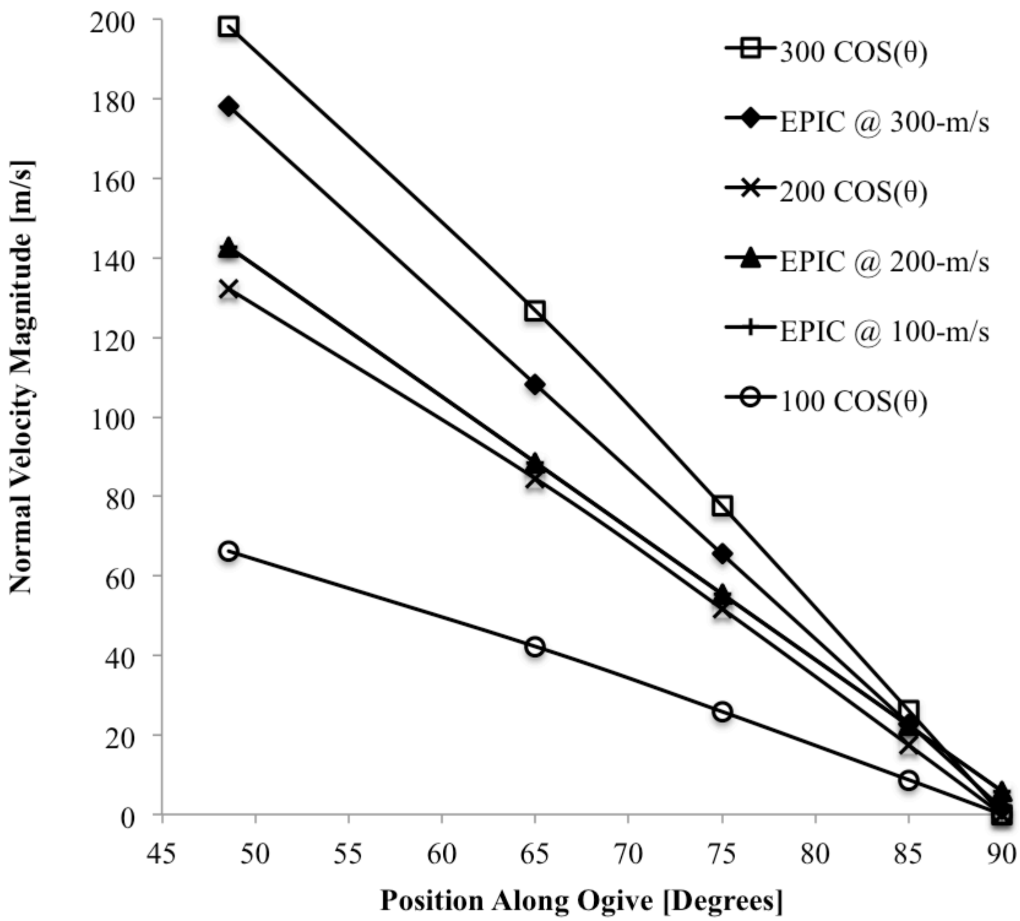

Figure 62. EPIC and $V_z\cos(\theta)$ Output for Data Set 5
36-MPa, 400-m/s Striking Velocity

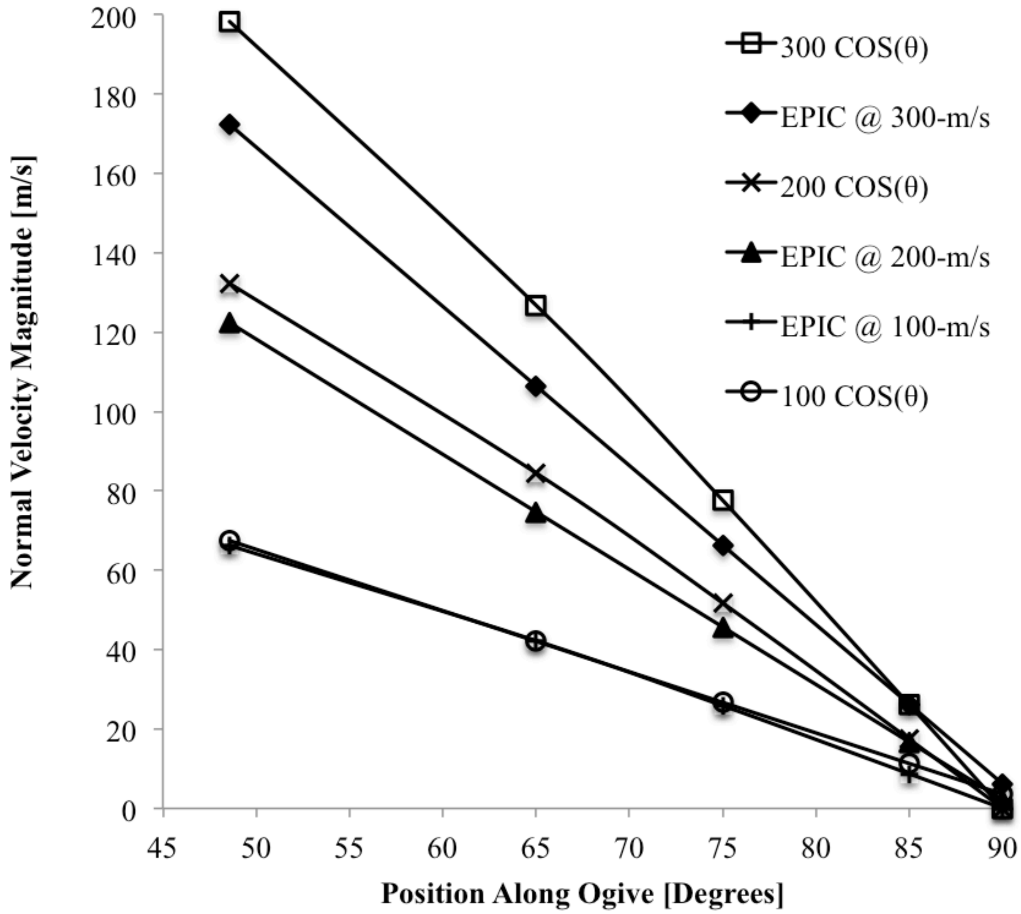

Figure 63. EPIC and $V_z \cos(\theta)$ Output for Data Set 7
157-MPa, 400-m/s Striking Velocity

In light of the discussion above, a reduction factor to be applied to the current analytical velocity profile assumption is proposed. Analytical models that account for the direction of the reported material flow, may show increased accuracy. This is elaborated upon further in the Conclusions section of this dissertation.

5.3 Analysis of the Flow of the Nodes in the Target Mesh

5.3.1 Selection of Expansion Comparison Model

As a high velocity projectile enters a target, a cavity is formed exerting stresses on the surrounding target material. The surrounding material responds by elastic and plastic deformation, cracking, failure, comminution, and densification. The nodes in the target mesh respond to this complex material behavior and move in a direction that best relieves stress in the target material. In this section, the movement of the nodes in the target mesh are compared to spherical cavity expansion. The decision to compare the nodal movement to spherical expansion rather than normal expansion was based upon the importance of the target material at the tip of the projectile as discussed earlier in Chapter 5 and upon a preliminary review of SECM and NECM results for material flow (Appendices 2 and 6). Figure 64 and Figure 65 show the NECM and SECM results for target material from Data Set 7 at a striking velocity of 800-m/s and a depth of penetration of 0.1m. Note that the SECM output could be described by a linear fit while the NECM output requires a quadratic or higher order ploynomial. Because of the linear nature of the SECM output, the decision was made to compare nodal movement to spherical expansion.

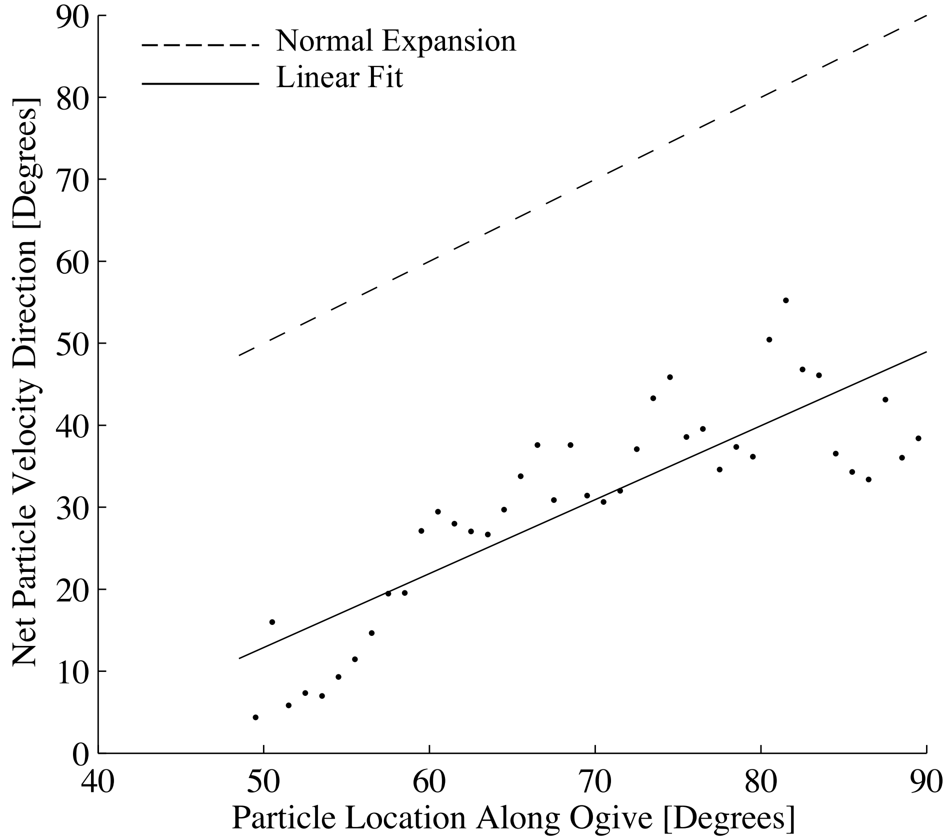

Figure 64. NECM Plot for Data Set 7, Striking Velocity 800-m/sTime Step: 0.13-ms, Zmin: -0.10-m, Slope: 0.90, Int: -32.3

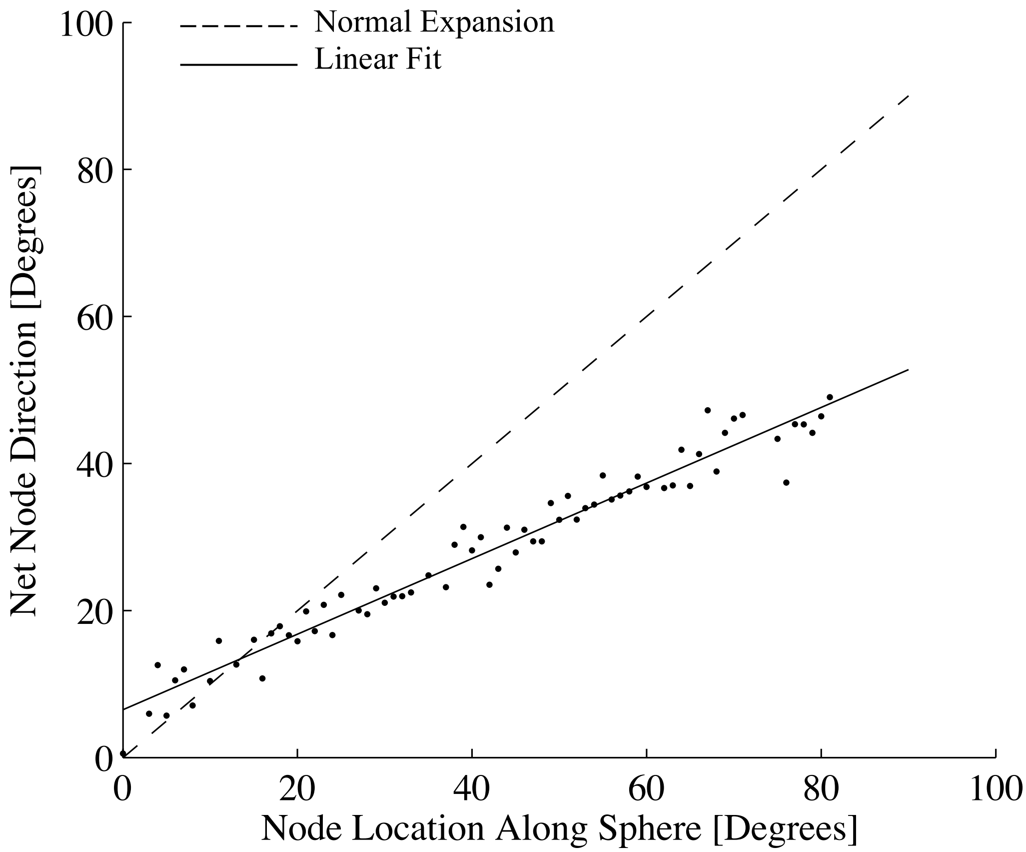

Figure 65. SECM Plot for Data Set 7, Striking Velocity 800-m/s
Time Step: 0.13-ms, Zmin: -0.10-m, Slope: 0.5, Int: 6.5

5.3.2 Effects of Varying Concrete Strength on Movement of Target Nodes

Appendix 4 lists the details for SECM slope values as a function of concrete strength. Table 24 provides an average of these values for striking velocities of 400, 600 and 800-m/s. The average slope data does not support a trend between nodal movement and concrete strength. The plots of the SECM data, however, show that as concrete strength increases, the point of intersection for the ogive-normal line and the linear fit increases. The y-intercept of the linear fit also provides a good estimate of this shift. The average y-intercept values for depths up to 0.3-m were 3.4, 7.3, and 9.6 for concrete strengths 36-MPa, 97-MPa, and 157-MPa, respectively.

Figure 66 through Figure 68 show how the SECM values shift upward as the strength of concrete is increased. Physically this upward shift in the SECM values means that the material at the tip of the projectile moves radially outward instead of downward as the concrete strength increases. Nodes located near $\theta_R = 90^\circ$ move at approximately 50° below spherical expansion. The direction of movement in this region ($\theta_R = 90^\circ$) is consistent across all strengths of concrete.

Table 24. Average NECM Values for 26.9-mm Projectile into Various Strength Concrete

Striking Velocity (m/s)	Concrete Strength (MPa)		
	36	97	157
800	0.7	1.2	1.0
600	1.2	1.2	1.1
400	1.6	-	1.0

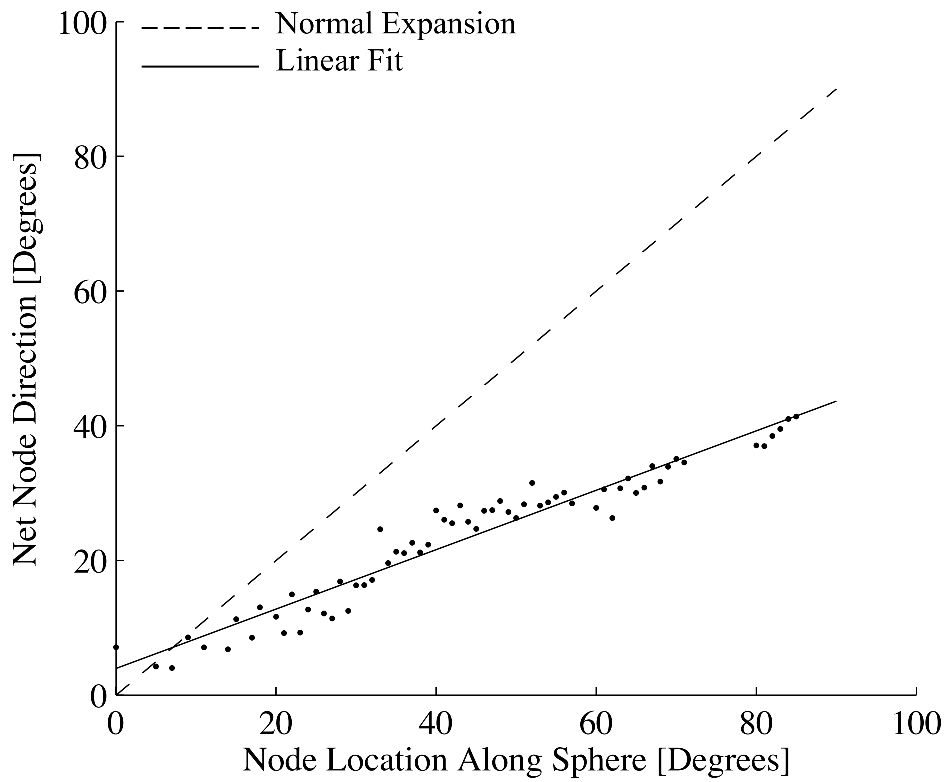

Figure 66. SECM Plot for Data Set 5, Striking Velocity 800-m/s
Time Step: 0.22-ms, Zmin: -0.2-m, Slope: 0.4, Int: 4.0

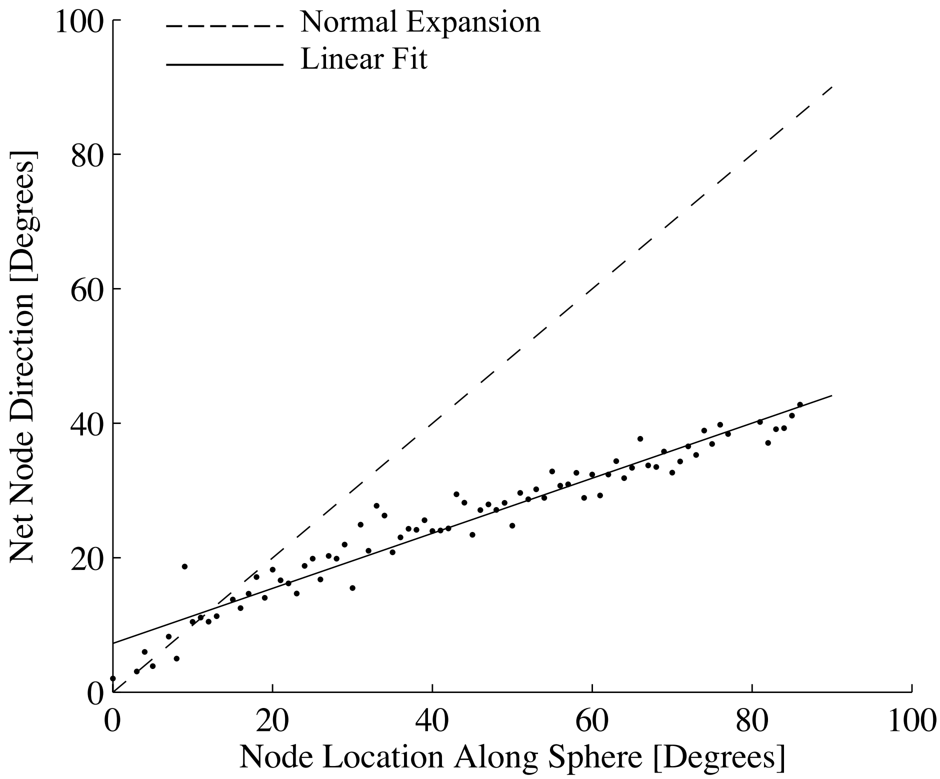

Figure 67. SECM Plot for Data Set 6, Striking Velocity 800-m/s
Time Step: 0.27-ms, Zmin: -0.20-m, Slope: 0.4, Int: 7.3

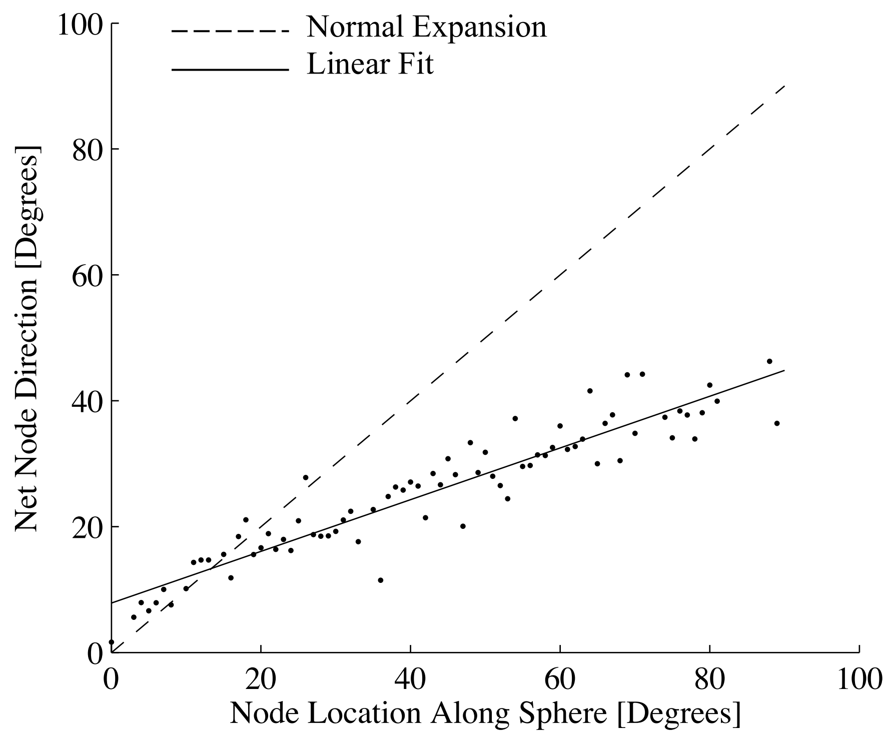

Figure 68. SECM Plot for Data Set 7, Striking Velocity 800-m/sTime Step: 0.28-ms, Zmin: -0.20-m, Slope: 0.4, Int: 7.9

5.3.3 Effects of Varying Striking Velocity on Movement of Target Nodes

Appendices 2 and 4 contain a full library of SECM plots and tables for Data Sets 3 through 7. The SECM slopes have very little variance across striking velocities.

Table 25. Spherical Flow Comparison: Increasing Striking Velocity/Increasing Instantaneous Depth for Data Set 5, 26.9-mm, 2-CRH Projectile into 36-MPa Target

Instantaneous Depth (m)	Striking Velocity (m/s)			
	200	400	600	800
0.1	0.7	0.5	0.6	0.5
0.2		0.3	0.5	0.4
0.3			0.4	0.4
0.4			0.4	0.4
0.5			0.4	0.4
0.6				0.3

Table 26. Spherical Flow Comparison: Increasing Striking Velocity/Decreasing Instantaneous Velocity for Data Set 5, 26.9-mm, 2-CRH Projectile into 36-MPa Target

Instantaneous Depth (m)	Striking Velocity (m/s)			
	200	400	600	800
700				0.5
600				0.4
500			0.5	0.3
400			0.4	0.4
300		0.5	0.4	0.4
200		0.5	0.4	0.5
100	0.7	0.5	0.5	0.5

Table 25 and Table 26 show that the range of SECM values is 0.3 to 0.7 for Data Set 5. These findings are typical of the values calculated for all data sets. The average values, as shown in Table 27 to Table 31, show that there is very little variance in the SECM slopes as striking velocity increases.

Table 27. Average SECM Values for Data Set 3
76.2-mm, 6-CRH Projectile into 39-MPa Target

Data Set	Striking Velocity (m/s)			
	250	325	400	425
3	0.5	0.4	0.4	0.4

Table 28. Average SECM Values for Data Set 4
76.2-mm, 6-CRH Projectile into 39-MPa Target

Data Set	Striking Velocity (m/s)			
	250	325	400	425
4	0.5	0.5	0.5	0.4

Table 29. Average SECM Values for Data Set 5
26.9-mm, 2-CRH Projectile into 36-MPa Target

Data Set	Striking Velocity (m/s)			
	200	400	600	800
5	0.7	0.5	0.5	0.4

Table 30. Average SECM Values for Data Set 6
26.9-mm, 2-CRH Projectile into 97-MPa Target

Data Set	Striking Velocity (m/s)			
	500	600	700	800
6	0.5	0.4	0.4	0.3

Table 31. Average SECM Values for Data Set 7
26.9-mm, 2-CRH Projectile into 157-MPa Target

Data Set	Striking Velocity (m/s)			
	200	400	600	800
7	0.4	0.5	0.4	0.4

The average y-intercepts of the SECM plots do not suggest a trend between intercept value and striking velocity. There are anecdotal examples of where the y-intercept increases with striking velocity as in Figure 69 and Figure 70, but the trend is not consistent at all depths of penetration.

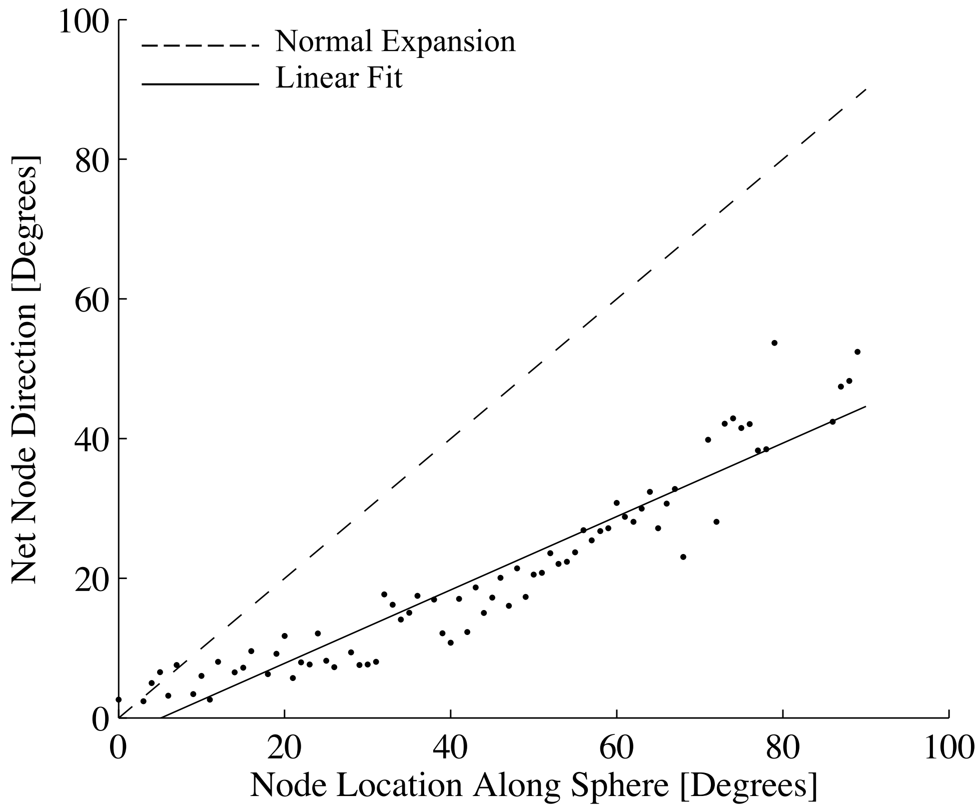

Figure 69. SECM Plot for Data Set 7, Striking Velocity 400-m/s
Time Step: 0.29-ms, Zmin: -0.10-m, Slope: 0.5, Int: -2.7

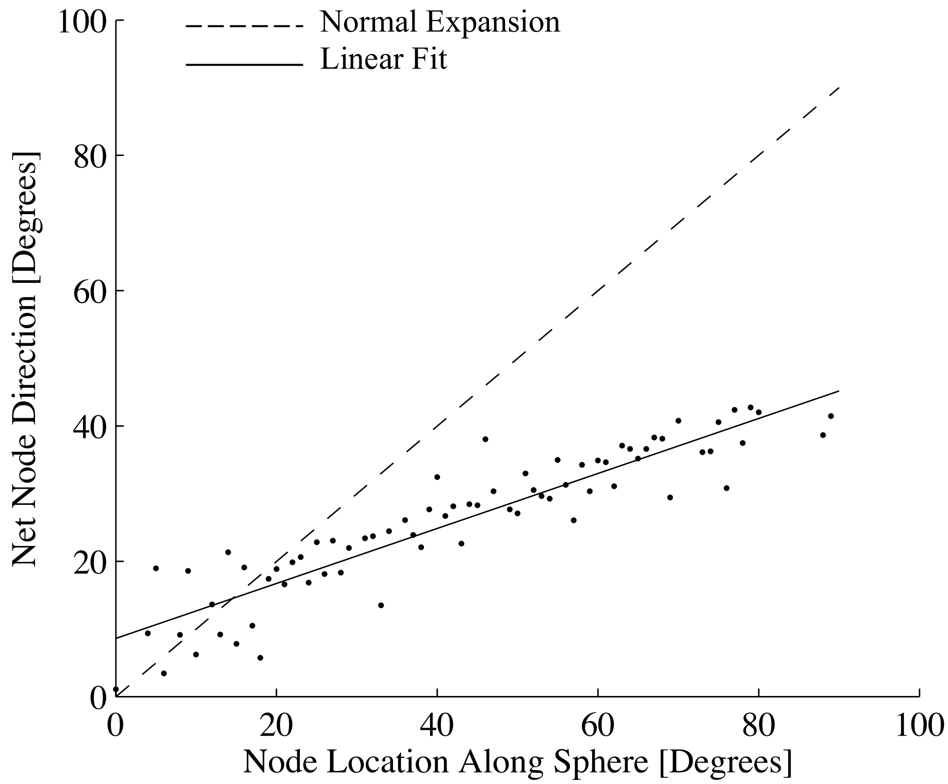

Figure 70. SECM Plot for Data Set 7, Striking Velocity 600-m/s
Time Step: 0.18-ms, Zmin: -0.10-m, Slope: 0.4, Int: 8.6

The varience of the SECM y-intercepts may be related to a physical process occuring in the concrete. For example, the varience may be related to a rapid release of stresses in the crushing zone or shearing zone. Table 32 shows the fluctuation of the y-intercept for Data Set 7 with an striking velocity of 800-m/s.

Table 32. SECM Y-Intercept Values for Data Set 7
800-m/s, 2-CRH Projectile into 157-MPa Target

Data Set	Instantaneous Depth (m)			
	0.1	0.2	0.3	0.4
7	6.5	10.5	9.5	9.4

CHAPTER 6: CONCLUSIONS

6.1 Conclusions

The main contribution of this research is the development of quantitative methods for characterizing concrete material flow during projectile penetration. Two methodologies, NECM and SECM, are presented that assess material flow from a series of finite element analysis output of different projectiles entering concrete targets of varying strengths. The finite element models developed in this study were validated based on published data from penetration experiments. The results from this research will impact future developments of analytical/semi-analytical equations for depth of penetration predictions.

Specific conclusions from this research include:

- The material flow of the comminuted concrete in the pulverized region is quantified using NECM, which analyzes the direction cosines and velocity profiles of the meshless particles at the projectile-target interface.
- In the pulverized region, the velocity profile was determined to be bilinear for low strength concrete (36-39-MPa) at striking velocities under 500-m/s.
- The projectile diameter, striking velocity, and concrete strength had little influence on the direction of meshless-particle flow below $\theta_R = 80^\circ$.

- Particle velocities along the length of the ogive were not accurately represented by V$cos(\theta)$ which has been a frequently cited assumption in existing analytical/semi-analytical equations used for calculating depth of penetration.
- The direction of particle flow below $\theta_R = 80^\circ$ was found to be 35° to 40° less than ogive-normal expansion.
- The material flow within ½-caliber of the projectile tip was quantified using SECM which analyzes the direction cosines and velocity profiles of the target nodes within the high velocity region.
- Near the tip of the projectile, where $\theta_r < 20^\circ$, the radial component of nodal velocity increased as the concrete strength increased.
- SECM slope values for nodal direction of flow consistently averaged 0.5, indicating that the direction cosine angle was about half the spherical position angle ($\theta_V = \frac{1}{2}\theta_r$).

6.2 Recommendations

Application of analytical methods to penetration problems are often predicated upon determining the resistive forces at the nose of the projectile. From the geometry shown in Figure 71., differential ring forces that are normal and tangent to the ogival nose can be defined as

$$dF_n = 2\pi s^2 \left[\sin(\theta) - \left(\frac{s-a}{s}\right)\right] \sigma_n\left(V_z, \theta_R\right) d\theta_R \qquad (52)$$

where the symbols are defined in Figure 71 (Forrestal, Okajima, and Luk, 1988). The normal stress on the nose of the projectile is given by $\sigma_n\left(V_z,\theta\right)d\theta$ and is dependent on V_Z and θ_R. This stress is often approximated as the pressure from the spherical or cylindrical cavity expansion analysis.

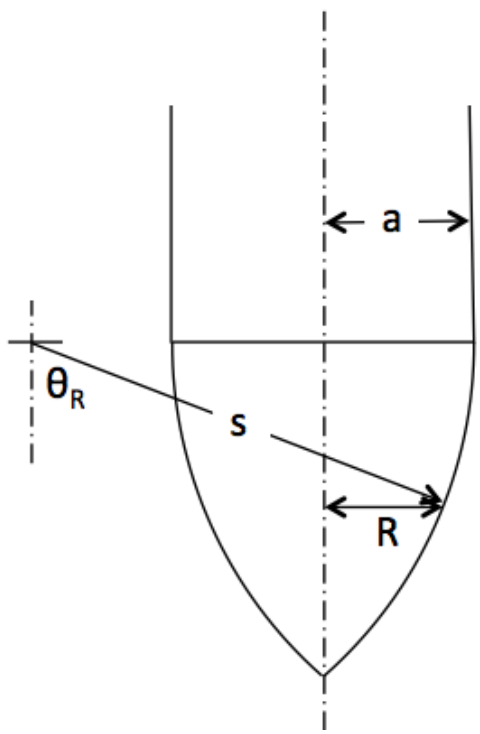

Figure 71. Ogive Nose Dimensions

The cavity expansion pressure, which is the pressure required to expand a cavity wall inside an infinite medium at a constant velocity, is taken as an approximation to the target resistance; where the constant velocity in the cavity expansion is related to the velocity of the projectile. A tangential frictional component of stress that relates to the normal stress by

$$dF_t = 2\pi s^2 \left[\sin(\theta) - \left(\frac{s-a}{s} \right) \right] \mu \sigma_n \left(V_z, \theta_R \right) d\theta_R \tag{53}$$

where μ is the sliding-friction coefficient was used by Forrestal, Okajima, and Luk (1988). The total axial force on the nose, therefore, can be determined by summing the axial components of the normal and tangential force differentials across the nose of the projectile. The total axial force is then given as

$$F_z = 2\pi s^2 \int_{\theta_0}^{\pi/2} \left\{ \left[\sin\theta_R \left(\frac{s-a}{s} \right) \right] \times \left(cos\theta_R + \mu \sin\theta_R \right) \right\} \sigma_n \left(V_z, \theta_R \right) d\theta_R \tag{54}$$

where

$$\theta_0 = \sin^{-1} \left(\frac{s-a}{s} \right). \tag{55}$$

The challenge of this approach is determining the value of $\sigma_n \left(V_z, \theta_R \right)$ at every point along the projectile target interface. To use the cavity expansion analysis, the velocity profile along the projectile-target interface must be known. This velocity is typically assumed to be $V_Z \cos(\theta_R)$. The findings from this research using NECM, however suggest that the velocity profile is not equal to $V_Z \cos(\theta_R)$.

Differences between the $V_Z \cos(\theta_R)$ assumption and the EPIC velocity profiles have been determined as a function of decaying velocity and concrete strength as shown in Figure 58 through Figure 63. Based on the findings from the analysis of the available data, it is recommended that a reduction factor as shown in Figure 72 be applied to the $V_Z \cos(\theta_R)$ assumption to account for the direction of particle flow, which may result in an improved prediction of the total axial force and subsequently the depth of penetration.

For the data in this dissertation a reduction factor of $F_R = -0.0004V + 1$ is proposed for the 36-MPa concrete and a reduction factor of $F_R = -0.00025V + 0.98$ is proposed for the 157-MPa concrete. As the form of the reduction factor suggests, the magnitude of the required correction decreased as the residual velocity of the projectile decreased. This can be seen for the 36-MPa concrete in Figure 72.

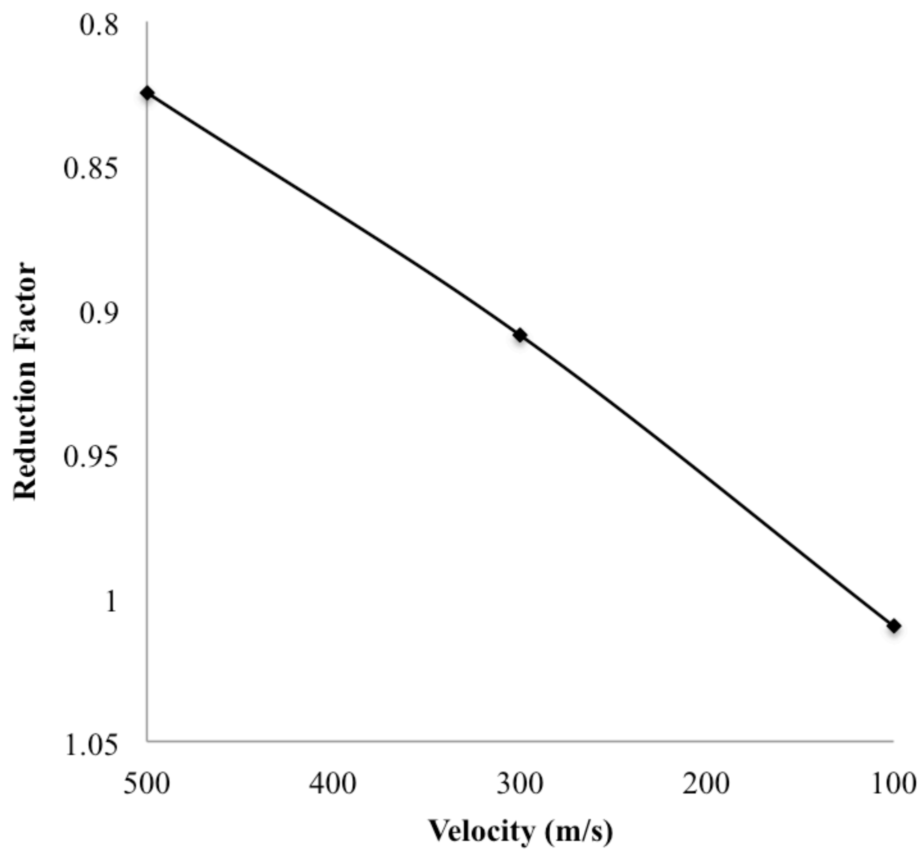

Figure 72. Proposed Reduction Factor for Data Set 5, at 600 m/s Striking Velocity

6.3 Limitations of the Study and Future Work

Limitations of the study include:

- Little to no availability of concrete penetration test data that is accompanied by the material test data needed to populate the finite element material models.
- The projectile velocity domain was restricted to 200 to 800-m/s.
- Angles of impact were restricted to near normal incidences with no projectile yaw, pitch, or spin.
- Target dimensions were kept sufficiently large to avoid edge effects.
- The application of NECM and SECM were limited to concrete strengths ranging from 36-MPa at the lower bound to 157-MPa at the upper bound.

Future efforts should be directed toward the following:

Refinement of the Approach Taken in This Dissertation. The approach in the current research was to capture snapshots of target velocity data at particular depths of penetration and instantaneous velocities. This allows for the side-by-side comparison of material flow for two or more concrete strengths. The goal was to identify differences and trends that could be attributed to known parameters such as striking velocity, instantaneous depth, concrete strength or projectile diameter. One of the conclusions of the study is that the velocity profile is bilinear for low strength concrete (36-39-MPa) at striking velocities under 500-m/s. This conclusion should be tested further using additional test data and material models. Future studies should focus on the bilinear effect and investigate the cause of the effect. The current research was limited to an upper concrete strength of 157-MPa. The NECM and SECM methodologies should be applied towards data pertaining to concretes in the Ultra High Performance category (> 190-MPa).

Application of Current Findings. Investigation of how a modification to the $V_z cos(\theta_R)$ assumption would affect cavity expansion results should be investigated. The dependency of the reduction factor on concrete strength should be investigated more thoroughly with additional concrete test data.

Parametric Studies. NECM and SECM provide a useful tool for comparing mateiral flow to an established baseline. It would be useful to conduct a parametric study of how material model parameters impact SECM and NECM results. The data from this research may help clarify the dominant material properties responsible for changing the direction of material flow which ultimately leads to changes in the resistance forces in the target.

APPENDIX 1: NECM PLOTS FOR PARTICLE DIRECTION

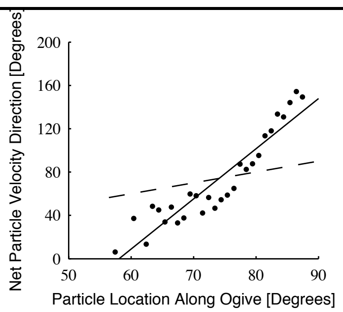

Time Step: 0.41-ms, Zmin: -0.1-m, Slope: 4.6, Int: -269.0

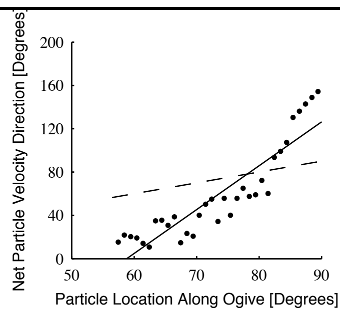

Time Step: 0.70-ms, Vi: -200-m/s, Slope: 4.1, Int: -237.8

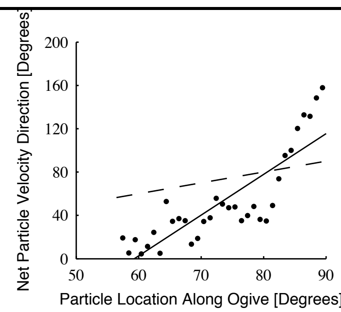

Time Step: 0.89-ms, Zmin: -0.2-m, Slope: 3.8, Int: -222.7

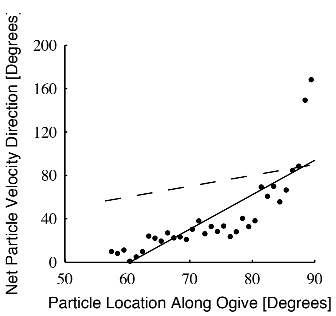

Time Step: 1.55-ms, Vi: -100-m/s, Slope: 3.2, Int: -191.8

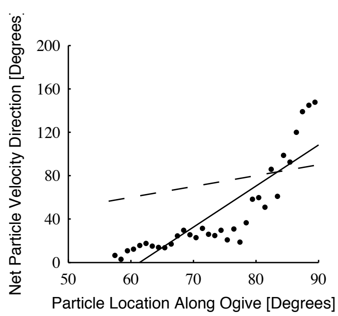

Time Step: 1.61-ms, Zmin: -0.30-m, Slope: 3.8, Int: -232.2

Figure 73. NECM Plots for Data Set 3, 250-m/s Striking Velocity, 39-MPa Concrete Target, 76.2-mm Diameter Projectile, 3-CRH Projectile Nose

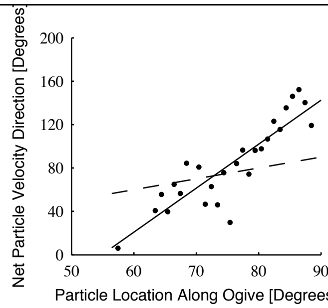

Time Step: 0.30-ms, Vi: -300-m/s, Slope: 4.1, Int: -222.2

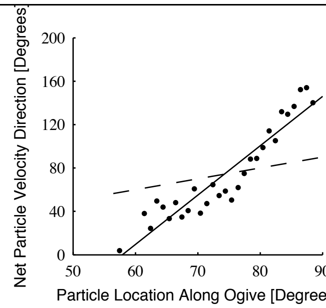

Time Step: 0.31-ms, Zmin: -0.1-m, Slope: 4.5, Int: -263.0

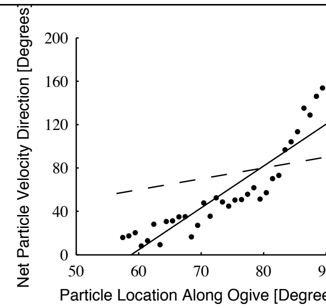

Time Step: 0.65-ms, Zmin: -0.2-m, Slope: 3.9, Int: -226.8

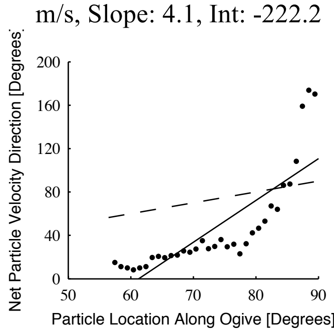

Time Step: 1.06-ms, Zmin: -0.3-m, Slope: 3.9, Int: -236.1

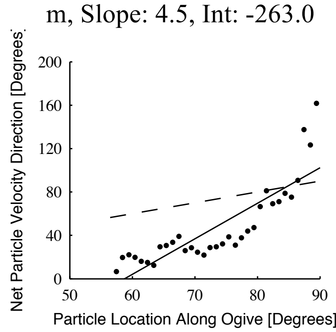

Time Step: 1.23-ms, Vi: -200-m/s, Slope: 3.3, Int: -192.2

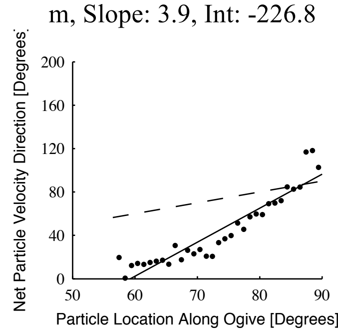

Time Step: 1.63-ms, Zmin: -0.40-m, Slope: 3.1, Int: -185.5

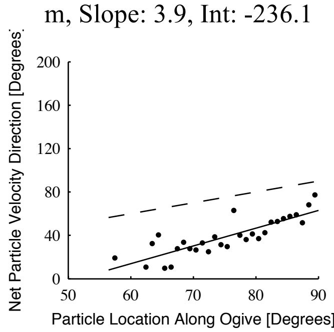

Time Step: 1.95-ms, Vi: -100-m/s, Slope: 1.6, Int: -84.0

Figure 74. NECM Plots for Data Set 3, 325-m/s Striking Velocity, 39-MPa Concrete Target, 76.2-mm Diameter Projectile, 3-CRH Projectile Nose

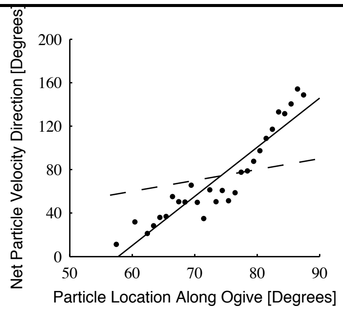

Time Step: 0.25-ms, Zmin: -0.1-m, Slope: 4.5, Int: -261.1

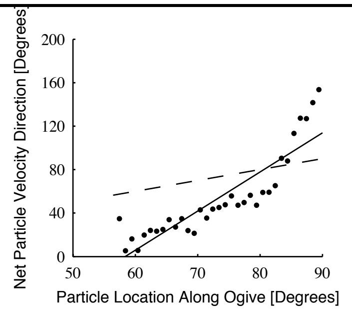

Time Step: 0.52-ms, Zmin: -0.2-m, Slope: 3.6, Int: -210.1

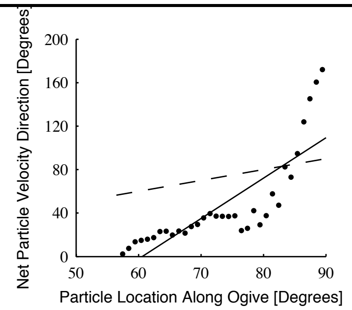

Time Step: 0.82-ms, Zmin: -0.30-m, Slope: 3.7, Int: -224.9

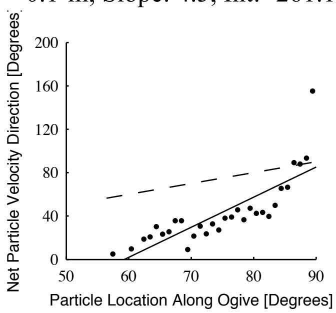

Time Step: 0.87-ms, Vi: -300-m/s, Slope: 2.8, Int: -164.1

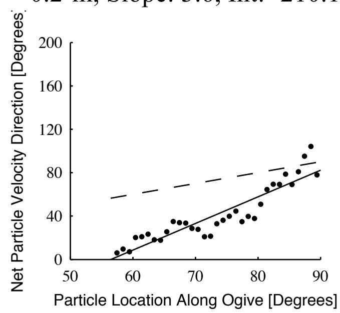

Time Step: 1.17-ms, Zmin: -0.40-m, Slope: 2.5, Int: -138.9

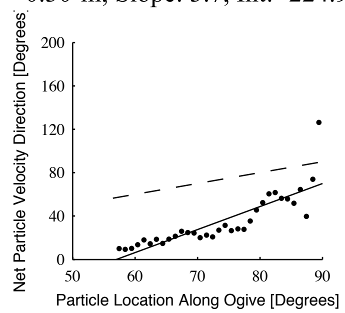

Time Step: 1.55-ms, Vi: -200-m/s, Slope: 2.1, Int: -120.8

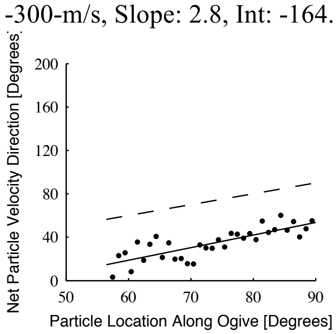

Time Step: 1.63-ms, Zmin: -0.5-m, Slope: 1.2, Int: -51.0

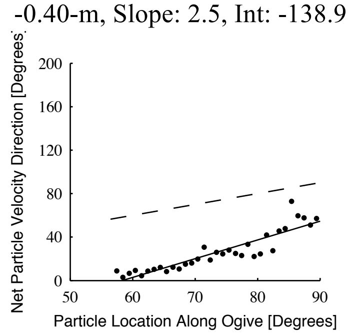

Time Step: 2.13-ms, Vi: -100-m/s, Slope: 1.7, Int: -100.5

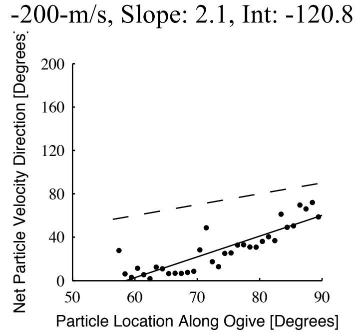

Time Step: 2.55-ms, Zmin: -0.6-m, Slope: 1.9, Int: -111.8

Figure 75. NECM Plots for Data Set 3, 400-m/s Striking Velocity, 39-MPa Concrete Target, 76.2-mm Diameter Projectile, 3-CRH Projectile Nose

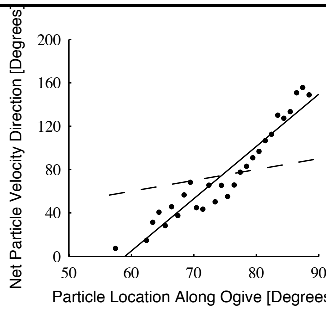

Time Step: 0.21-ms, Zmin: -0.1-m, Slope: 4.8, Int: -283.8

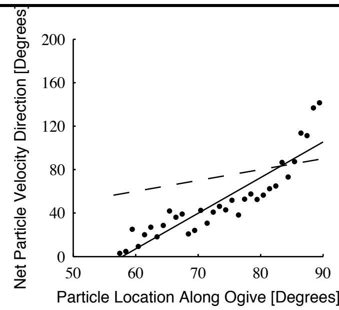

Time Step: 0.44-ms, Zmin: -0.2-m, Slope: 3.3, Int: -189.4

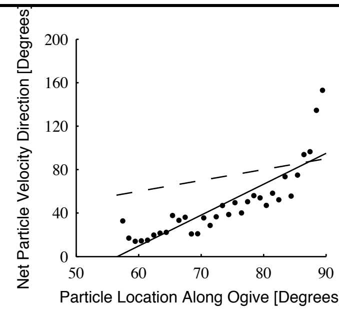

Time Step: 0.58-ms, Vi: -400-m/s, Slope: 2.8, Int: -160.5

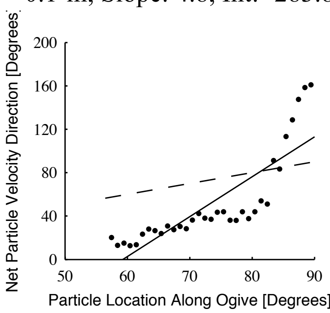

Time Step: 0.68-ms, Zmin: -0.30-m, Slope: 3.7, Int: -218.0

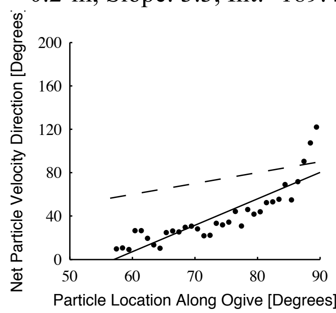

Time Step: 0.94-ms, Zmin: -0.40-m, Slope: 2.4, Int: -138.7

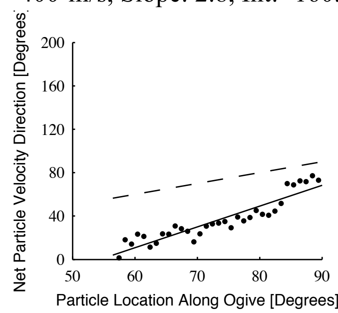

Time Step: 1.24-ms, Zmin: -0.5-m, Slope: 1.9, Int: -104.2

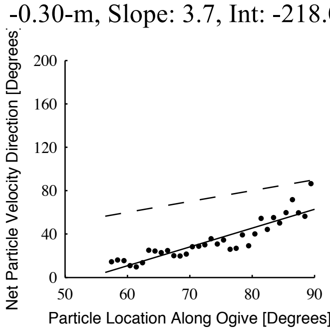

Time Step: 1.28-ms, Vi: -300-m/s, Slope: 1.7, Int: -92.9

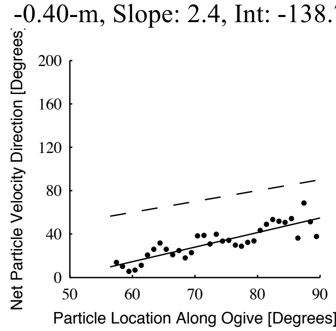

Time Step: 1.61-ms, Zmin: -0.6-m, Slope: 1.3, Int: -66.2

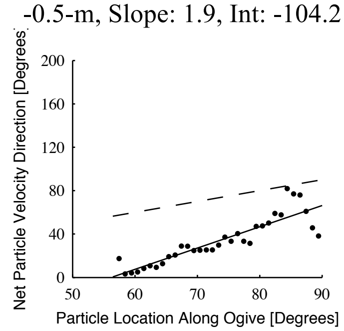

Time Step: 1.93-ms, Vi: -200-m/s, Slope: 2.0, Int: -110.1

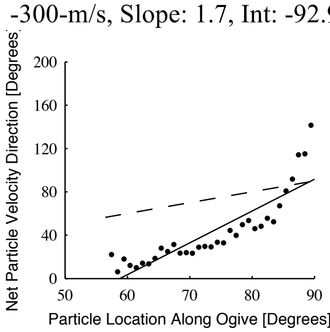

Time Step: 2.11-ms, Zmin: -0.70-m, Slope: 2.9, Int: -172.7

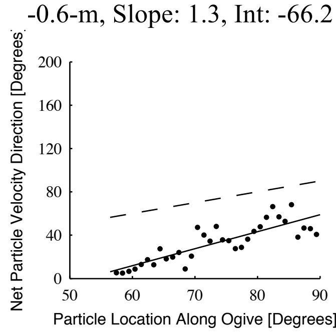

Time Step: 2.52-ms, Vi: -100-m/s, Slope: 1.6, Int: -82.3

Figure 76. NECM Plots for Data Set 3, 475-m/s Striking Velocity, 39-MPa Concrete Target, 76.2-mm Diameter Projectile, 3-CRH Projectile Nose

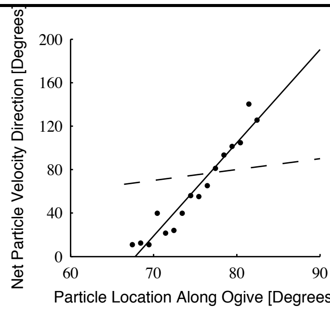

Time Step: 0.41-ms, Zmin: -0.1-m, Slope: 8.57, Int: -580.8

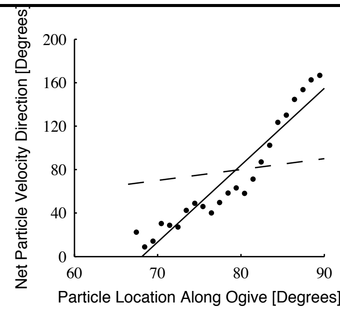

Time Step: 0.83-ms, Vi: -200-m/s, Slope: 7.07, Int: -481.3

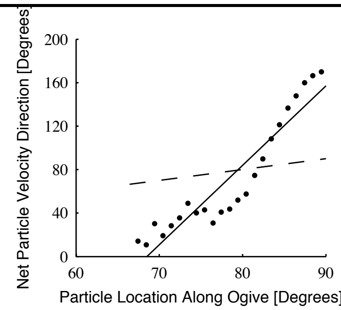

Time Step: 0.85-ms, Zmin: -0.2-m, Slope: 7.31, Int: -500.8

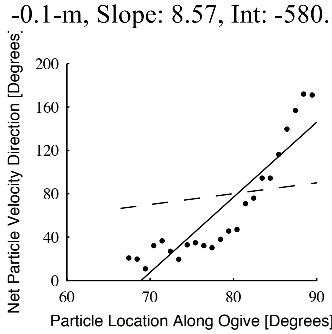

Time Step: 1.43-ms, Zmin: -0.30-m, Slope: 6.92, Int: -477.1

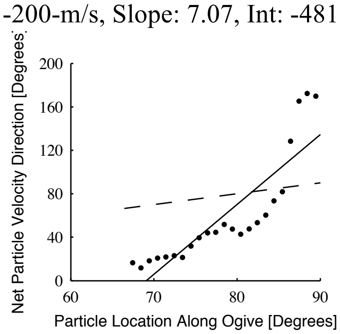

Time Step: 1.73-ms, Vi: -100-m/s, Slope: 6.42, Int: -443.7

Figure 77. NECM Plots for Data Set 4, 250-m/s Striking Velocity, 39-MPa Concrete Target, 76.2-mm Diameter Projectile, 6-CRH Projectile Nose

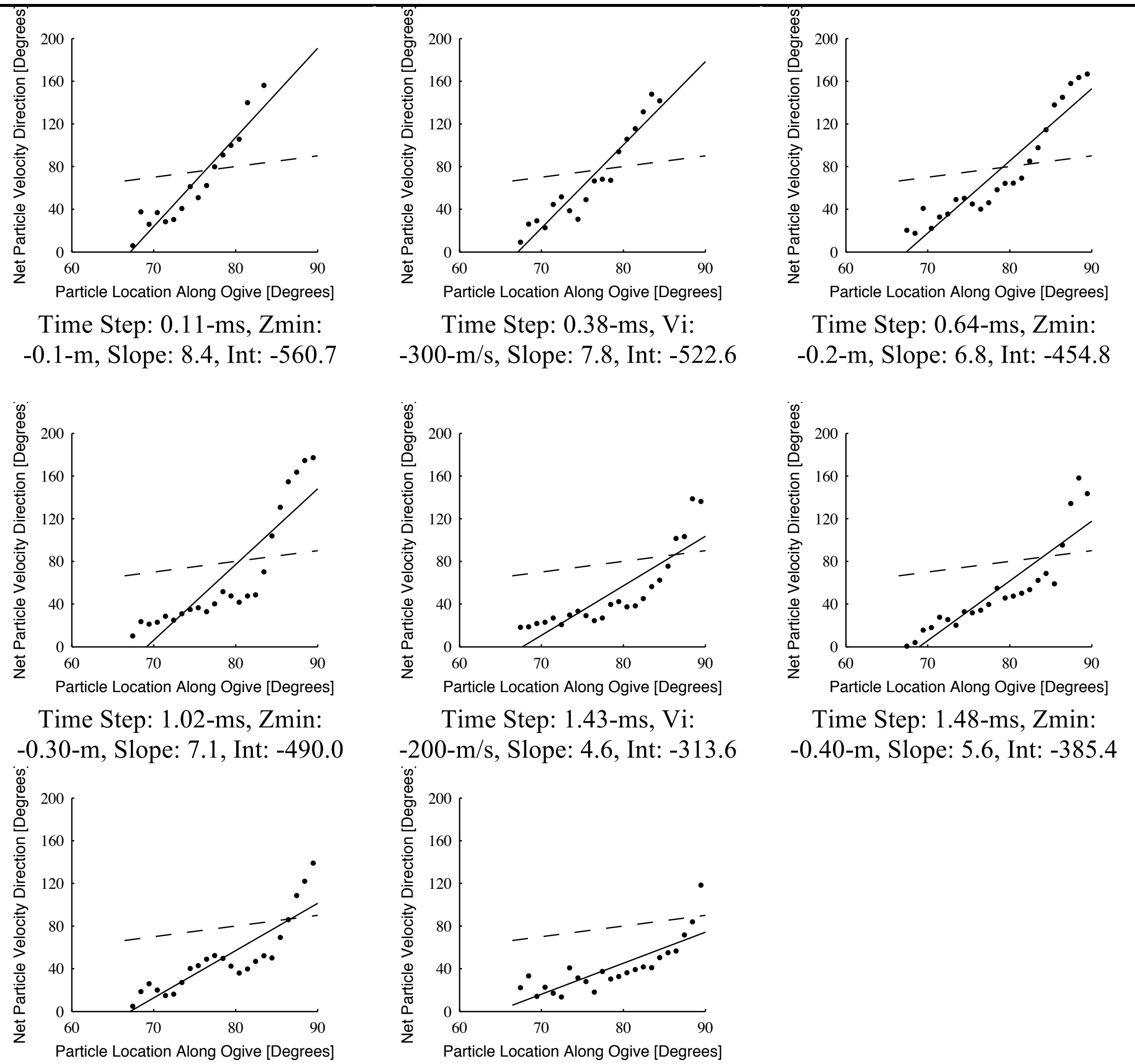

Time Step: 0.11-ms, Zmin: -0.1-m, Slope: 8.4, Int: -560.7

Time Step: 0.38-ms, Vi: -300-m/s, Slope: 7.8, Int: -522.6

Time Step: 0.64-ms, Zmin: -0.2-m, Slope: 6.8, Int: -454.8

Time Step: 1.02-ms, Zmin: -0.30-m, Slope: 7.1, Int: -490.0

Time Step: 1.43-ms, Vi: -200-m/s, Slope: 4.6, Int: -313.6

Time Step: 1.48-ms, Zmin: -0.40-m, Slope: 5.6, Int: -385.4

Time Step: 2.20-ms, Vi: -100-m/s, Slope: 4.4, Int: -296.8

Time Step: 2.25-ms, Zmin: -0.5-m, Slope: 2.9, Int: -187.6

Figure 78. NECM Plots for Data Set 4, 325-m/s Striking Velocity, 39-MPa Concrete Target, 76.2-mm Diameter Projectile, 6-CRH Projectile Nose

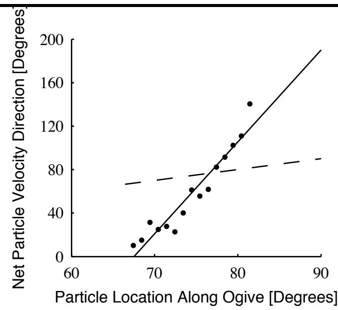

Time Step: 0.25-ms, Zmin: -0.1-m, Slope: 8.5, Int: -570.6

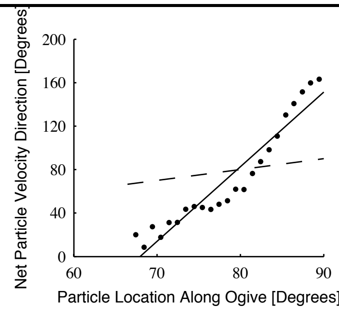

Time Step: 0.51-ms, Zmin: -0.2-m, Slope: 6.9, Int: -466.3

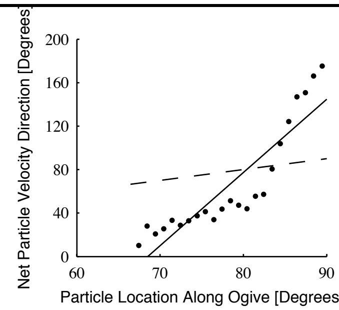

Time Step: 0.80-ms, Zmin: -0.30-m, Slope: 6.7, Int: -461.0

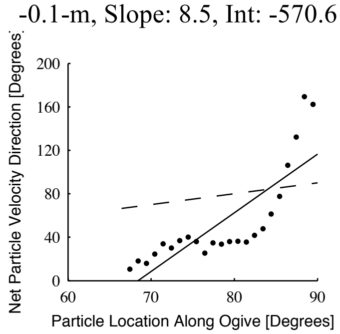

Time Step: 1.08-ms, Vi: -300-m/s, Slope: 5.4, Int: -368.9

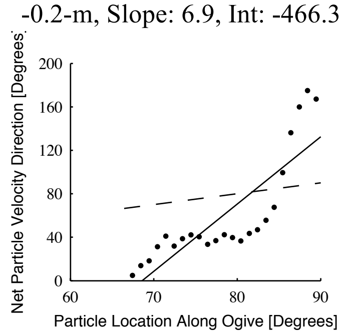

Time Step: 1.11-ms, Zmin: -0.4-m, Slope: 6.2, Int: -423.7

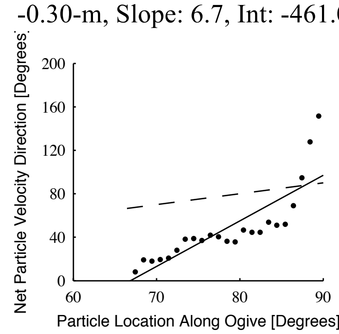

Time Step: 1.49-ms, Zmin: -0.5-m, Slope: 4.2, Int: -279.7

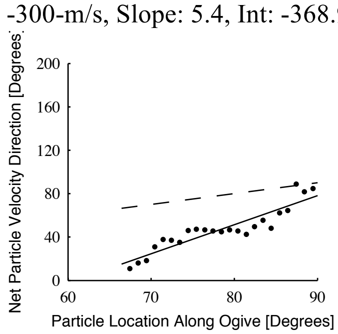

Time Step: 1.75-ms, Vi: -200-m/s, Slope: 2.7, Int: -162.4

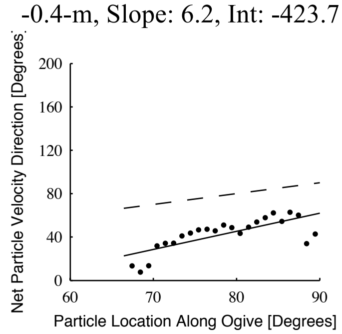

Time Step: 2.00-ms, Zmin: -0.60-m, Slope: 1.7, Int: -88.2

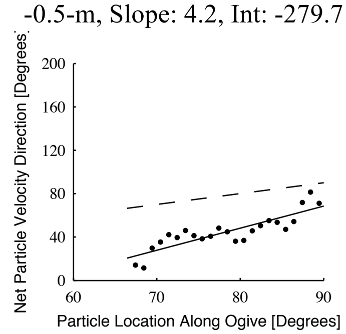

Time Step: 2.44-ms, Vi: -100-m/s, Slope: 2.0, Int: -114.3

Figure 79. NECM Plots for Data Set 4, 400-m/s Striking Velocity, 39-MPa Concrete Target, 76.2-mm Diameter Projectile, 6-CRH Projectile Nose

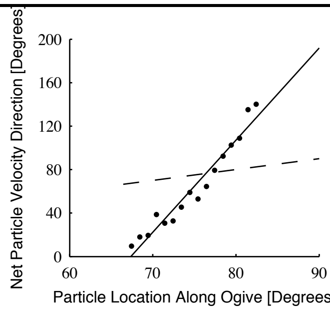

Time Step: 0.21-ms, Zmin: -0.1-m, Slope: 8.5 Int: -570.4

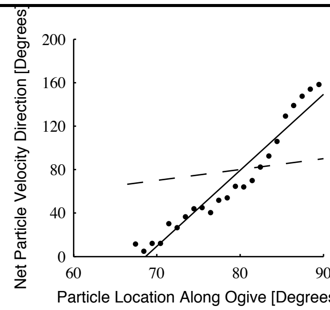

Time Step: 0.43-ms, Zmin: -0.2-m, Slope: 7.0, Int: -480.3

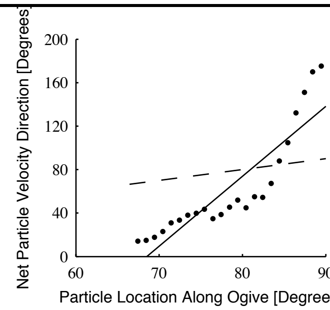

Time Step: 0.66-ms, Zmin: -0.30-m, Slope: 6.4, Int: -441.0

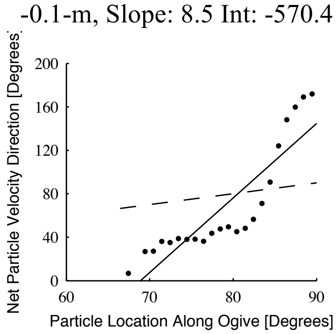

Time Step: 0.75-ms, Vi: -400-m/s, Slope: 6.9, Int: -472.2

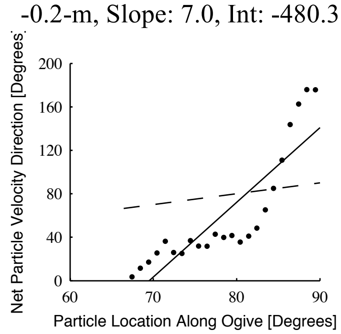

Time Step: 0.91-ms, Zmin: -0.40-m, Slope: 6.9, Int: -477.2

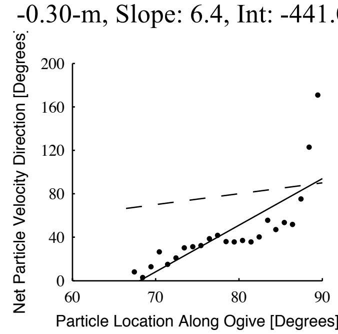

Time Step: 1.18-ms, Zmin: -0.5-m, Slope: 4.3, Int: -292.0

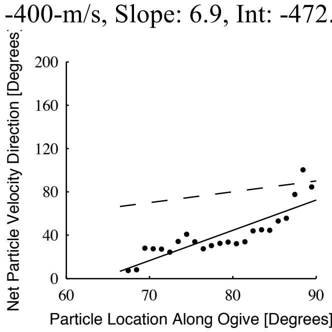

Time Step: 1.43-ms, Vi: -300-m/s, Slope: 2.8, Int: -179.1

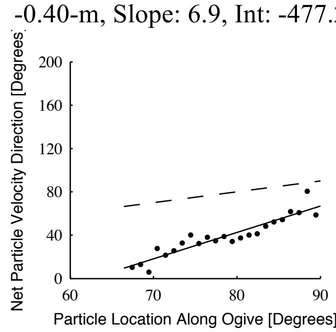

Time Step: 1.50-ms, Zmin: -0.60-m, Slope: 2.4, Int: -152.4

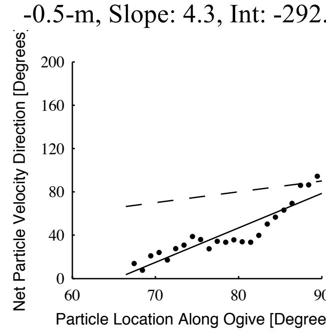

Time Step: 1.89-ms, Zmin: -0.70-m, Slope: 3.2, Int: -208.2

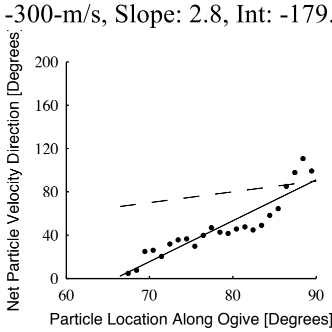

Time Step: 2.13-ms, Vi: -200-m/s, Slope: 3.8, Int: -248.7

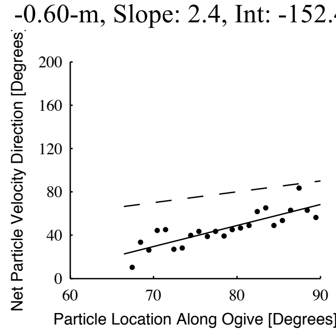

Time Step: 2.40-ms, Zmin: -0.8-m, Slope: 1.9, Int: -106.1

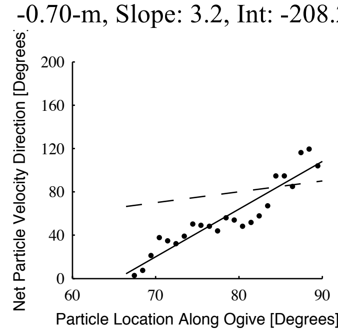

Time Step: 2.83-ms, Vi: -100-m/s, Slope: 4.4, Int: -288.0

Figure 80. NECM Plots for Data Set 4, 475-m/s Striking Velocity, 39-MPa Concrete Target, 76.2-mm Diameter Projectile, 6-CRH Projectile Nose

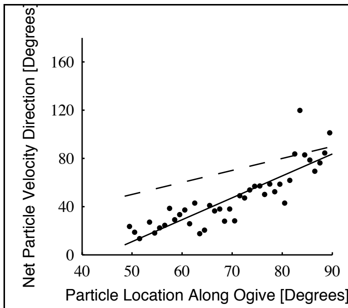

Time Step: 0.56-ms, Vi: -100-m/s, Slope: 1.8, Int: -80.2

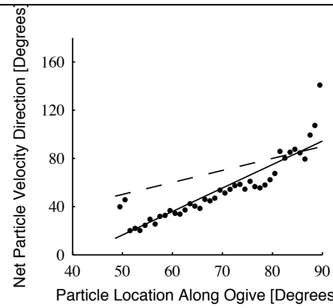

Time Step: 0.67-ms, Zmin: -0.10-m, Slope: 2.0, Int: -81.1

Figure 81. NECM Plots for Data Set 5, 200-m/s Striking Velocity, 36-MPa Concrete Target, 26.9-mm Diameter Projectile, 2-CRH Projectile Nose

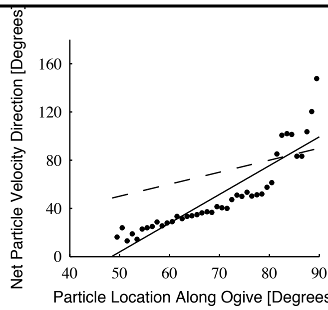

Time Step: 0.26-ms, Zmin: -0.10-m, Slope: 2.4, Int: -115.4

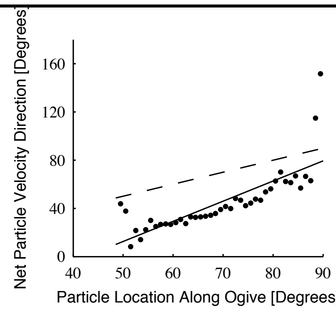

Time Step: 0.40-ms, Vi: -300-m/s, Slope: 1.7, Int: -71.0

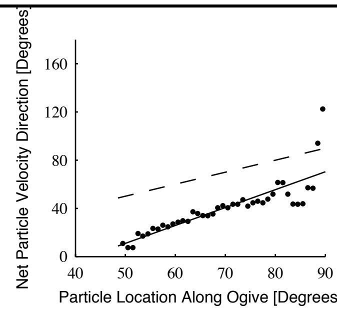

Time Step: 0.56-ms, Vi: -200-m/s, Slope: 1.5, Int: -63.2

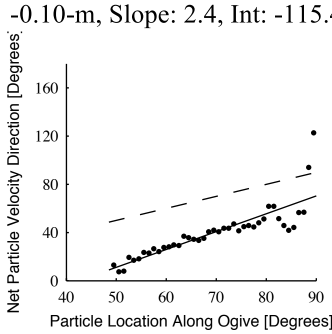

Time Step: 0.56-ms, Vi: -100-m/s, Slope: 1.5, Int: -62.6

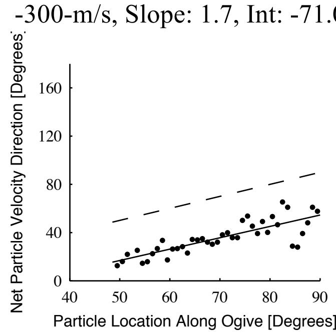

Time Step: 0.62-ms, Zmin: -0.20-m, Slope: 0.9, Int: -30.4

Figure 82. NECM Plots for Data Set 5, 400-m/s Striking Velocity, 36-MPa Concrete Target, 26.9-mm Diameter Projectile, 2-CRH Projectile Nose

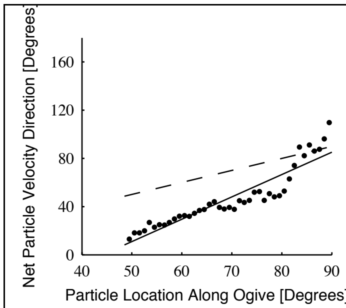

Time Step: 0.17-ms, Zmin: -0.10-m, Slope: 1.9, Int: -81.9

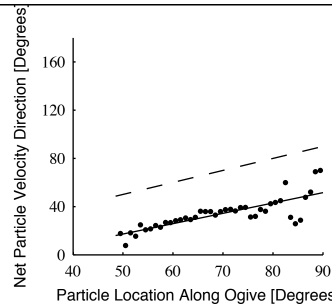

Time Step: 0.33-ms, Vi: -500-m/s, Slope: 0.9, Int: -25.7

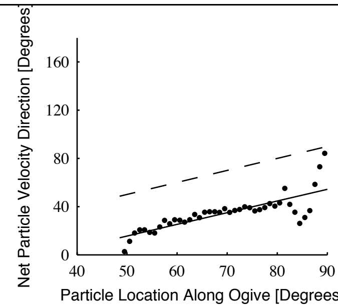

Time Step: 0.34-ms, Zmin: -0.2-m, Slope: 1.0, Int: -32.7

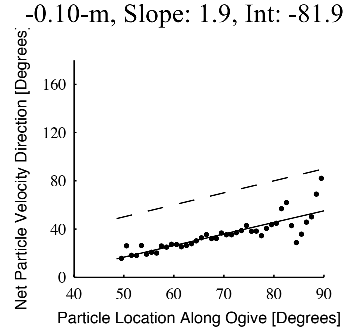

Time Step: 0.55-ms, Zmin: -0.3-m, Slope: 1.0, Int: -31.5

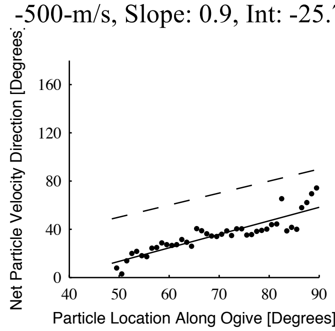

Time Step: 0.59-ms, Vi: -400-m/s, Slope: 1.1, Int: -42.9

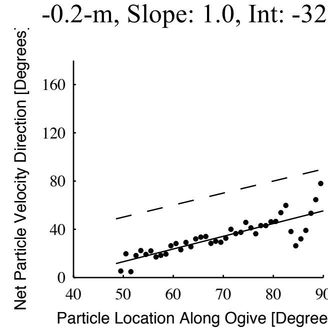

Time Step: 0.82-ms, Zmin: -0.4-m, Slope: 1.1, Int: -39.7

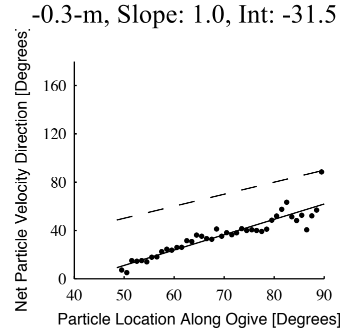

Time Step: 0.84-ms, Vi: -300-m/s, Slope: 1.3, Int: -52.4

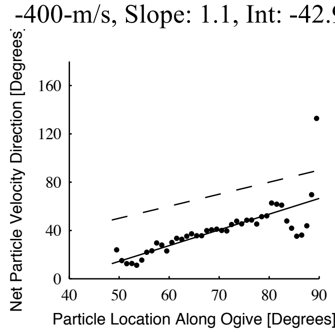

Time Step: 1.12-ms, Vi: -200-m/s, Slope: 1.3, Int: -50.6

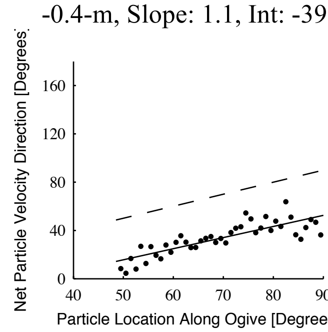

Time Step: 1.13-ms, Zmin: -0.5-m, Slope: 0.9, Int: -30.3

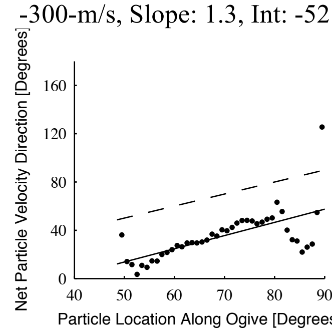

Time Step: 1.41-ms, Vi: -100-m/s, Slope: 1.1, Int: -41.0

Figure 83. NECM Plots for Data Set 5, 600-m/s Striking Velocity, 36-MPa Concrete Target, 26.9-mm Diameter Projectile, 2-CRH Projectile Nose

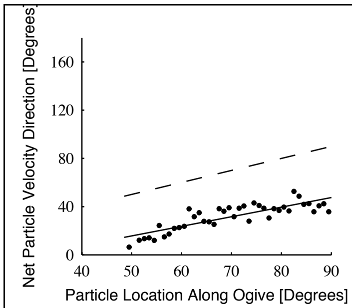

Time Step: 0.12-ms, Zmin: -0.10-m, Slope: 0.8, Int: -23.9

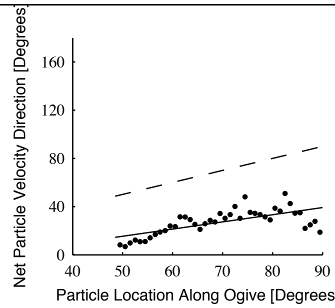

Time Step: 0.17-ms, Vi: -700-m/s, Slope: 0.6, Int: -14.7

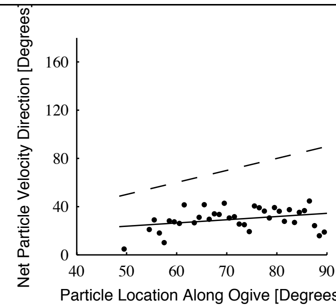

Time Step: 0.22-ms, Zmin: -0.2-m, Slope: 0.3, Int: -10.4

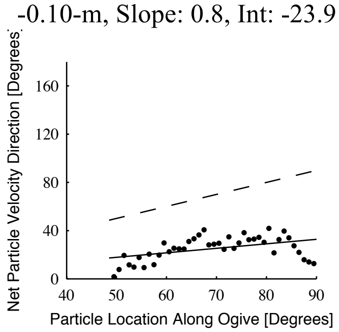

Time Step: 0.36-ms, Zmin: -0.3-m, Slope: 0.4, Int: -1.0

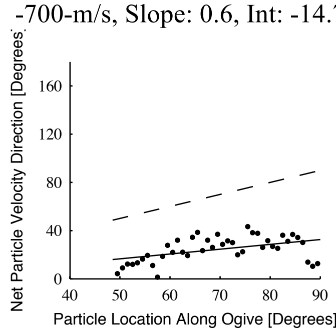

Time Step: 0.38-ms, Vi: -600-m/s, Slope: 0.4, Int: -3.7

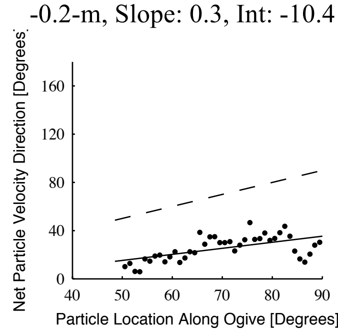

Time Step: 0.51-ms, Vi: -500-m/s, Slope: 0.5, Int: -10.1

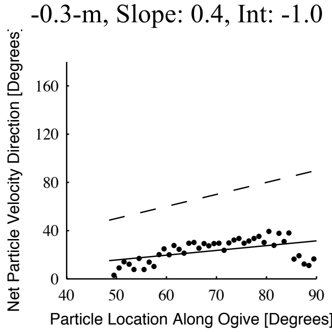

Time Step: 0.52-ms, Zmin: -0.4-m, Slope: 0.4, Int: -4.2

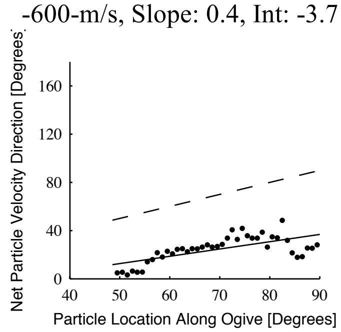

Time Step: 0.60-ms, Vi: -400-m/s, Slope: 0.6, Int: -17.6

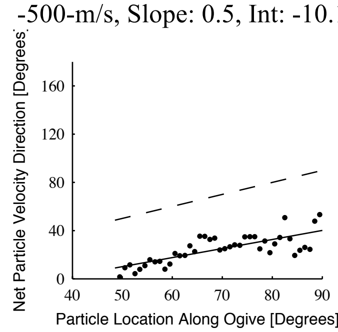

Time Step: 0.70-ms, Zmin: -0.5-m, Slope: 0.8, Int: -27.6

Figure 84. NECM Plots for Data Set 5, 800-m/s Striking Velocity, 36-MPa Concrete Target, 26.9-mm Diameter Projectile, 2-CRH Projectile Nose

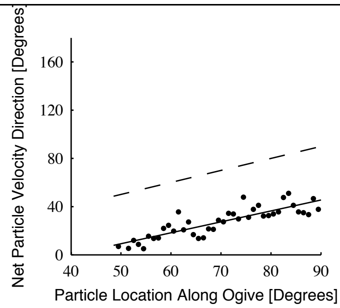

Time Step: 0.91-ms, Zmin: -0.6-m, Slope: 0.9, Int: -36.2

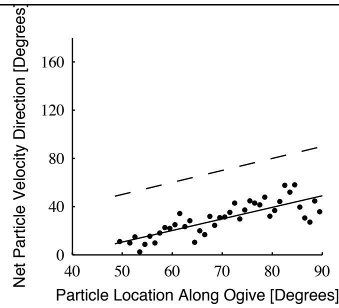

Time Step: 1.15-ms, Zmin: -0.7-m, Slope: 1.0, Int: -37.4

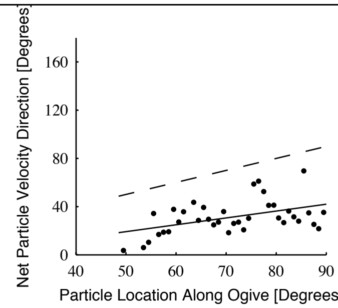

Time Step: 1.22-ms, Vi: -300-m/s, Slope: 0.6, Int: -9.4

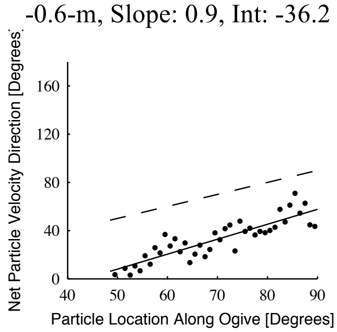

Time Step: 1.40-ms, Zmin: -0.8-m, Slope: 1.2, Int: -54.2

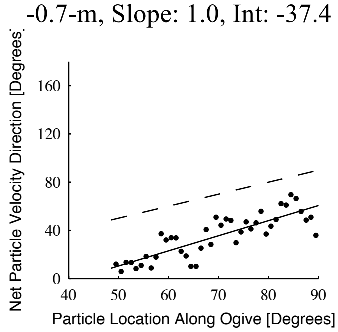

Time Step: 1.52-ms, Vi: -200-m/s, Slope: 1.3, Int: -52.4

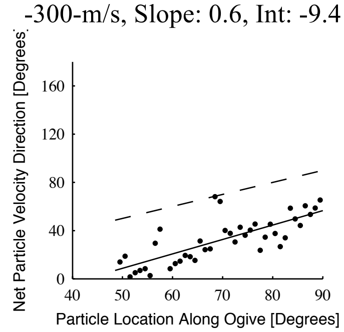

Time Step: 1.99-ms, Vi: -100-m/s, Slope: 1.2, Int: -51.2

Figure 85. NECM Plots for Data Set 5, 800-m/s Striking Velocity, 36-MPa Concrete Target, 26.9-mm Diameter Projectile, 2-CRH Projectile Nose

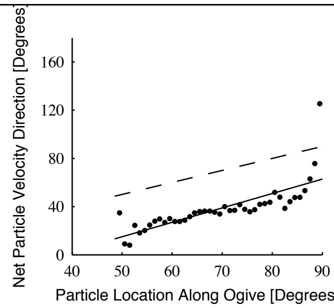

Time Step: 0.21-ms, Zmin: -0.10-m, Slope: 1.2, Int: -44.7

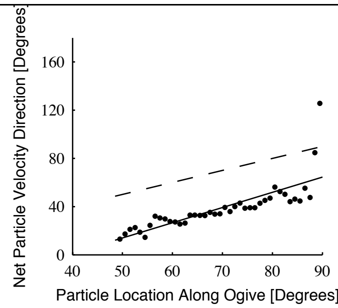

Time Step: 0.26-ms, Vi: -400-m/s, Slope: 1.3, Int: -49.0

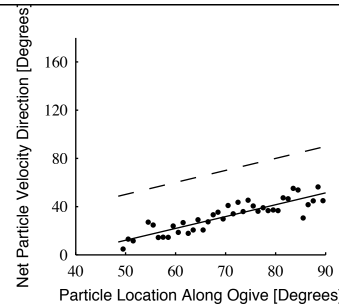

Time Step: 0.48-ms, Zmin: -0.20-m, Slope: 1.0, Int: -36.9

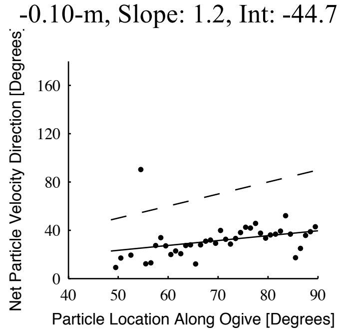

Time Step: 0.50-ms, Vi: -300-m/s, Slope: 0.4, Int: -3.4

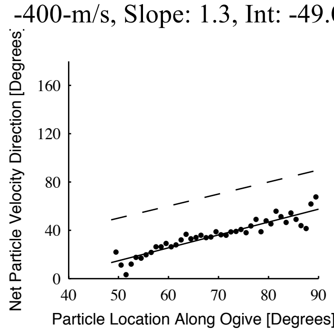

Time Step: 0.73-ms, Vi: -200-m/s, Slope: 1.1, Int: -38.5

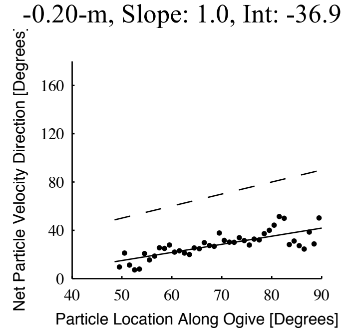

Time Step: 0.95-ms, Vi: -100-m/s, Slope: 0.7, Int: -18.6

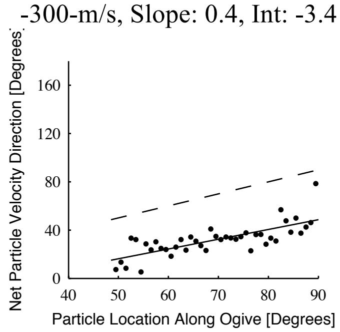

Time Step: 1.02-ms, Zmin: -0.30-m, Slope: 0.8, Int: -24.4

Figure 86. NECM Plots for Data Set 6, 500-m/s Striking Velocity, 97-MPa Concrete Target, 26.9-mm Diameter Projectile, 2-CRH Projectile Nose

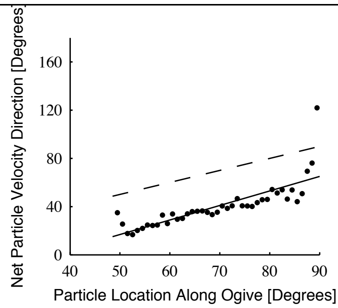

Time Step: 0.17-ms, Zmin: -0.10-m, Slope: 1.2, Int: -43.6

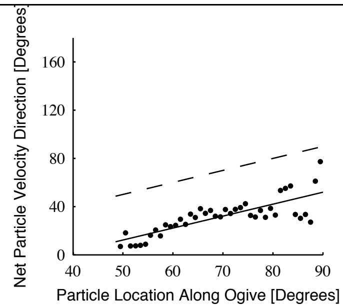

Time Step: 0.23-ms, Vi: -500-m/s, Slope: 1.0, Int: -37.3

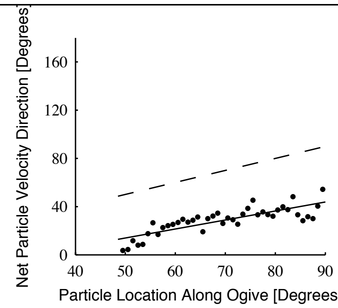

Time Step: 0.38-ms, Zmin: -0.20-m, Slope: 0.8, Int: -23.3

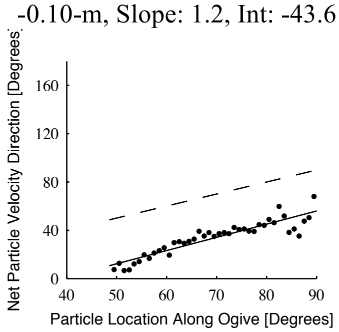

Time Step: 0.46-ms, Vi: -400-m/s, Slope: 1.1, Int: -42.4

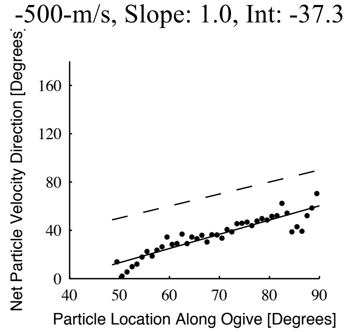

Time Step: 0.65-ms, Zmin: -0.30-m, Slope: 1.2, Int: -45.9

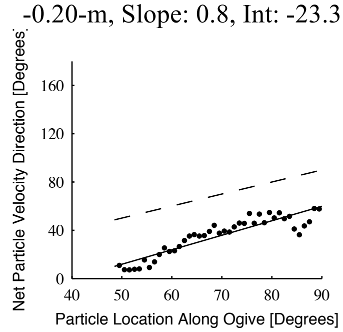

Time Step: 0.68-ms, Vi: -300-m/s, Slope: 1.2, Int: -48.2

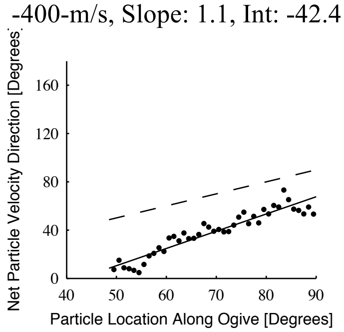

Time Step: 0.90-ms, Vi: -200-m/s, Slope: 1.4, Int: -60.8

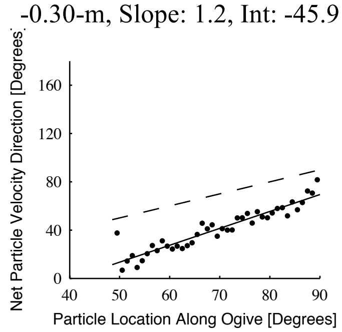

Time Step: 1.11-ms, Vi: -100-m/s, Slope: 1.4, Int: -56.8

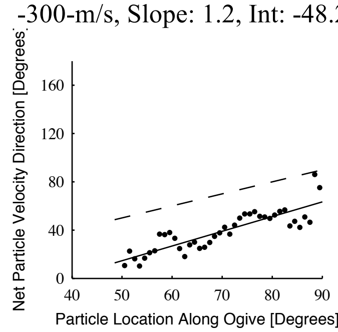

Time Step: 1.17-ms, Zmin: -0.40-m, Slope: 1.2, Int: -46.4

Figure 87. NECM Plots for Data Set 6, 600-m/s Striking Velocity, 97-MPa Concrete Target, 26.9-mm Diameter Projectile, 2-CRH Projectile Nose

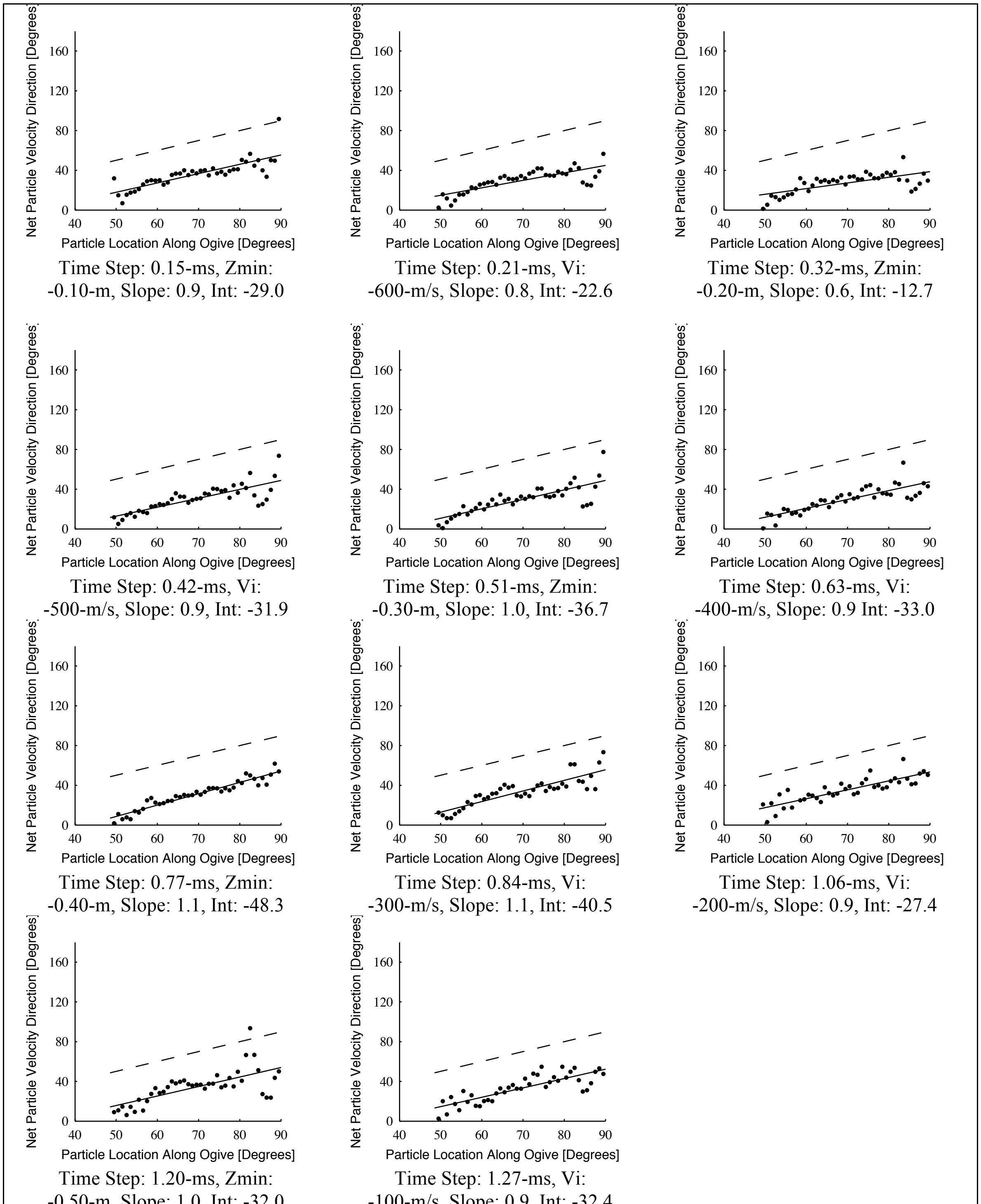

Figure 88. NECM Plots for Data Set 6, 700-m/s Striking Velocity, 97-MPa Concrete Target, 26.9-mm Diameter Projectile, 2-CRH Projectile Nose

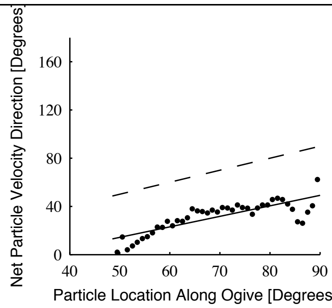

Time Step: 0.13-ms, Zmin: -0.10-m, Slope: 0.9, Int: -29.2

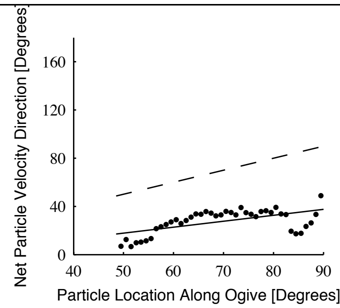

Time Step: 0.19-ms, Vi: -700-m/s, Slope: 0.5, Int: -6.8

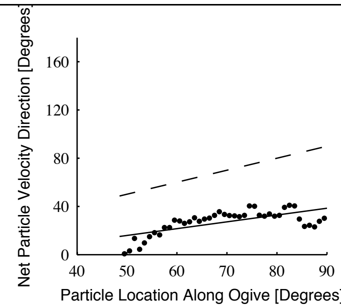

Time Step: 0.27-ms, Zmin: -0.20-m, Slope: 0.6, Int: -12.5

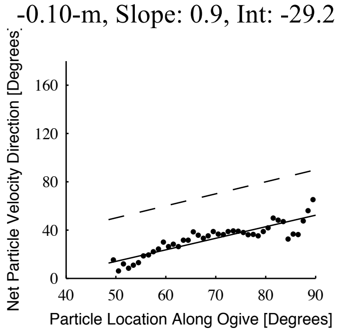

Time Step: 0.39-ms, Vi: -600-m/s, Slope: 1.0, Int: -33.5

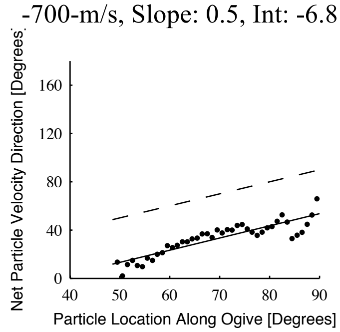

Time Step: 0.43-ms, Zmin: -0.30-m, Slope: 1.0, Int: -37.4

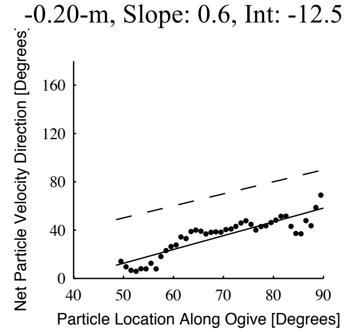

Time Step: 0.59-ms, Vi: -500-m/s, Slope: 1.2, Int: -44.9

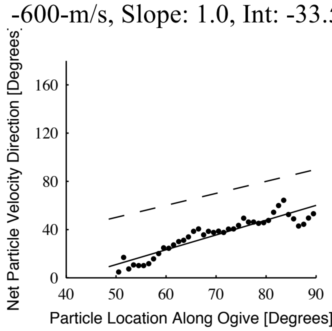

Time Step: 0.62-ms, Zmin: -0.40-m, Slope: 1.2, Int: -50.4

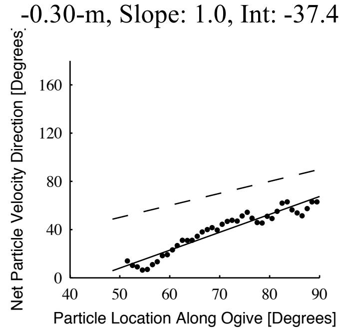

Time Step: 0.79-ms, Vi: -400-m/s, Slope: 1.5, Int: -66.0

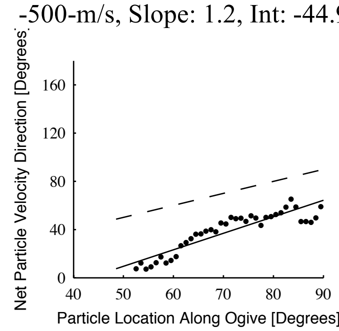

Time Step: 0.85-ms, Zmin: -0.50-m, Slope: 1.4, Int: -58.8

Figure 89. NECM Plots for Data Set 6, 800-m/s Striking Velocity, 97-MPa Concrete Target, 26.9-mm Diameter Projectile, 2-CRH Projectile Nose

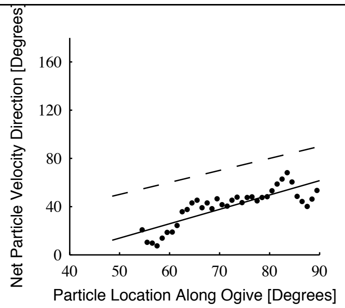

Time Step: 1.01-ms, Vi:
-300-m/s, Slope: 1.2, Int: -45.7

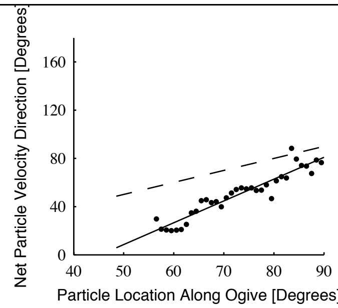

Time Step: 1.19-ms, Zmin:
-0.60-m, Slope: 1.8, Int: -81.7

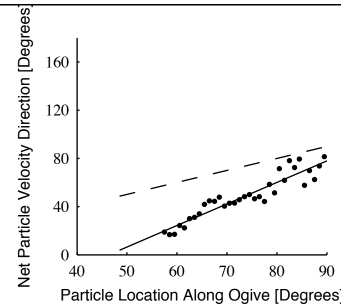

Time Step: 1.22-ms, Vi:
-200-m/s, Slope: 1.8, Int: -82.9

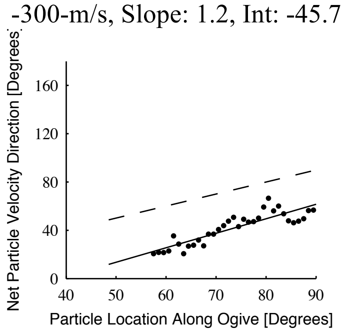

Time Step: 1.45-ms, Vi:
-100-m/s, Slope: 1.2, Int: -46.4

Figure 90. NECM Plots for Data Set 6, 800-m/s Striking Velocity, 97-MPa Concrete Target, 26.9-mm Diameter Projectile, 2-CRH Projectile Nose

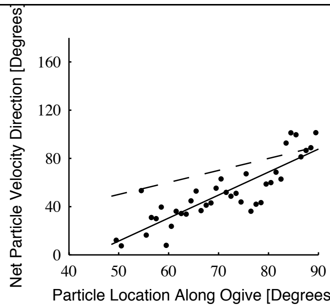

Time Step: 0.343570-ms, Vi:
-100-m/s, Slope: 1.9, Int: -83.8

Figure 91. NECM Plots for Data Set 7, 200-m/s Striking Velocity, 157-MPa Concrete Target, 26.9-mm Diameter Projectile, 2-CRH Projectile Nose

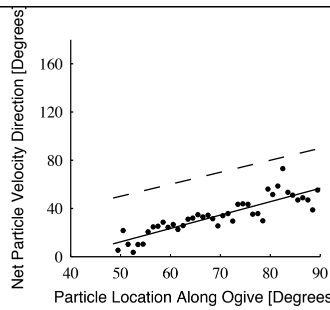

Time Step: 0.25-ms, Vi:
-300-m/s, Slope: 1.1, Int: -43.3

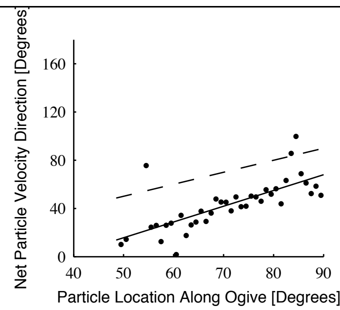

Time Step: 0.29-ms, Zmin:
-0.10-m, Slope: 1.3, Int: -49.8

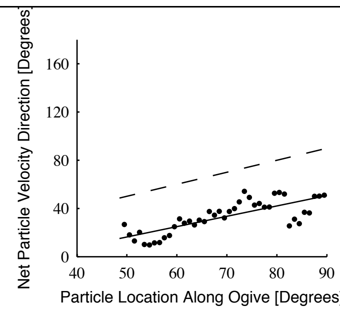

Time Step: 0.40-ms, Vi:
-200-m/s, Slope: 0.9, Int: -26.6

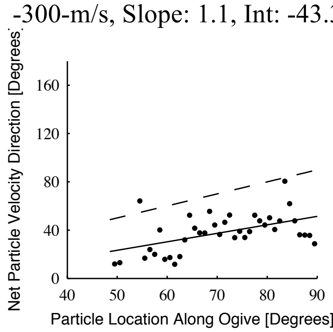

Time Step: 0.56-ms, Vi:
-100-m/s, Slope: 0.7, Int: -11.6

Figure 92. NECM Plots for Data Set 7, 400-m/s Striking Velocity, 157-MPa Concrete Target, 26.9-mm Diameter Projectile, 2-CRH Projectile Nose

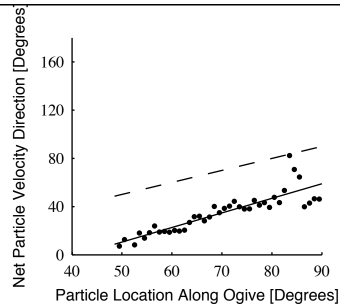

Time Step: 0.18-ms, Zmin: -0.10-m, Slope: 1.2, Int: -49.9

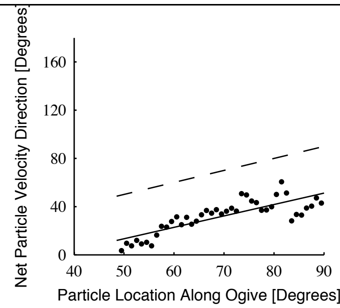

Time Step: 0.19-ms, Vi: -500-m/s, Slope: 0.9, Int: -33.8

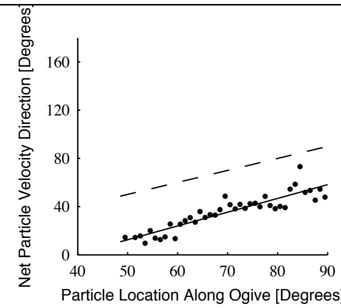

Time Step: 0.34-ms, Vi: -400-m/s, Slope: 1.1, Int: -44.6

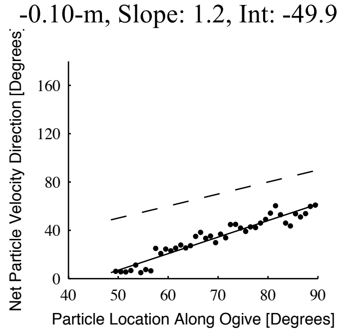

Time Step: 0.41-ms, Zmin: -0.20-m, Slope: 1.4, Int: -61.4

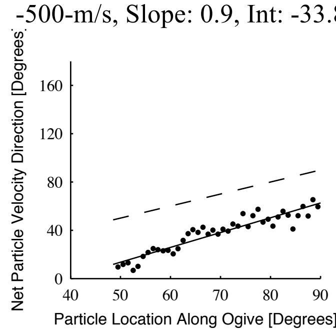

Time Step: 0.47-ms, Vi: -300-m/s, Slope: 1.2, Int: -47.8

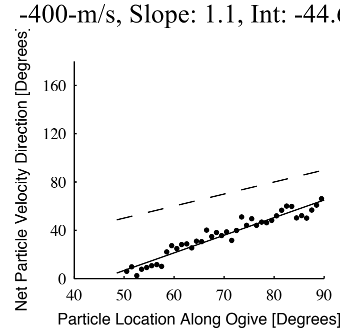

Time Step: 0.62-ms, Vi: -200-m/s, Slope: 1.5, Int: -66.2

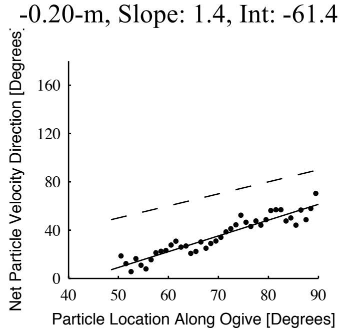

Time Step: 0.78-ms, Vi: -100-m/s, Slope: 1.3, Int: -56.5

Figure 93. NECM Plots for Data Set 7, 600-m/s Striking Velocity, 157-MPa Concrete Target, 26.9-mm Diameter Projectile, 2-CRH Projectile Nose

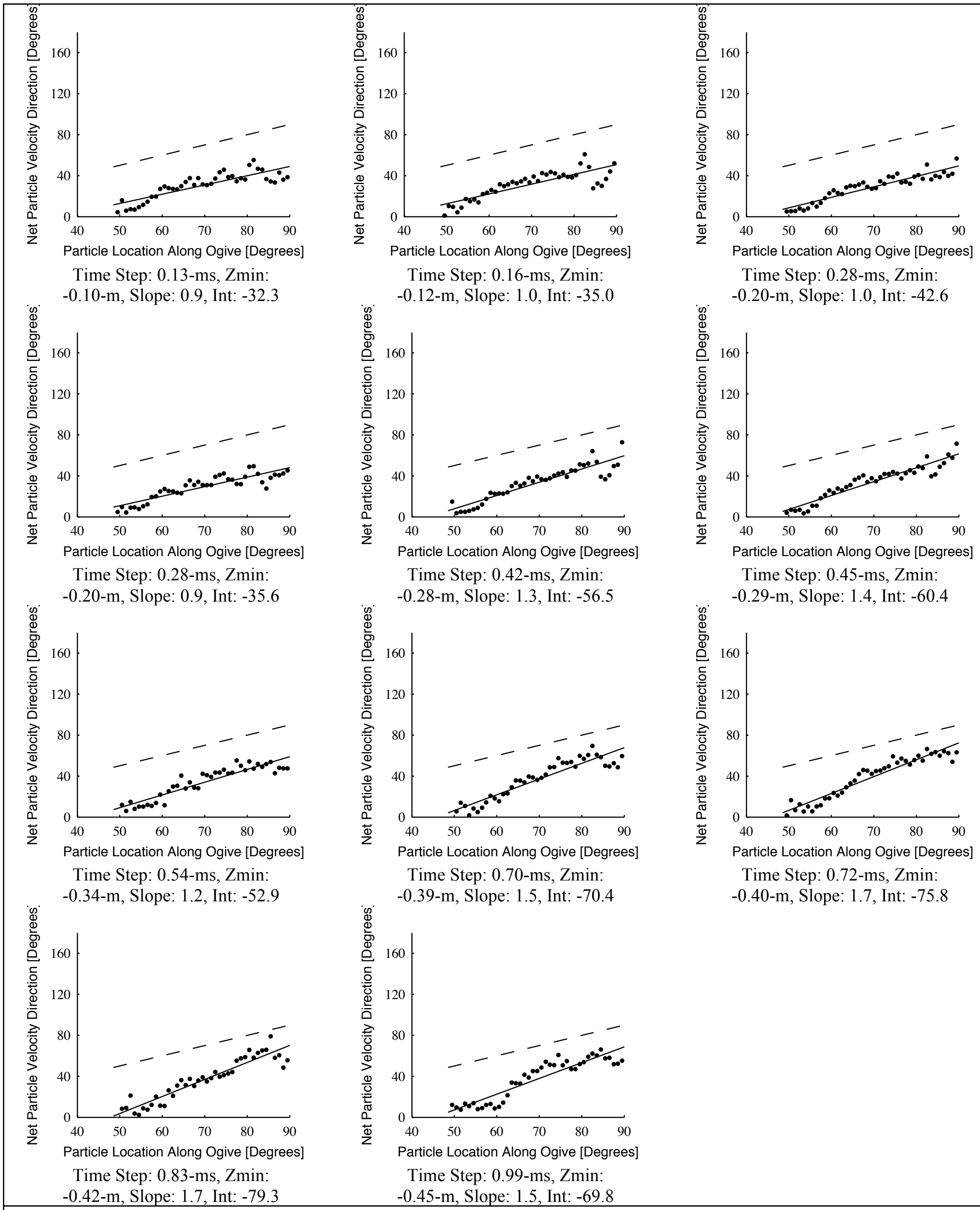

Time Step: 0.13-ms, Zmin: -0.10-m, Slope: 0.9, Int: -32.3

Time Step: 0.16-ms, Zmin: -0.12-m, Slope: 1.0, Int: -35.0

Time Step: 0.28-ms, Zmin: -0.20-m, Slope: 1.0, Int: -42.6

Time Step: 0.28-ms, Zmin: -0.20-m, Slope: 0.9, Int: -35.6

Time Step: 0.42-ms, Zmin: -0.28-m, Slope: 1.3, Int: -56.5

Time Step: 0.45-ms, Zmin: -0.29-m, Slope: 1.4, Int: -60.4

Time Step: 0.54-ms, Zmin: -0.34-m, Slope: 1.2, Int: -52.9

Time Step: 0.70-ms, Zmin: -0.39-m, Slope: 1.5, Int: -70.4

Time Step: 0.72-ms, Zmin: -0.40-m, Slope: 1.7, Int: -75.8

Time Step: 0.83-ms, Zmin: -0.42-m, Slope: 1.7, Int: -79.3

Time Step: 0.99-ms, Zmin: -0.45-m, Slope: 1.5, Int: -69.8

Figure 94. NECM Plots for Data Set 7, 800-m/s Striking Velocity, 157-MPa Concrete Target, 26.9-mm Diameter Projectile, 2-CRH Projectile Nose

APPENDIX 2: SECM PLOTS FOR NODAL DIRECTION

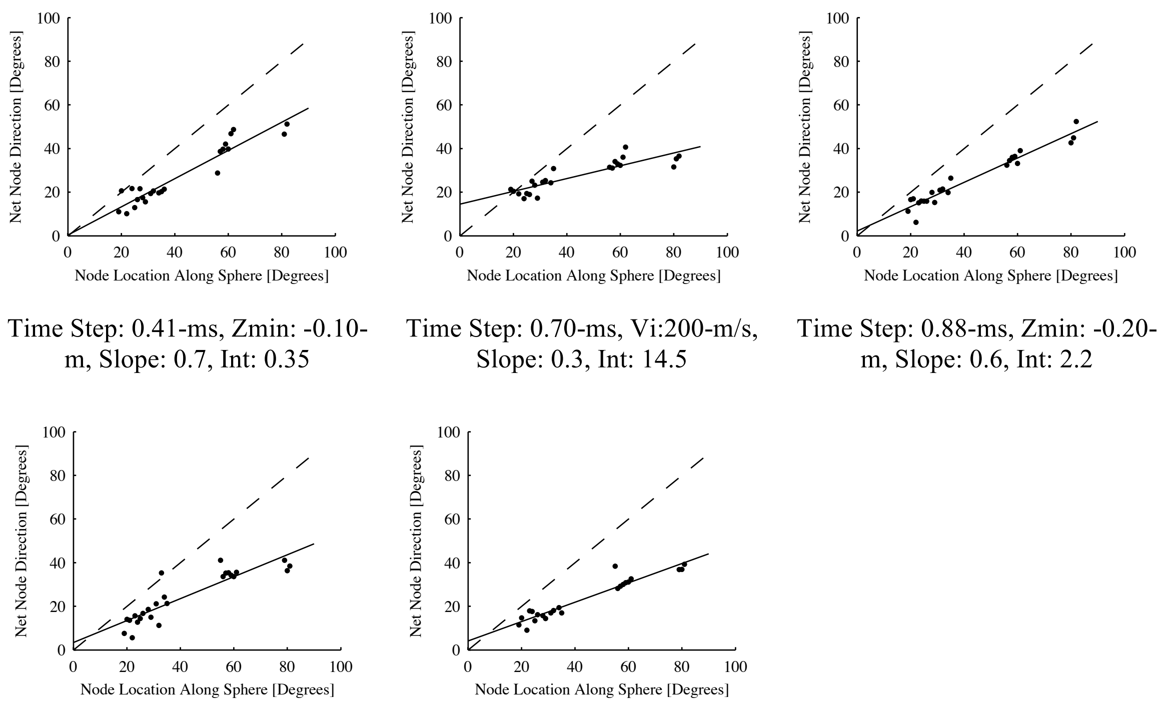

Time Step: 0.41-ms, Zmin: -0.10-m, Slope: 0.7, Int: 0.35

Time Step: 0.70-ms, Vi:200-m/s, Slope: 0.3, Int: 14.5

Time Step: 0.88-ms, Zmin: -0.20-m, Slope: 0.6, Int: 2.2

Time Step: 1.54-ms, Vi:100-m/s, Slope: 0.5, Int: 3.4

Time Step: 1.78-ms, Zmin: -0.3-m, Slope: 0.4, Int: 4.1

Figure 95. SECM Plots for Data Set 3, 250-m/s Striking Velocity, 39-MPa Concrete Target, 76.2-mm Diameter Projectile, 3-CRH Projectile Nose

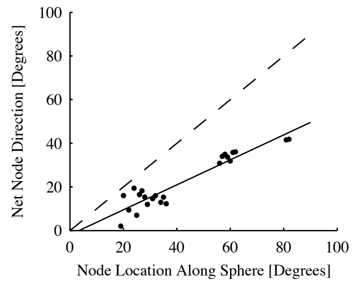

Time Step: 0.30-ms, Vi:300-m/s, Slope: 0.6, Int: -1.9

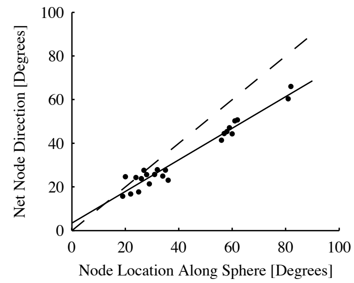

Time Step: 0.31-ms, Zmin: -0.1-m, Slope: 0.7, Int: 3.4

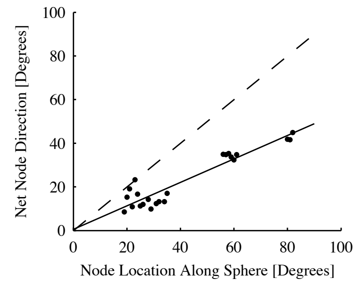

Time Step: 0.65-ms, Zmin: -0.2-m, Slope: 0.5, Int: 0.6

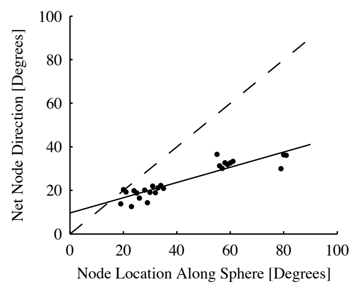

Time Step: 1.05-ms, Zmin: -0.3-m, Slope: 0.4, Int: 9.6

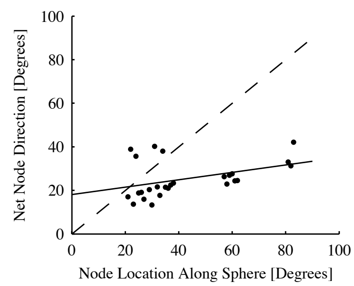

Time Step: 1.23-ms, Vi:200-m/s, Slope: 0.2, Int: 18.1

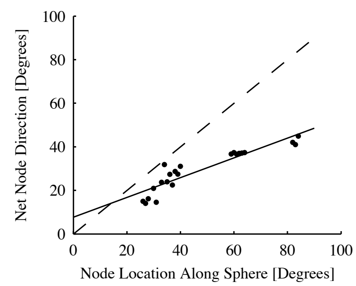

Time Step: 1.63-ms, Zmin: -0.40-m, Slope: 0.5, Int: 7.7

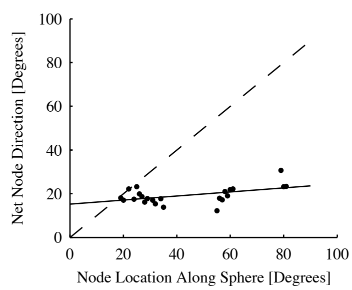

Time Step: 1.95-ms, Vi:100-m/s, Slope: 0.1, Int: 15.2

Figure 96. SECM Plots for Data Set 3, 325-m/s Striking Velocity, 39-MPa Concrete Target, 76.2-mm Diameter Projectile, 3-CRH Projectile Nose

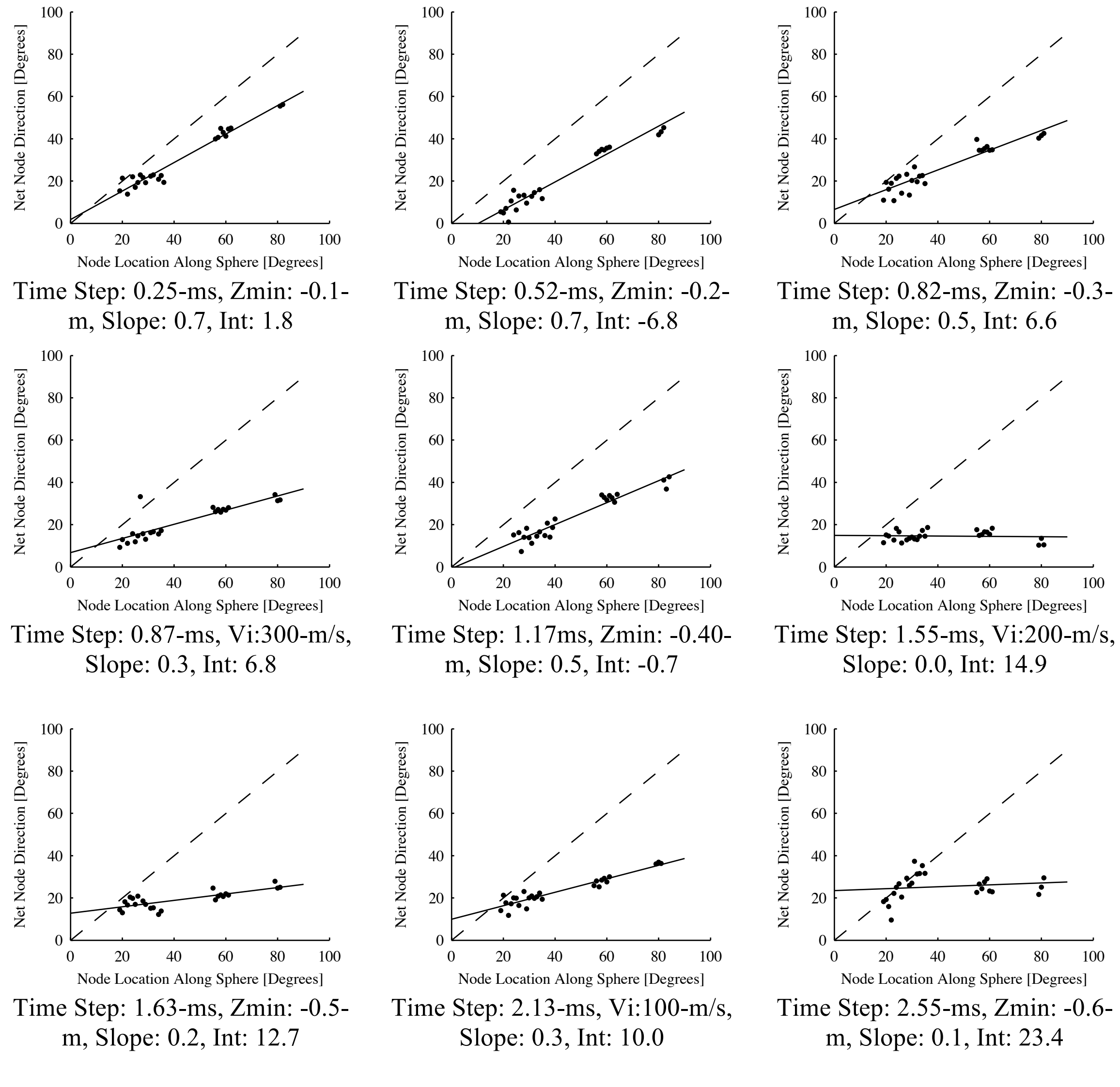

Time Step: 0.25-ms, Zmin: -0.1-m, Slope: 0.7, Int: 1.8

Time Step: 0.52-ms, Zmin: -0.2-m, Slope: 0.7, Int: -6.8

Time Step: 0.82-ms, Zmin: -0.3-m, Slope: 0.5, Int: 6.6

Time Step: 0.87-ms, Vi:300-m/s, Slope: 0.3, Int: 6.8

Time Step: 1.17ms, Zmin: -0.40-m, Slope: 0.5, Int: -0.7

Time Step: 1.55-ms, Vi:200-m/s, Slope: 0.0, Int: 14.9

Time Step: 1.63-ms, Zmin: -0.5-m, Slope: 0.2, Int: 12.7

Time Step: 2.13-ms, Vi:100-m/s, Slope: 0.3, Int: 10.0

Time Step: 2.55-ms, Zmin: -0.6-m, Slope: 0.1, Int: 23.4

Figure 97. SECM Plots for Data Set 3, 400-m/s Striking Velocity, 39-MPa Concrete Target, 76.2-mm Diameter Projectile, 3-CRH Projectile Nose

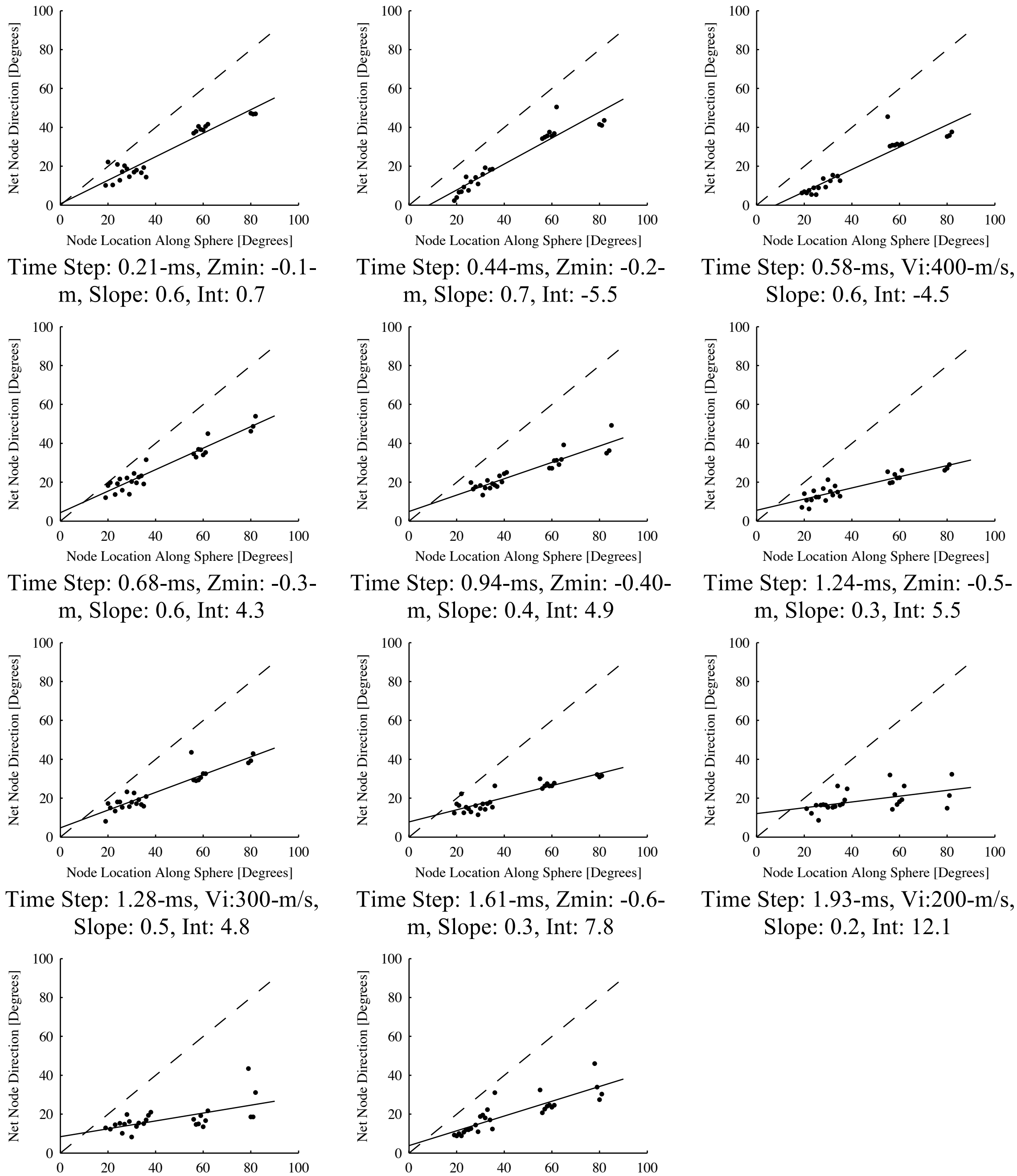

Time Step: 0.21-ms, Zmin: -0.1-m, Slope: 0.6, Int: 0.7

Time Step: 0.44-ms, Zmin: -0.2-m, Slope: 0.7, Int: -5.5

Time Step: 0.58-ms, Vi:400-m/s, Slope: 0.6, Int: -4.5

Time Step: 0.68-ms, Zmin: -0.3-m, Slope: 0.6, Int: 4.3

Time Step: 0.94-ms, Zmin: -0.40-m, Slope: 0.4, Int: 4.9

Time Step: 1.24-ms, Zmin: -0.5-m, Slope: 0.3, Int: 5.5

Time Step: 1.28-ms, Vi:300-m/s, Slope: 0.5, Int: 4.8

Time Step: 1.61-ms, Zmin: -0.6-m, Slope: 0.3, Int: 7.8

Time Step: 1.93-ms, Vi:200-m/s, Slope: 0.2, Int: 12.1

Time Step: 2.11-ms, Zmin: -0.7-m, Slope: 0.2, Int: 8.4

Time Step: 2.52-ms, Vi:100-m/s, Slope: 0.4, Int: 3.8

Figure 98. SECM Plots for Data Set 3, 475-m/s Striking Velocity, 39-MPa Concrete Target, 76.2-mm Diameter Projectile, 3-CRH Projectile Nose

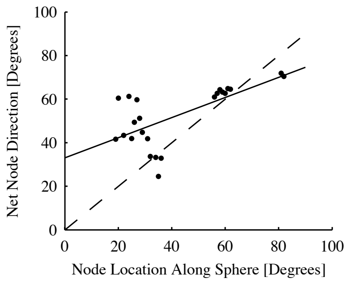

Time Step: 0.41-ms, Zmin: -0.1-m, Slope: 0.5, Int: 33.0

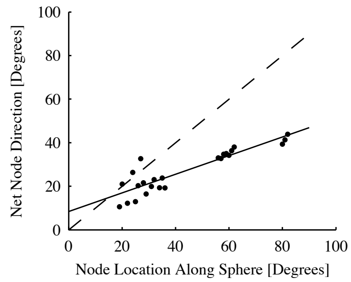

Time Step: 0.83-ms, Vi: -200-m/s, Slope: 0.4, Int: 8.4

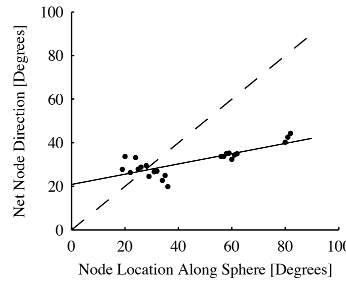

Time Step: 0.85-ms, Zmin: -0.2-m, Slope: 0.2, Int: 20.9

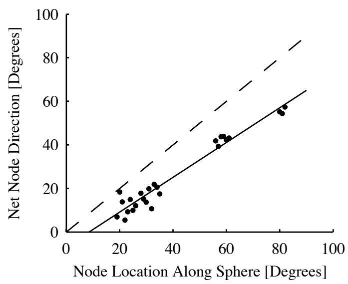

Time Step: 1.43-ms, Zmin: -0.3-m, Slope: 0.8, Int: -6.9

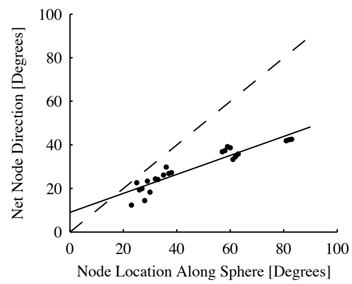

Time Step: 1.73-ms, Vi: -100-m/s, Slope: 0.4, Int: 9.0

Figure 99. SECM Plots for Data Set 4, 250-m/s Striking Velocity, 39-MPa Concrete Target, 76.2-mm Diameter Projectile, 6-CRH Projectile Nose

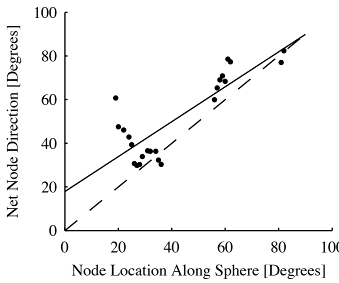

Time Step: 0.31-ms, Zmin: -0.1-m, Slope: 0.8, Int: 17.8

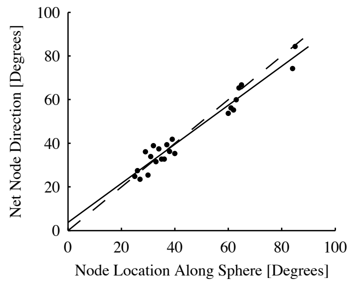

Time Step: 0.38-ms, Vi: -300-m/s, Slope: 0.9, Int: 3.7

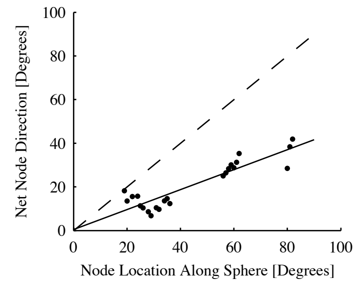

Time Step: 0.64-ms, Zmin: -0.2-m, Slope: 0.5, Int: 0.4

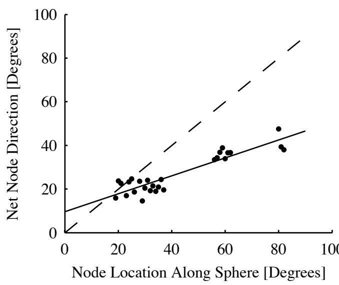

Time Step: 1.02-ms, Zmin: -0.3-m, Slope: 0.4, Int: 9.6

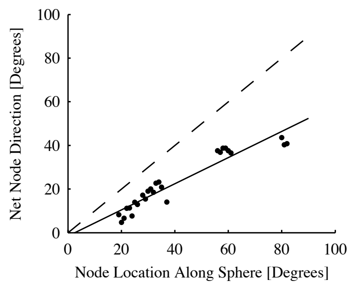

Time Step: 1.43-ms, Vi: -200-m/s, Slope: 0.6, Int: -1.5

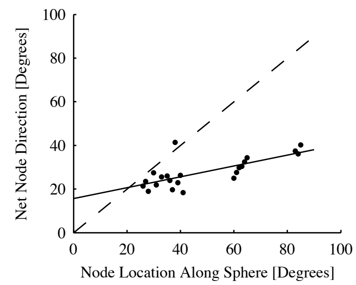

Time Step: 1.48-ms, Zmin: -0.40-m, Slope: 0.3, Int: 15.6

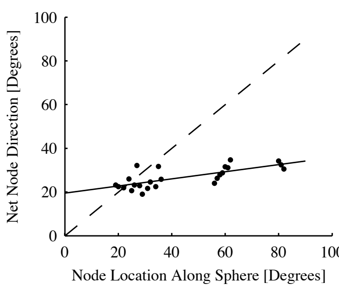

Time Step: 2.20-ms, Vi: -100-m/s, Slope: 0.2, Int: 19.5

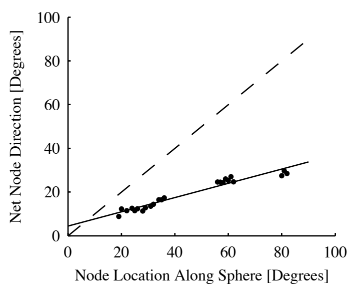

Time Step: 2.25-ms, Zmin: -0.5-m, Slope: 0.3, Int: 4.4

Figure 100. SECM Plots for Data Set 4, 325-m/s Striking Velocity, 39-MPa Concrete Target, 76.2-mm Diameter Projectile, 6-CRH Projectile Nose

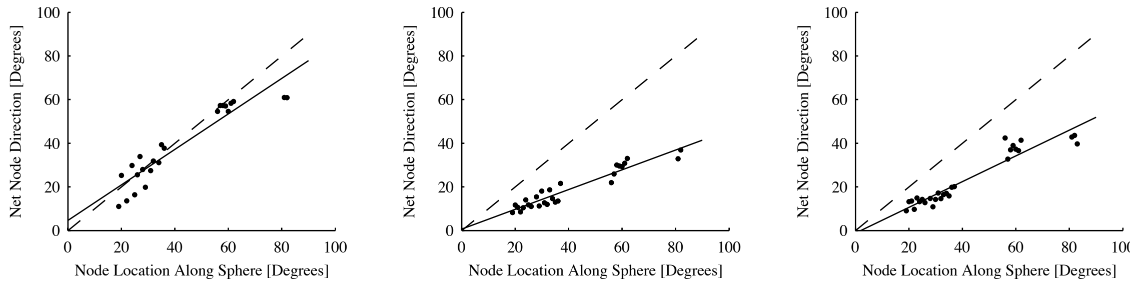

Time Step: 0.25-ms, Zmin: -0.1-m, Slope: 0.8, Int: 4.7

Time Step: 0.51-ms, Zmin: -0.2-m, Slope: 0.5, Int: 0.6

Time Step: 0.80-ms, Zmin: -0.3-m, Slope: 0.6, Int: -1.2

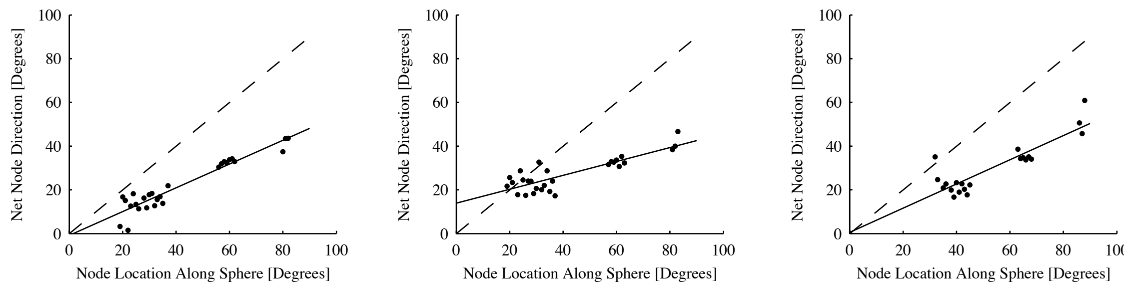

Time Step: 1.08-ms, Vi: -300-m/s, Slope: 0.5, Int: -0.8

Time Step: 1.11-ms, Zmin: -0.40-m, Slope: 0.3, Int: 13.9

Time Step: 1.49-ms, Zmin: -0.5-m, Slope: 0.6, Int: 0.6

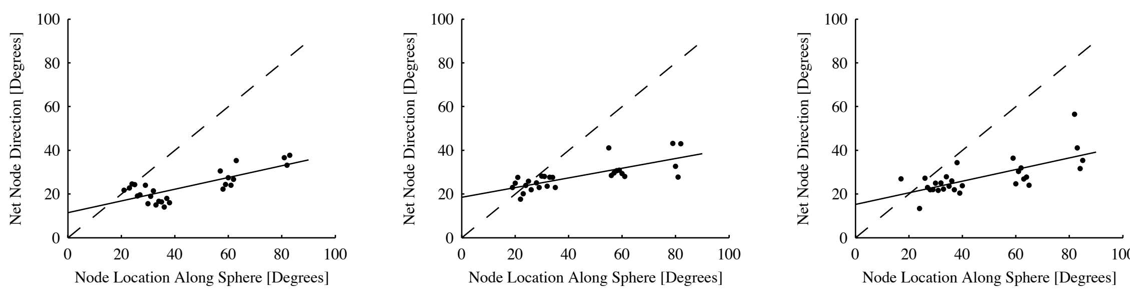

Time Step: 1.75-ms, Vi: -200-m/s, Slope: 0.3, Int: 11.5

Time Step: 2.00-ms, Zmin: -0.6-m, Slope: 0.2, Int: 18.5

Time Step: 2.44-ms, Vi: -100-m/s, Slope: 0.3, Int: 15.2

Figure 101. SECM Plots for Data Set 4, 400-m/s Striking Velocity, 39-MPa Concrete Target, 76.2-mm Diameter Projectile, 6-CRH Projectile Nose

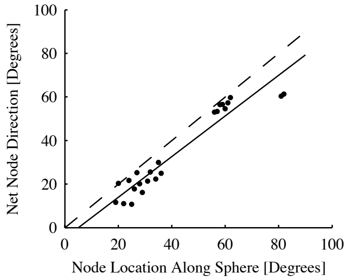

Time Step: 0.21-ms, Zmin: -0.1-m, Slope: 0.9, Int: -4.7

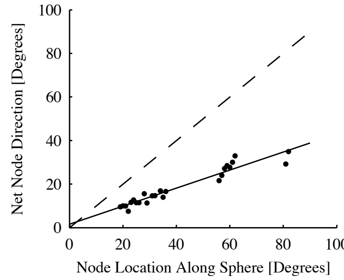

Time Step: 0.43-ms, Zmin: -0.2-m, Slope: 0.4, Int: 1.6

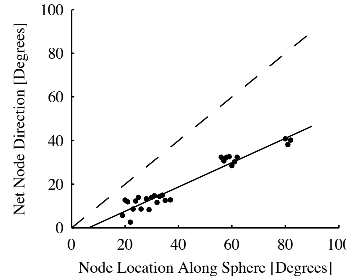

Time Step: 0.66-ms, Zmin: -0.3-m, Slope: 0.6, Int: -3.5

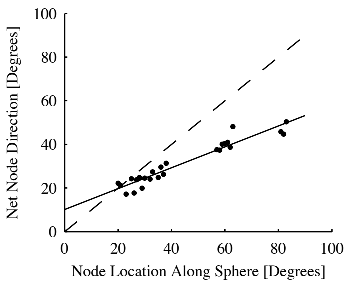

Time Step: 0.75-ms, Vi: -400-m/s, Slope: 0.5, Int: 10.1

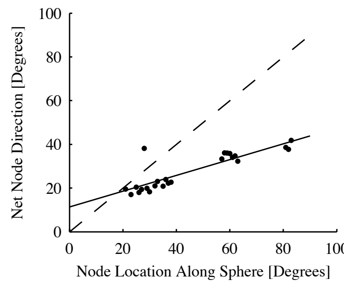

Time Step: 0.91-ms, Zmin: -0.40-m, Slope: 0.4, Int: 11.3

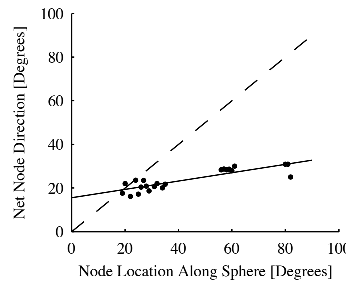

Time Step: 1.18-ms, Zmin: -0.5-m, Slope: 0.2, Int: 15.6

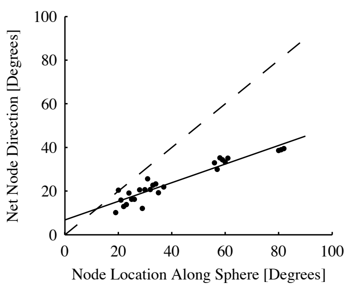

Time Step: 1.43-ms, Vi: -300-m/s, Slope: 0.4, Int: 6.7

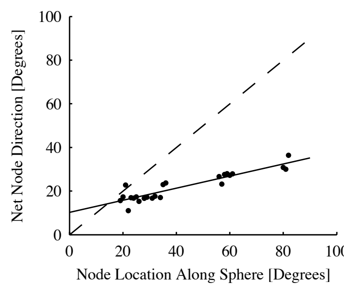

Time Step: 1.50-ms, Zmin: -0.6-m, Slope: 0.3, Int: 10.2

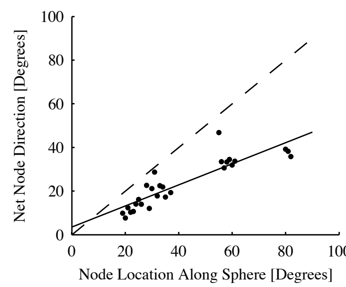

Time Step: 1.89-ms, Zmin: -0.70-m, Slope: 0.5, Int: 3.5

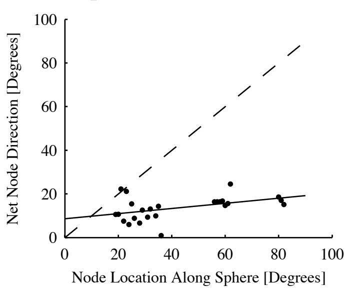

Time Step: 2.13-ms, Vi: -200-m/s, Slope: 0.1, Int: 8.7

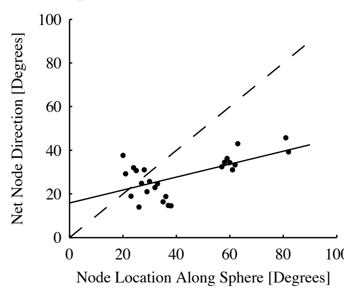

Time Step: 2.40-ms, Zmin: -0.80-m, Slope: 0.3, Int: 15.9

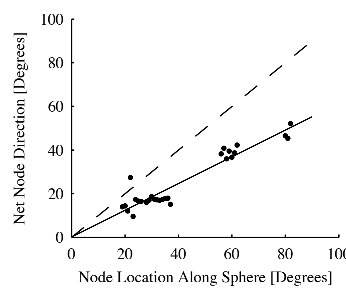

Time Step: 2.83-ms, Vi: -100-m/s, Slope: 0.6, Int: 0.2

Figure 102. SECM Plots for Data Set 4, 475-m/s Striking Velocity, 39-MPa Concrete Target, 76.2-mm Diameter Projectile, 6-CRH Projectile Nose

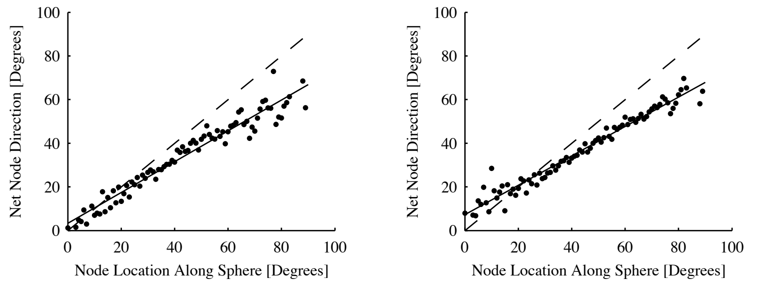

Time Step: 0.56-ms, Vi: -100-m/s, Slope: 0.7, Int: 3.3

Time Step: 0.67-ms, Zmin: -0.10-m, Slope: 0.7, Int: 7.3

Figure 103. SECM Plots for Data Set 5, 200-m/s Striking Velocity, 36-MPa Concrete Target, 26.9-mm Diameter Projectile, 2-CRH Projectile Nose

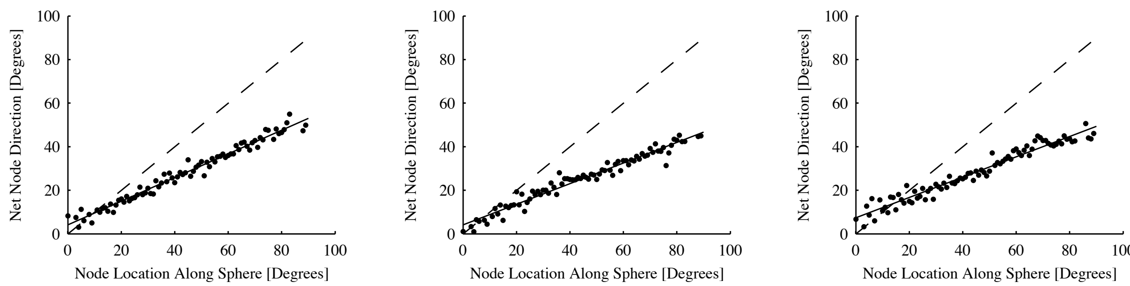

Time Step: 0.26-ms, Zmin: -0.10-m, Slope: 0.5, Int: 4.1

Time Step: 0.40-ms, Vi: -300-m/s, Slope: 0.5, Int: 4.1

Time Step: 0.56-ms, Vi: -200-m/s, Slope: 0.5, Int: 7.3

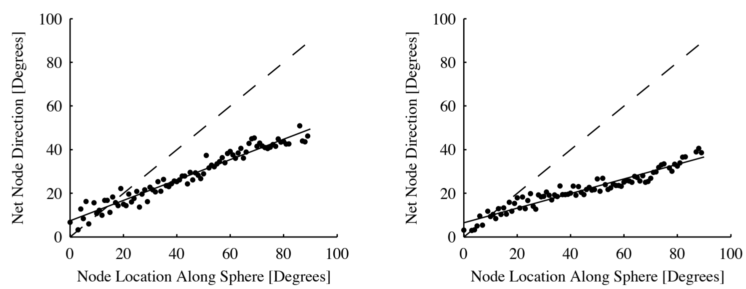

Time Step: 0.57-ms, Vi: -100-m/s, Slope: 0.5, Int: 7.4

Time Step: 0.62-ms, Zmin: -0.20-m, Slope: 0.3, Int: 6.5

Figure 104. SECM Plots for Data Set 5, 400-m/s Striking Velocity, 36-MPa Concrete Target, 26.9-mm Diameter Projectile, 2-CRH Projectile Nose

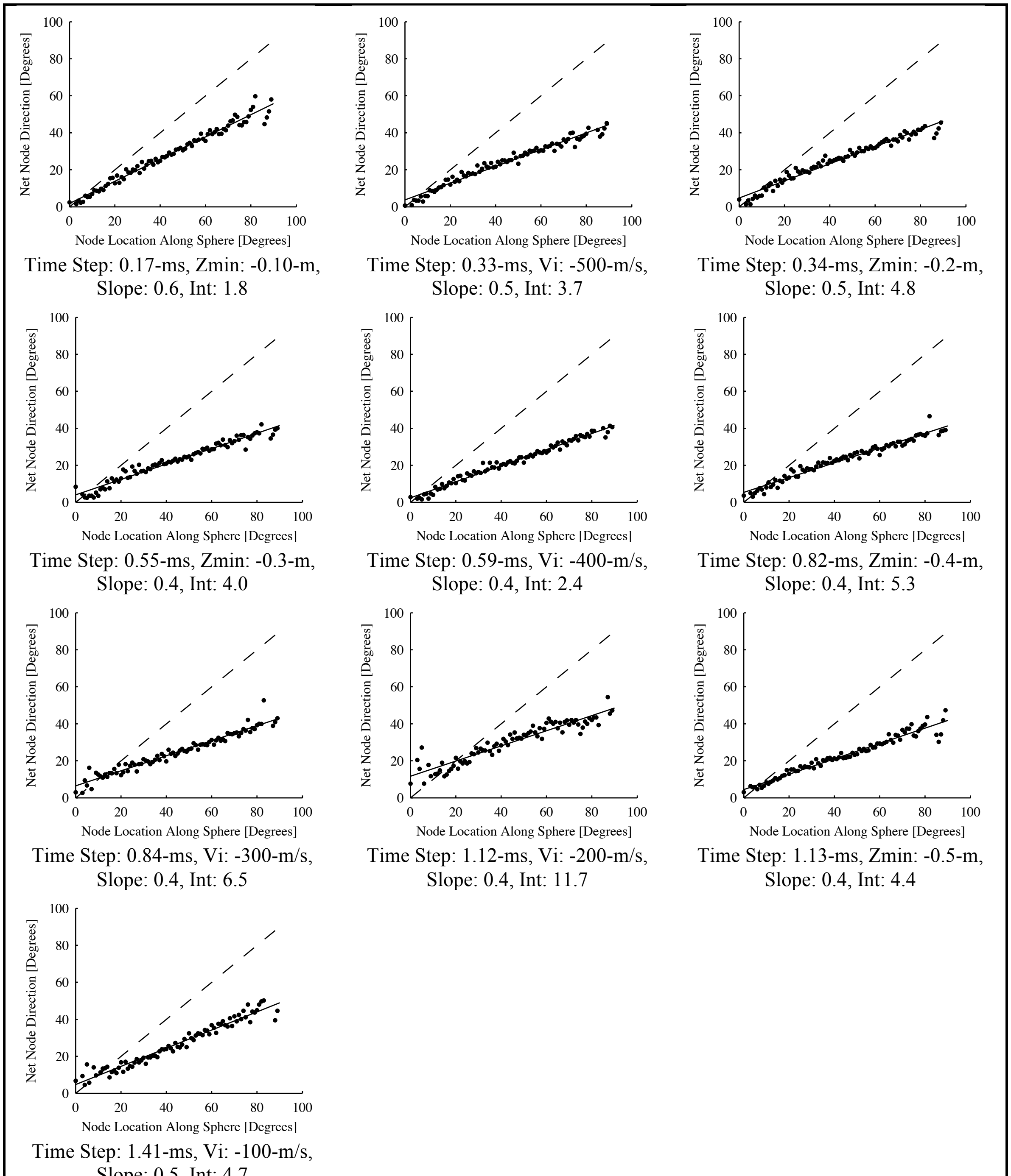

Figure 105. SECM Plots for Data Set 5, 600-m/s Striking Velocity, 36-MPa Concrete Target, 26.9-mm Diameter Projectile, 2-CRH Projectile Nose

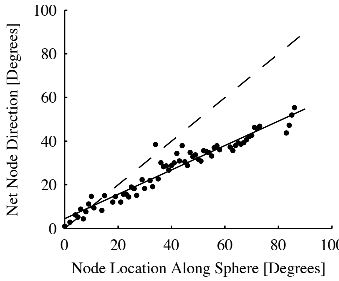

Time Step: 0.121480-ms, Zmin: -0.10-m, Slope: 0.6, Int: 4.4

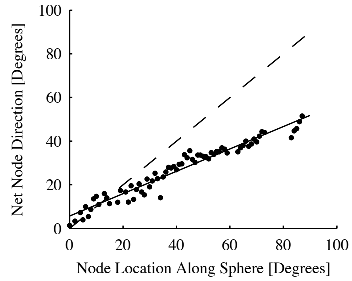

Time Step: 0.173871-ms, Vi: -700-m/s, Slope: 0.5, Int: 5.7

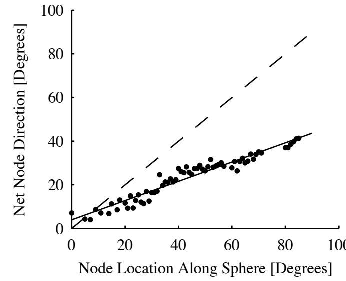

Time Step: 0.221306-ms, Zmin: -0.2-m, Slope: 0.4, Int: 4.0

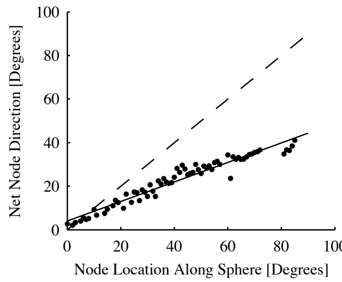

Time Step: 0.362837-ms, Zmin: -0.3-m, Slope: 0.5, Int: 4.1

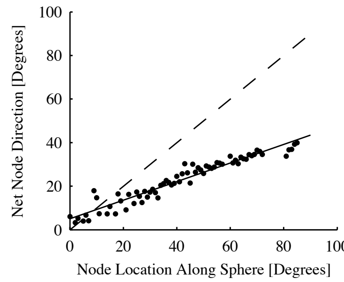

Time Step: 0.375990-ms, Vi: -600-m/s, Slope: 0.4, Int: 5.1

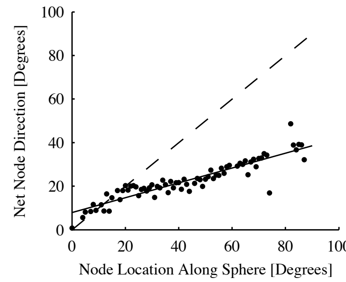

Time Step: 0.509087-ms, Vi: -500-m/s, Slope: 0.3, Int: 7.8

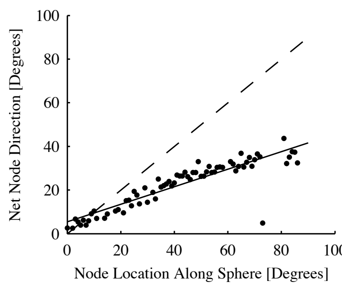

Time Step: 0.52-ms, Zmin: -0.4-m, Slope: 0.4, Int: 5.4

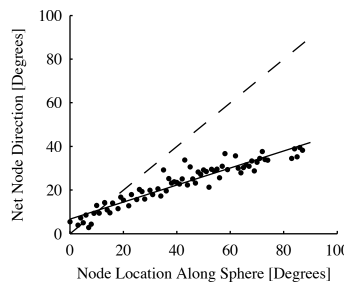

Time Step: 0.60-ms, Vi: -400-m/s, Slope: 0.4, Int: 6.7

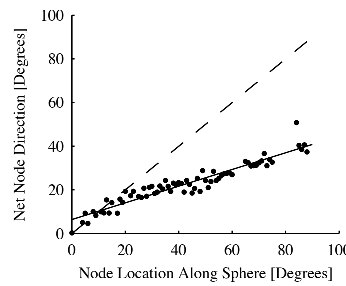

Time Step: 0.70-ms, Zmin: -0.5-m, Slope: 0.4, Int: 6.4

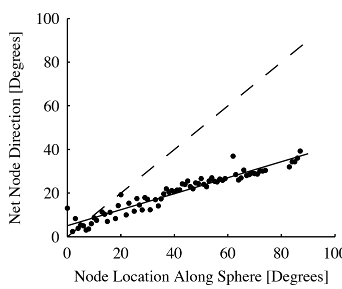

Time Step: 0.91-ms, Zmin: -0.6-m, Slope: 0.4, Int: 5.0

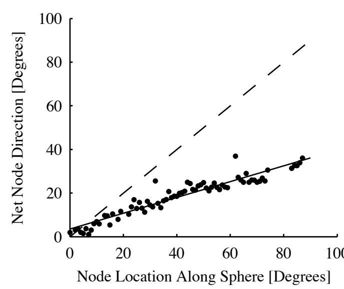

Time Step: 1.15-ms, Zmin: -0.7-m, Slope: 0.4, Int: 3.5

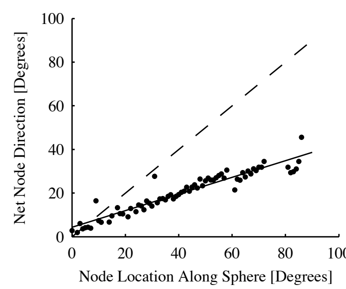

Time Step: 1.22-ms, Vi: -300-m/s, Slope: 0.4, Int: 4.3

Figure 106. SECM Plots for Data Set 5, 800-m/s Striking Velocity, 36-MPa Concrete Target, 26.9-mm Diameter Projectile, 2-CRH Projectile Nose

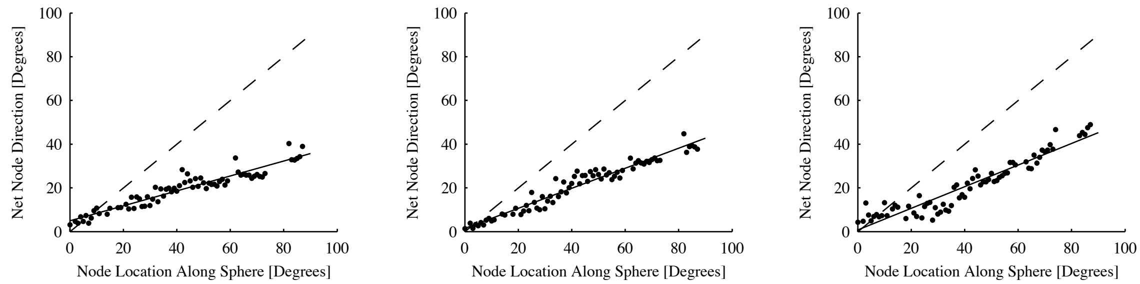

Time Step: 1.40-ms, Zmin: -0.8-m, Slope: 0.3, Int: 4.9

Time Step: 1.52-ms, Vi: -200-m/s, Slope: 0.5, Int: 1.5

Time Step: 2.00-ms, Vi: -100-m/s, Slope: 0.5, Int: 0.8

Figure 107. SECM Plots for Data Set 5, 800-m/s Striking Velocity, 36-MPa Concrete Target, 26.9-mm Diameter Projectile, 2-CRH Projectile Nose

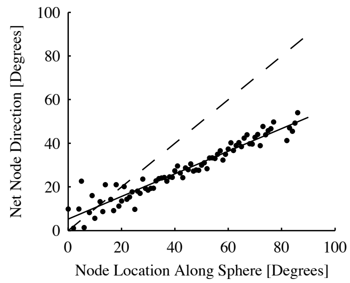

Time Step: 0.21-ms, Zmin: -0.10-m, Slope: 0.5, Int: 5.3

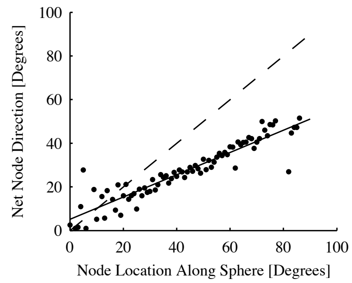

Time Step: 0.26-ms, Vi: -400-m/s, Slope: 0.5, Int: 5.1

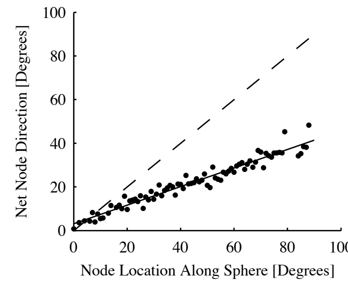

Time Step: 0.48-ms, Zmin: -0.20-m, Slope: 0.4, Int: 3.1

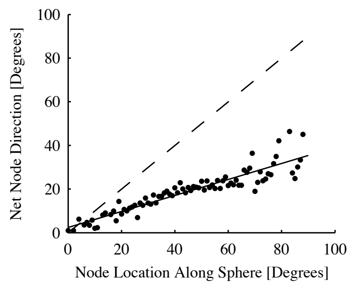

Time Step: 0.50-ms, Vi: -300-m/s, Slope: 0.4, Int: 2.4

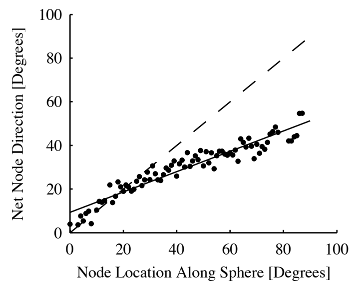

Time Step: 0.73-ms, Vi: -200-m/s, Slope: 0.5, Int: 9.4

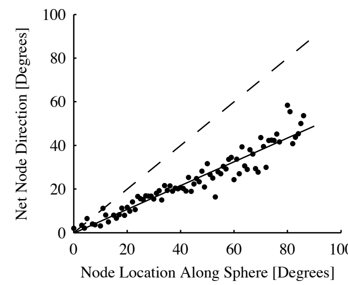

Time Step: 0.95-ms, Vi: -100-m/s, Slope: 0.5, Int: -0.2

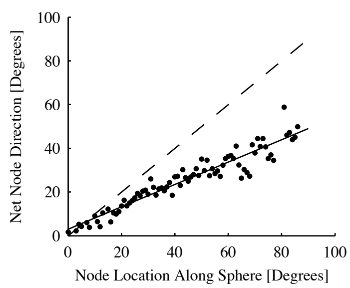

Time Step: 1.02-ms, Zmin: -0.30-m, Slope: 0.5, Int: 3.0

Figure 108. SECM Plots for Data Set 6, 500-m/s Striking Velocity, 97-MPa Concrete Target, 26.9-mm Diameter Projectile, 2-CRH Projectile Nose

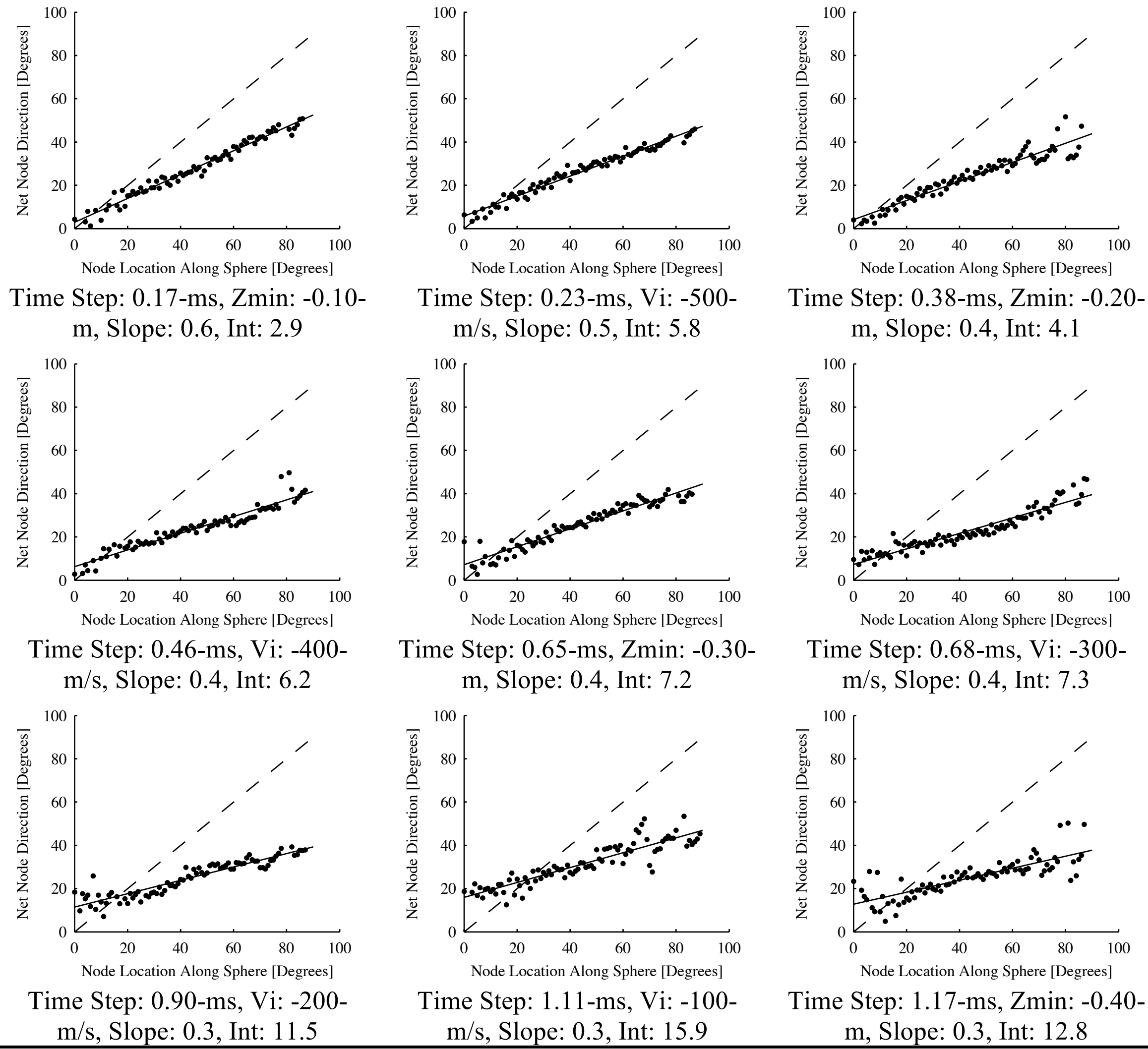

Time Step: 0.17-ms, Zmin: -0.10-m, Slope: 0.6, Int: 2.9

Time Step: 0.23-ms, Vi: -500-m/s, Slope: 0.5, Int: 5.8

Time Step: 0.38-ms, Zmin: -0.20-m, Slope: 0.4, Int: 4.1

Time Step: 0.46-ms, Vi: -400-m/s, Slope: 0.4, Int: 6.2

Time Step: 0.65-ms, Zmin: -0.30-m, Slope: 0.4, Int: 7.2

Time Step: 0.68-ms, Vi: -300-m/s, Slope: 0.4, Int: 7.3

Time Step: 0.90-ms, Vi: -200-m/s, Slope: 0.3, Int: 11.5

Time Step: 1.11-ms, Vi: -100-m/s, Slope: 0.3, Int: 15.9

Time Step: 1.17-ms, Zmin: -0.40-m, Slope: 0.3, Int: 12.8

Figure 109. SECM Plots for Data Set 6, 600-m/s Striking Velocity, 97-MPa Concrete Target, 26.9-mm Diameter Projectile, 2-CRH Projectile Nose

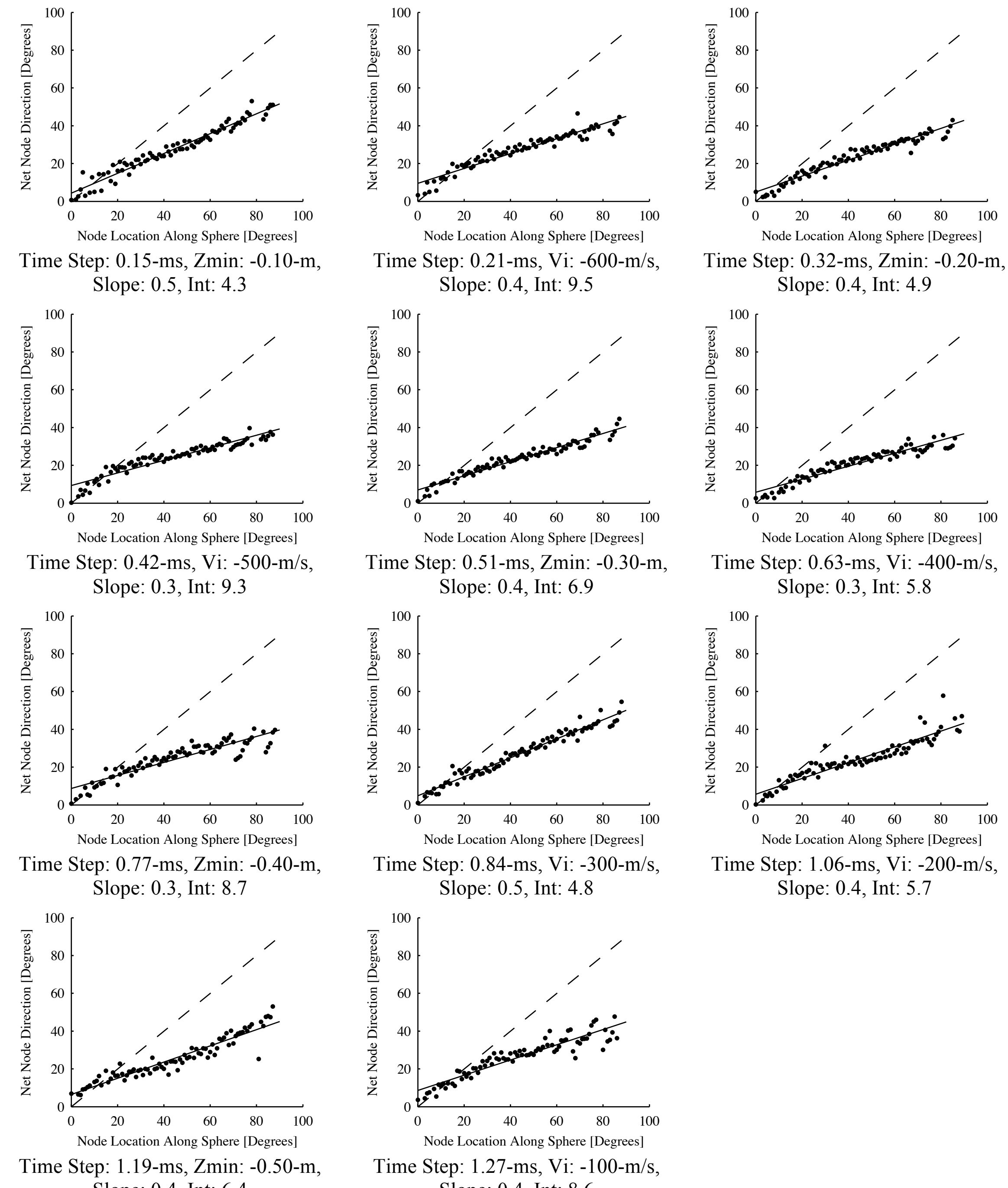

Figure 110. SECM Plots for Data Set 6, 700-m/s Striking Velocity, 97-MPa Concrete Target, 26.9-mm Diameter Projectile, 2-CRH Projectile Nose

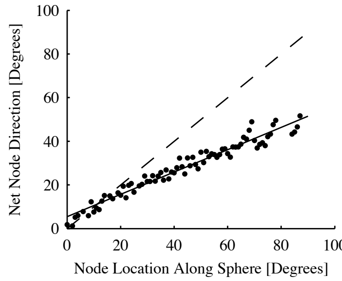

Time Step: 0.13-ms, Zmin: -0.10-m,
Slope: 0.5, Int: 5.4

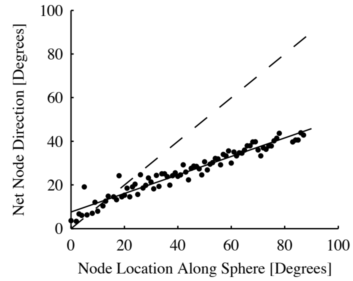

Time Step: 0.19-ms, Vi: -700-m/s,
Slope: 0.4, Int: 7.6

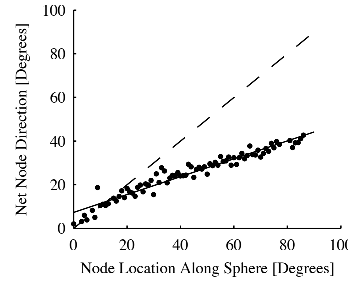

Time Step: 0.27-ms, Zmin: -0.20-m,
Slope: 0.4, Int: 7.3

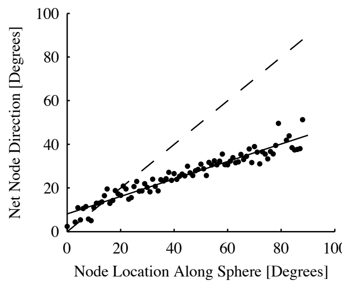

Time Step: 0.39-ms, Vi: -600-m/s,
Slope: 0.4, Int: 8.1

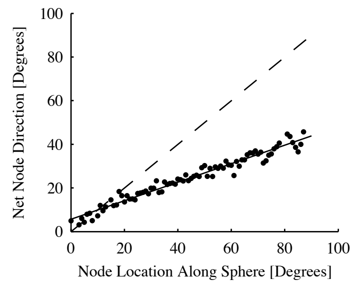

Time Step: 0.43-ms, Zmin: -0.30-m,
Slope: 0.4, Int: 5.6

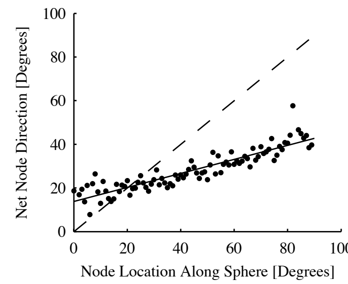

Time Step: 0.59-ms, Vi: -500-m/s,
Slope: 0.3, Int: 13.8

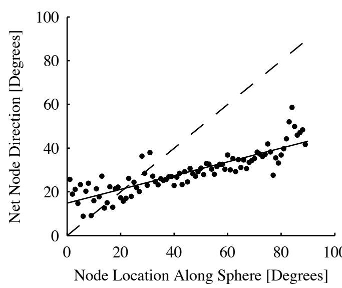

Time Step: 0.62-ms, Zmin: -0.40-m,
Slope: 0.3, Int: 14.8

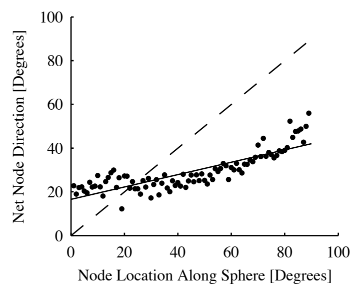

Time Step: 0.79-ms, Vi: -400-m/s,
Slope: 0.3, Int: 16.6

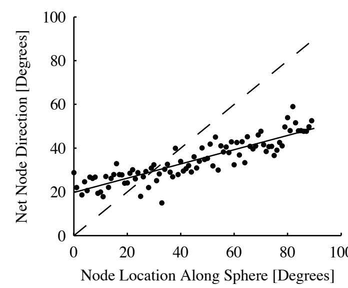

Time Step: 0.85-ms, Zmin: -0.50-m,
Slope: 0.3, Int: 19.7

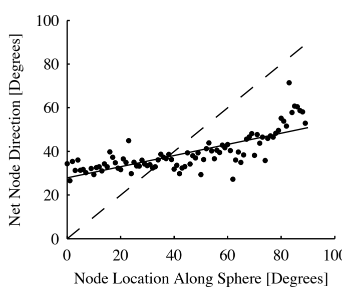

Time Step: 1.01-ms, Vi: -300-m/s,
Slope: 0.3, Int: 27.8

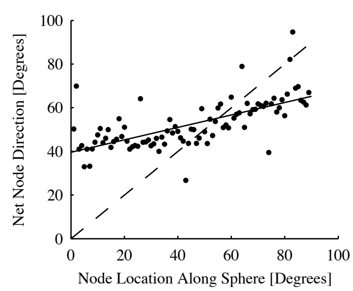

Time Step: 1.19-ms, Zmin: -0.6-m,
Slope: 0.3, Int: 39.6

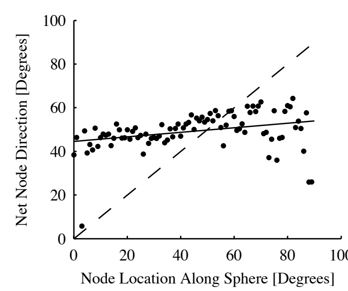

Time Step: 1.22-ms, Vi: -200-m/s,
Slope: 0.1, Int: 44.5

Figure 111. SECM Plots for Data Set 6, 800-m/s Striking Velocity, 97-MPa Concrete Target, 26.9-mm Diameter Projectile, 2-CRH Projectile Nose

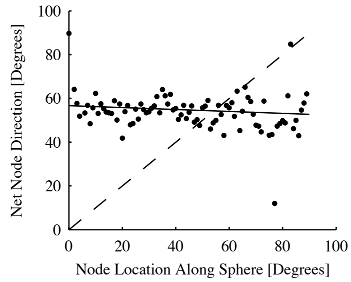

Time Step: 1.45-ms, Vi: -100-m/s,
Slope: -0.0, Int: 56.7

Figure 112. SECM Plots for Data Set 6, 800-m/s Striking Velocity, 97-MPa Concrete Target, 26.9-mm Diameter Projectile, 2-CRH Projectile Nose

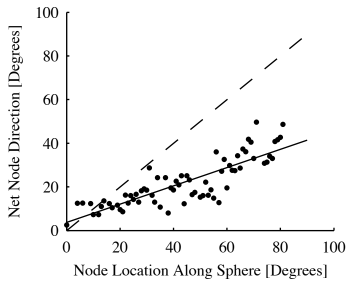

Time Step: 0.34-ms, Vi: -100-m/s, Slope: 0.4, Int: 3.7

Figure 113. SECM Plots for Data Set 7, 200-m/s Striking Velocity, 157-MPa Concrete Target, 26.9-mm Diameter Projectile, 2-CRH Projectile Nose

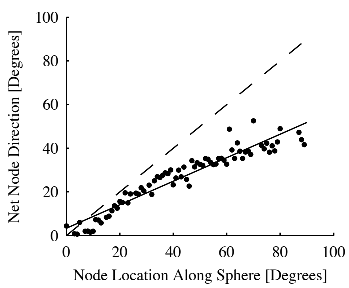

Time Step: 0.25-ms, Vi: -300-m/s, Slope: 0.5, Int: 3.4

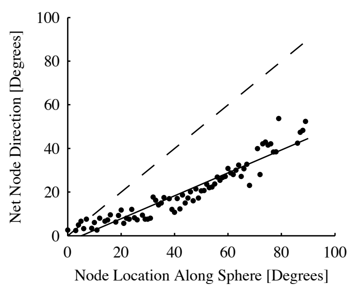

Time Step: 0.29-ms, Zmin: -0.10-m, Slope: 0.5, Int: -2.7

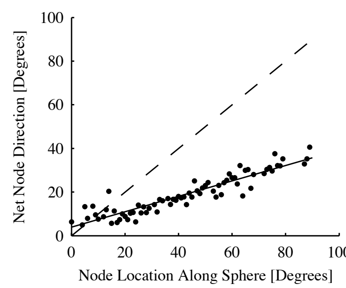

Time Step: 0.40-ms, Vi: -200-m/s, Slope: 0.4, Int: 4.0

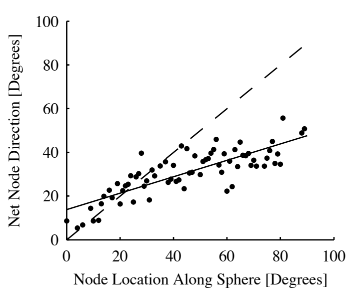

Time Step: 0.56-ms, Vi: -100-m/s, Slope: 0.4, Int: 13.8

Figure 114. SECM Plots for Data Set 7, 400-m/s Striking Velocity, 157-MPa Concrete Target, 26.9-mm Diameter Projectile, 2-CRH Projectile Nose

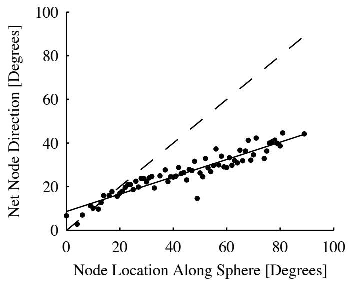

Time Step: 0.18-ms, Zmin: -0.10-m, Slope: 0.4, Int: 8.6

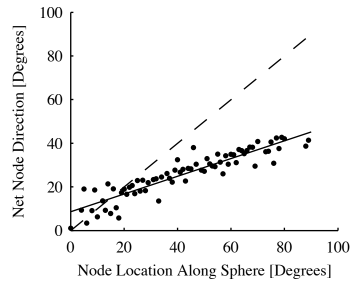

Time Step: 0.19-ms, Vi: -500-m/s, Slope: 0.4, Int: 8.6

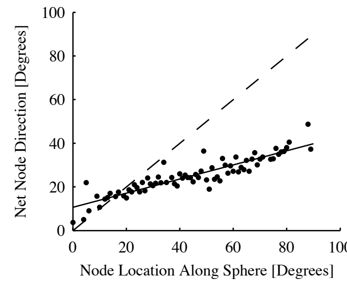

Time Step: 0.34-ms, Vi: -400-m/s, Slope: 0.3, Int: 10.6

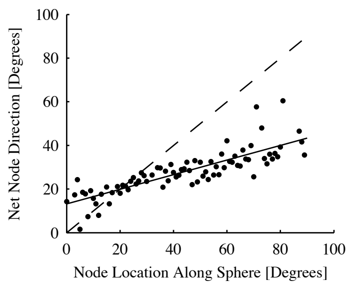

Time Step: 0.41-ms, Zmin: -0.20-m, Slope: 0.3, Int: 13.2

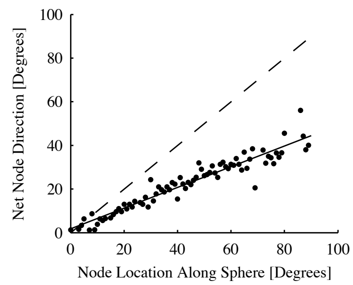

Time Step: 0.47-ms, Vi: -300-m/s, Slope: 0.5, Int: 1.8

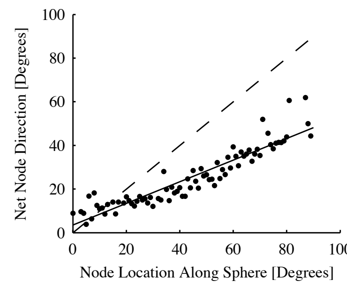

Time Step: 0.62-ms, Vi: -200-m/s, Slope: 0.5, Int: 3.5

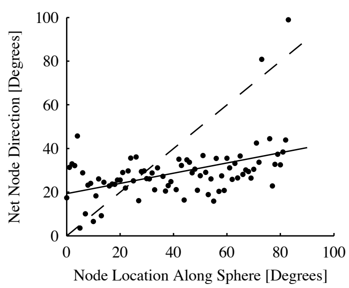

Time Step: 0.78-ms, Vi: -100-m/s, Slope: 0.2, Int: 19.4

Figure 115. SECM Plots for Data Set 7, 600-m/s Striking Velocity157-MPa Concrete Target 26.9-mm Diameter Projectile, 2-CRH Projectile Nose

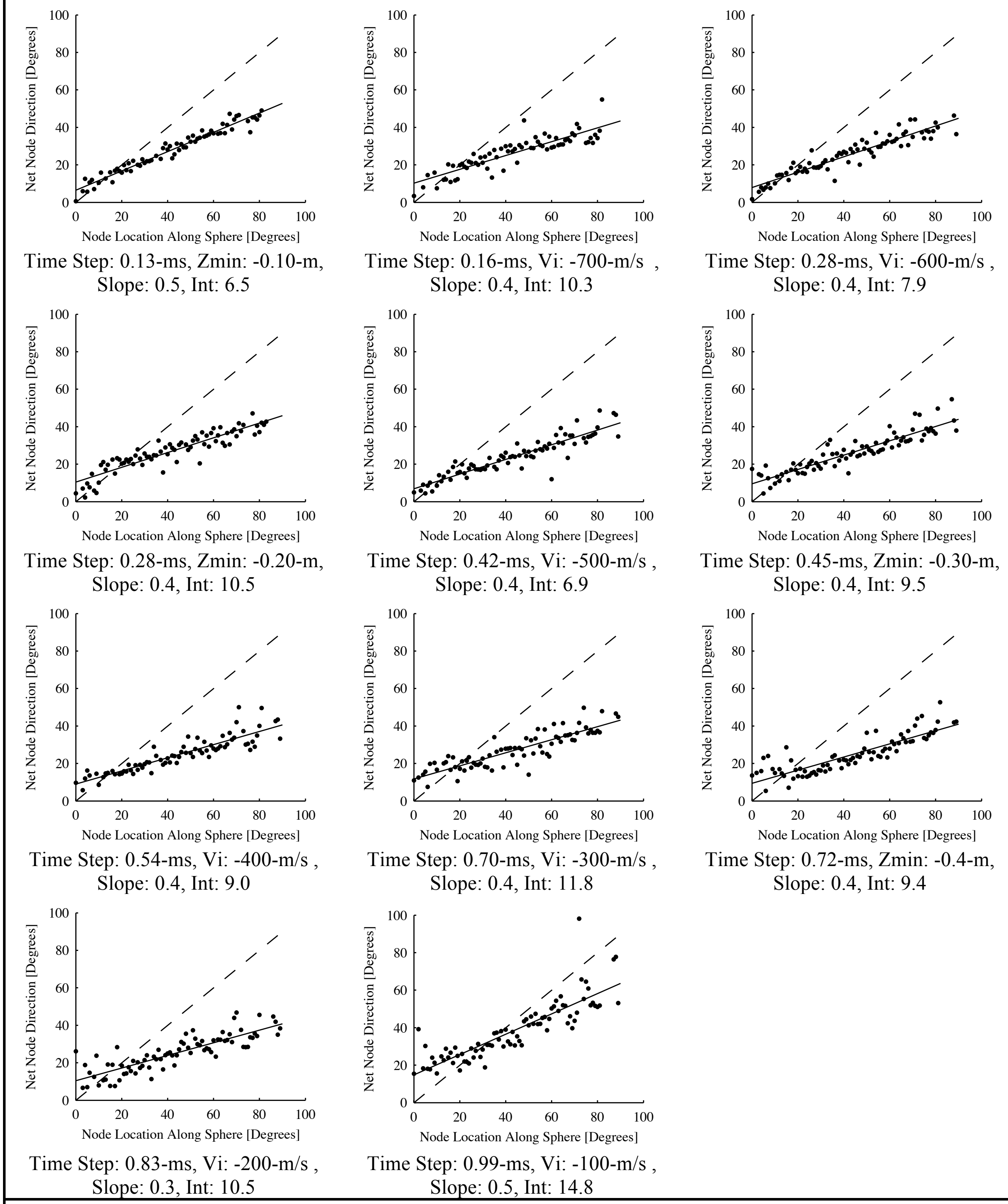

Time Step: 0.13-ms, Zmin: -0.10-m, Slope: 0.5, Int: 6.5

Time Step: 0.16-ms, Vi: -700-m/s , Slope: 0.4, Int: 10.3

Time Step: 0.28-ms, Vi: -600-m/s , Slope: 0.4, Int: 7.9

Time Step: 0.28-ms, Zmin: -0.20-m, Slope: 0.4, Int: 10.5

Time Step: 0.42-ms, Vi: -500-m/s , Slope: 0.4, Int: 6.9

Time Step: 0.45-ms, Zmin: -0.30-m, Slope: 0.4, Int: 9.5

Time Step: 0.54-ms, Vi: -400-m/s , Slope: 0.4, Int: 9.0

Time Step: 0.70-ms, Vi: -300-m/s , Slope: 0.4, Int: 11.8

Time Step: 0.72-ms, Zmin: -0.4-m, Slope: 0.4, Int: 9.4

Time Step: 0.83-ms, Vi: -200-m/s , Slope: 0.3, Int: 10.5

Time Step: 0.99-ms, Vi: -100-m/s , Slope: 0.5, Int: 14.8

Figure 116. SECM Plots for Data Set 7, 800-m/s Striking Velocity
157-MPa Concrete Target, 26.9-mm Diameter Projectile, 2-CRH Projectile Nose

APPENDIX 3: NECM OUTPUT TABLES FOR PARTICLE DIRECTION

Table 33. Ogive-Normal Flow Comparison: IncreasingStriking Velocity/Increasing Instantaneous Depth for Data Set 3, 76.2-mm, 3CRH Projectile into 39-MPa Target

Instantaneous Depth (m)	Striking Velocity (m/s) 250	325	400	475
0.1	4.6	4.5	4.5	4.8
0.2	3.8	3.9	3.6	3.3
0.3	3.8	3.9	3.7	3.7
0.4		3.1	2.5	2.4
0.5			1.2	1.9
0.6			1.9	1.3
0.7				2.9

Table 34. Ogive-Normal Flow Comparison: IncreasingStriking Velocity/Decreasing Instantaneous Velocity for Data Set 3, 76.2-mm, 3CRH Projectile into 39-MPa Target

Instantaneous Velocity (m/s)	Striking Velocity (m/s) 250	325	400	475
400				2.8
300		4.1	2.8	1.7
200	4.1	3.3	2.1	2.0
100	3.2	1.6	1.7	1.6

Table 35. Average NECM Values for Data Set 3 76.2-mm, 3CRH, Projectile into 39-MPa Target

Data Set	Striking Velocity (m/s) 250	325	400	475
3	3.9	3.5	2.7	2.6

Table 36. Ogive-Normal Flow Comparison: Increasing Striking Velocity/Increasing Instantaneous Depth for Data Set 4, 76.2-mm, 6CRH Projectile into 39-MPa Target

Instantaneous Depth (m)	Striking Velocity (m/s)			
	250	325	400	475
0.1	8.5	8.4	8.5	8.5
0.2	7.3	6.8	6.9	7.0
0.3	6.9	7.1	6.7	6.4
0.4		5.6	6.2	6.9
0.5		2.9	4.2	4.3
0.6			1.7	2.4
0.7				3.2
0.8				1.9

Table 37. Ogive-Normal Flow Comparison: Increasing Striking Velocity/Decreasing Instantaneous Velocity for Data Set 4, 76.2-mm, 6CRH Projectile into 39-MPa Target

Instantaneous Velocity (m/s)	Striking Velocity (m/s)			
	250	325	400	475
400				6.9
300		7.8	5.4	2.8
200	7.1	4.6	2.7	3.8
100	6.4	4.4	2.0	4.4

Table 38. Average NECM values for Data Set 4 76.2-mm, 6CRH Projectile into 39-MPa Target

Data Set	Striking Velocity (m/s)			
	250	325	400	475
4	7.2	6.0	4.9	4.9

Table 39. Ogive-Normal Flow Comparison: Increasing Striking Velocity/Increasing Instantaneous Depth for Data Set 5, 26.9-mm, 2-CRH Projectile into 36-MPa Target

Instantaneous Depth (m)	Striking Velocity (m/s)			
	200	400	600	800
0.1	2.0	2.4	1.9	0.8
0.2		0.9	1.0	0.3
0.3			1.0	0.4
0.4			1.1	0.4
0.5			0.9	0.8
0.6				0.9
0.7				1.0
0.8				1.2

Table 40. Ogive-Normal Flow Comparison: Increasing Striking Velocity/Decreasing Instantaneous Velocity for Data Set 5, 26.9-mm, 2-CRH Projectile into 36-MPa Target

Instantaneous Velocity (m/s)	Striking Velocity (m/s)			
	200	400	600	800
700				0.6
600				0.4
500			0.9	0.5
400			1.1	0.6
300		1.7	1.3	0.6
200		1.5	1.3	1.3
100	1.8	1.5	1.1	1.2

Table 41. Average NECM Values for Data Set 5 26.9-mm, 2-CRH Projectile into 36-MPa Target

Data Set	Striking Velocity (m/s)			
	200	400	600	800
5	1.9	1.6	1.2	0.7

Table 42. Ogive-Normal Flow Comparison: Increasing Striking Velocity/ Increasing Instantaneous Depth for Data Set 6, 26.9-mm, 2-CRH Projectile into 97-MPa Target

Instantaneous Depth (m)	Striking Velocity (m/s) 500	600	700	800
0.1	1.2	1.2	0.9	0.9
0.2	1.0	0.8	0.6	0.6
0.3	0.8	1.2	1.0	1.0
0.4		1.2	1.1	1.2
0.5			1.0	1.4
0.6				1.8

Table 43. Ogive-Normal Flow Comparison: Increasing Striking Velocity/Decreasing Instantaneous Velocity for Data Set 6, 26.9-mm, 2-CRH Projectile into 97-MPa Target

Instantaneous Velocity (m/s)	Striking Velocity (m/s) 500	600	700	800
700				0.5
600			0.8	1.0
500		1.0	0.9	1.2
400	1.3	1.1	0.9	1.5
300	0.4	1.2	1.1	1.2
200	1.4	1.4	0.9	1.8
100	0.7	1.4	0.9	1.2

Table 44. Average NECM Values for Data Set 6 26.9-mm, 2-CRH Projectile into 97-MPa Target

Data Set	Striking Velocity (m/s) 500	600	700	800
6	1.0	1.2	0.9	1.2

Table 45. Ogive-Normal Flow Comparison: Increasing Striking Velocity/ Increasing Instantaneous Depth for Data Set 7, 26.9-mm, 2-CRH Projectile into 157-MPa Target

Instantaneous Depth (m)	Striking Velocity (m/s) 200	400	600	800
0.1	-	1.4	1.2	0.9
0.2			1.1	0.8
0.3				1.1
0.4				1.2

Table 46. Ogive-Normal Flow Comparison: Increasing Striking Velocity/Decreasing Instantaneous Velocity for Data Set 7, 26.9-mm, 2-CRH Projectile into 157-MPa Target

Instantaneous Velocity (m/s)	Striking Velocity (m/s) 200	400	600	800
700				0.9
600				0.9
500			0.9	1.1
400			1.2	1.1
300		1.0	0.9	1.0
200		0.8	1.2	1.3
100	2.0	0.9	1.4	1.2

Table 47. Average NECM Values for Data Set 7 26.9-mm, 2-CRH Projectile into 157-MPa Target

Data Set	Striking Velocity (m/s) 200	400	600	800
7	2.0	1.0	1.1	1.0

Table 48. Ogive-Normal Flow Comparison: Increasing Concrete Strength/Increasing Depth for Data Sets 5, 6, and 7 26.9-mm, 2-CRH Projectile, 800-m/s Striking Velocity

Instantaneous Depth (m)	Concrete Strength (MPa) 36	97	157
0.1	0.8	0.9	0.9
0.2	0.3	0.6	0.8
0.3	0.4	1.0	1.1
0.4	0.4	1.2	1.2
0.5	0.8	1.4	
0.6	0.9	1.8	
0.7	1.0		
0.8	1.2		

Table 49. Ogive-Normal Flow Comparison: Increasing Concrete Strength/Decreasing Velocity for Data Sets 5, 6, and 7 26.9-mm, 2-CRH Projectile, 800-m/s Striking Velocity

Instantaneous Velocity (m/s	Concrete Strength (MPa) 36	97	157
700	0.6	0.5	0.9
600	0.4	1.0	0.9
500	0.5	1.2	1.1
400	0.6	1.5	1.1
300	0.6	1.2	1.0
200	1.3	1.8	1.3
100	1.2	1.2	1.2

Table 50. Ogive-Normal Flow Comparison: Increasing Concrete Strength/Increasing Depth for Data Sets 5, 6, and 7 26.9-mm, 2-CRH Projectile, 600-m/s Striking Velocity

Instantaneous Depth (m)	Concrete Strength (MPa)		
	36	97	157
0.1	1.9	1.2	1.2
0.2	1.0	0.8	1.1
0.3	1.0	1.2	
0.4	1.1	1.2	
0.5	0.9		

Table 51. Ogive-Normal Flow Comparison: Increasing Concrete Strength/Decreasing Velocity for Data Sets 5, 6, and 7 26.9-mm, 2-CRH Projectile, 600-m/s Striking Velocity

Instantaneous Velocity (m/s	Concrete Strength (MPa)		
	36	97	157
500	0.9	1.0	0.9
400	1.1	1.1	1.2
300	1.3	1.2	0.9
200	1.3	1.4	1.2
100	1.1	1.4	1.4

Table 52. Ogive-Normal Flow Comparison: Increasing Concrete Strength/Increasing Depth for Data Sets 5, 6, and 7
26.9-mm, 2-CRH Projectile, 400-m/s Striking Velocity

Instantaneous Depth (m)	Concrete Strength (MPa)		
	36	97	157
0.1	2.4	-	1.3
0.2	0.9	-	-

Table 53. Ogive-Normal Flow Comparison: Increasing Concrete Strength/Decreasing Velocity for Data Sets 5, 6, and 7
26.9-mm, 2-CRH Projectile, 400-m/s Striking Velocity

Instantaneous Velocity (m/s	Concrete Strength (MPa)		
	36	97	157
300	1.7	-	1.1
200	1.5	-	0.9
100	1.5	-	0.7

Table 54. Average NECM Values for Data Sets 5, 6, and 7
26.9-mm, 2-CRH Projectile into Various Strength Concretes

Striking Velocity (m/s)	Concrete Strength (MPa)		
	36	97	157
800	0.7	1.2	1.0
600	1.2	1.2	1.1
400	1.6	-	1.0

APPENDIX 4: SECM OUTPUT TABLES FOR NODAL DIRECTION

Table 55. Spherical Flow Comparison: Increasing Striking Velocity/ Increasing Instantaneous Depth for Data Set 3, 76.2-mm, 3-CRH Projectile into 39-MPa Target

Instantaneous Depth (m)	Striking Velocity (m/s)			
	250	325	400	475
0.1	0.7	0.7	0.7	0.6
0.2	0.6	0.5	0.7	0.7
0.3	0.4	0.4	0.5	0.6
0.4		0.5	0.5	0.4
0.5			0.2	0.3
0.6			0.1	0.3
0.7				0.2

Table 56. Spherical Flow Comparison: Increasing Striking Velocity/Decreasing Instantaneous Velocity for Data Set 3, 76.2-mm, 3-CRH Projectile into 39-MPa Target

Instantaneous Velocity (m/s	Striking Velocity (m/s)			
	250	325	400	475
400				0.6
300		0.6	0.3	0.5
200	0.3	0.2	0.0	0.2
100	0.5	0.1	0.3	0.4

Table 57. Average SECM Values for Data Set 3 76.2-mm, 3-CRH Projectile into 39-MPa Target

Data Set	Striking Velocity (m/s)			
	250	325	400	425
3	0.5	0.4	0.4	0.4

Table 58. Spherical Flow Comparison: Increasing Striking Velocity/ Increasing Instantaneous Depth for Data Set 4, 76.2-mm, 6-CRH Projectile into 39-MPa Target

Instantaneous Depth (m)	Striking Velocity (m/s)			
	250	325	400	425
0.1	0.5	0.8	0.8	0.9
0.2	0.2	0.5	0.5	0.4
0.3	0.8	0.4	0.6	0.6
0.4		0.3	0.3	0.4
0.5		0.3	0.6	0.2
0.6			0.2	0.3
0.7				0.5
				0.3

Table 59. Spherical Flow Comparison: Increasing Striking Velocity/Decreasing Instantaneous Velocity for Data Set 4, 76.2-mm, 6-CRH Projectile into 39-MPa Target

Instantaneous Velocity (m/s	Striking Velocity (m/s)			
	250	325	400	425
400				0.5
300		0.9	0.5	0.4
200	0.4	0.6	0.3	0.1
100	0.4	0.2	0.3	0.6

Table 60. Average SECM Values for Data Set 3 76.2-mm, 6-CRH Projectile into 39-MPa Target

Data Set	Striking Velocity (m/s)			
	250	325	400	425
4	0.5	0.5	0.5	0.4

Table 61. Spherical Flow Comparison: Increasing Striking Velocity/ Increasing Instantaneous Depth for Data Set 5, 26.9-mm, 2-CRH Projectile into 36-MPa Target

Instantaneous Depth (m)	Striking Velocity (m/s) 200	400	600	800
0.1	0.7	0.5	0.6	0.6
0.2		0.3	0.5	0.4
0.3			0.4	0.5
0.4			0.4	0.4
0.5			0.4	0.4
0.6				0.3

Table 62. Spherical Flow Comparison: Increasing Striking Velocity/Decreasing Instantaneous Velocity for Data Set 5, 26.9-mm, 2-CRH Projectile into 36-MPa Target

Instantaneous Velocity (m/s	Striking Velocity (m/s) 200	400	600	800
700				0.5
600				0.4
500			0.5	0.3
400			0.4	0.4
300		0.5	0.4	0.4
200		0.5	0.4	0.5
100	0.7	0.5	0.5	0.5

Table 63. Average SECM Values for Data Set 3 26.9-mm, 2-CRH Projectile into 36-MPa Target

Data Set	Striking Velocity (m/s) 200	400	600	800
5	0.7	0.5	0.5	0.4

Table 64. Spherical Flow Comparison: Increasing Striking Velocity/ Increasing Instantaneous Depth for Data Set 6, 26.9-mm, 2-CRH Projectile into 97-MPa Target

Instantaneous Depth (m)	Striking Velocity (m/s)			
	500	600	700	800
0.1	0.5	0.6	0.5	0.5
0.2	0.4	0.4	0.4	0.4
0.3	0.5	0.4	0.4	0.4
0.4		0.3	0.3	0.3
0.5			0.4	0.3
0.6				0.3

Table 65. Spherical Flow Comparison: Increasing Striking Velocity/Decreasing Instantaneous Velocity for Data Set 6, 26.9-mm, 2-CRH Projectile into 97-MPa Target

Instantaneous Velocity (m/s	Striking Velocity (m/s)			
	500	600	700	800
700				0.4
600			0.4	0.4
500		0.5	0.3	0.3
400	0.5	0.4	0.3	0.3
300	0.4	0.4	0.5	0.3
200	0.5	0.3	0.4	0.1
100	0.5	0.3	0.4	0.0

Table 66. Average SECM Values for Data Set 6 26.9-mm, 2-CRH Projectile into 97-MPa Target

Data Set	Striking Velocity (m/s)			
	500	600	700	800
6	0.5	0.4	0.4	0.3

Table 67. Spherical Flow Comparison: Increasing Striking Velocity/Increasing Instantaneous Depth for Data Set 7, 26.9-mm, 2-CRH Projectile into 157-MPa Target

Instantaneous	Striking Velocity (m/s)			
Depth (m)	200	400	600	800
0.1	-	0.5	0.4	0.5
0.2			0.3	0.4
0.3				0.4
0.4				0.4

Table 68. Spherical Flow Comparison: Increasing Striking Velocity/Decreasing Instantaneous Velocity for Data Set 7, 26.9-mm, 2-CRH Projectile into 157-MPa Target

Instantaneous	Striking Velocity (m/s)			
Velocity (m/s	200	400	600	800
700				0.4
600				0.4
500			0.4	0.4
400			0.3	0.4
300		0.5	0.5	0.4
200		0.4	0.5	0.3
100	0.4	0.4	0.2	0.5

Table 69. Average SECM Values for Data Set 7 Data Set 6, 26.9-mm, 2-CRH Projectile into 157-MPa Target

Data Set	Striking Velocity (m/s)			
	200	400	600	800
7	0.4	0.5	0.4	0.4

Table 70. Spherical Flow Comparison: Increasing Concrete Strength/Increasing Depth for Data Sets 5, 6, and 7 26.9-mm, 2-CRH Projectile, 800-m/s Striking Velocity

Instantaneous Depth (m)	Concrete Strength (MPa)		
	36	97	157
0.1	0.6	0.5	0.5
0.2	0.4	0.4	0.4
0.3	0.5	0.4	0.4
0.4	0.4	0.3	0.4
0.5	0.4	0.3	
0.6	0.3	0.3	

Table 71. Spherical Flow Comparison: Increasing Concrete Strength/Decreasing Velocity for Data Sets 5, 6, and 7 26.9-mm, 2-CRH Projectile, 800-m/s Striking Velocity

Instantaneous Velocity (m/s	Concrete Strength (MPa)		
	36	97	157
700	0.5	0.4	0.4
600	0.4	0.4	0.4
500	0.3	0.3	0.4
400	0.4	0.3	0.4
300	0.4	0.3	0.4
200	0.5	0.1	0.3
100	0.5	0.0	0.5

Table 72. Spherical Flow Comparison: Increasing Concrete Strength/Increasing Depth for Data Sets 5, 6, and 7
26.9-mm, 2-CRH Projectile, 600-m/s Striking Velocity

Instantaneous Depth (m)	Concrete Strength (MPa) 36	97	157
0.1	0.6	0.6	0.4
0.2	0.5	0.4	0.3
0.3	0.4	0.4	
0.4	0.4	0.3	
0.5	0.4		
0.6			
0.7			
0.8			

Table 73. Spherical Flow Comparison: Increasing Concrete Strength/Decreasing Velocity for Data Sets 5, 6, and 7
26.9-mm, 2-CRH Projectile, 600-m/s Striking Velocity

Instantaneous Velocity (m/s	Concrete Strength (MPa) 36	97	157
500	0.5	0.5	0.4
400	0.4	0.4	0.3
300	0.4	0.4	0.5
200	0.4	0.3	0.5
100	0.5	0.3	0.2

Table 74. Spherical Flow Comparison: Increasing Concrete Strength/Increasing Depth for Data Sets 5, 6, and 7 26.9-mm, 2-CRH Projectile, 400-m/s Striking Velocity

Instantaneous Depth (m)	Concrete Strength (MPa)		
	36	97	157
0.1	0.5	-	0.5
0.2	0.3	-	-

Table 75. Spherical Flow Comparison: Increasing Concrete Strength/Decreasing Velocity for Data Sets 5, 6, and 7 26.9-mm, 2-CRH Projectile, 400-m/s Striking Velocity

Instantaneous Velocity (m/s	Concrete Strength (MPa)		
	36	97	157
300	0.5	-	0.5
200	0.5	-	0.4
100	0.5	-	0.4

Table 76. Average SECM Values for Data Sets 5, 6, and 7 26.9-mm, 2-CRH Projectile into Various Strength Concretes

Striking Velocity (m/s)	Concrete Strength (MPa)		
	36	97	157
800	0.4	0.3	0.4
600	0.5	0.4	0.4
400	0.5	-	0.5

APPENDIX 5: MESH GEOMETRY SUMMARIES

Table 77. Mesh Geometry for Data Sets 1 and 3

Geometry Summary	Projectile	Target	Total
Number of Nodes	25,888	492,817	518,705
Number of Elements	111,120	2,323,200	2,434,320
Average Element Volume (m^3)	7.39E-09	1.04E-06	9.88E-07
Maximum Element Volume (m^3)	2.86E-08	6.53E-06	6.53E-06
Minimum Element Volume (m^3)	2.27E-09	8.16E-09	2.27E-09
Average Aspect Ratio	0.279418	0.248113	0.249542
Maximum Aspect Ratio	0.450378	0.481722	0.481722
Minimum Aspect Ratio	0.025681	0.024355	0.024355
Average Minimum Height (m)	0.001785	0.007167	0.006921
Maximum Minimum Height (m)	0.003307	0.025131	0.025131
Minimum Minimum Height (m)	0.000624	0.000743	0.000624

Table 78. Mesh Geometry for Data Sets 2 and 4

Geometry Summary	Projectile	Target	Total
Number of Nodes	21,441	492,817	514,258
Number of Elements	90,960	2,323,200	2,414,160
Average Element Volume (m^3)	9.04E-09	1.04E-06	9.96E-07
Maximum Element Volume (m^3)	2.51E-08	6.53E-06	6.53E-06
Minimum Element Volume (m^3)	1.36E-09	8.16E-09	1.36E-09
Average Aspect Ratio	0.300295	0.248113	0.250079
Maximum Aspect Ratio	0.462502	0.481722	0.481722
Minimum Aspect Ratio	0.035589	0.024355	0.024355
Average Minimum Height (m)	0.001952	0.007167	0.006971
Maximum Minimum Height (m)	0.003785	0.025131	0.025131
Minimum Minimum Height (m)	0.000511	0.000743	0.000511

Table 79. Mesh Geometry for Data Set 5

Geometry Summary	Projectile	Target	Total
Number of Nodes	2,061	840,626	842,687
Number of Elements	8,256	3,964,160	3,972,416
Average Element Volume (m^3)	6.86E-09	2.69E-07	2.69E-07
Maximum Element Volume (m^3)	3.37E-08	1.68E-06	1.68E-06
Minimum Element Volume (m^3)	4.22E-10	4.48E-10	4.22E-10
Average Aspect Ratio	0.162182	0.231186	0.231042
Maximum Aspect Ratio	0.616392	0.49266	0.616392
Minimum Aspect Ratio	0.0238	0.031049	0.0238
Average Minimum Height (m)	0.0012	0.003674	0.003669
Maximum Minimum Height (m)	0.00216	0.009541	0.009541
Minimum Minimum Height (m)	0.000343	0.000299	0.000299

Table 80. Mesh Geometry for Data Set 6

Geometry Summary	Projectile	Target	Total
Number of Nodes	2,061	857,740	859,801
Number of Elements	8,256	4,045,184	4,053,440
Average Element Volume (m^3)	6.86E-09	2.22E-07	2.21E-07
Maximum Element Volume (m^3)	3.37E-08	1.30E-06	1.30E-06
Minimum Element Volume (m^3)	4.22E-10	3.04E-10	3.04E-10
Average Aspect Ratio	0.162182	0.216032	0.215923
Maximum Aspect Ratio	0.616392	0.483077	0.616392
Minimum Aspect Ratio	0.0238	0.045258	0.0238
Average Minimum Height (m)	0.0012	0.002911	0.002907
Maximum Minimum Height (m)	0.00216	0.006497	0.006497
Minimum Minimum Height (m)	0.000343	0.000299	0.000299

Table 81. Mesh Geometry for Data Set 7

Geometry Summary	Projectile	Target	Total
Number of Nodes	2,061	169,171	171,232
Number of Elements	8,256	780,000	788,256
Average Element Volume (m^3)	6.86E-09	2.64E-07	2.61E-07
Maximum Element Volume (m^3)	3.37E-08	1.82E-06	1.82E-06
Minimum Element Volume (m^3)	4.22E-10	4.51E-10	4.22E-10
Average Aspect Ratio	0.162182	0.219504	0.218903
Maximum Aspect Ratio	0.616392	0.488592	0.616392
Minimum Aspect Ratio	0.0238	0.036488	0.0238
Average Minimum Height (m)	0.0012	0.002859	0.002842
Maximum Minimum Height (m)	0.00216	0.007292	0.007292
Minimum Minimum Height (m)	0.000343	0.000352	0.000343

APPENDIX 6: NECM PLOTS FOR NODAL DIRECTION

This Appendix includes the node normal expansion profiles for Data Sets 3, 5, and 7.

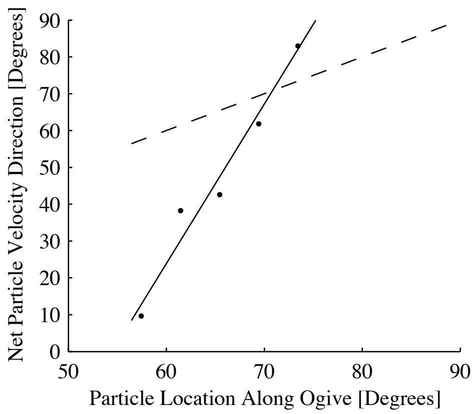

Time Step: 0.41-ms, Depth: -0.1-m,
Slope: 4.3, Int: -236.4

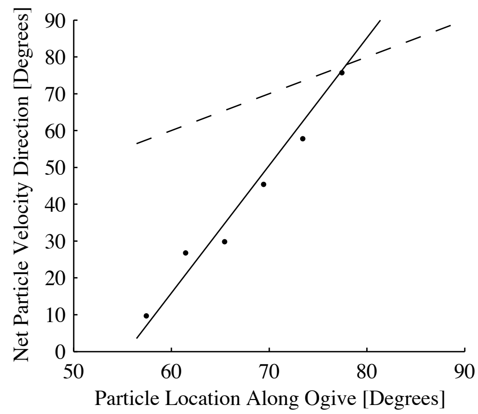

Time Step: 0.70-ms, Veloc: -200-m/s,
Slope: 3.5, Int: -192.1

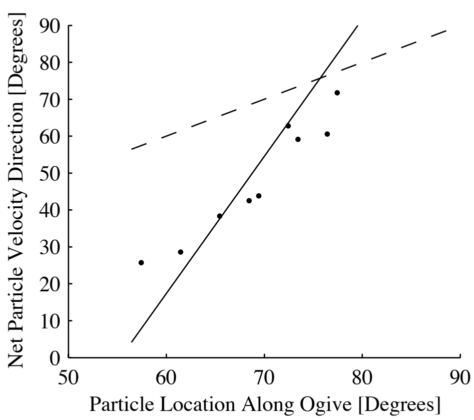

Time Step: 0.89-ms, Depth: -0.2-m,
Slope: 3.7, Int: -205.6

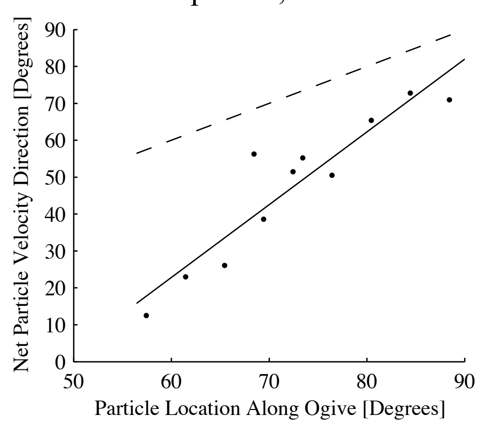

Time Step: 1.55-ms, Veloc: 100-m/s,
Slope: 2.0, Int: -95.6

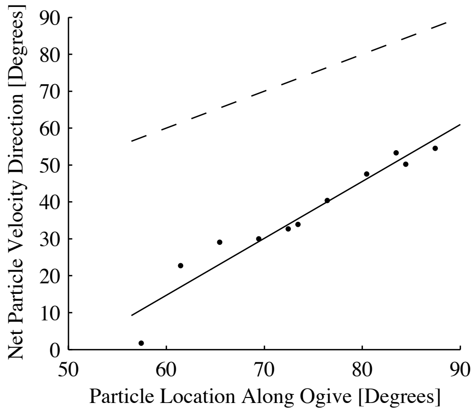

Time Step: 1.78-ms, Depth: -0.3-m,
Slope: 1.5, Int: -77.9

Figure 117. Data Set 3, 250-m/s Striking Velocity, 39-MPa Concrte, 76.2-mm, 3-CRH Projectile

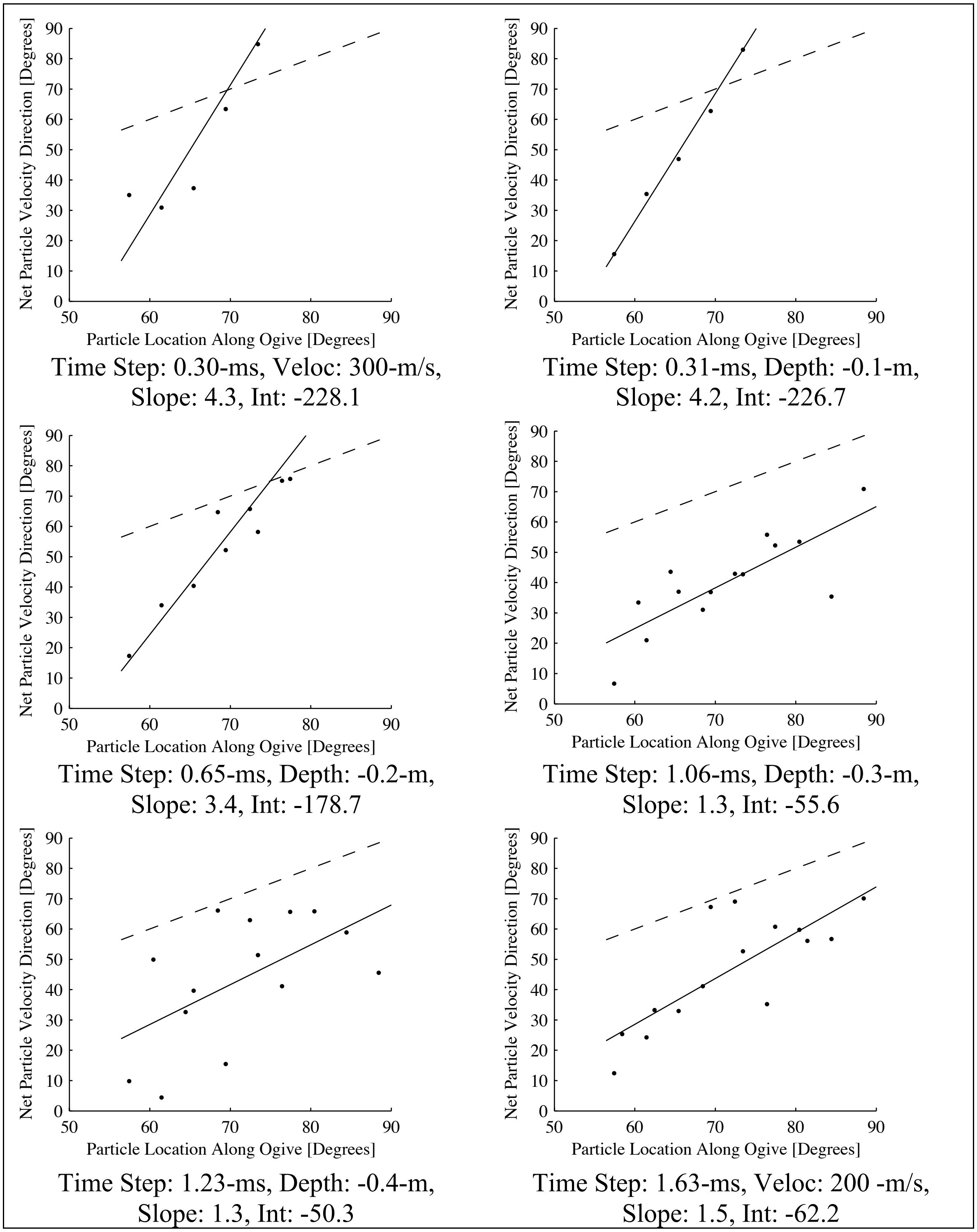

Time Step: 0.30-ms, Veloc: 300-m/s, Slope: 4.3, Int: -228.1

Time Step: 0.31-ms, Depth: -0.1-m, Slope: 4.2, Int: -226.7

Time Step: 0.65-ms, Depth: -0.2-m, Slope: 3.4, Int: -178.7

Time Step: 1.06-ms, Depth: -0.3-m, Slope: 1.3, Int: -55.6

Time Step: 1.23-ms, Depth: -0.4-m, Slope: 1.3, Int: -50.3

Time Step: 1.63-ms, Veloc: 200 -m/s, Slope: 1.5, Int: -62.2

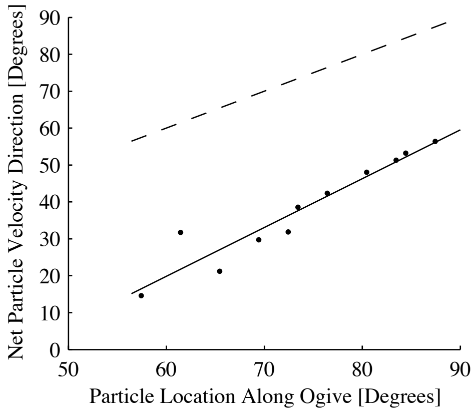

Time Step: 1.95-ms, Veloc: 100 -m/s,
Slope: 1.3, Int: -59.7

Figure 118. Data Set 3, 325-m/s Striking Velocity, 39-MPa Concrte, 76.2-mm, 3-CRH Projectile

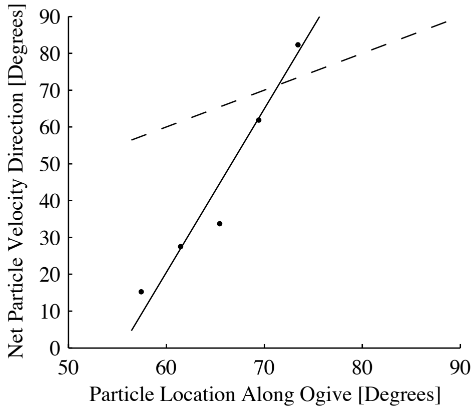

Time Step: 0.25-ms, Depth: -0.1-m,
Slope: 4.4, Int: -246.0

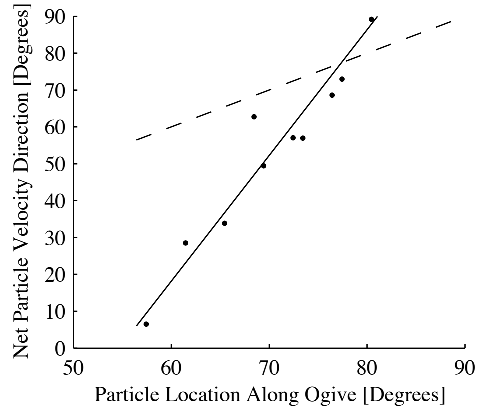

Time Step: 0.52-ms, Depth: -0.2-m,
Slope: 3.4, Int: -186.4

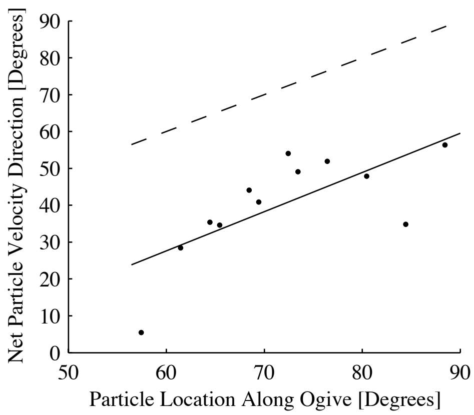

Time Step: 0.82-ms, Depth: -0.3-m,
Slope: 1.1, Int: -36.2

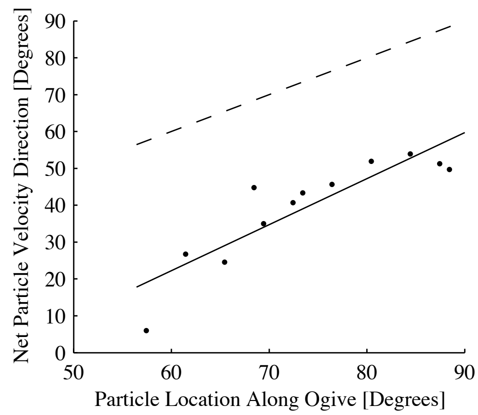

Time Step: 0.87-ms, Veloc: -m/s 300-m,
Slope: 1.3, Int: -52.7

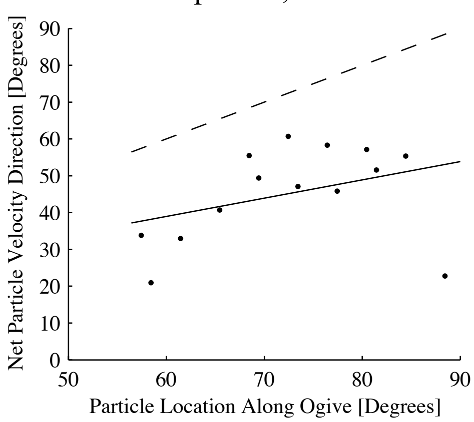

Time Step: 1.17-ms, Depth: -0.40-m,
Slope: 0.5, Int: 9.2

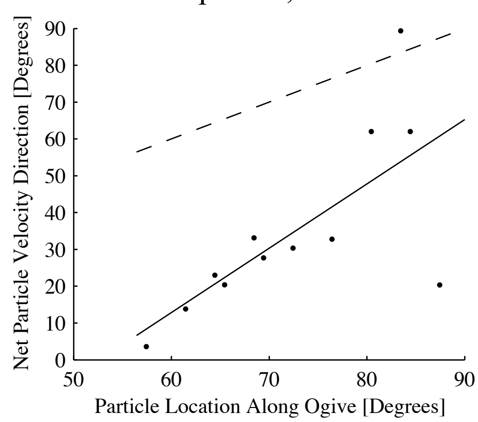

Time Step: 1.55-ms, Veloc: 200-m/s,
Slope: 1.8, Int: -92.0

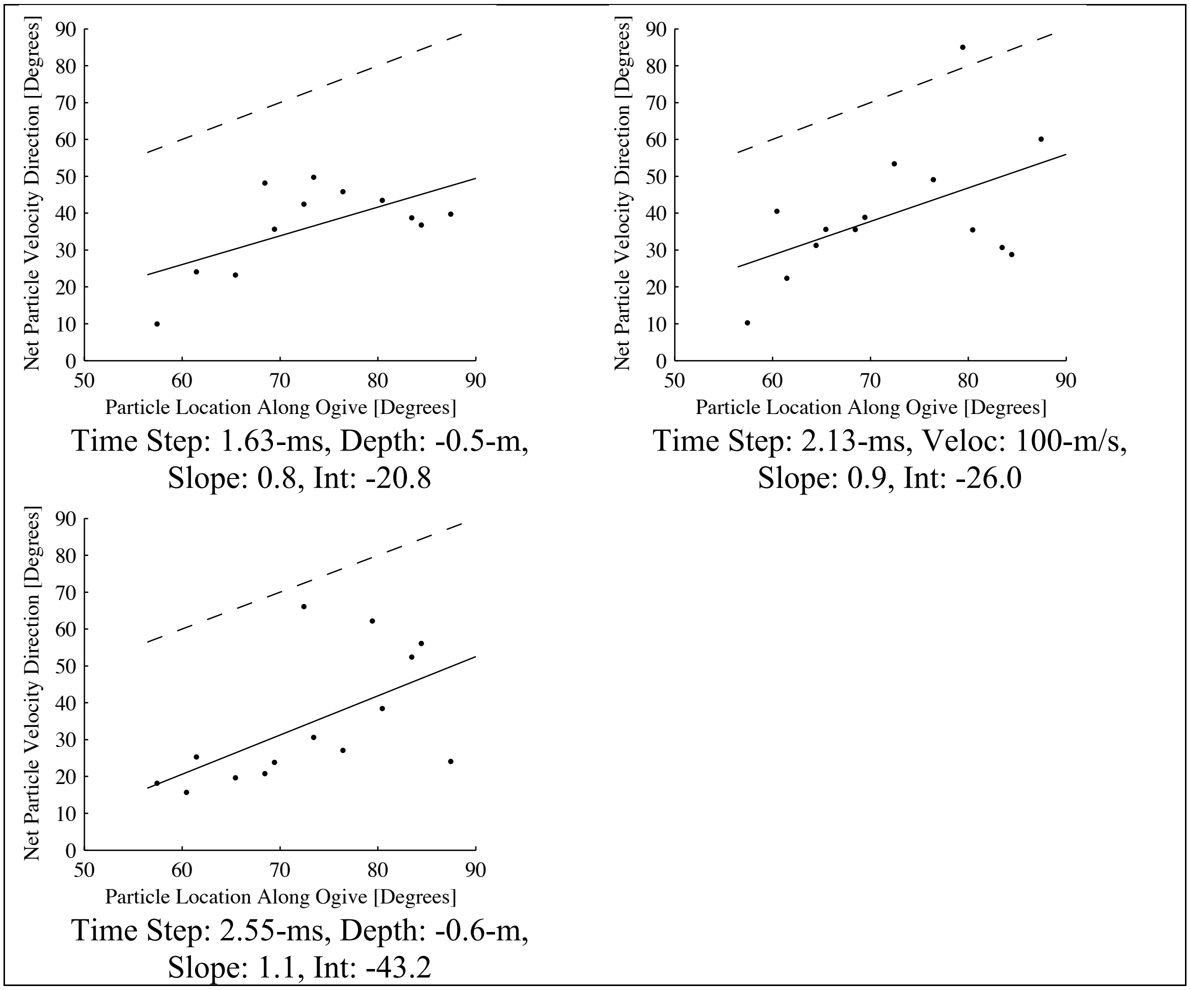

Time Step: 1.63-ms, Depth: -0.5-m,
Slope: 0.8, Int: -20.8

Time Step: 2.13-ms, Veloc: 100-m/s,
Slope: 0.9, Int: -26.0

Time Step: 2.55-ms, Depth: -0.6-m,
Slope: 1.1, Int: -43.2

Figure 119. Data Set 3, 400-m/s Striking Velocity, 39-MPa Concrte, 76.2-mm, 3-CRH Projectile

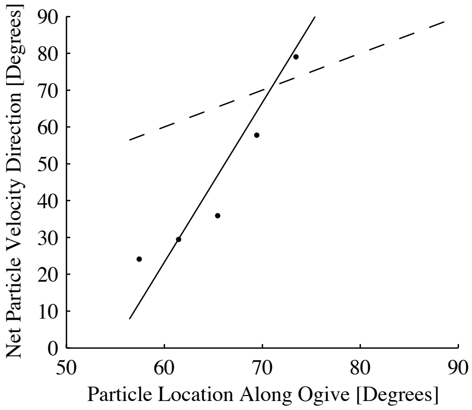

Time Step: 0.21-ms, Depth: -0.1-m,
Slope: 4.3, Int: -237.2

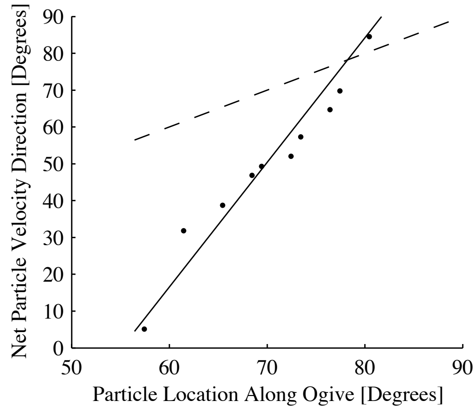

Time Step: 0.44-ms, Depth: -0.2-m,
Slope: 3.4, Int: -186.6

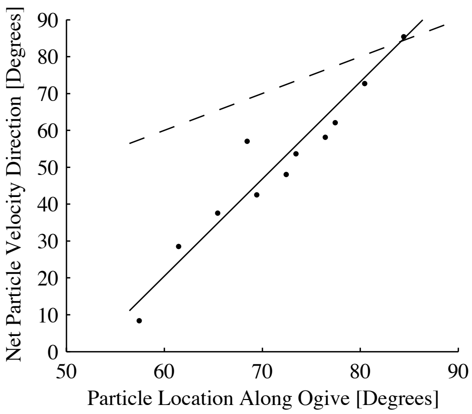

Time Step: 0.58-ms, Veloc: 400-m/s,
Slope: 2.6, Int: -137.8

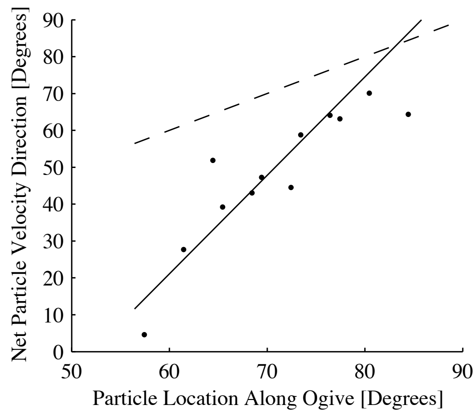

Time Step: 0.68-ms, Depth: -0.3-m,
Slope: 2.7, Int: -139.3

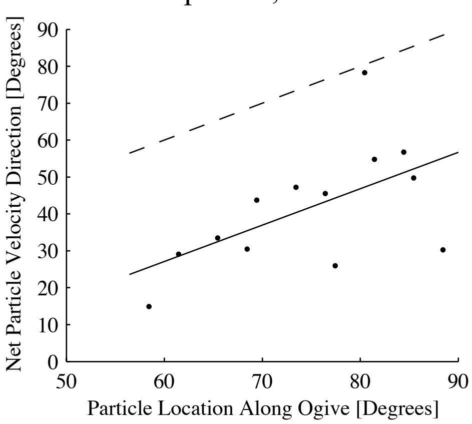

Time Step: 0.94-ms, Depth: -0.4-m,
Slope: 1.0, Int: -32.1

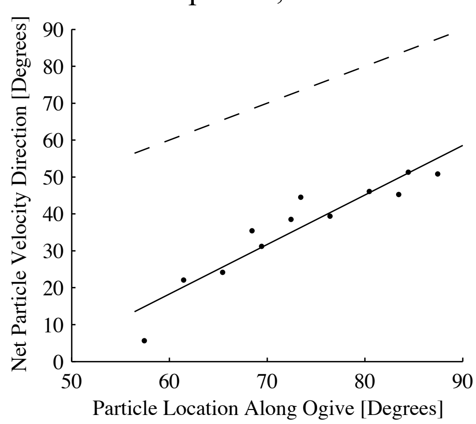

Time Step: 1.24-ms, Depth: -0.5-m,
Slope: 1.3, Int: -62.2

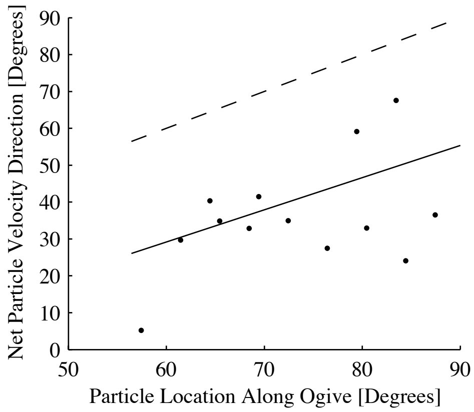

Time Step: 1.28-ms, Veloc: 300-m/s,
Slope: 0.9, Int: -23.2

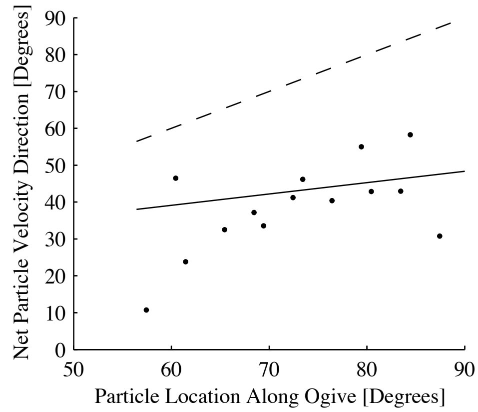

Time Step: 1.61-ms, Depth: -0.6-m,
Slope: 0.3, Int: 20.7

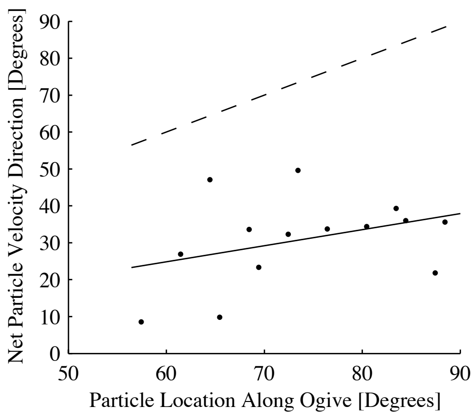

Time Step: 1.93-ms, Veloc: 200-m/s,
Slope: 0.4, Int: -1.3

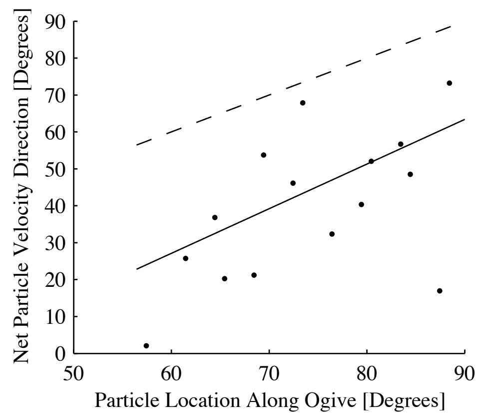

Time Step: 2.11-ms, Depth: -0.7-m,
Slope: 1.2, Int: -45.4

Time Step: 2.52-ms, Ve

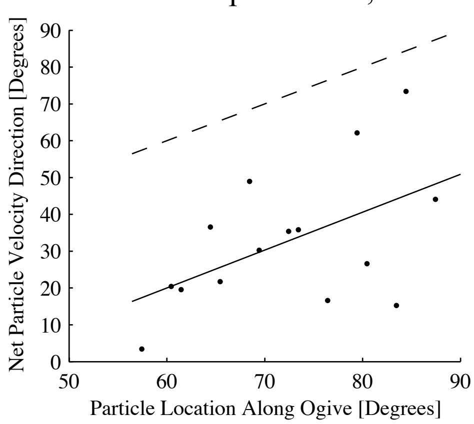

loc:
100-m/s, Slope: 1.0, Int: -41.7

Figure 120. Data Set 3, 475-m/s Striking Velocity, 39-MPa Concrte, 76.2-mm, 3-CRH Projectile

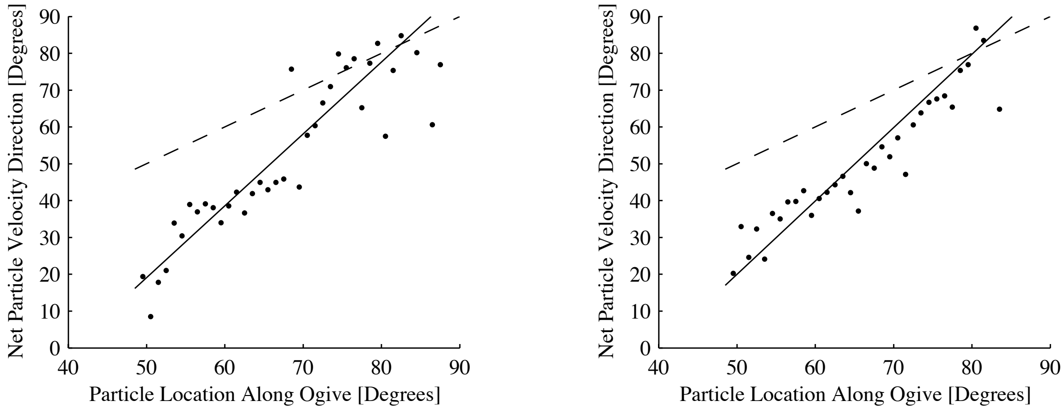

Time Step: 0.56-ms, Veloc: -100-m/s, Slope: 2.0, Int: -78.6

Time Step: 0.67-ms, Depth: -0.10-m, Slope: 2.0, Int: -79.7

Figure 121. Data Set 5, 200-m/s Striking Velocity, 36-MPa Concrte, 26.9-mm, 2-CRH Projectile

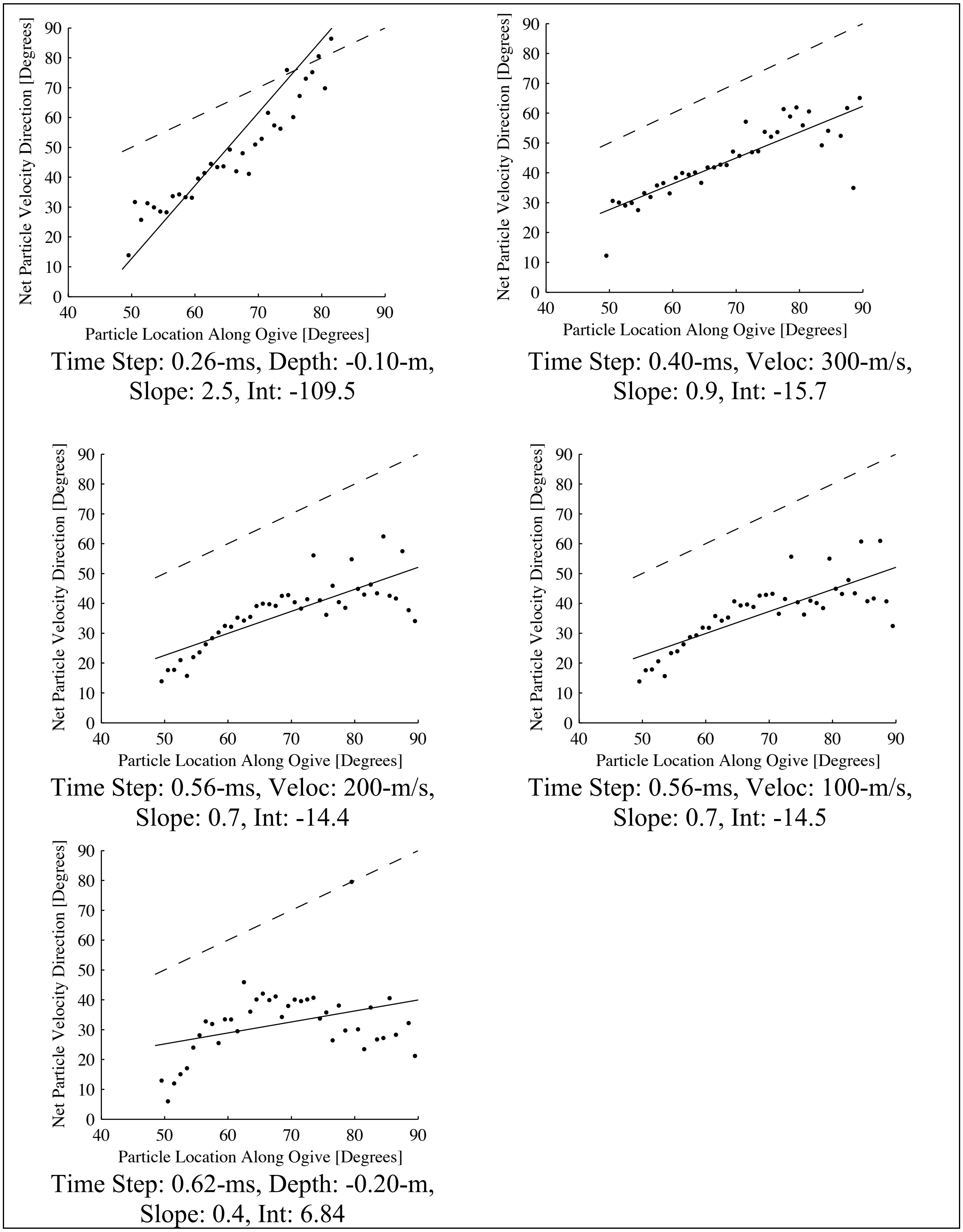

Time Step: 0.26-ms, Depth: -0.10-m, Slope: 2.5, Int: -109.5

Time Step: 0.40-ms, Veloc: 300-m/s, Slope: 0.9, Int: -15.7

Time Step: 0.56-ms, Veloc: 200-m/s, Slope: 0.7, Int: -14.4

Time Step: 0.56-ms, Veloc: 100-m/s, Slope: 0.7, Int: -14.5

Time Step: 0.62-ms, Depth: -0.20-m, Slope: 0.4, Int: 6.84

Figure 122. Data Set 5, 400-m/s Striking Velocity, 36-MPa Concrte, 26.9-mm, 2-CRH Projectile.

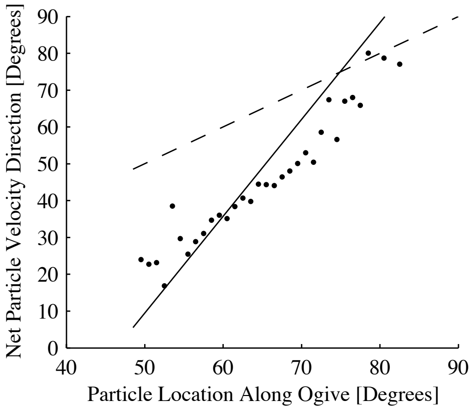

Time Step: 0.17-ms, Depth: -0.10-m,
Slope: 2.6, Int: -122.1

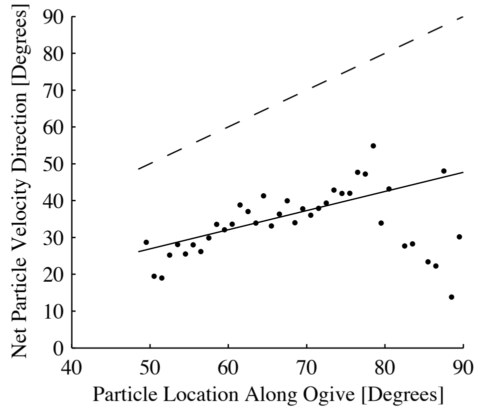

Time Step: 0.33-ms, Veloc: 500-m/s,
Slope: 0.5, Int: 0.9

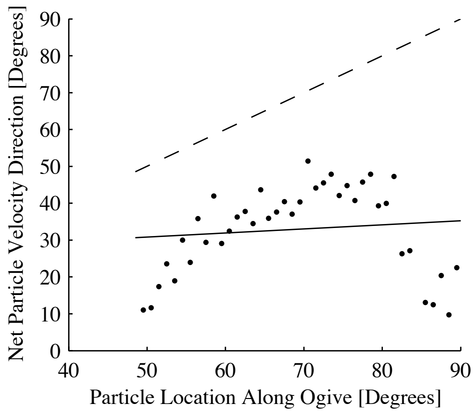

Time Step: 0.34-ms, Depth: -0.2-m,
Slope: 0.1, Int: 25.3

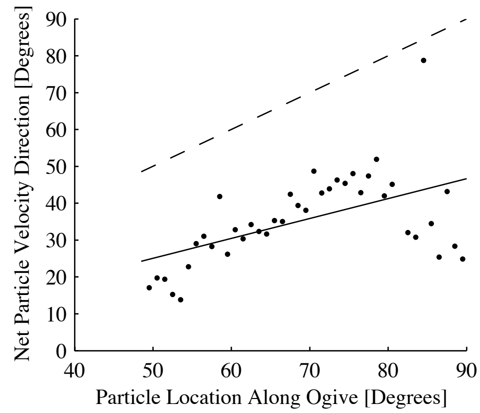

Time Step: 0.55-ms, Depth: -0.3-m,
Slope: 0.5, Int: -1.9

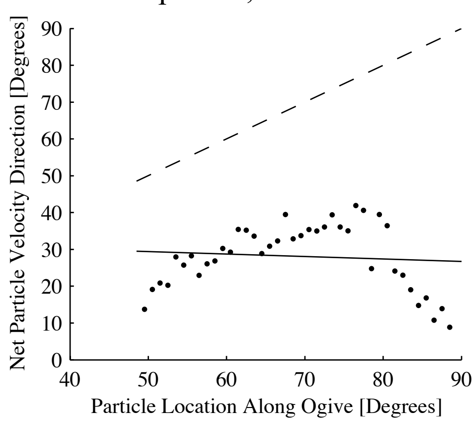

Time Step: 0.59-ms, Veloc: 400-m/s,
Slope: -0.1, Int: 32.8

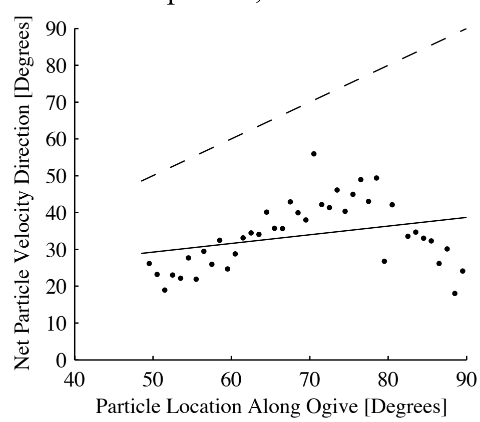

Time Step: 0.82-ms, Depth: -0.4-m,
Slope: 0.2, Int: 17.5

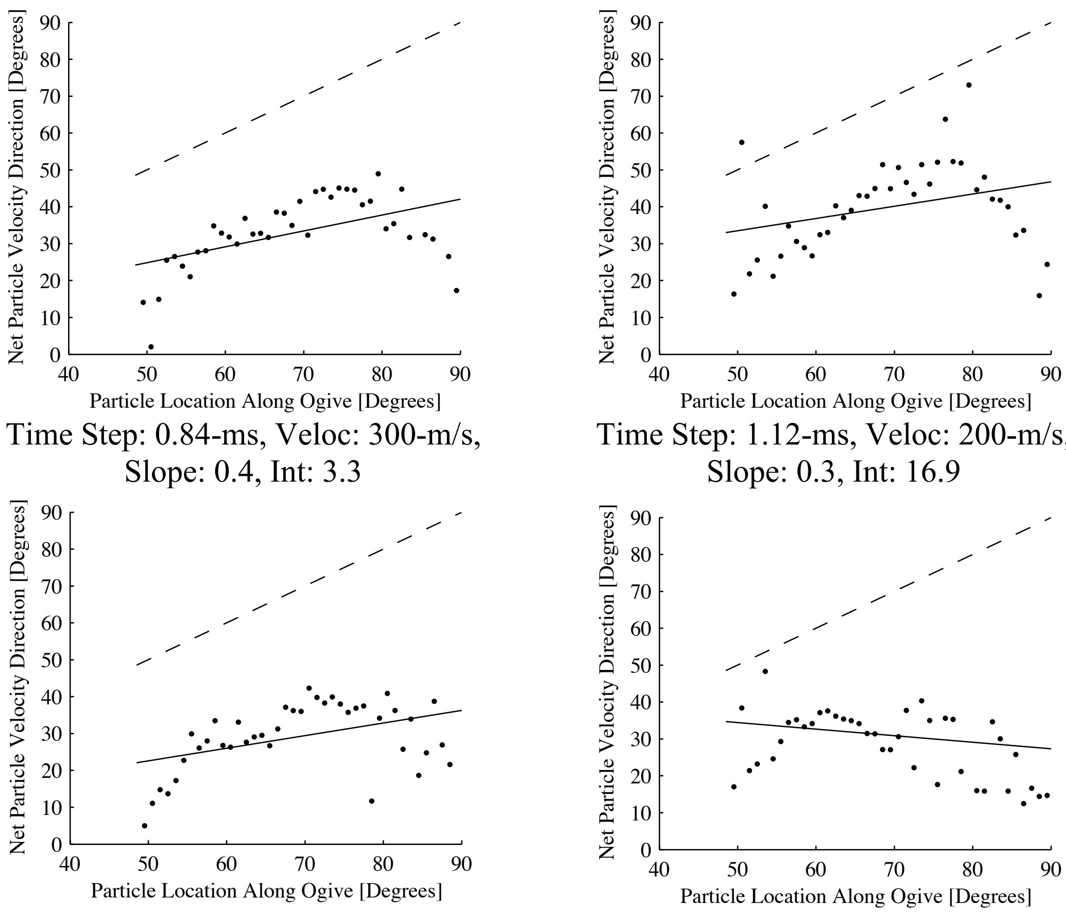

Time Step: 0.84-ms, Veloc: 300-m/s,
Slope: 0.4, Int: 3.3

Time Step: 1.12-ms, Veloc: 200-m/s,
Slope: 0.3, Int: 16.9

Time Step: 1.13-ms, Depth: -0.5-m,
Slope: 0.3, Int: 5.4

Time Step: 1.41-ms, Veloc: 100-m/s,
Slope: -0.2, Int: 43.3

Figure 123. Data Set 5, 600-m/s Striking Velocity, 36-MPa Concrte, 26.9-mm, 2-CRH Projectile

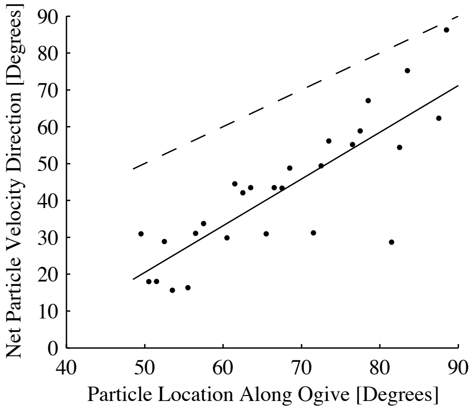

Time Step: 0.12-ms, Depth: -0.10-m,
Slope: 1.3, Int: -43.0

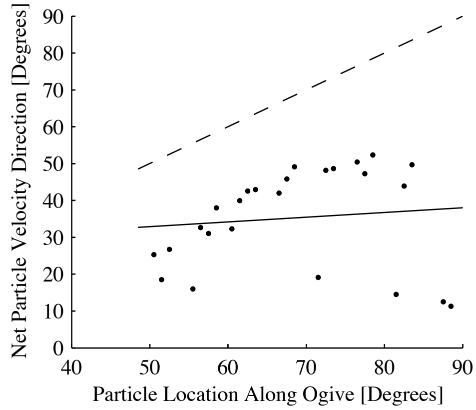

Time Step: 0.17-ms, Veloc: 700-m/s,
Slope: 0.1, Int: 26.5

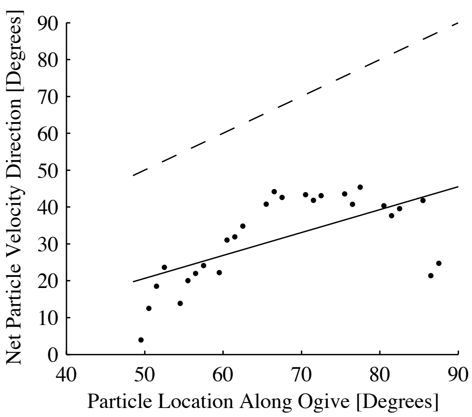

Time Step: 0.22-ms, Depth: -0.2-m,
Slope: 0.6, Int: -10.5

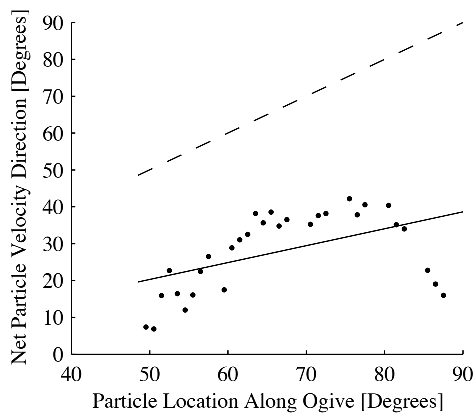

Time Step: 0.36-ms, Depth: -0.3-m,
Slope: 0.5, Int: -2.6

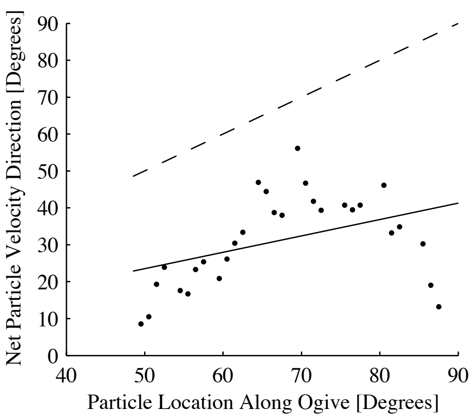

Time Step: 0.38-ms, Veloc: 600-m/s,
Slope: 0.4, Int: 1.4

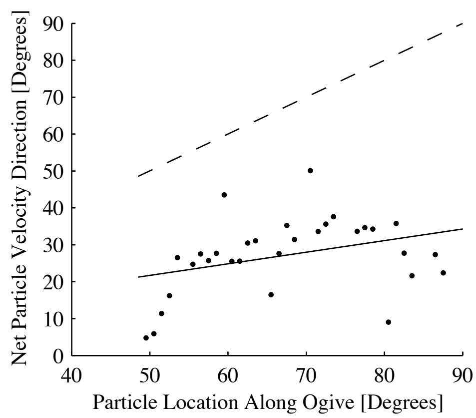

Time Step: 0.51-ms, Veloc: 500-m/s,
Slope: 0.3, Int: 6.0

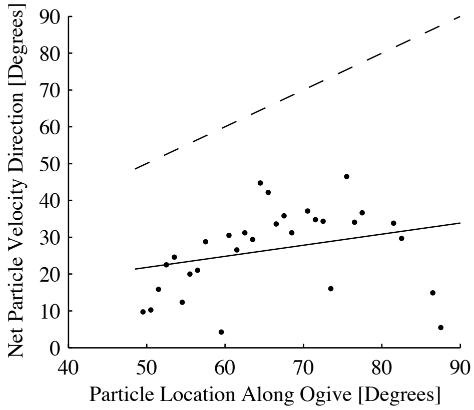

Time Step: 0.52-ms, Depth: -0.4-m,
Slope: 0.3, Int: 6.7

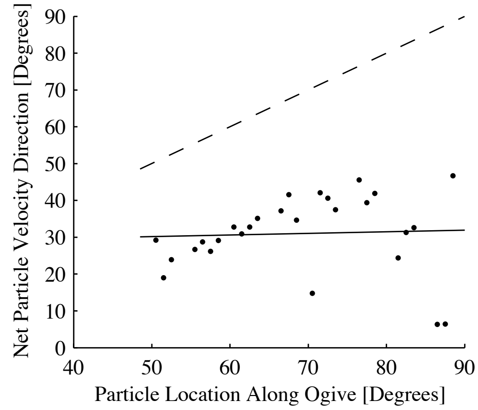

Time Step: 0.60-ms, Veloc: 400-m/s,
Slope: 0.0, Int: 28.0

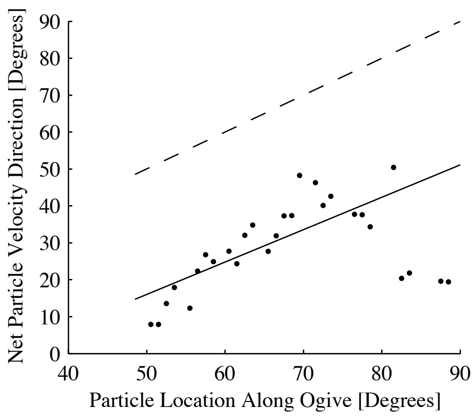

Time Step: 0.70-ms, Depth: -0.5-m,
Slope: 0.9, Int: -28.0

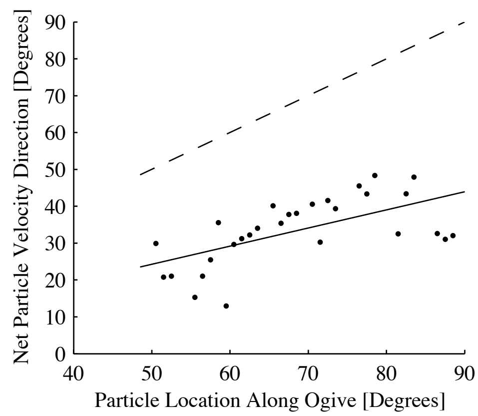

Time Step: 0.91-ms, Depth: -0.6-m,
Slope: 0.5, Int: -0.3

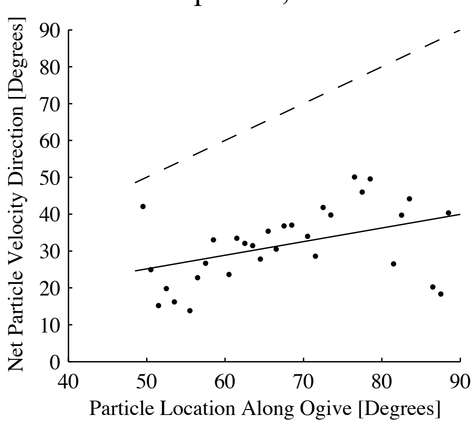

Time Step: 1.15-ms, Depth: -0.7-m,
Slope: 0.4, Int: 6.6

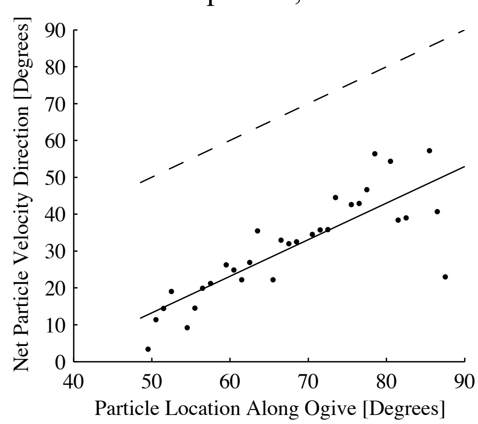

Time Step: 1.22-ms, Veloc: 300-m/s,
Slope: 1.0, Int: -36.5

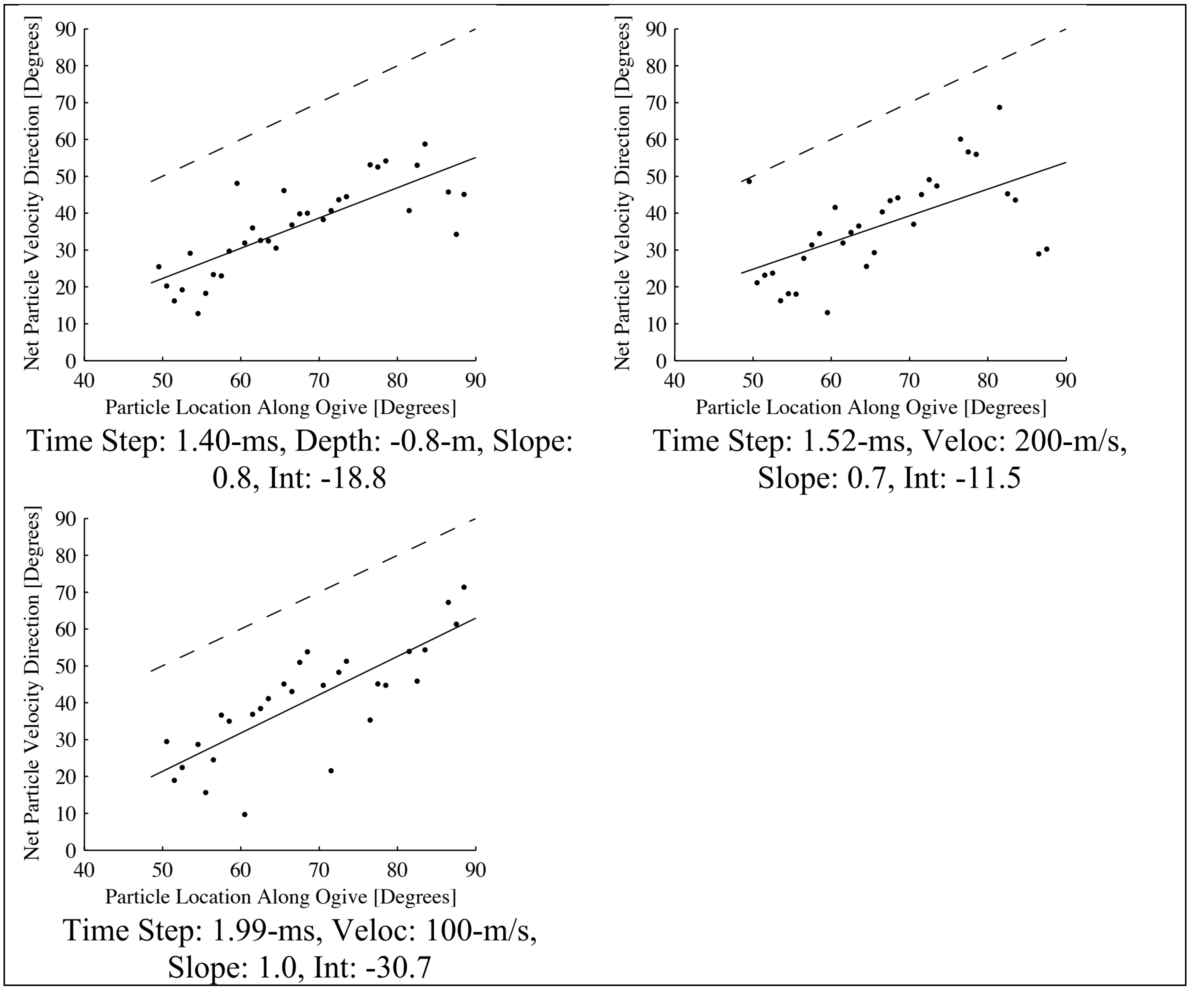

Time Step: 1.40-ms, Depth: -0.8-m, Slope: 0.8, Int: -18.8

Time Step: 1.52-ms, Veloc: 200-m/s, Slope: 0.7, Int: -11.5

Time Step: 1.99-ms, Veloc: 100-m/s, Slope: 1.0, Int: -30.7

Figure 124. Data Set 5, 800-m/s Striking Velocity, 36-MPa Concrte, 26.9-mm, 2-CRH Projectile

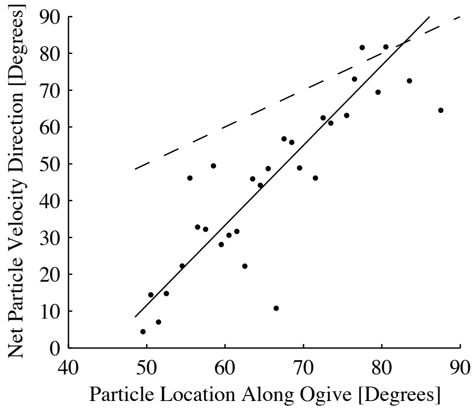

Time Step: 0.34-ms, Veloc: 100-m/s,
Slope: 2.2, Int: -97.0

Figure 125. Data Set 7, 200-m/s Striking Velocity, 157-MPa Concrte, 26.9-mm, 2-CRH Projectile

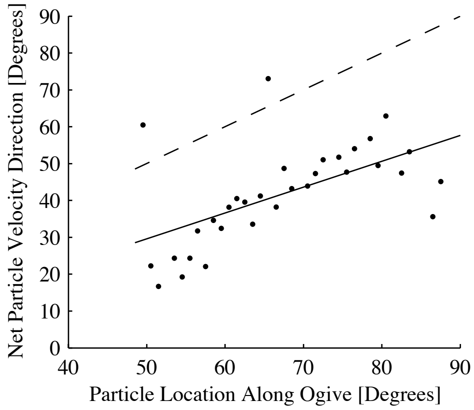

Time Step: 0.25-ms, Veloc: 300-m/s,
Slope: 0.7, Int: -5.5

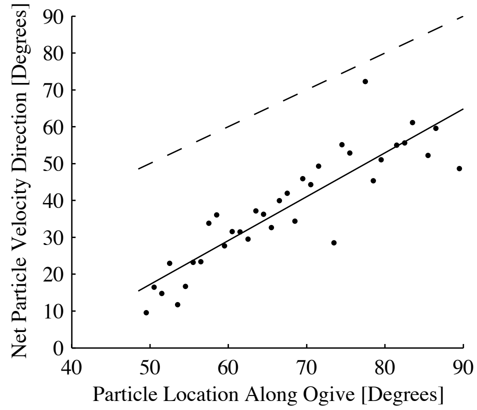

Time Step: 0.29-ms, Depth: -0.10-m,
Slope: 1.2, Int: -42.2

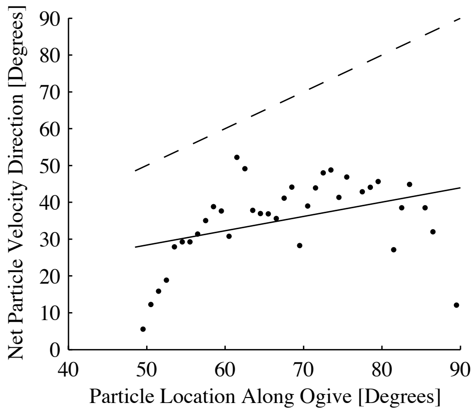

Time Step: 0.40-ms, Veloc: 200-m/s,
Slope: 0.4, Int: 8.9

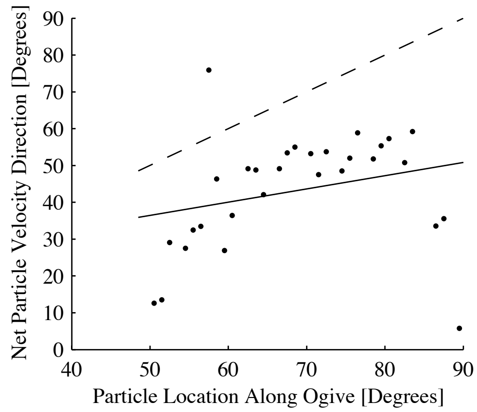

Time Step: 0.56-ms, Veloc: 100-m/s,
Slope: 0.4, Int: 18.5

Figure 126. Data Set 7, 400-m/s Striking Velocity, 157-MPa Concrte, 26.9-mm, 2-CRH Projectile

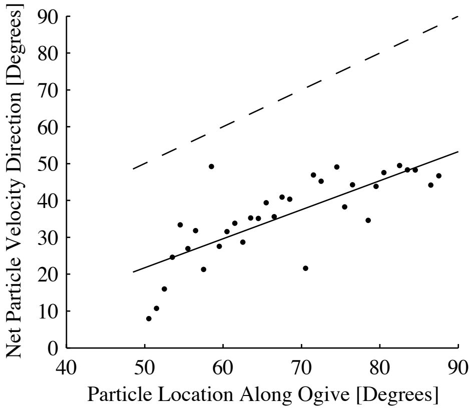

Time Step: 0.18-ms, Depth: -0.1-m,
Slope: 0.8, Int: -17.7

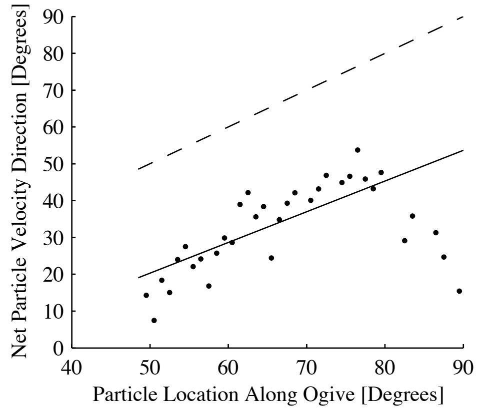

Time Step: 0.19-ms, Veloc: -500-m/s,
Slope: 0.8, Int: -21.4

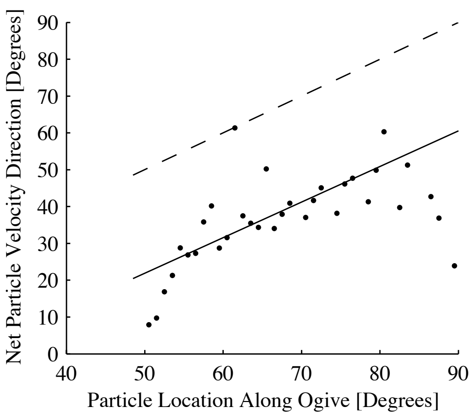

Time Step: 0.34-ms, Veloc: -400-m/s,
Slope: 1.0, Int: -26.4

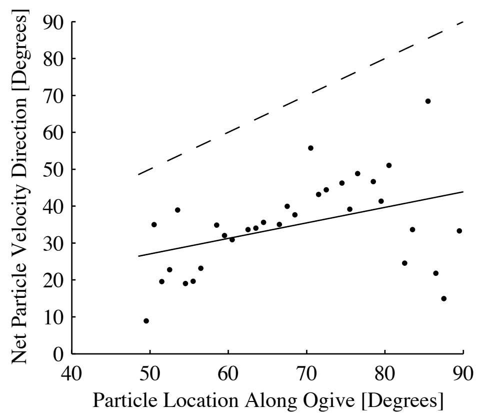

Time Step: 0.41-ms, Depth: -0.2-m,
Slope: 0.4, Int: 6.02

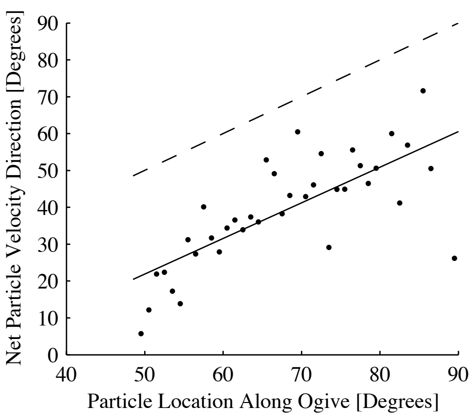

Time Step: 0.47-ms, Veloc: -300-m/s,
Slope: 1.0, Int: -26.5

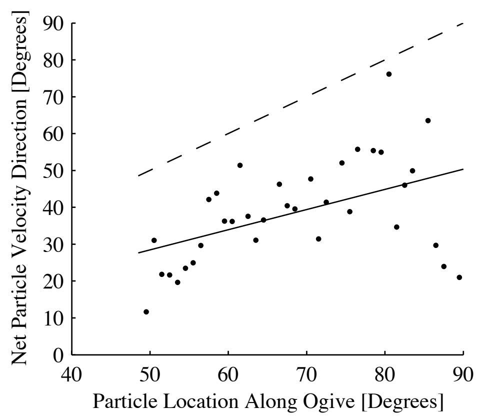

Time Step: 0.62-ms, Veloc: -200-m/s,
Slope: 0.6, Int: 1.1

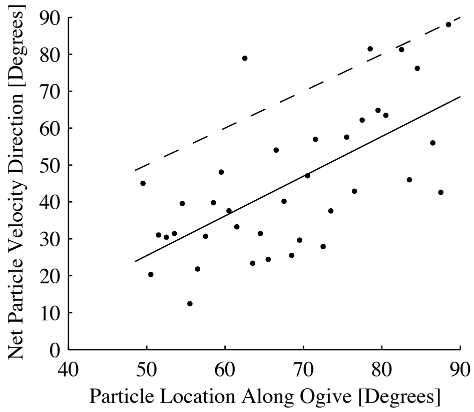

Time Step: 0.78-ms, Veloc: -100-m/s,
Slope: 1.1, Int: -28.4

Figure 127. Data Set 7, 600-m/s Striking Velocity, 157-MPa Concrte, 26.9-mm, 2-CRH Projectile

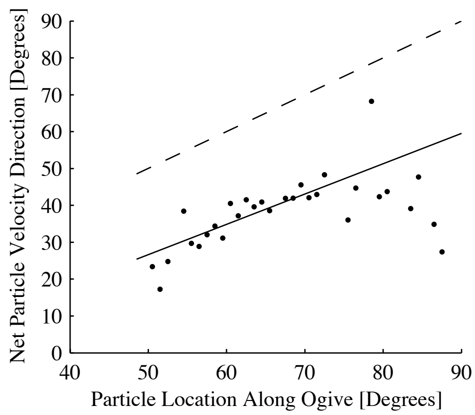

Time Step: 0.13-ms, Depth: -0.10-m,
Slope: 0.8, Int: -14.5

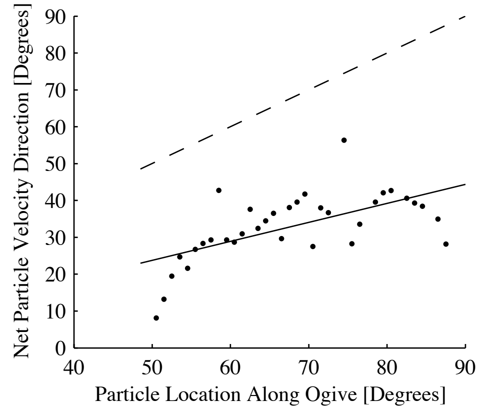

Time Step: 0.16-ms, Veloc: -700-m/s,
Slope: 0.5, Int: -2.0

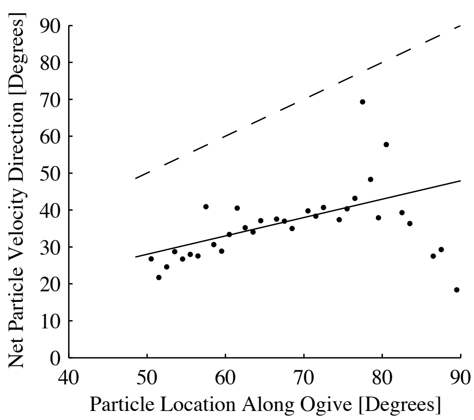

Time Step: 0.28-ms, Veloc: -600-m/s,
Slope: 0.5, Int: 3.2

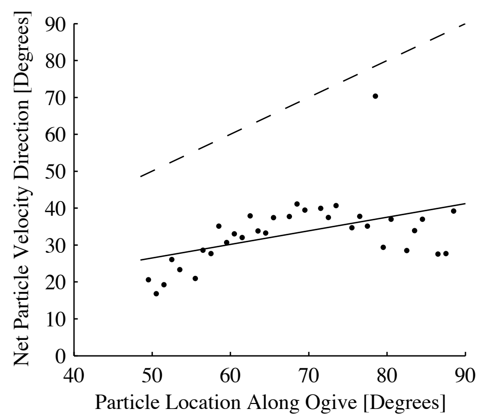

Time Step: 0.28-ms, Depth: -0.2-m,
Slope: 0.4, Int: 8.0

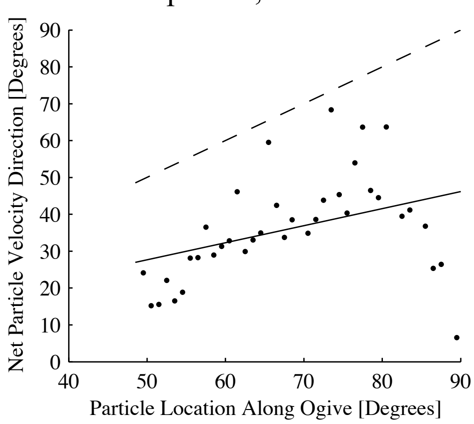

Time Step: 0.42-ms, Veloc: -500-m/s,
Slope: 0.5, Int: 4.6

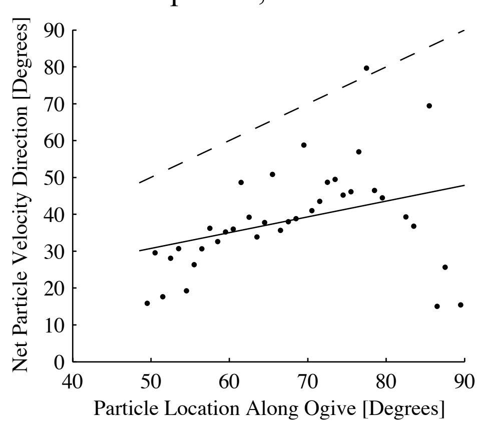

Time Step: 0.45-ms, Depth: -0.3-m,
Slope: 0.4 Int: 9.3

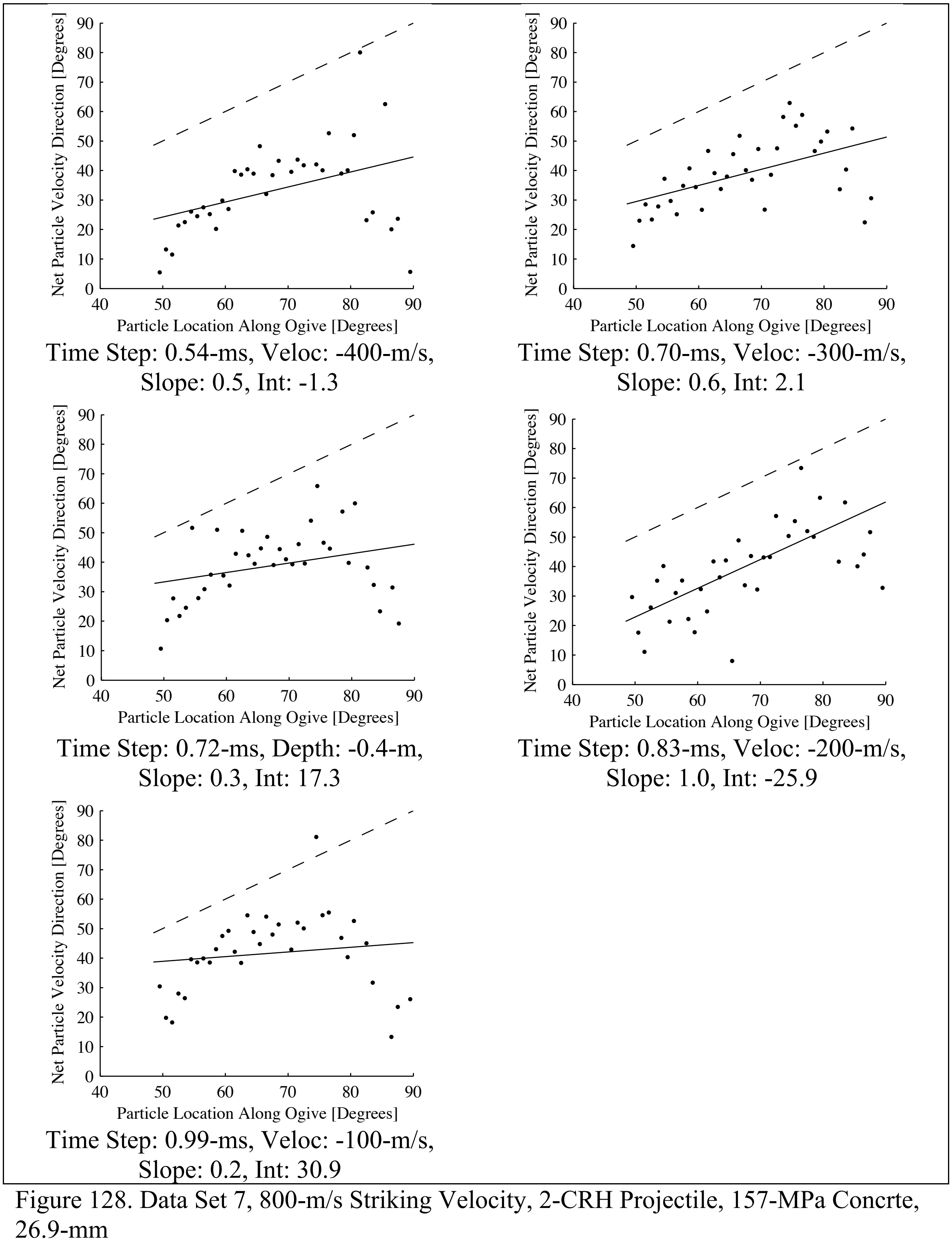

Time Step: 0.54-ms, Veloc: -400-m/s,
Slope: 0.5, Int: -1.3

Time Step: 0.70-ms, Veloc: -300-m/s,
Slope: 0.6, Int: 2.1

Time Step: 0.72-ms, Depth: -0.4-m,
Slope: 0.3, Int: 17.3

Time Step: 0.83-ms, Veloc: -200-m/s,
Slope: 1.0, Int: -25.9

Time Step: 0.99-ms, Veloc: -100-m/s,
Slope: 0.2, Int: 30.9

Figure 128. Data Set 7, 800-m/s Striking Velocity, 2-CRH Projectile, 157-MPa Concrte, 26.9-mm

APPENDIX 7: MATLAB CODE - NORMAL EXPANSION COMPARISON METHODOLGY (NECM)

```
% Normal Expansion Comparison Methodology (NECM)
% For Meshless Particles

for shll=1:1                    %Allows for concentric shells
runname = 'Run_List.txt';       %FILE WITH LIST OF DATA FILES
Flist = importdata(runname);    %Reads file names into struct Flist
Fsize=size(Flist);              %Counts the number of files
NumInputFiles=Fsize(1);         %Number of data files

fname1 = sprintf('Outfile-%d',shll); %Opens an Output File
fid1 = fopen(fname1, 'w');      %File is writeable

for loop=1:NumInputFiles        %Performs analysis on all files on list
%for loop=3:3

filename = Flist{loop};         %Id's the data file to be plotted
uplim = 80;                     %90 typical; 80 avoids bilinear data
type = 2;                       %INPUT VALUE (CRH 2, 3, or 6)

if (type > 1.5)&(type < 2.5)
  noselength=0.0356;            %Geometry Specs for small projectile
  Rogive=0.0536;
  Rproj=0.01345;
end
if (type > 2.5)&(type < 5.5)
  noselength=0.126;             %Geometry Specs for large 3-crh projectile
  Rogive=0.2286;
  Rproj=0.0381;
end
if (type > 5.5)
  noselength=0.183;             %Geometry Specs for large 6-crh projectile
  Rogive=0.4572;
  Rproj=0.0381;
end
```

```
thetanot=180/pi*asin((Rogive-Rproj)/Rogive);


h=Rogive-Rproj;           %Distance from z axis to ogive origin
fid = fopen(filename);     %Opens the nth file

InputText=textscan(fid,'%s',13,'delimiter','\n');  %USER INPUT VALUE
Intro=InputText{1};                              %Reads header info
Str = [Intro{10}];                %Grabs the 10th line of header info
Str(strfind(Str, '=')) = [];        %Extracts the number of particles from
Key   = 'I';                     %the header string following the
Index = strfind(Str, Key);          % "I" string
numpoints = sscanf(Str(Index(1) + length(Key):end), '%g', 1); %No. of parts

Str = [Intro{9}];                  %Grabs the 9th line of header info
Str(strfind(Str, '=')) = [];        %Extracts the time-step from
Key   = 'SOLUTIONTIME';             %the header string following the
Index = strfind(Str, Key);          %"SOLUTIONTIME' string
stime = sscanf(Str(Index(1) + length(Key):end), '%g', 1);


A=textscan(fid,'%f %f %f %f %f %f',numpoints,...
                    'delimiter','\n');  %READS data into a
                                    %6 by numpoints struct, A

fclose(fid);                              %and closes the data file

B(numpoints,7)=0;       %Initializes a 7 by numpoints matrix B

  for k=1:6
     B(:,k)=A{1,k}(:); % Places data in matrix B
  end

clearvars A;            % Throws out struct A; So all data is in B

j=1;
for i=1:numpoints
   B(i,7)=sqrt(B(i,1)^2+B(i,2)^2);  %  Puts Rz into B7
end

Zmin=min(B(:,3));       %finds the min value of B(3). This is ~ Z min
                 %of the projectile

shoulder=Zmin+noselength; %calculates the location of the shoulder
```

```
D(numpoints,7) = 0;     %initializes D

j=1;
for i=1:numpoints
   if (B(i,3) < shoulder)

       D(j,:)=B(i,:);  %strips away particles above the shoulder
                   %and places remaining particles in matrix D
      j=j+1;
   end
end

numpoints=j-1;           %this is the new reduced number of points

totvel(numpoints) = 0;
Vr(numpoints) = 0;
R(numpoints,4) = 0;        %Initiallizes matrices to used next
Rtheta(numpoints) = 0;
O(numpoints,3)=0;

for i=1:numpoints
   O(i,1)=-h*D(i,1)/D(i,7);   %Cal x ord of ogive origin
   O(i,2)=-h*D(i,2)/D(i,7);   %Cal y ord of ogive origin
   O(i,3)=shoulder;           %Cal z ord of ogive origin

   totvel(i)=sqrt(D(i,4)*D(i,4)+D(i,5)*D(i,5)+D(i,6)*D(i,6));
   DirCos(i)=180-180/pi*acos(D(i,6)/totvel(i));%Calcs the direction cos
   Vr(i)=sqrt(D(i,4)*D(i,4)+D(i,5)*D(i,5));%Cals radial vel

   R(i,1)=D(i,1)-O(i,1);              %For each node
   R(i,2)=D(i,2)-O(i,2);              %Calculates the position vectors
   R(i,3)=D(i,3)-O(i,3);              %w/ origin at the ogive center

   R(i,4)=sqrt(R(i,1)*R(i,1)+R(i,2)*R(i,2)+...
                  R(i,3)*R(i,3)); %Calcs magnitude of R

   Rtheta(i)=180-180/pi*(acos(R(i,3)/R(i,4)));%Calcs direction of R

end
E(numpoints,7) = 0; %Initializes matrix E
j=1;
for i=1:numpoints
```

```
    if (R(i,4)<Rogive+(shll)*0.004)&(R(i,4)>Rogive+(shll-1)*0.004)...
        &(Rtheta(i)<uplim)%sets boundary for nodes to keep
                 %within .007mm shell and under theta R = uplim

    %if (R(i,4)<Rogive+(shll)*0.004)&(R(i,4)>Rogive+(shll-1)*0.004)
        %sets boundary for nodes to keep
        %within .004mm shell does not account for bilinear

      for k=1:7
        E(j,k)=D(i,k);  %strips away particles leaving shell of points
      end             %and places it in matrix E

      Vr2(j)=Vr(i);    % along surface of the particle boundary
      Rtheta2(j)=Rtheta(i);
      DirCos2(j)=DirCos(i);  %kept separate from E to avoid confusion
      totvel2(j)=totvel(i);  %matrix sized reduced to just shell
      j=j+1;
   end
end
numpoints=j-1;              %this is the new number of particles

F(numpoints,7) = 0;
Vr3(numpoints)=0;
Rtheta3(numpoints)=0;
Dircos3(numpoints)=0;  %Initial new set of matrices
totvel3(numpoints)=0;
Vnorm(numpoints)=0;

for i=1:numpoints
   for j=1:7
      F(i,j)=E(i,j);  %makes a duplicate matrix
   end
      Vr3(i)=Vr2(i);    % along surface of the particle boundary
      Rtheta3(i)=Rtheta2(i);
      DirCos3(i)=DirCos2(i);
      totvel3(i)=totvel2(i);
      Vnorm(i)=totvel3(i)*cos(pi/180*(Rtheta3(i)-DirCos3(i)));
end

myfit2=polyfit(Rtheta3,DirCos3,1);  %lin fit for unbin DirCos data
linfit2(1)=myfit2(1)*thetanot+myfit2(2);
linfit2(2)=myfit2(1)*uplim+myfit2(2);

myfit3=polyfit(Rtheta3,Vnorm,1);  %linfit  for the Vnorm Data
```

```
linfit3(1)=myfit3(1)*thetanot+myfit3(2);
linfit3(2)=myfit3(1)*uplim+myfit3(2);


%END OF CALCS:  Matrix F has partices and XX3 has calc'ed numbers


%ORIGIN AND THE SHELL OF PARTICLES
on = 1;  %turn on or off (0 is off 1 is on)
%----------------------------------------------------------------------
if (on > 0.5)
   figure('Name', sprintf('Particle Shell - Time Step: %f Shell:%d',...
                                        stime,shll));
   hold on;
      scatter3(O(:,1),O(:,2),O(:,3));
      scatter3(F(:,1),F(:,2),F(:,3),'.');
   hold off;
end
%----------------------------------------------------------------------

%DirCos VS Rtheta
on = 1;  %turn on or off (0 is off 1 is on)
%----------------------------------------------------------------------
if (on > 0.5)
   figure('Name', sprintf('DIRCOS - Time Step: %f  Shell:%d',...
                                        stime,shll));
   hold on;
      scatter(Rtheta3,DirCos3,'.','red');
      plot([thetanot,uplim],linfit2,'black');
   hold off;
end
%----------------------------------------------------------------------


%MAGNITUDE OF NORMAL VELOCITY VECTORS VS Rtheta
on = 1;  %turn on or off (0 is off 1 is on)
%----------------------------------------------------------------------
if (on > 0.5)
     figure('Name', sprintf('Norm Vel - Time Step: %f  Shell:%d',...
                                        stime,shll));
   hold on;
     scatter(Rtheta3,Vnorm,'.');
     plot([thetanot,uplim],linfit3,'black');
   hold off;
```

```
end
%----------------------------------------------------------------------

Vx = F(:,4);
Vy = F(:,5);
Vz = F(:,6);

numBins = uplim-thetanot; % define number of bins
binEdges = linspace(thetanot, uplim, numBins+1);
for i =1:numBins
  axis(i)=i+thetanot;
end

[H,whichBin] = histc(Rtheta2, binEdges);

for i = 1:numBins
    flagBinMembers = (whichBin == i);
    binMembers4     = Vx(flagBinMembers);  %Puts values of E into bins
    binMembers5     = Vy(flagBinMembers);
    binMembers6     = Vz(flagBinMembers);

    binSum4(i)     = nansum(binMembers4);
    binSum5(i)     = nansum(binMembers5);
    binSum6(i)     = nansum(binMembers6);

end
for i=1:numBins

    binSumVt(i)=sqrt(binSum4(i)*binSum4(i)+binSum5(i)*binSum5(i)+...
                                      binSum6(i)*binSum6(i));
    binTheta(i)=180-180/pi*acos(binSum6(i)/(binSumVt(i)+0.000000001));

    if (sqrt(binSum6(i)*binSum6(i)) < 0.00000001)
        binTheta(i) = NaN;
    end

end


    validdata = ~isnan(binTheta);
    keep2 = binTheta(validdata);
    keep1 = axis(validdata);
```

```
    myfit=polyfit(keep1(:),keep2(:),1);
    linfit(1)=myfit(1)*thetanot+myfit(2);
    linfit(2)=myfit(1)*uplim+myfit(2);

%Binned NET DIRCOS vs Binned Rtheta
on = 1;  %turn on or off (0 is off 1 is on)
%--------------------------------------------------------------------
if (on > 0.5)


figure('Name', sprintf('Binned - Time Step: %f  Shell:%d',stime,shll),...
                                                    'Color','w');

hold on;
    %title('Net DirCos vs Binned Rtheta','FontSize',12);

    xlabel('Particle Location Along Ogive [Degrees]','FontSize',12);
    ylabel('Net Particle Velocity Direction [Degrees]','FontSize',12);

    scatter(axis,binTheta,'.','black');

    x=[thetanot,uplim];
    y=x;
    plot(x,y,'--','color','black');

    plot([thetanot,uplim],linfit,'black');
    set(0,'DefaultAxesFontName', 'Times New Roman');
    set(0,'DefaultTextFontname', 'Times New Roman');

    set(gca,'OuterPosition',[0.1 0.1 0.9 0.9]);
    xlim=get(gca,'XLim');
    ylim=get(gca,'YLim');

hold off;

end
%--------------------------------------------------------------------
    outtext1 = [sprintf('Time Step: %f-ms',stime*1000)];
    outtext2 = [sprintf('Zmin: %3.2f-m',Zmin)];


%SELECT OUTPUT
OUT = 3;  % (1 is UNBINNED; 2 IS NORMAL; 3 IS BINNED)
%--------------------------------------------------------------------
```

```
if (OUT<1.5)
    outtext3 = [sprintf('Slope: %3.2f',myfit2(1))];%UNBINNED OUTPUT
    outtext4 = [sprintf('Int: %3.2f',myfit2(2))];
end
if (OUT>1.5)&(OUT<2.5)
    outtext3 = [sprintf('Slope: %3.2f',myfit3(1))];%NORMAL OUTPUT
    outtext4 = [sprintf('Int: %3.2f',myfit3(2))];
end
if (OUT>2.5)
    outtext3 = [sprintf('Slope: %3.2f',myfit(1))];%BINNED OUTPUT
    outtext4 = [sprintf('Int: %3.2f',myfit(2))];
end

fprintf(fid1, '%s\t %s\t %s\t %s\n', outtext1,outtext2,outtext3,outtext4);

clearvars -except Flist loop NumInputFiles fname fid1 shll;
hgsave(sprintf('Figure%d-%d',shll,loop));
end

fclose(fid1);


clearvars -except shll;
end
clearvars;
```

APPENDIX 8: MATLAB CODE - SPHERICAL EXPANSION COMPARISON METHODOLOGY (SECM)

```
%Spherical Expansion Comparison Methodology (SECM)
%For analysis of NODES

for inc=0:0  %Allows the spherical origin to be moved up in increments
for shll=1:1 %Allows for multiple concentric shells
runname = 'Run_List.txt';      %List of data files to be plotted
Flist = importdata(runname);   %Reads list of data file names into Flist
Fsize=size(Flist);             %Determines number of files in list
NumInputFiles=Fsize(1);        %Number of data files
fname = sprintf('Outfile%d',shll);  %Name for output file
fid1 = fopen(fname, 'w');           %Opens output file
for loop=1:NumInputFiles   %For each input file, do the following...
filename = Flist{loop};    %Id's the name of the data file to be plotted
type= -1;                  %Input Value (-1 small  or +1 large)
if (type < 0)
  noselength=0.0356;        %Geometry Specs for small projectile
  Rogive=0.0538;
  Rproj=0.01345;
end
if (type > 0)
  noselength=0.126;         %Geometry Specs for large projectile
  Rogive=0.2286;
  Rproj=0.0381;
end
h=Rogive-Rproj;            %Calculate distance from z axis to ogive origin
fid = fopen(filename);     %Open input file
InputText=textscan(fid,'%s',13,'delimiter','\n');  %INPUT VALUE
Intro=InputText{1};                    %Reads header info
Str = [Intro{10}];                     %Number of nodes
Str(strfind(Str, '=')) = [];           %Extracts the number of nodes from
Key   = 'Nodes';                       %the header string following the
Index = strfind(Str, Key);             %nodes string
numpoints = sscanf(Str(Index(1) + length(Key):end), '%g', 1);
Str = [Intro{9}];
```

```
Str(strfind(Str, '=')) = [];           %Extracts the solutiontime from
Key   = 'SOLUTIONTIME';                %the header string following the
Index = strfind(Str, Key);             %time step string
xyc1 = sscanf(Str(Index(1) + length(Key):end), '%g', 1);
A=textscan(fid,'%f %f %f %f %f %f',numpoints,'delimiter','\n');
                                 %READS data into a
                                 %6 by numpoints matrix, A
fclose(fid);              %closes the input file
B(numpoints,7)=0;          %Initializes matrix B
  for k=1:6
     B(:,k)=A{1,k}(:); % Places data in matrix B from A
  end
clearvars A;           % Deletes the A matrix
j=1;
for i=1:numpoints
   B(i,7)=sqrt(B(i,1)^2+B(i,2)^2);  %Cals Rz and places into B7
   if (B(i,7)<0.001)
         C(j)=B(i,3);  %Looks at elements very close to z axis
         j=j+1;       %and places data in matrix C.
   end
end
Zmin=max(C);             %finds the mazimum value of C.  This is ~ Z min
                    %of the projectile
shoulder=Zmin+noselength; %calculates the location of the shoulder
Ox=0;                  %id's the spherical origin
Oy=0;
Oz=Zmin+(Rproj+((inc-1)*0.002));     %sets origin at Rproj above Zmin
D(numpoints,7) = 0;                %Inititalizes matrix D2
j=1;
for i=1:numpoints
   if (B(i,3) < Oz)
        D(j,:)=B(i,:);  %strips away nodes above the origin
                  %and places remaining data in matrix D2
       j=j+1;
   end
end
numpoints=j-1;             %number of points below origin
totvel(numpoints) = 0;      %initializes matrix
Vr(numpoints) = 0;         %initializes matrix
R(numpoints,4) = 0;        %initializes matrix
Rtheta(numpoints) = 0;      %initializes matrix
for i=1:numpoints
   totvel(i)=sqrt(D(i,4)*D(i,4)+D(i,5)*D(i,5)+D(i,6)*D(i,6));
   DirCos(i)=180-180/pi*acos(D(i,6)/totvel(i));
```

```
   Vr(i)=sqrt(D(i,4)*D(i,4)+D(i,5)*D(i,5));%Calcs the position vectors
   R(i,1)=D(i,1)-Ox;             %w/ origin at the ogive center
   R(i,2)=D(i,2)-Oy;             %Also calcs the direction cos of
   R(i,3)=D(i,3)-Oz;             %the vel vector at all points
   R(i,4)=sqrt(R(i,1)*R(i,1)+R(i,2)*R(i,2)+R(i,3)*R(i,3));%Distance to
   Rtheta(i)=180-180/pi*(acos(R(i,3)/R(i,4)));          %node and
                                             %direction
end
j=1;
for i=1:numpoints
 if Rtheta(i)<90
  plotx1(j)=Rtheta(i);
  ploty1(j)=DirCos(i);
  j=j+1;
 end
end

figure('Name', sprintf('Node Shell - Time Step: %f  Shell:%d',xyc1,shll));
scatter(plotx1,ploty1,'.');

E(numpoints,7) = 0;
j=1;
for i=1:numpoints
   if (R(i,4)<(Rproj+((inc)*0.002))+(shll)*0.004)& ...   %sets boundary
      (R(i,4)>(Rproj+((inc)*0.002))+(shll-1)*0.004)     %for shell
      for k=1:7
         E(j,k)=D(i,k);  %strips away points leaving thin shell of data
      end               %and places that data into matrix E
      Vr2(j)=Vr(i);
      Rtheta2(j)=Rtheta(i);
      DirCos2(j)=DirCos(i);
      j=j+1;
   end
end
numpoints=j-1;
F(numpoints,7) = 0;
Vr3(numpoints)=0;
Rtheta3(numpoints)=0;
Dircos3(numpoints)=0;
for i=1:numpoints
   for j=1:7
      F(i,j)=E(i,j);
   end
      Vr3(i)=Vr2(i);
```

```
        Rtheta3(i)=Rtheta2(i); %one more time to reduce size of
        DirCos3(i)=DirCos2(i); %matrix to number of point in the shell
end

figure('Name', sprintf('Node Shell - Time Step: %f  Shell:%d',xyc1,shll));
hold on;
scatter3(F(:,1),F(:,2),F(:,3));
scatter3(Ox,Oy,Oz,'.');  %Plot Origin and Nodes in Shell
hold off;
j=1;
for i=1:numpoints
        plotx(j)=Rtheta3(i);
        ploty(j)=DirCos3(i);  %Plot SECM before binning
        j=j+1;
end
figure('Name', sprintf('Node Shell - Time Step: %f  Shell:%d',xyc1,shll));
scatter(plotx,ploty,'.');
Vx = F(:,4);
Vy = F(:,5);
Vz = F(:,6);
numBins = 90; % define number of bins
binEdges = linspace(0, 90, numBins+1);
[H,whichBin] = histc(Rtheta2, binEdges);
for i = 1:numBins
    flagBinMembers = (whichBin == i);
    binMembers4     = Vx(flagBinMembers);  %Puts values of E into bins
    binMembers5     = Vy(flagBinMembers);
    binMembers6     = Vz(flagBinMembers);
    binSum4(i)     = nansum(binMembers4);
    binSum5(i)     = nansum(binMembers5);
    binSum6(i)     = nansum(binMembers6);
end
for i=1:numBins
    binSumVt(i)=sqrt(binSum4(i)*binSum4(i)+ ...
                     binSum5(i)*binSum5(i)+binSum6(i)*binSum6(i));
    binTheta(i)=180-180/pi*acos(binSum6(i)/(binSumVt(i)+0.000000001));
    if (sqrt(binSum6(i)*binSum6(i)) < 0.00000001)
        binTheta(i) = NaN;   %Determine Resultant Vector and Direction
    end
end
for i =1:numBins
    axis(i)=i-1;
end
validdata = ~isnan(binTheta);
```

```
keep2 = binTheta(validdata);
keep1 = axis(validdata);
myfit=polyfit(keep1(:),keep2(:),1);% Determine Linear Fit to Data
set(0,'DefaultAxesFontName', 'Times New Roman');
set(0,'DefaultTextFontname', 'Times New Roman');


figure('Name', sprintf('Time Step: %f-ms  Zmin: %3.2f-m  Slope: %3.2f'...
        'Int: %3.2f',xyc1*1000,Zmin,myfit(1),myfit(2)),'Color','w');
hold on;
xlabel('Node Location Along Sphere [Degrees]','FontSize',12);
ylabel('Net Node Direction [Degrees]','FontSize',12);
scatter(axis,binTheta,'.','black'); %Plot Binned SECM Data
x=[0,90];
y=x;
plot(x,y,'--','color','black');%Plot Spherical Exp. Dashed Line
inter=myfit(2)/(1-myfit(1));
linfit(1)=myfit(1)*0+myfit(2);
linfit(2)=myfit(1)*90+myfit(2);
plot([0,90],linfit,'black'); %Plot Linear Fit of SECM Data
set(gca,'OuterPosition',[0.1 0.1 0.9 0.9]);
xlim=get(gca,'XLim');
ylim=get(gca,'YLim');
eqn = ['y = ' sprintf('%3.2fx - %3.2f',myfit(1),-myfit(2))];
dop = ['Z Min = ' sprintf('%3.2f',Zmin)];
solu = ['Solution Time = ' sprintf('%3.6f', xyc1)];
outtext1 = [sprintf('Time Step: %f-ms',xyc1*1000)];
outtext2 = [sprintf('Zmin: %3.2f-m',Zmin)];
outtext3 = [sprintf('Slope: %3.2f',myfit(1))];  %Create output
outtext4 = [sprintf('Int: %3.2f',myfit(2))];
hgsave(sprintf('Figure%d-%d-%d',shll,loop,inc));
hold off;
fprintf(fid1, '%s\t %s\t %s\t %s\n', outtext1, ...
                    outtext2, outtext3, outtext4);
clearvars -except Flist inc loop NumInputFiles fname fid1 fid2 shll;
end
fclose(fid1);
clearvars -except shll inc;
end
end
clearvars;
```

APPENDIX 9: STREAMTRACES AT VARIOUS CONCRETE STRENGTHS

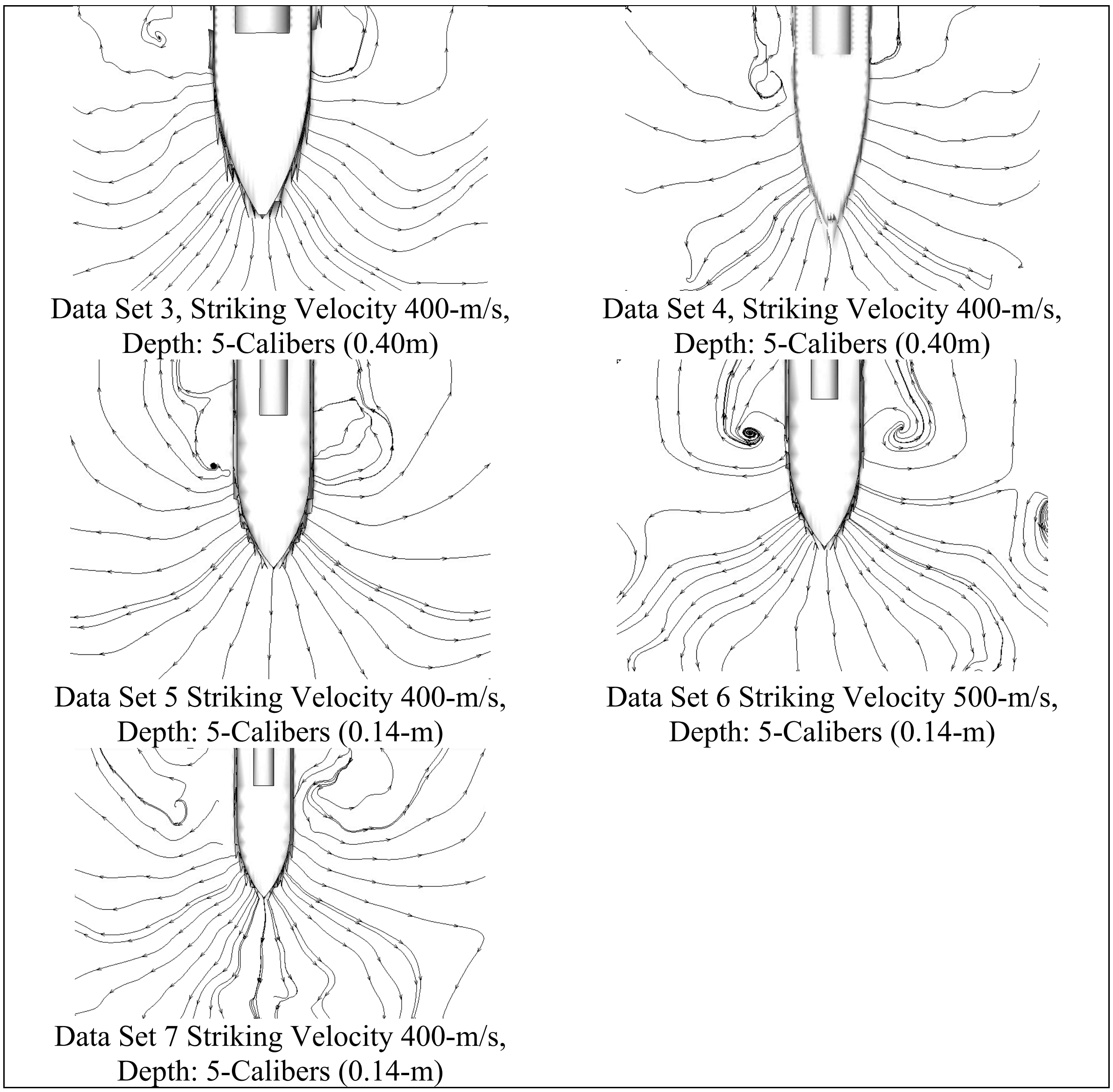

Data Set 3, Striking Velocity 400-m/s, Depth: 5-Calibers (0.40m)

Data Set 4, Striking Velocity 400-m/s, Depth: 5-Calibers (0.40m)

Data Set 5 Striking Velocity 400-m/s, Depth: 5-Calibers (0.14-m)

Data Set 6 Striking Velocity 500-m/s, Depth: 5-Calibers (0.14-m)

Data Set 7 Striking Velocity 400-m/s, Depth: 5-Calibers (0.14-m)

Figure 129. Comparison of Vector Streamtraces at Various Concrete Strengths

APPENDIX 10: EFFECTS OF SOAKERS ON DATA SETS 5 AND 7 PENETRATION DEPTH RESULTS

A soaker is an artificial boundary that has energy absorbing non-reflective characteristics. When a soaker is properly applied to a boundary in the far field, the impact of the soaker on the results of the computations is minimal, but the run time for the problem can be greatly reduced. All calculations in this dissertation use soakers on the sides of the target. The justification for their use is the same as the justification for not removing the metal culverts from the targets. The distance is assumed to be to great to play a significant part of the solution. This Appendix looks at the effects of soakers on the calculated depth of penetration for Data Sets 5 and 7. Data set 5 is based on 36-MPa concrete while data set 7 is based on 157-MPa concrete. Both data sets employ 26.9-mm projectiles and vary the striking velocity from 200 to 800-m/s. Results are summarized in Table 82.

Table 82. Depth of Penetration With and Without Soakers

Data Set	Striking Velocity (m/s)	Depth of Penetration (m)		
		Experiment	Soaker	No Soaker
5	200	0.10	0.11	0.10
	800	0.96	0.85	0.84
7	200	0.07	0.07	0.08
	800	0.51	0.46	0.48

The results of the comparison indicate that the soakers do not introduce a significant amount of error. The effect of the soakers was slightly greater for the high strength concrete.

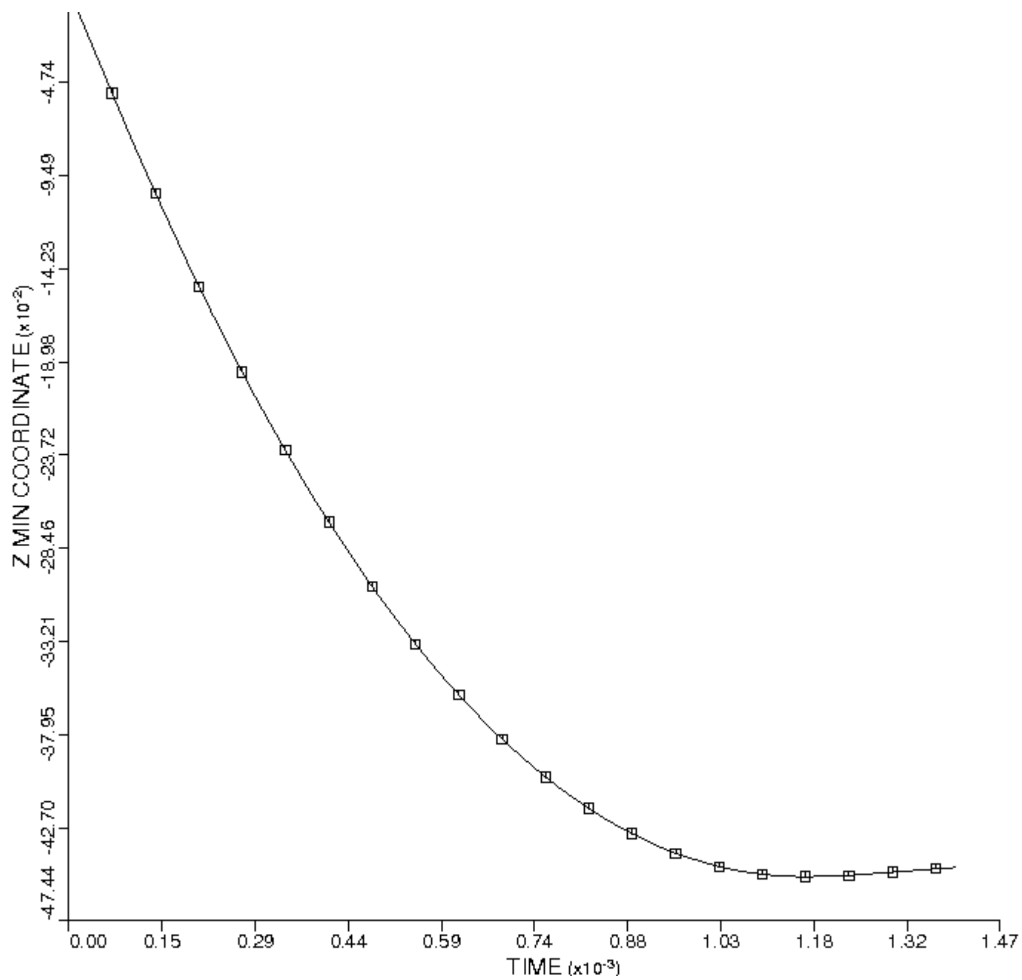

Figure 130. Projectile Depth (m) as a Function of Time (s) with Soakers for Data Set 7, with Striking Velocity 800-m/s.

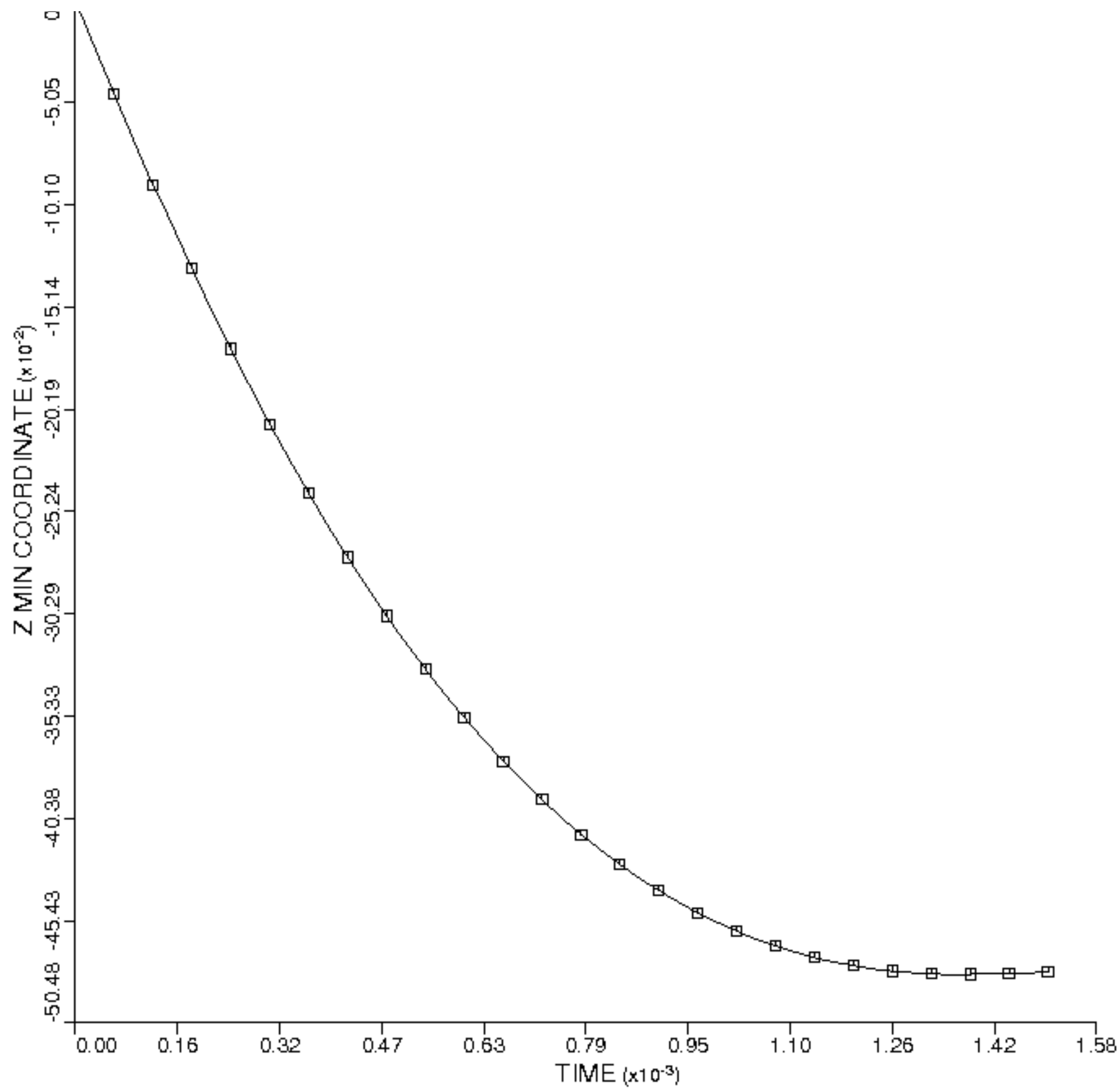

Figure 131. Projectile Depth (m) as a Function of Time (s) with No Soakers for Data Set 7, with Striking Velocity 800-m/s.

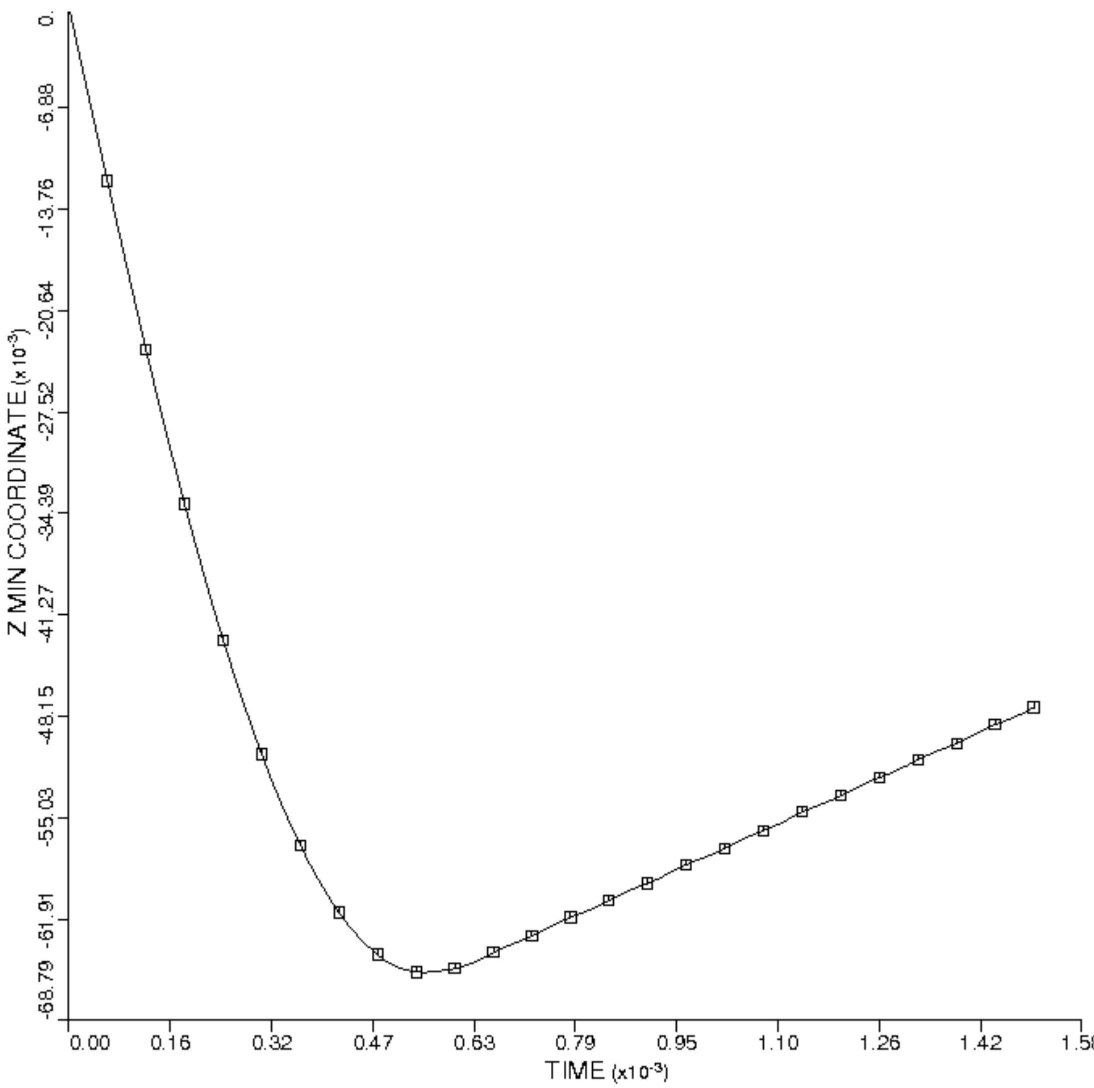

Figure 132. Projectile Depth (m) as a Function of Time (s) with No Soakers for Data Set 7, with Striking Velocity 200-m/s.

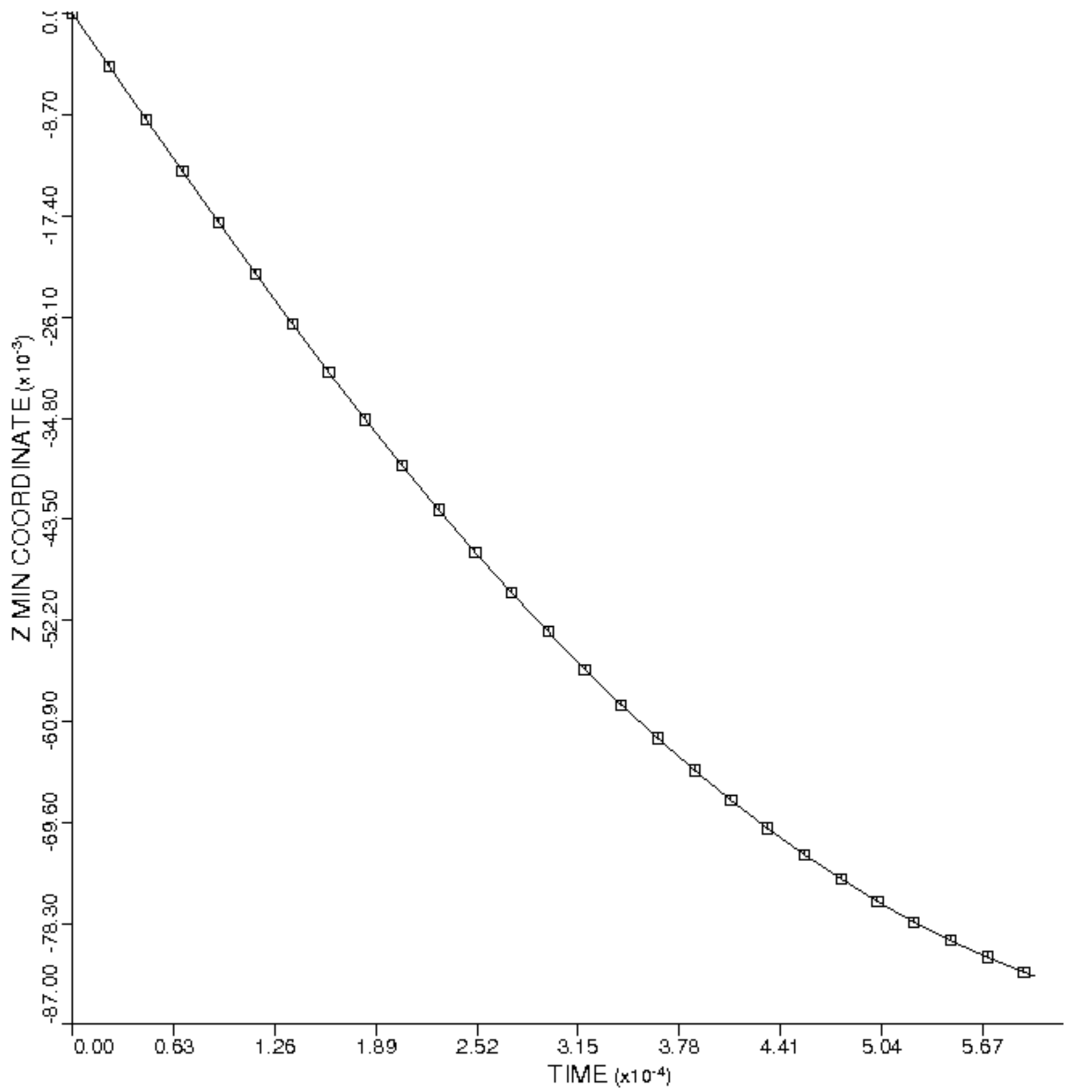

Figure 133. Projectile Depth (m) as a Function of Time (s) with Soakers for Data Set 7, with Striking Velocity 200-m/s.

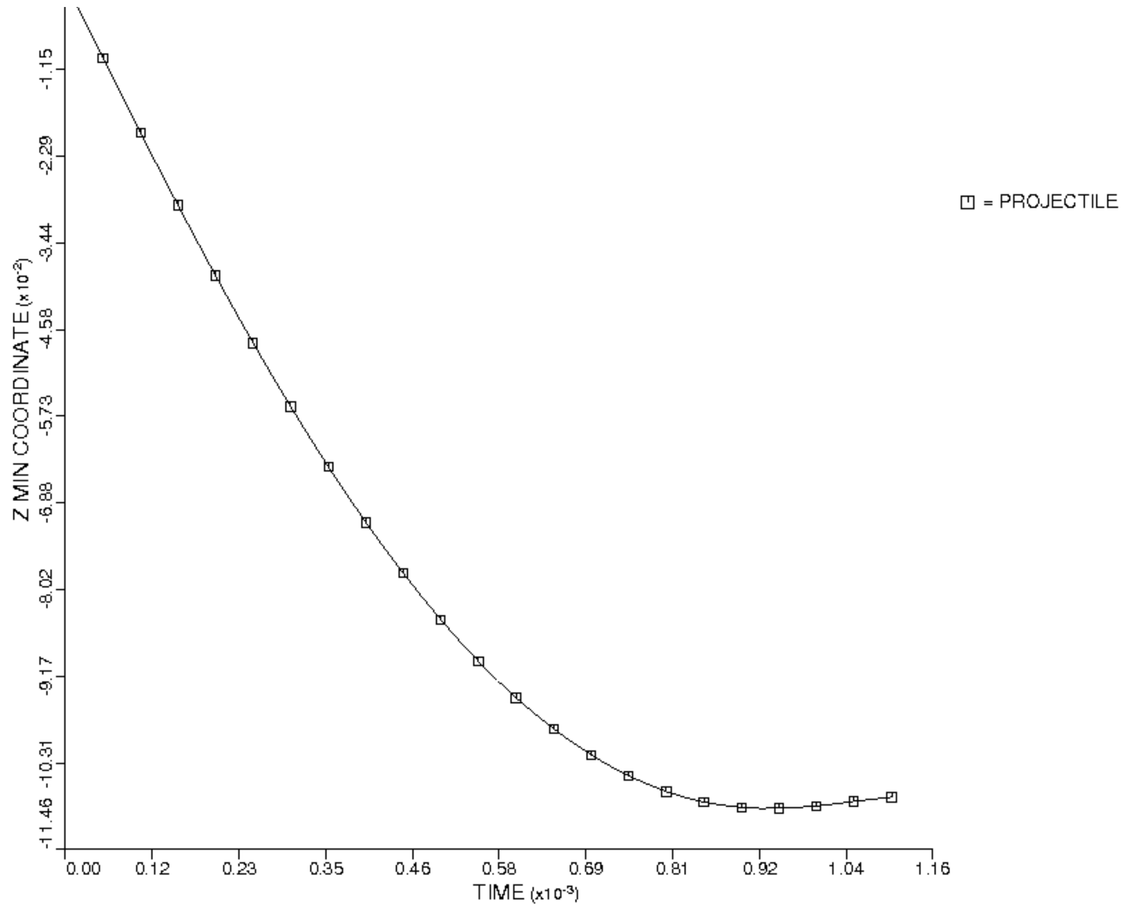

Figure 134. Projectile Depth (m) as a Function of Time (s) with Soakers for Data Set 5, with Striking Velocity 200-m/s.

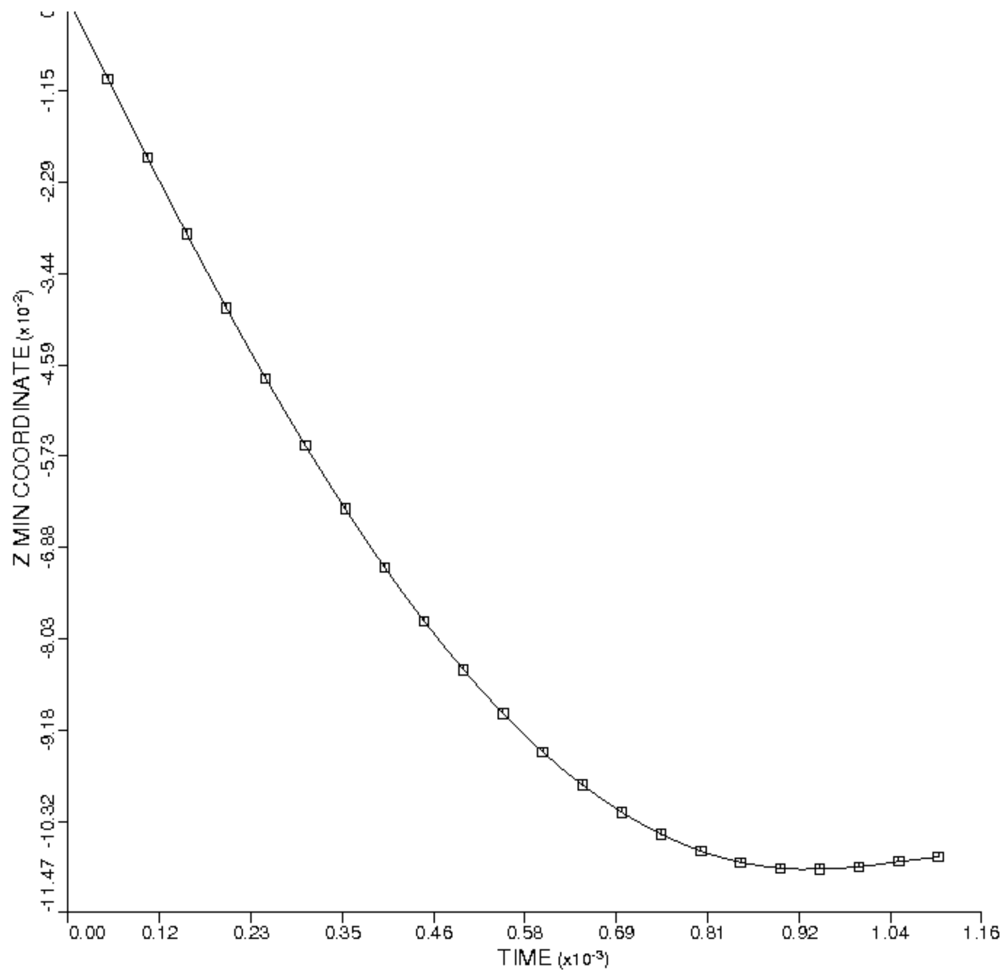

Figure 135. Projectile Depth (m) as a Function of Time (s) with No Soakers for Data Set 5, with Striking Velocity 200-m/s.

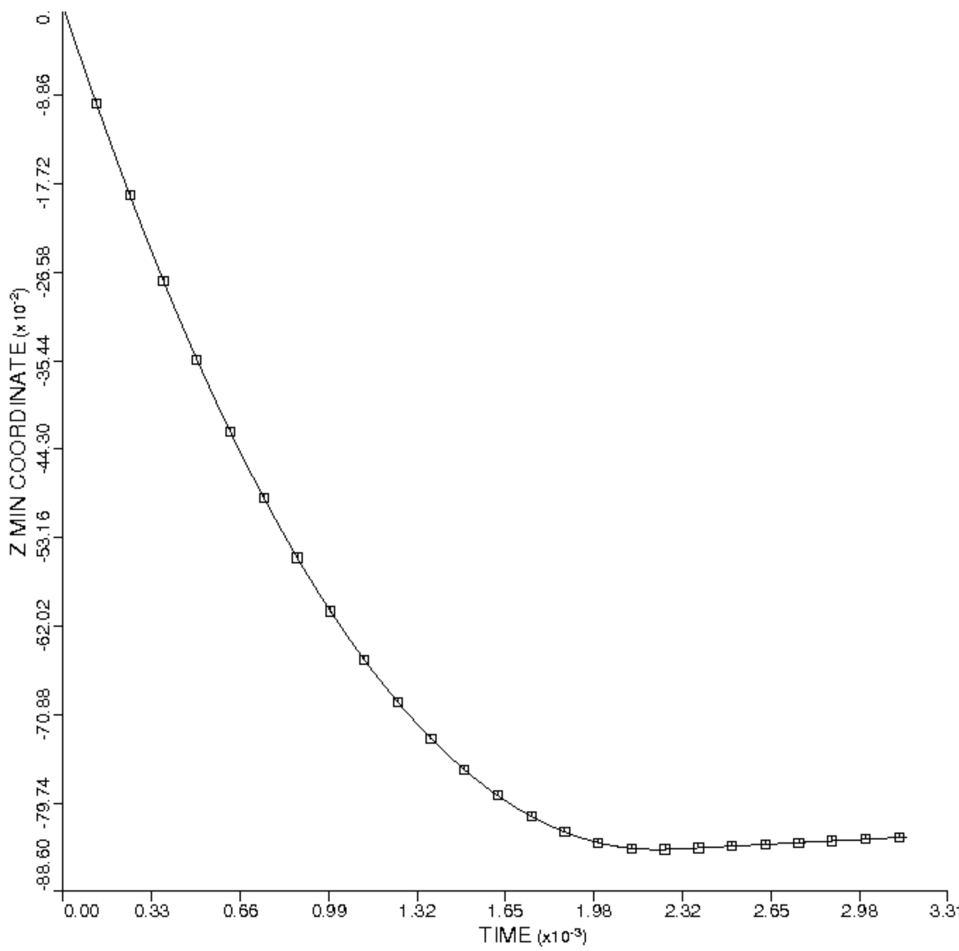

Figure 136. Projectile Depth (m) as a Function of Time (s) with Soakers for Data Set 5, with Striking Velocity 800-m/s.

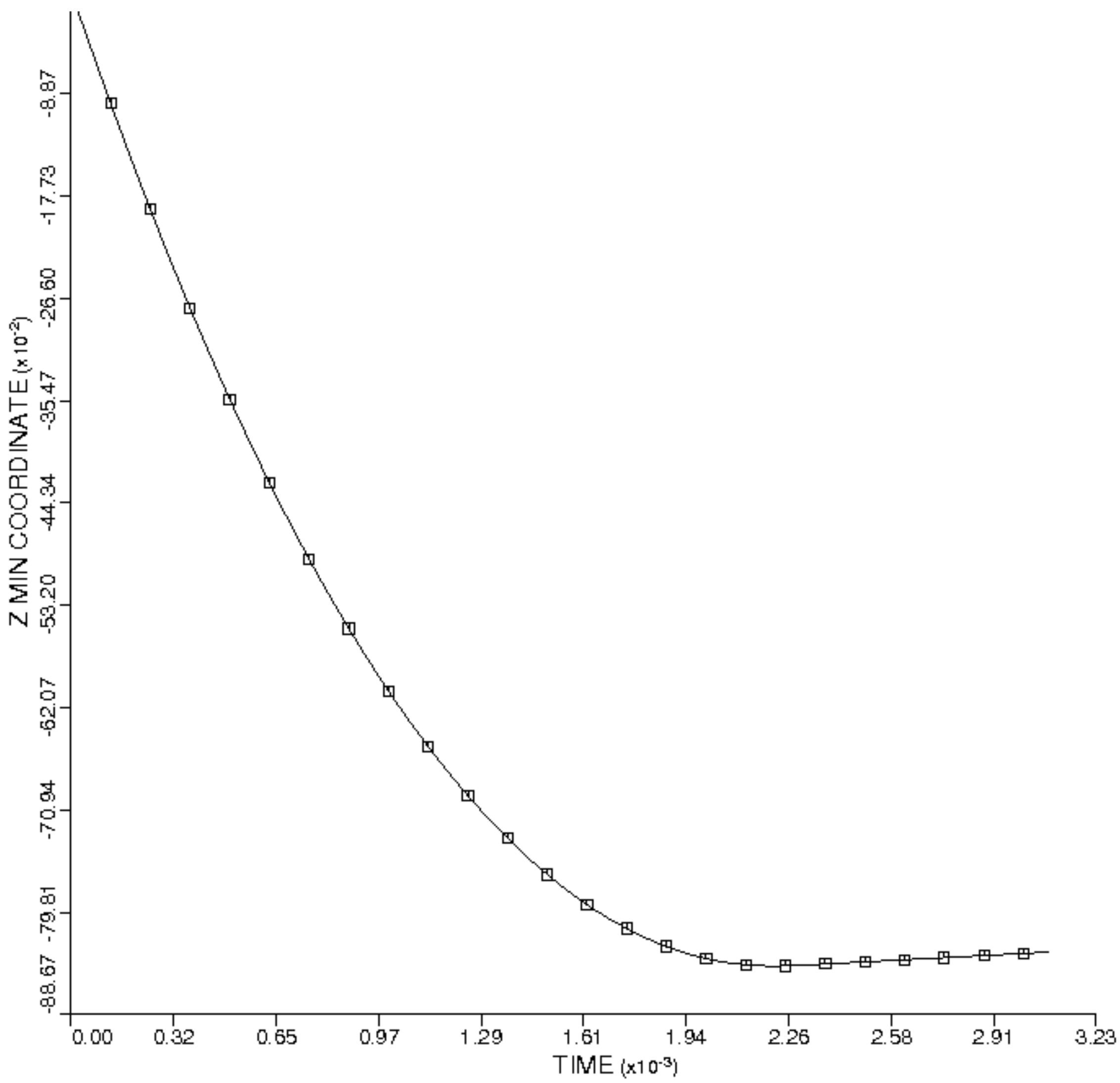

Figure 137. Projectile Depth (m) as a Function of Time (s) with No Soakers
for Data Set 5, with Striking Velocity 800-m/s.

APPENDIX 11: NECM PLOTS FOR PARTICLE VELOCITY MAGNITUDE

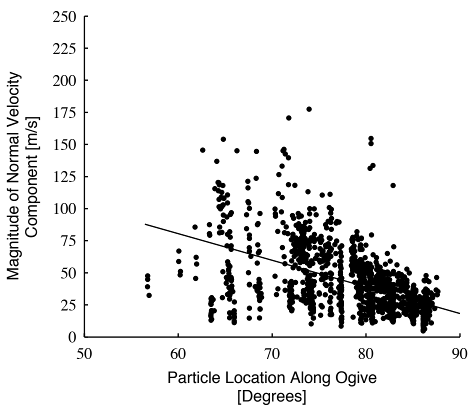

Time Step: 0.41-ms, Depth: -0.1-m,
Slope: -2.1, Int: 204.7

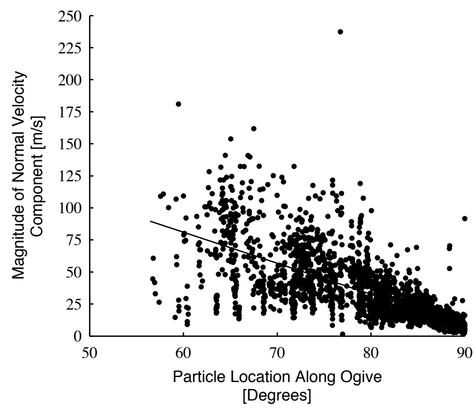

Time Step: 0.70-ms, Veloc: -200-m/s,
Slope: -2.4, Int: 226.2

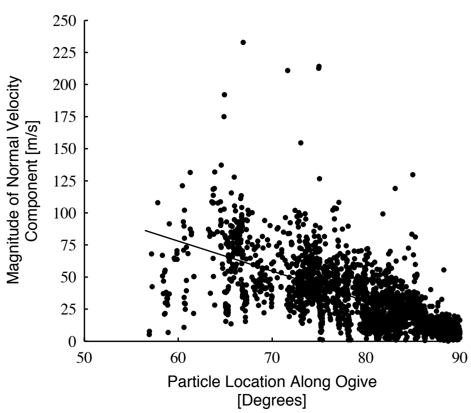

Time Step: 0.89-ms, Depth: -0.2-m,
Slope: -2.3, Int: 218.2

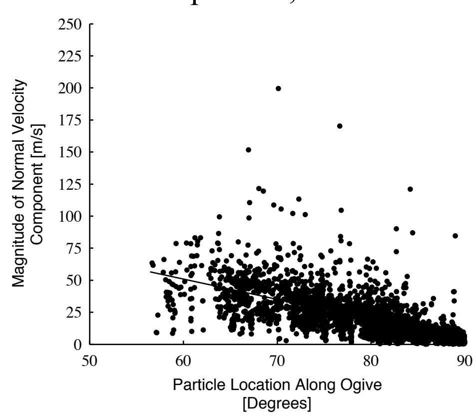

Time Step: 1.55-ms, Veloc: 100-m/s,
Slope: -1.6, Int: 146.1

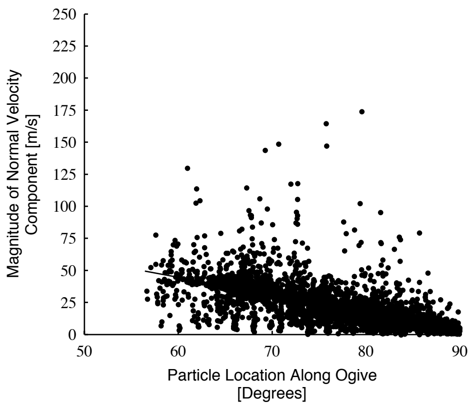

Time Step: 1.78-ms, Depth: -0.3-m,
Slope: -1.4, Int: 126.4

Figure 138. Data Set 3, 250-m/s Striking Velocity, 39-MPa Concrete, 76.2-mm, 3-CRH Projectile

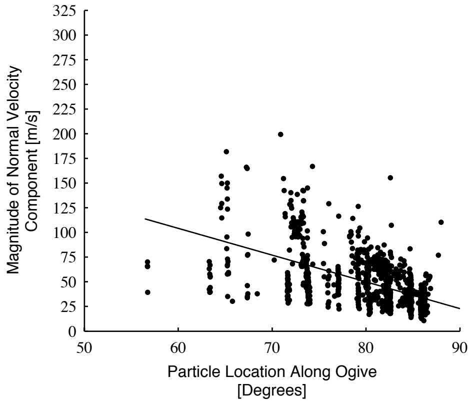

Time Step: 0.30-ms, Veloc: 300-m/s,
Slope: -2.7, Int: 266.8

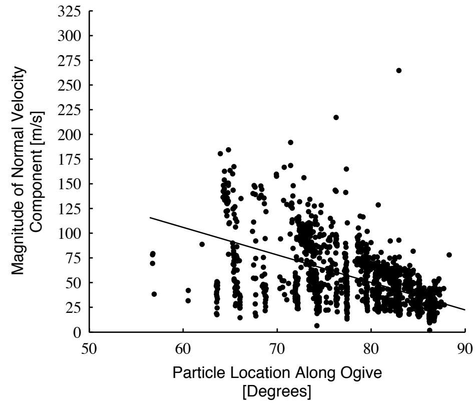

Time Step: 0.31-ms, Depth: -0.1-m,
Slope: -2.8, Int: 272.9

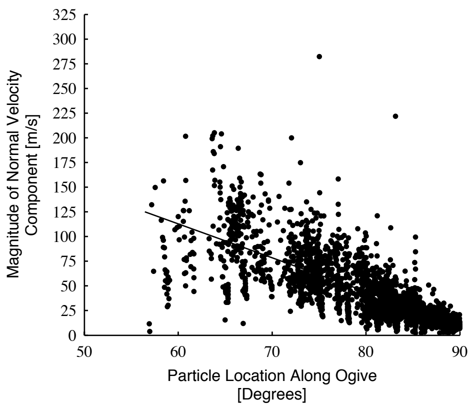

Time Step: 0.65-ms, Depth: -0.2-m,
Slope: -3.4, Int: 318.9

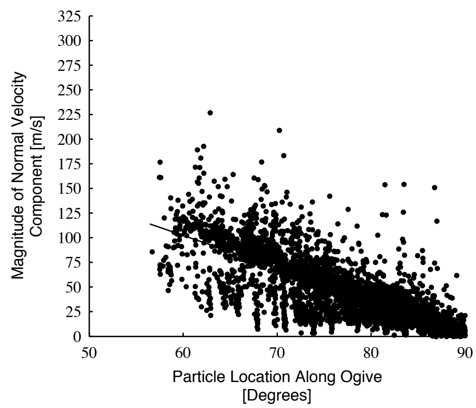

Time Step: 1.06-ms, Depth: -0.3-m,
Slope: -3.3, Int: 299.2

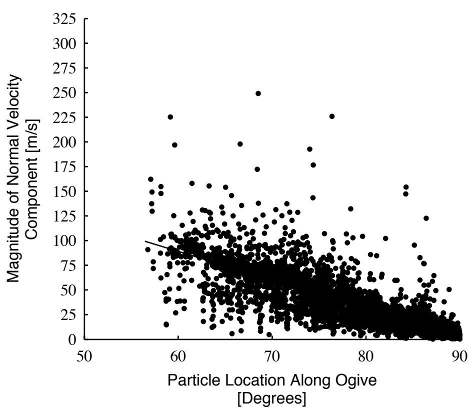

Time Step: 1.23-ms, Depth: -0.4-m,
Slope: -2.9, Int: 263.0

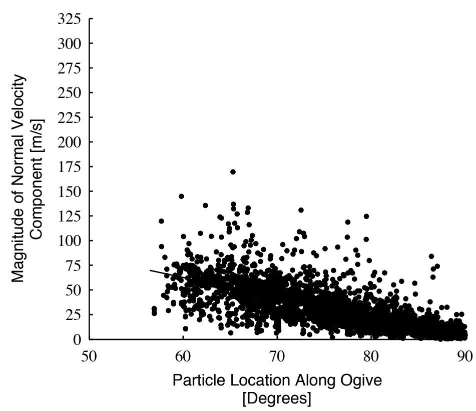

Time Step: 1.63-ms, Veloc: 200 -m/s,
Slope: -2.0, Int: 184.0

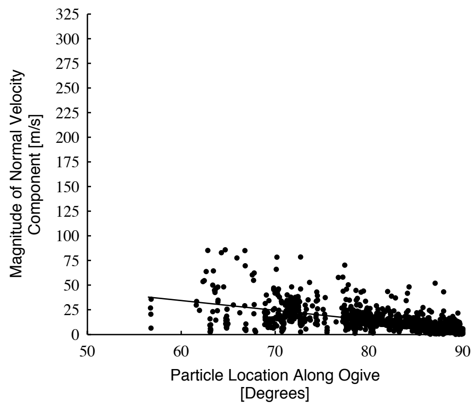

Time Step: 1.95-ms, Veloc: 100 -m/s,
Slope: 1.0, Int: 94.4

Figure 139. Data Set 3, 325-m/s Striking Velocity, 39-MPa Concrete, 76.2-mm, 3-CRH Projectile

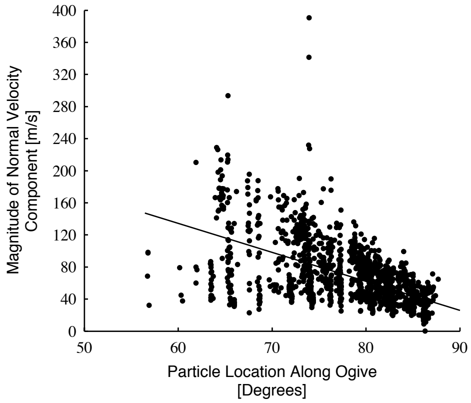

Time Step: 0.25-ms, Depth: -0.1-m,
Slope: -3.6, Int: 351.6

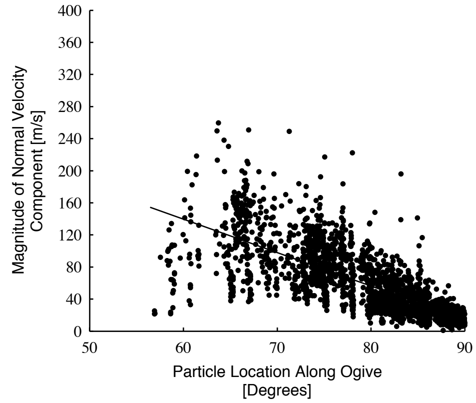

Time Step: 0.52-ms, Depth: -0.2-m,
Slope: -4.2, Int: 390.1

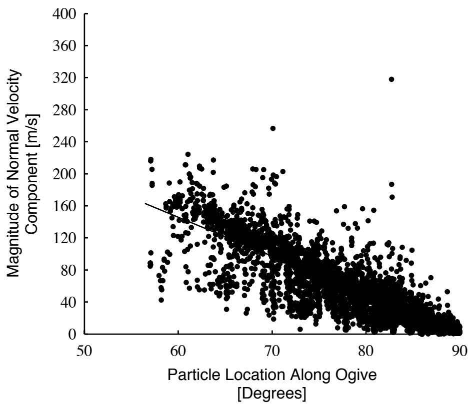

Time Step: 0.82-ms, Depth: -0.3-m,
Slope: -4.9, Int: 437.2

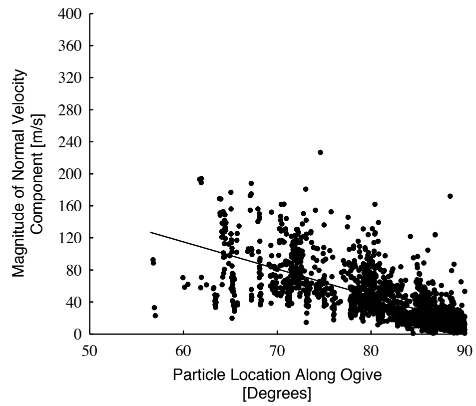

Time Step: 0.87-ms, Veloc: -m/s 300-m,
Slope: -3.4, Int: 317.8

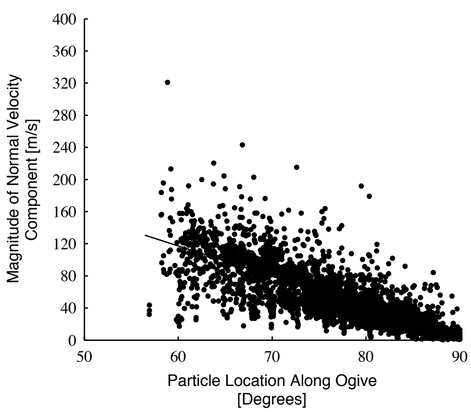

Time Step: 1.17-ms, Depth: -0.40-m,
Slope: -3.8, Int: 342.7

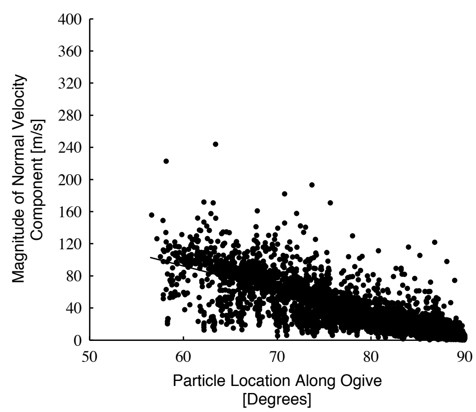

Time Step: 1.55-ms, Veloc: 200-m/s,
Slope: -3.0, Int: 272.1

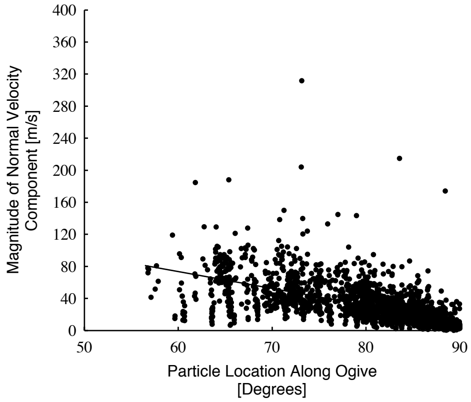

Time Step: 1.63-ms, Depth: -0.5-m,
Slope: -2.1, Int: 200.5

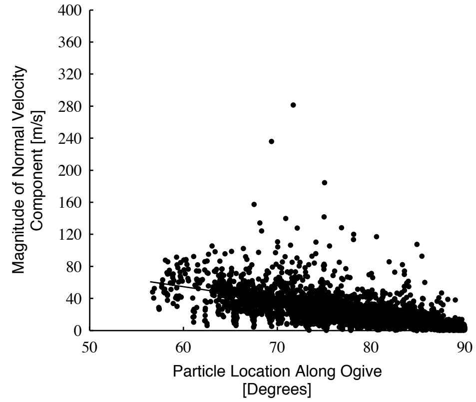

Time Step: 2.13-ms, Veloc: 100-m/s,
Slope: -1.7, Int: 158.1

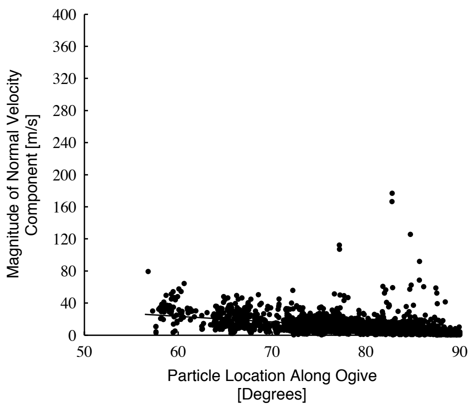

Time Step: 2.55-ms, Depth: -0.6-m,
Slope: -0.7, Int: 64.9

Figure 140. Data Set 3, 400-m/s Striking Velocity, 39-MPa Concrete, 76.2-mm, 3-CRH Projectile

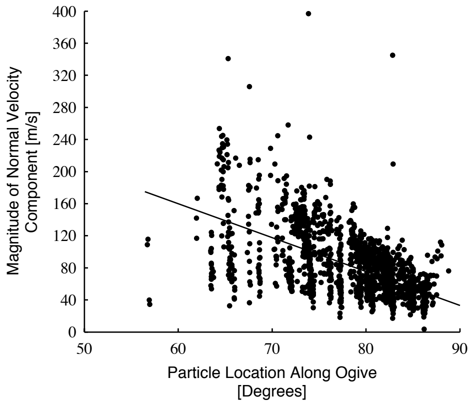

Time Step: 0.21-ms, Depth: -0.1-m,
Slope: -4.2, Int: 413.1

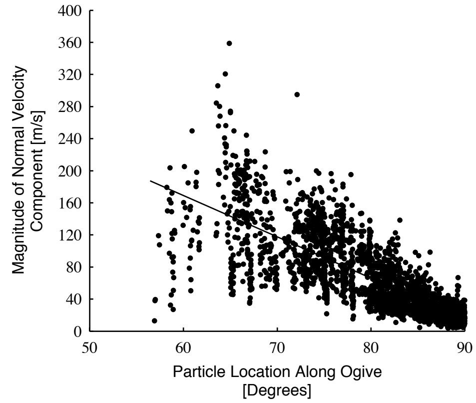

Time Step: 0.44-ms, Depth: -0.2-m,
Slope: -5.2, Int: 478.4

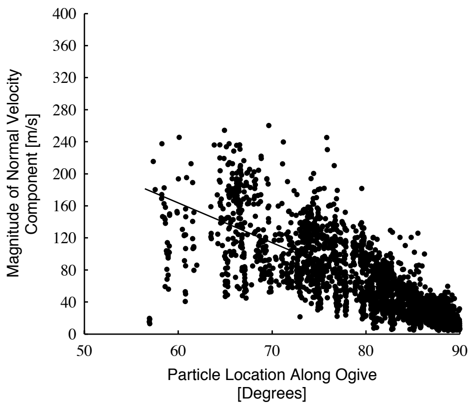

Time Step: 0.58-ms, Veloc: 400-m/s,
Slope: -5.0, Int: 461.8

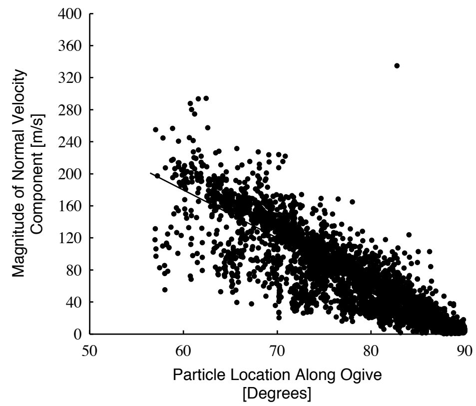

Time Step: 0.68-ms, Depth: -0.3-m,
Slope: -6.0, Int: 539.3

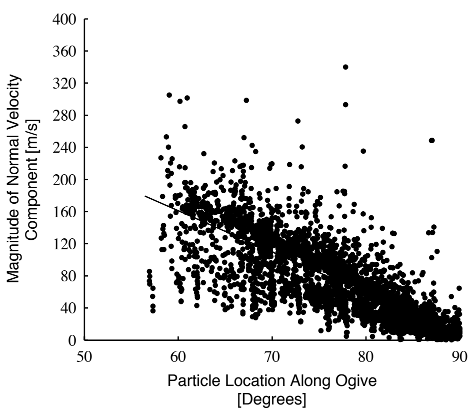

Time Step: 0.94-ms, Depth: -0.4-m,
Slope: -5.1, Int: 469.1

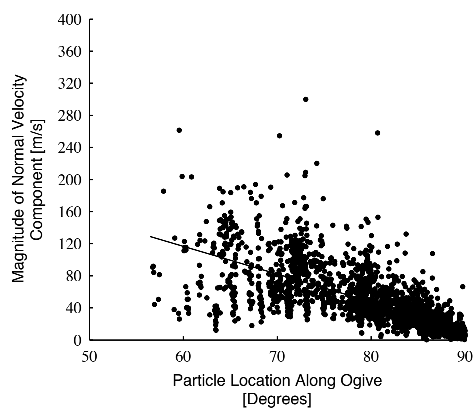

Time Step: 1.24-ms, Depth: -0.5-m,
Slope: -3.5, Int: 323.8

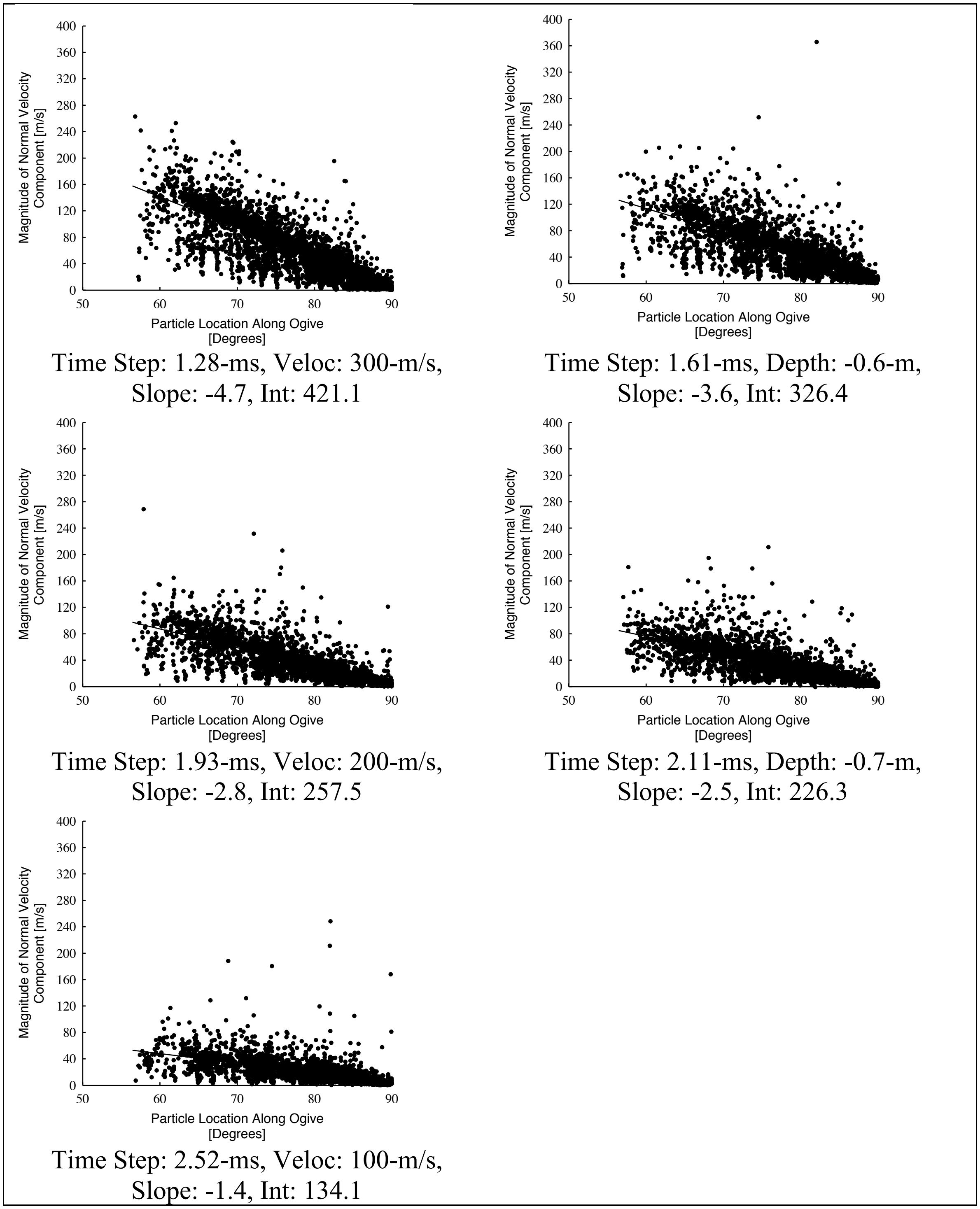

Time Step: 1.28-ms, Veloc: 300-m/s, Slope: -4.7, Int: 421.1

Time Step: 1.61-ms, Depth: -0.6-m, Slope: -3.6, Int: 326.4

Time Step: 1.93-ms, Veloc: 200-m/s, Slope: -2.8, Int: 257.5

Time Step: 2.11-ms, Depth: -0.7-m, Slope: -2.5, Int: 226.3

Time Step: 2.52-ms, Veloc: 100-m/s, Slope: -1.4, Int: 134.1

Figure 141. Data Set 3, 475-m/s Striking Velocity, 39-MPa Concrete, 76.2-mm, 3-CRH Projectile

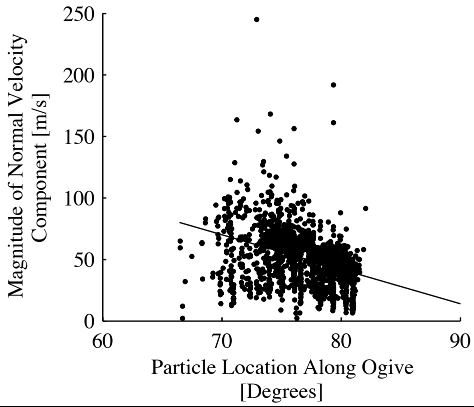

Time Step: 0.41-ms, Depth: -0.11-m, Slope: -2.8, Int: 266.8

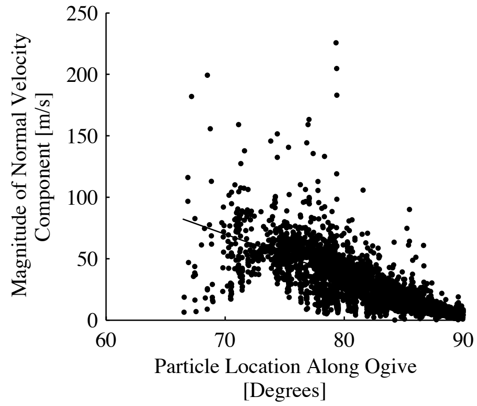

Time Step: 0.83-ms, Veloc: -200-m/s, Slope: -3.5, Int: 312.6

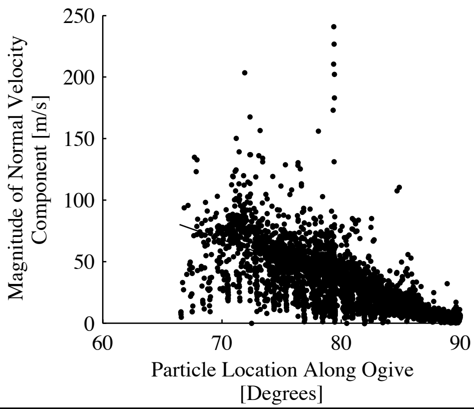

Time Step: 0.85-ms, Depth: -0.21-m, Slope: -3.4, Int: 307.5

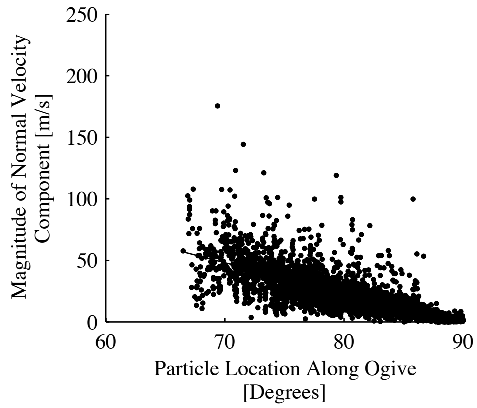

Time Step: 1.43-ms, Depth: -0.30-m, Slope: -2.5, Int: 222.9

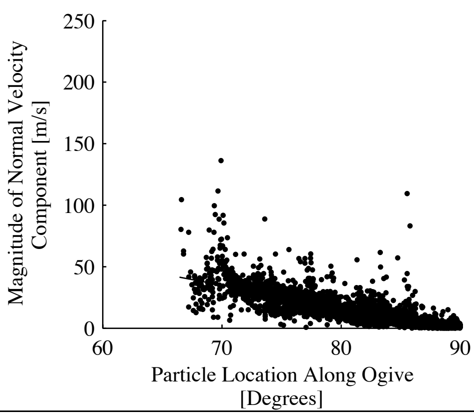

Time Step: 1.73-ms, Veloc: -100-m/s, Slope: -1.8, Int: 163.2

Figure 142. Data Set 4, 250-m/s Striking Velocity, 39-MPa Concrete, 76.2-mm, 6-CRH Projectile

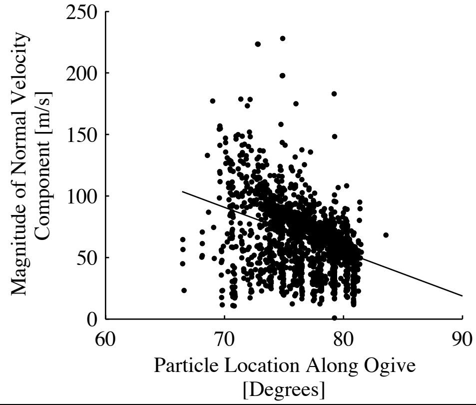

Time Step: 0.31-ms, Depth: -0.11-m,
Slope: -3.6, Int: 343.4

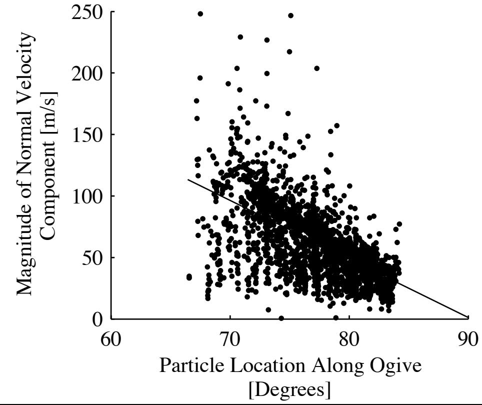

Time Step: 0.38-ms, Veloc: -300-m/s,
Slope: -4.8, Int: 429.7

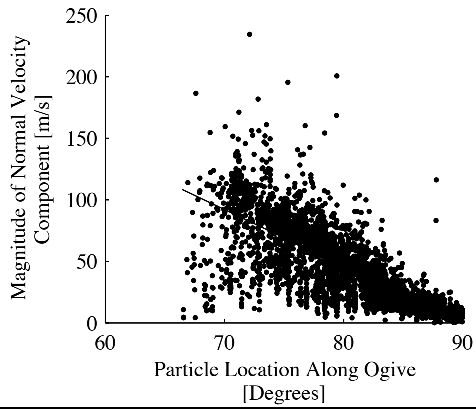

Time Step: 0.64-ms, Depth: -0.21-m,
Slope: -4.6, Int: 413.5

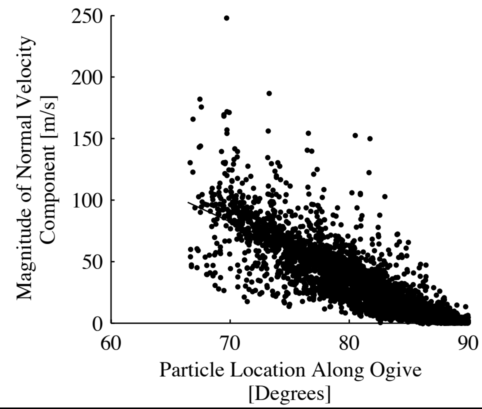

Time Step: 1.02-ms, Depth: -0.30-m,
Slope: -4.4, Int: 392.6

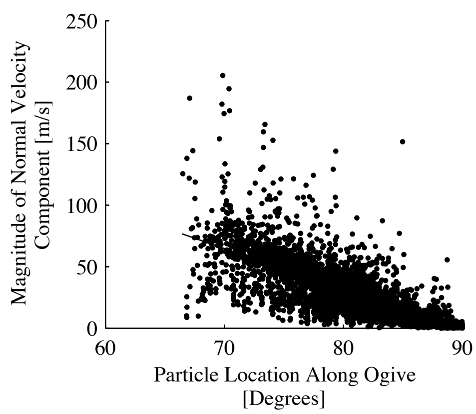

Time Step: 1.43-ms, Veloc: -200-m/s,
Slope: -3.4, Int: 300.4

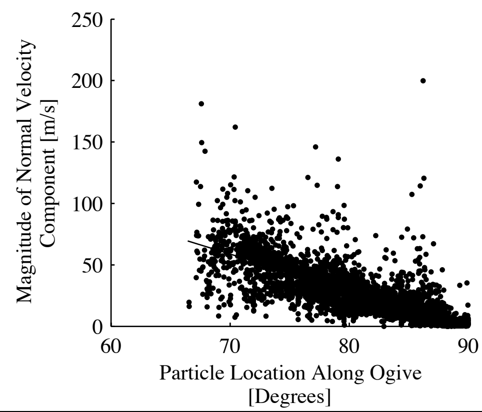

Time Step: 1.48-ms, Depth: -0.40-m,
Slope: -3.0, Int: 268.1

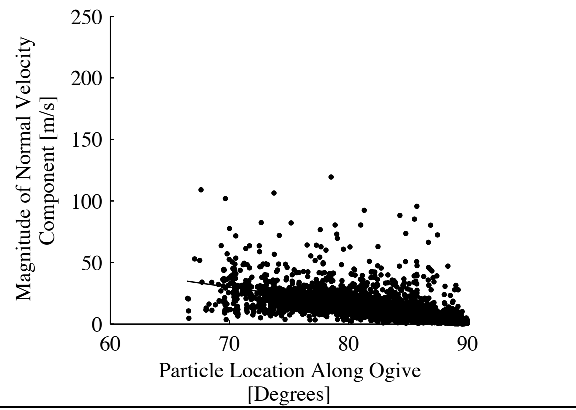

Time Step: 2.20-ms, Veloc: -100-m/s, Slope: -1.4, Int: 126.5

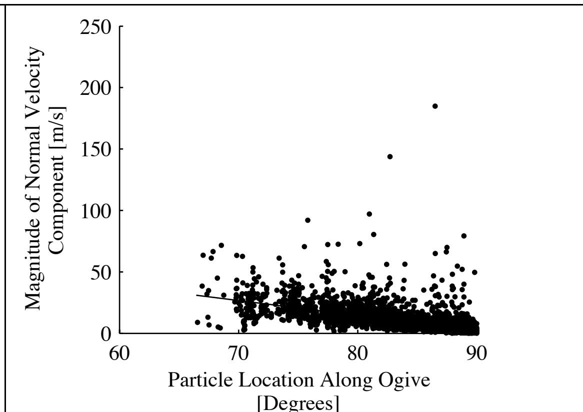

Time Step: 2.25-ms, Depth: -0.51-m, Slope: -1.2, Int: 111.2

Figure 143. Data Set 4, 325-m/s Striking Velocity, 39-MPa Concrete, 76.2-mm, 6-CRH Projectile

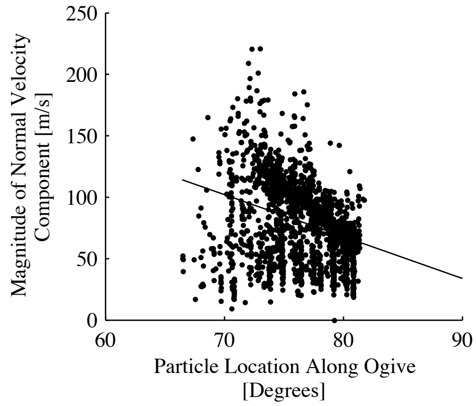

Time Step: 0.25-ms, Depth: -0.11-m, Slope: -3.4, Int: 340.6

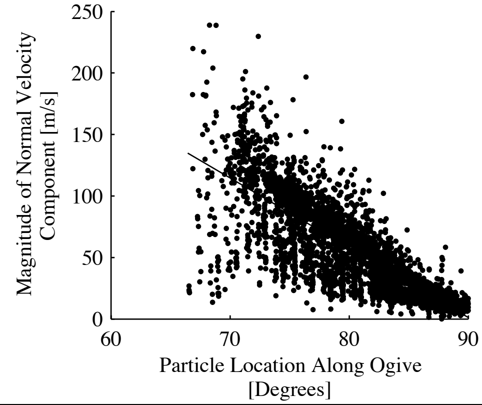

Time Step: 0.51-ms, Depth: -0.21-m, Slope: -5.7, Int: 512.1

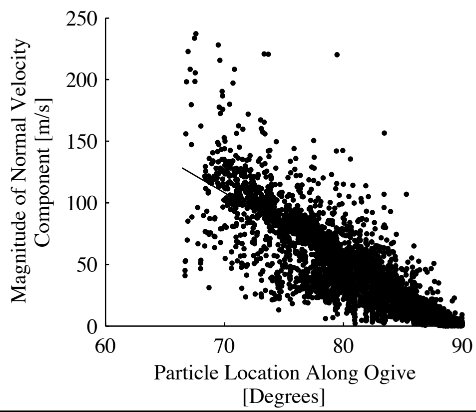

Time Step: 0.80-ms, Depth: -0.30-m, Slope: -5.7, Int: 504.8

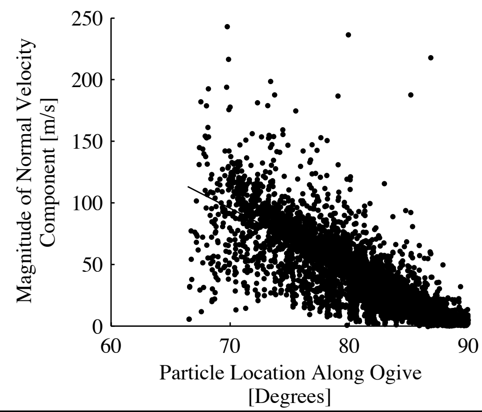

Time Step: 1.08-ms, Veloc: -300-m/s, Slope: -4.9, Int: 441.2

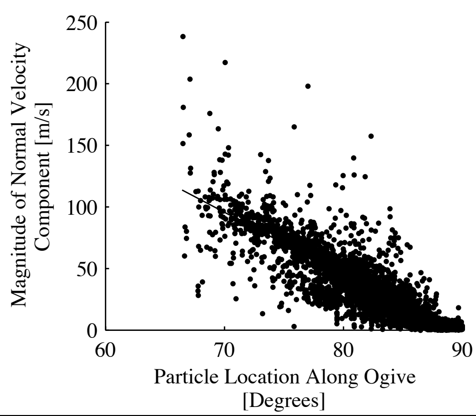

Time Step: 1.11-ms, Depth: -0.39-m, Slope: -5.1, Int: 450.3

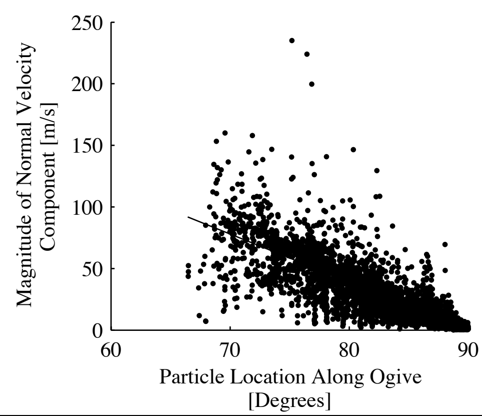

Time Step: 1.49-ms, Depth: -0.51-m, Slope: -3.9, Int: 350.6

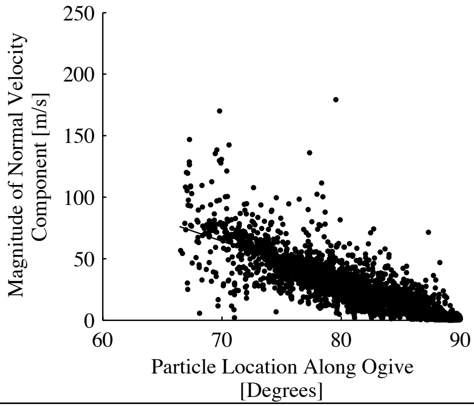

Time Step: 1.75-ms, Veloc: -200-m/s, Slope: -3.4, Int: 298.6

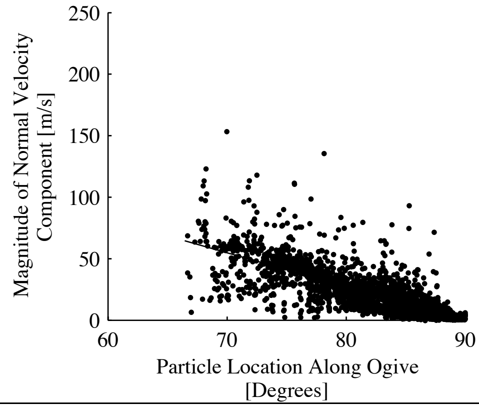

Time Step: 2.00-ms, Depth: -0.60-m, Slope: -2.8, Int: 247.2

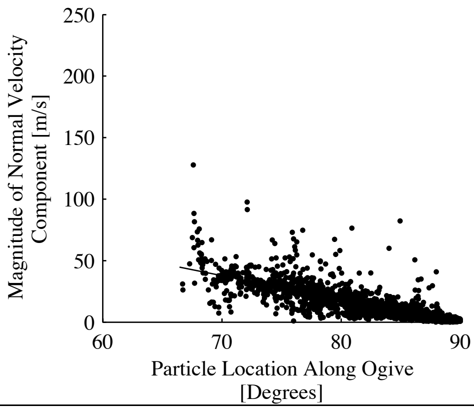

Time Step: 2.44-ms, Veloc: -100-m/s, Slope: -1.9, Int: 173.5

Figure 144. Data Set 4, 400-m/s Striking Velocity, 39-MPa Concrete, 76.2-mm, 6-CRH Projectile

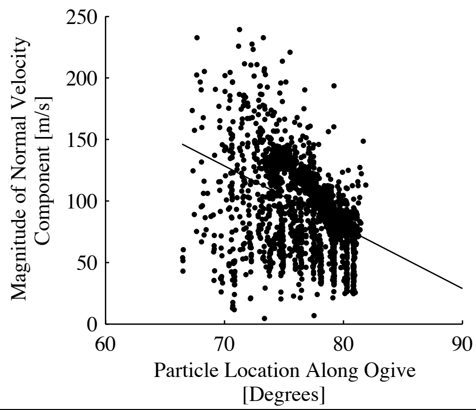

Time Step: 0.21-ms, Depth: -0.11-m, Slope: -5.0, Int: 477.7

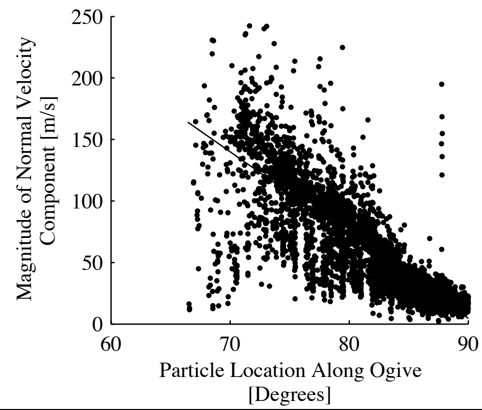

Time Step: 0.43-ms, Depth: -0.21-m, Slope: -6.8, Int: 614.4

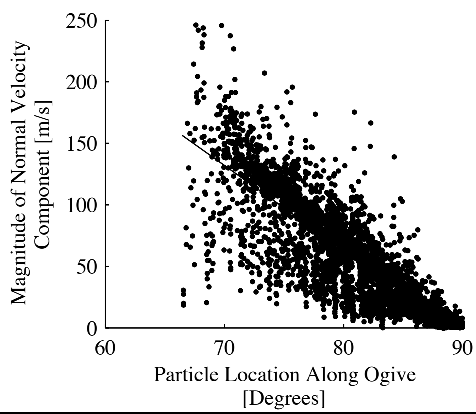

Time Step: 0.66-ms, Depth: -0.30-m, Slope: -6.9, Int: 613.5

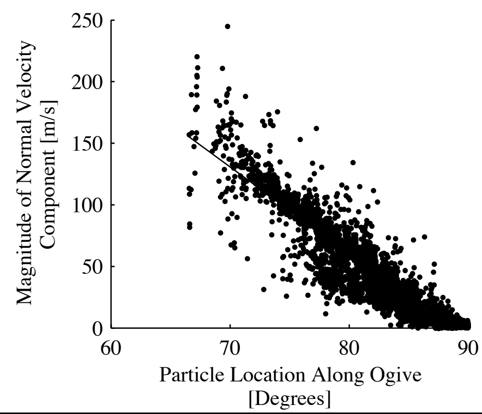

Time Step: 0.75-ms, Veloc: -400-m/s, Slope: -7.1, Int: 626.8

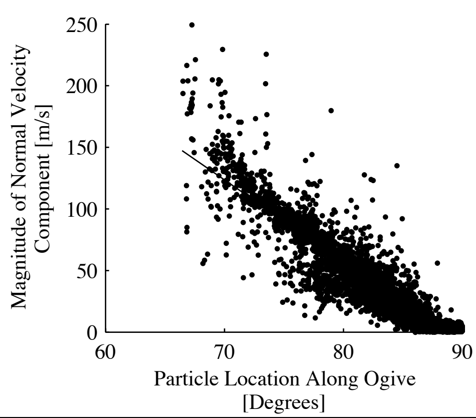

Time Step: 0.91-ms, Depth: -0.40-m, Slope: -6.7, Int: 589.6

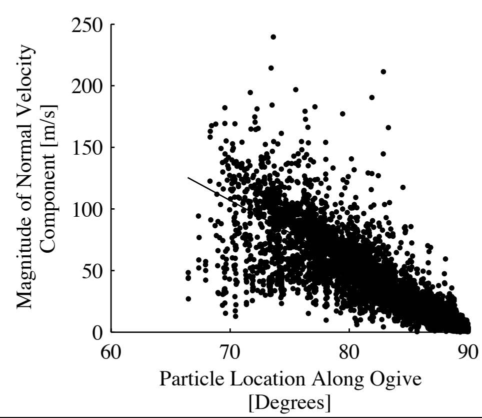

Time Step: 1.18-ms, Depth: -0.51-m, Slope: -5.2, Int: 472.7

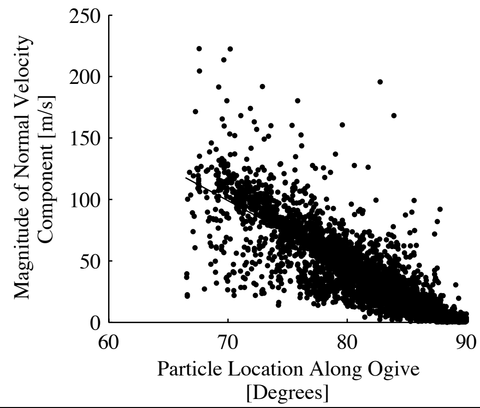

Time Step: 1.43-ms, Veloc: -300-m/s, Slope: -5.2, Int: 466.0

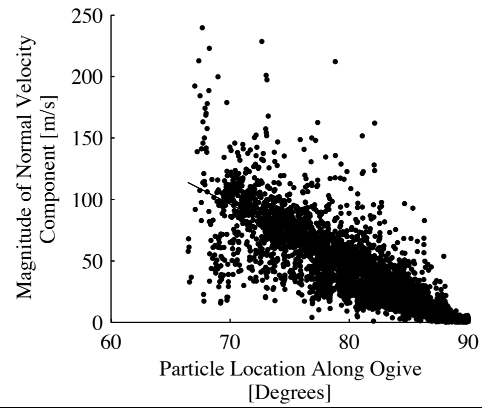

Time Step: 1.50-ms, Depth: -0.60-m, Slope: -5.0, Int: 443.6

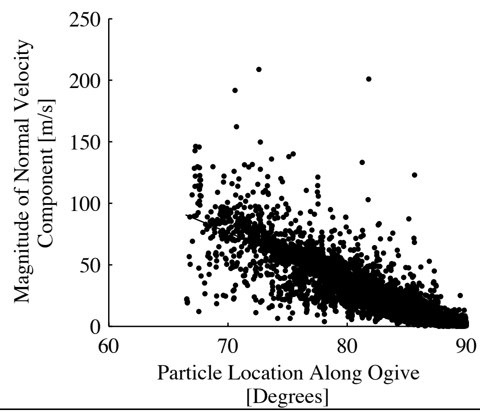

Time Step: 1.89-ms, Depth: -0.70-m, Slope: -4.0, Int: 356.4

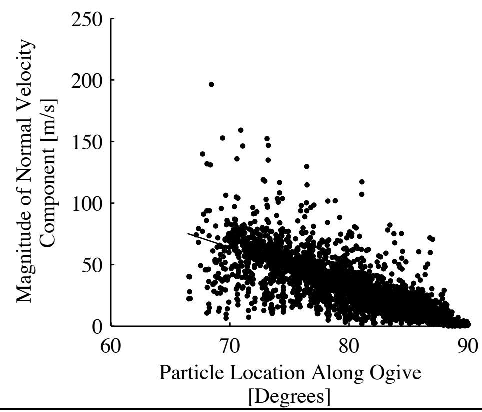

Time Step: 2.13-ms, Veloc: -200-m/s, Slope: -3.2, Int: 287.7

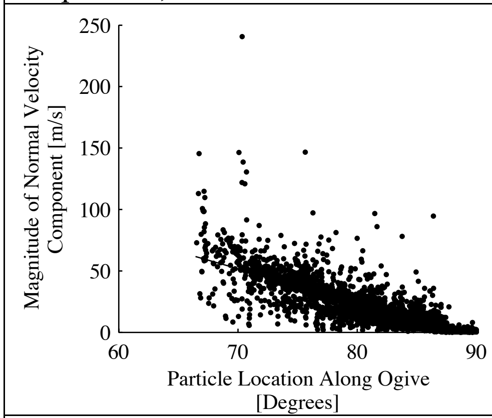

Time Step: 2.40-ms, Depth: -0.79-m, Slope: -2.8, Int: 246.1

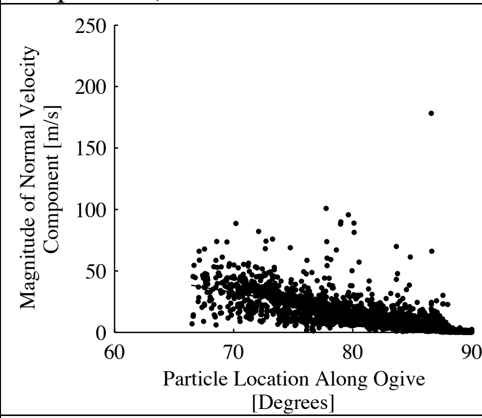

Time Step: 2.83-ms, Veloc: -100-m/s, Slope: -1.7, Int: 149.6

Figure 145. Data Set 4, 475-m/s Striking Velocity, 39-MPa Concrete, 76.2-mm, 6-CRH Projectile

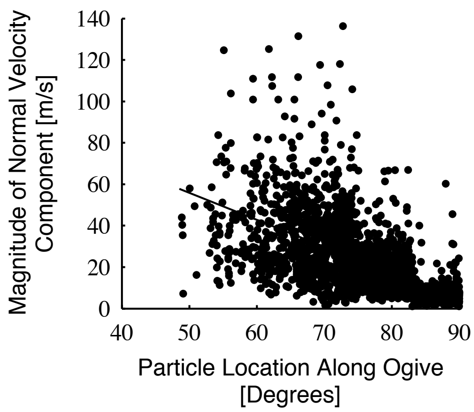

Time Step: 0.56-ms, Veloc: -100-m/s, Slope: -1.3, Int: 121.0

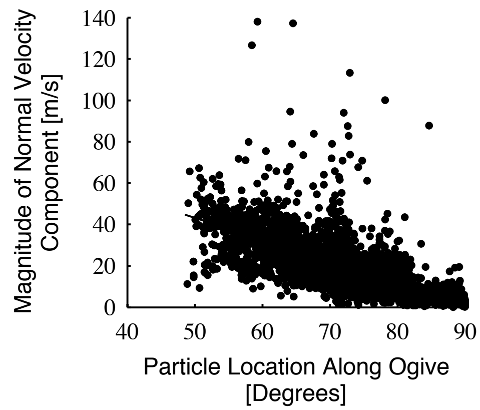

Time Step: 0.67-ms, Depth: -0.10-m, Slope: -1.1, Int: 95.8

Figure 146. Data Set 5, 200-m/s Striking Velocity, 36-MPa Concrete, 26.9-mm, 2-CRH Projectile

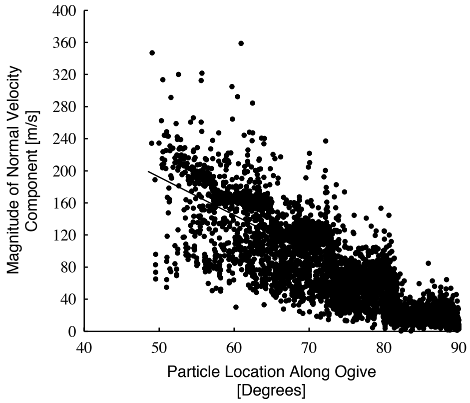

Time Step: 0.26-ms, Depth: -0.10-m,
Slope: -4.8, Int: 429.4

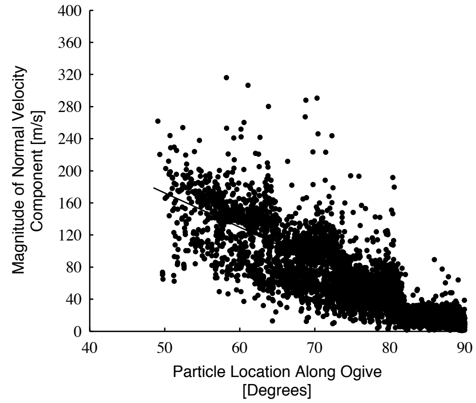

Time Step: 0.40-ms, Veloc: 300-m/s,
Slope: -4.3, Int: 385.8

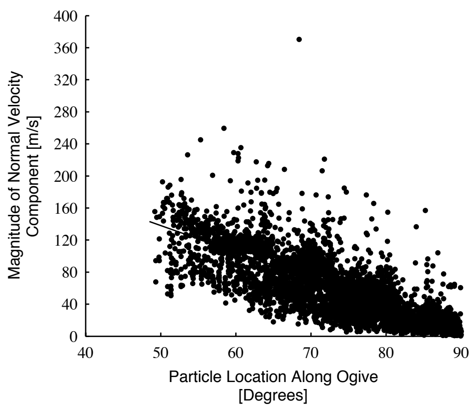

Time Step: 0.56-ms, Veloc: 200-m/s,
Slope: -3.3, Int: 303.8.

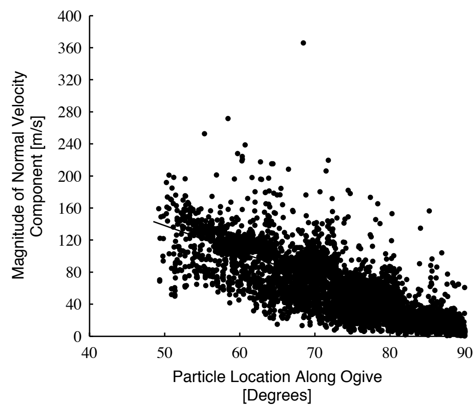

Time Step: 0.56-ms, Veloc: 100-m/s,
Slope: -3.3, Int: 303.7.

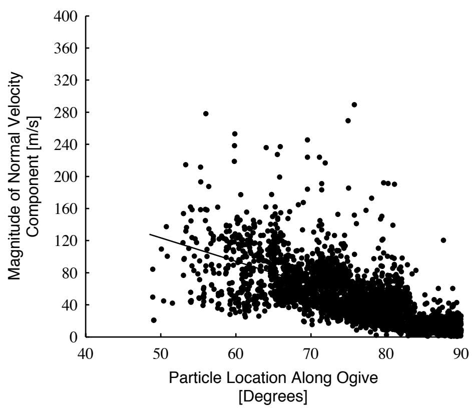

Time Step: 0.62-ms, Depth: -0.20-m,
Slope: -2.9, Int: 269.4.

Figure 147. Data Set 5, 400-m/s Striking Velocity, 36-MPa Concrete, 26.9-mm, 2-CRH Projectile

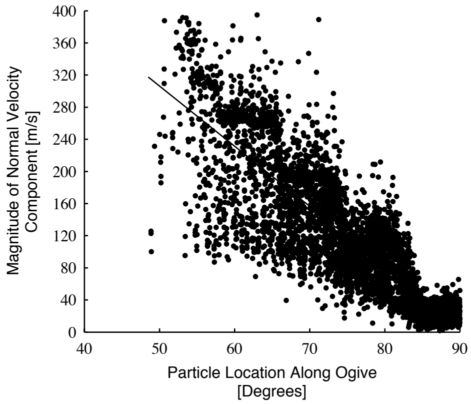

Time Step: 0.17-ms, Depth: -0.10-m,
Slope: -7.5, Int: 681.0

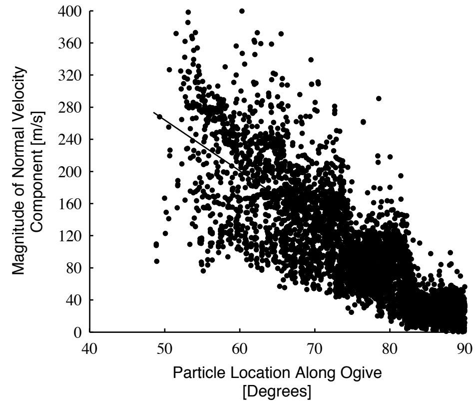

Time Step: 0.33-ms, Veloc: 500-m/s,
Slope: -6.3, Int: 581.0

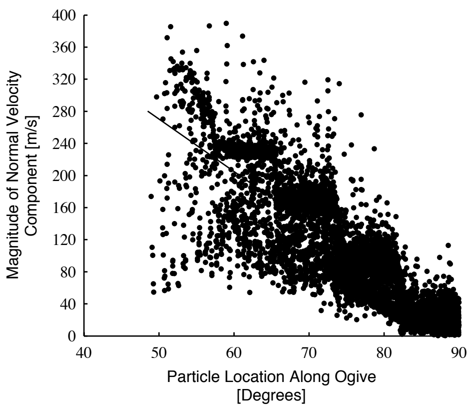

Time Step: 0.34-ms, Depth: -0.2-m,
Slope: -6.5, Int: 597.6

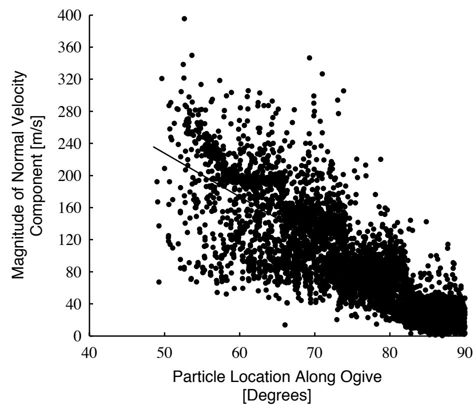

Time Step: 0.55-ms, Depth: -0.3-m,
Slope: -5.4, Int: 498.9

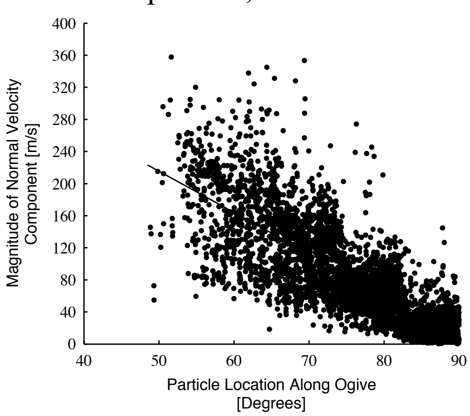

Time Step: 0.59-ms, Veloc: 400-m/s,
Slope: -5.1, Int: 472.1

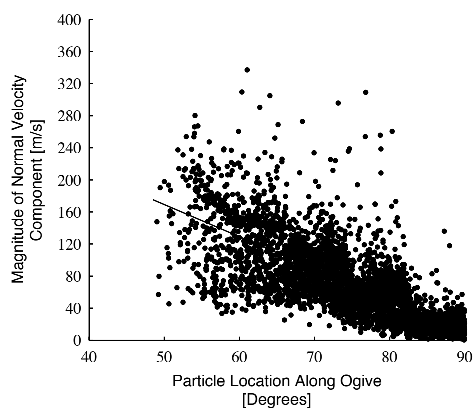

Time Step: 0.82-ms, Depth: -0.4-m,
Slope: -4.0, Int: 369.7

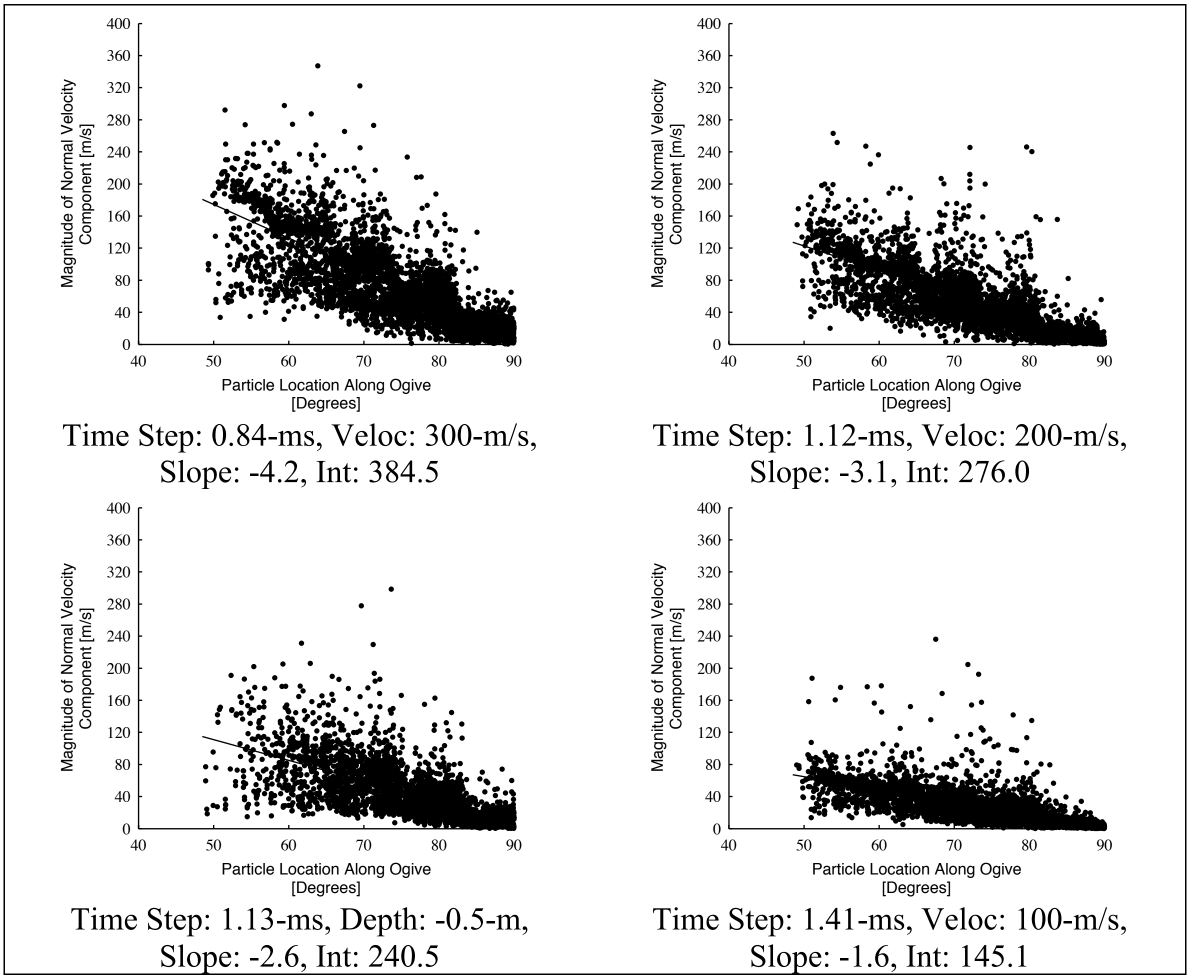

Time Step: 0.84-ms, Veloc: 300-m/s, Slope: -4.2, Int: 384.5

Time Step: 1.12-ms, Veloc: 200-m/s, Slope: -3.1, Int: 276.0

Time Step: 1.13-ms, Depth: -0.5-m, Slope: -2.6, Int: 240.5

Time Step: 1.41-ms, Veloc: 100-m/s, Slope: -1.6, Int: 145.1

Figure 148. Data Set 5, 600-m/s Striking Velocity, 36-MPa Concrete, 26.9-mm, 2-CRH Projectile

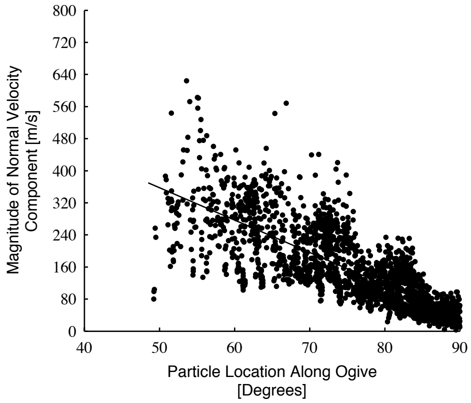

Time Step: 0.12-ms, Depth: -0.10-m,
Slope: -8.1, Int: 762.1

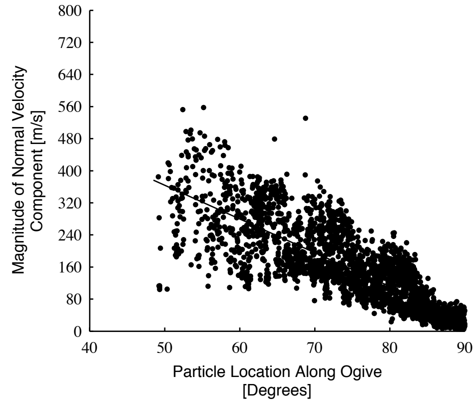

Time Step: 0.17-ms, Veloc: 700-m/s,
Slope: -8.4, Int: 288.63

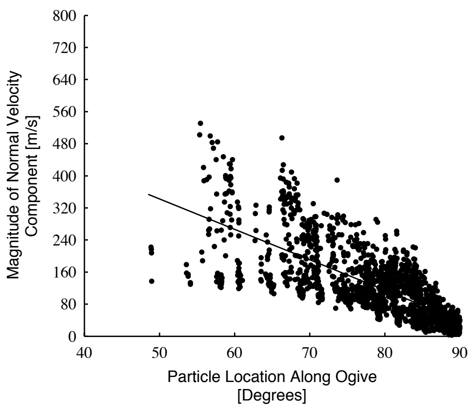

Time Step: 0.22-ms, Depth: -0.2-m,
Slope: -7.6, Int: 721.1

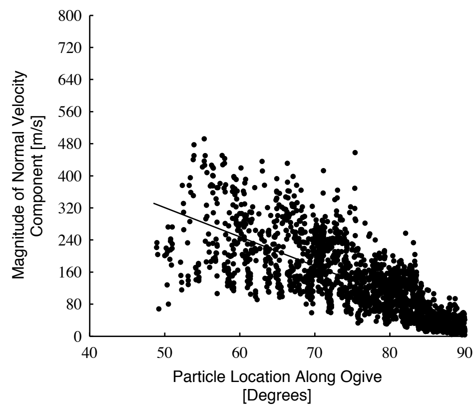

Time Step: 0.36-ms, Depth: -0.3-m,
Slope: -7.3, Int: 684.6

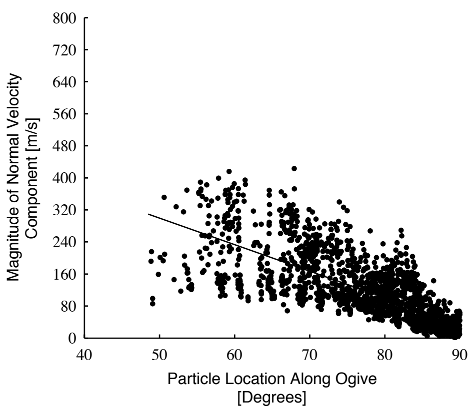

Time Step: 0.38-ms, Veloc: 600-m/s,
Slope: -6.6, Int: 630.2

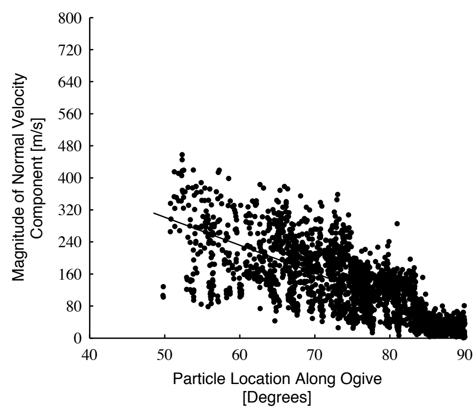

Time Step: 0.51-ms, Veloc: 500-m/s,
Slope: -7.0, Int: 650.1

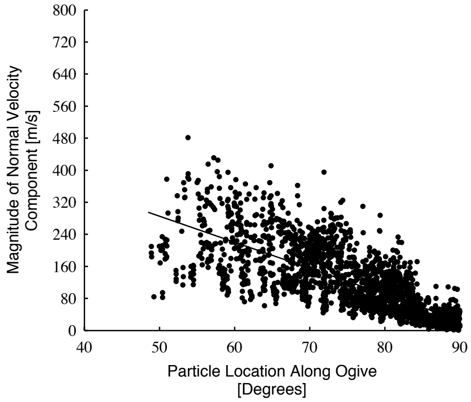

Time Step: 0.52-ms, Depth: -0.4-m,
Slope: -6.5, Int: 610.3

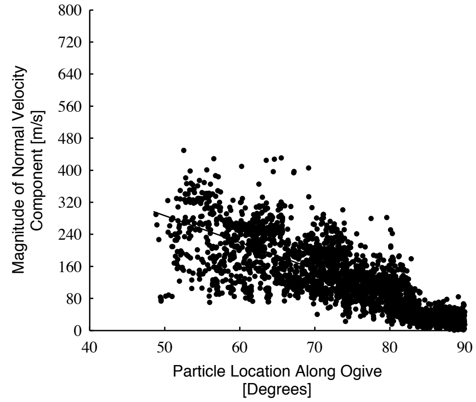

Time Step: 0.60-ms, Veloc: 400-m/s,
Slope: -6.7, Int: 621.1

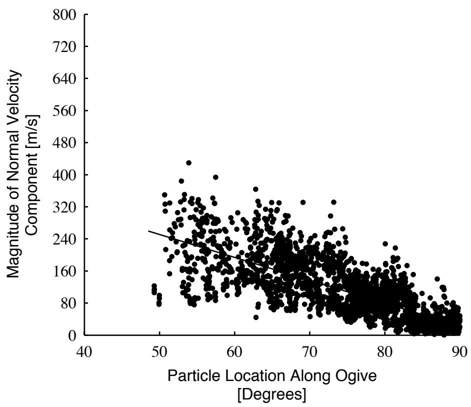

Time Step: 0.70-ms, Depth: -0.5-m,
Slope: -5.7, Int: 536.5

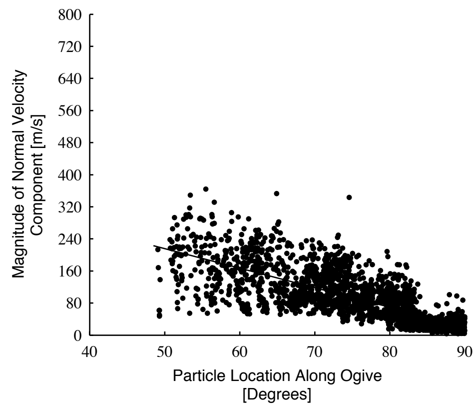

Time Step: 0.91-ms, Depth: -0.6-m,
Slope: -4.9, Int: 459.5

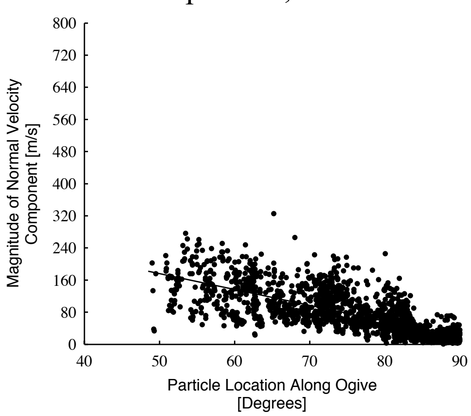

Time Step: 1.15-ms, Depth: -0.7-m,
Slope: -3.9, Int: 373.0

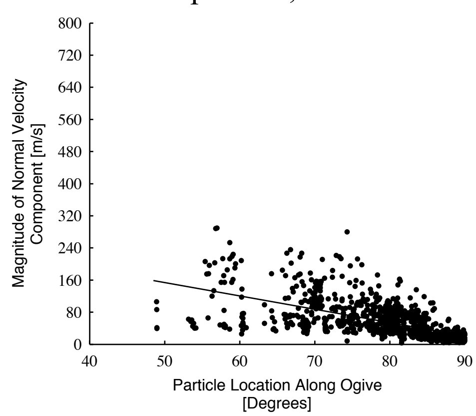

Time Step: 1.22-ms, Veloc: 300-m/s,
Slope: -3.3, Int: 320.4

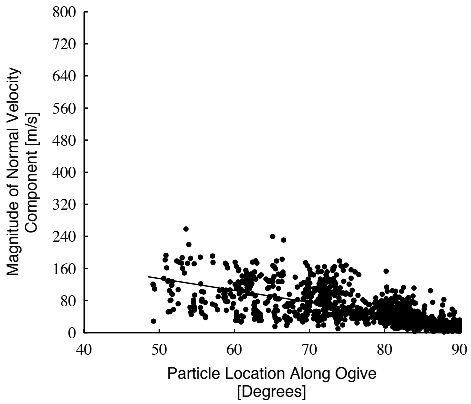

Time Step: 1.40-ms, Depth: -0.8-m, Slope: -3.0, Int: 282.6

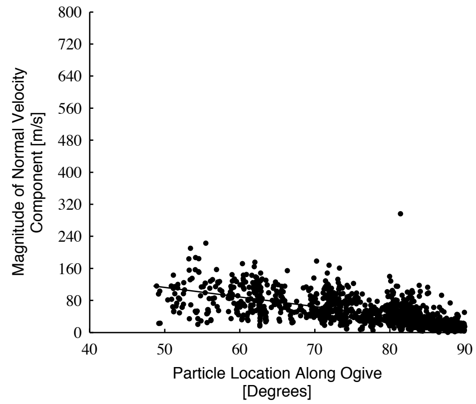

Time Step: 1.52-ms, Veloc: 200-m/s, Slope: -2.4, Int: 231.3

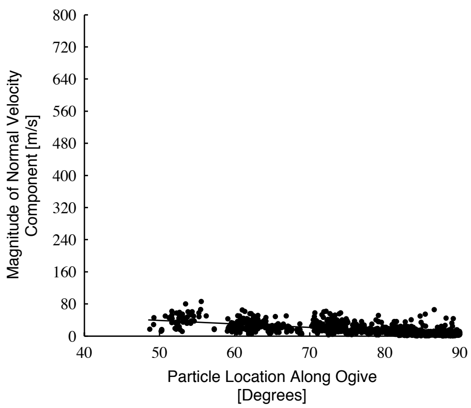

Time Step: 1.99-ms, Veloc: 100-m/s, Slope: -0.9, Int: 82.2

Figure 149. Data Set 5, 800-m/s Striking Velocity, 36-MPa Concrete, 26.9-mm, 2-CRH Projectile

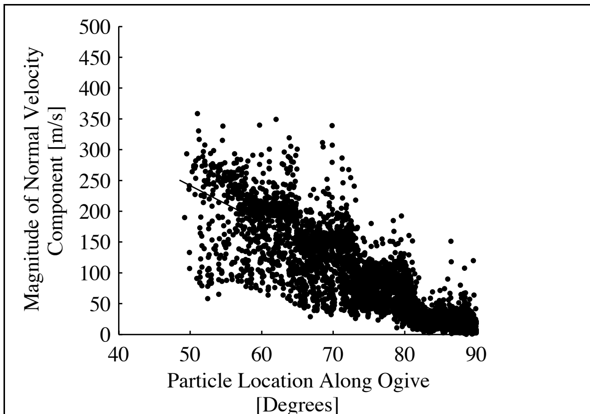

Time Step: 0.21-ms, Depth: -0.1-m, Slope: -6.0, Int: 539.9.

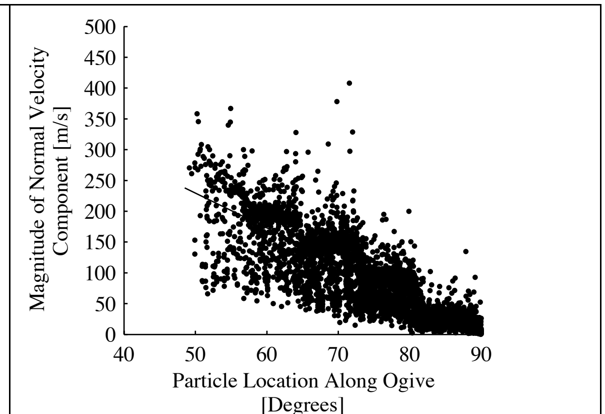

Time Step: 0.26-ms, Veloc: -400-m/s, Slope: -5.7, Int: 512.2.

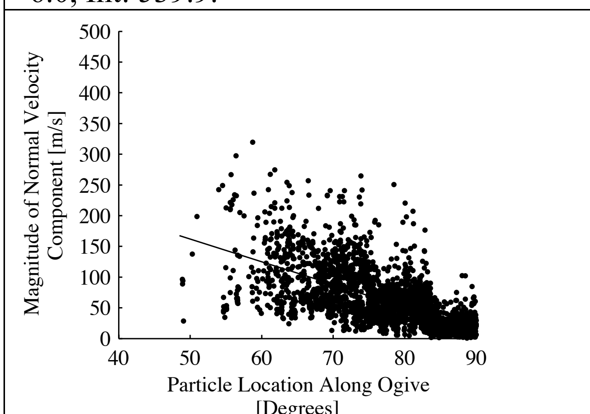

Time Step: 0.48-ms, Depth: -0.2-m, Slope: -3.7, Int: 347.0.

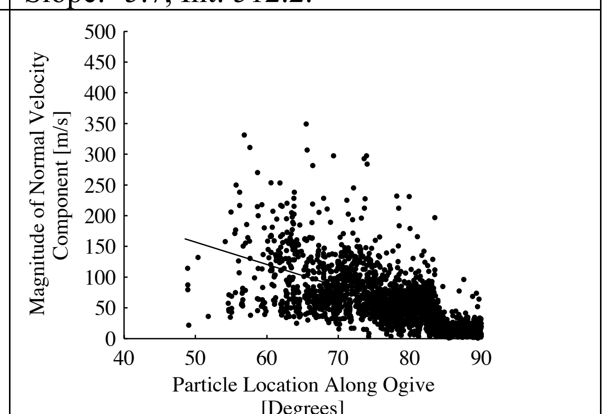

Time Step: 0.50-ms, Veloc: -300-m/s, Slope: -3.6, Int: 338.7.

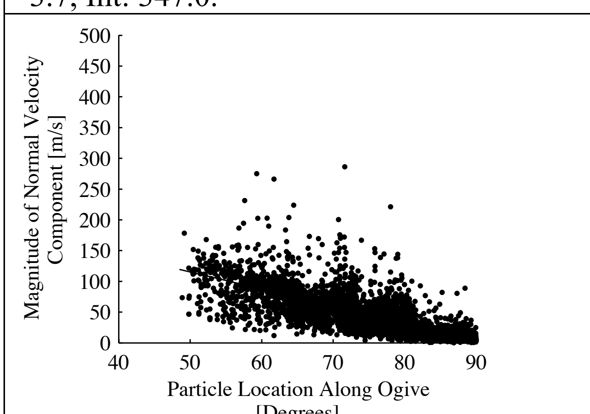

Time Step: 0.73-ms, Veloc: -200-m/s, Slope: -2.8, Int: 254.3.

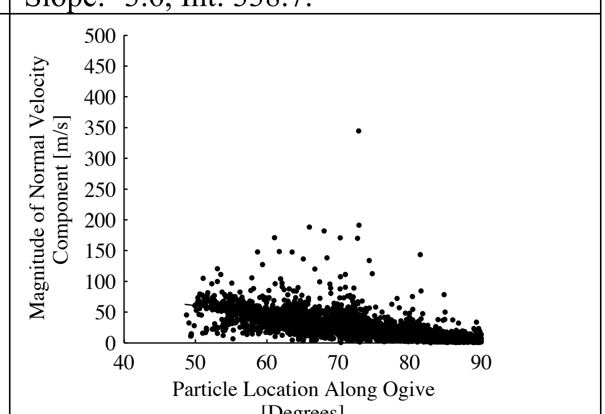

Time Step: 0.95-ms, Veloc: -100-m/s, Slope: -1.5, Int: 133.9.

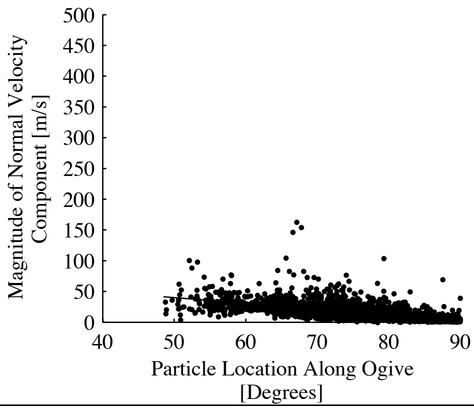	
Time Step: 1.02-ms, Depth: -0.3-m, Slope: -0.9, Int: 86.3.	

Figure 150. Data Set 6, 500-m/s Striking Velocity, 97-MPa Concrete, 26.9-mm, 2-CRH Projectile

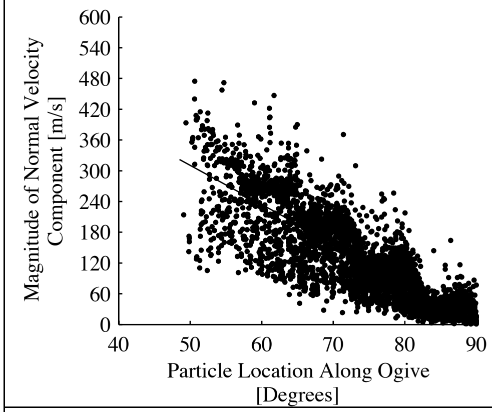

Time Step: 0.17-ms, Depth: -0.1-m, Slope: -7.6, Int: 692.6.

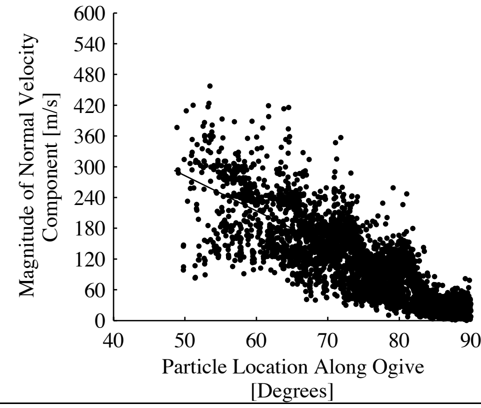

Time Step: 0.23-ms, Veloc: -500-m/s, Slope: -6.9, Int: 626.5.

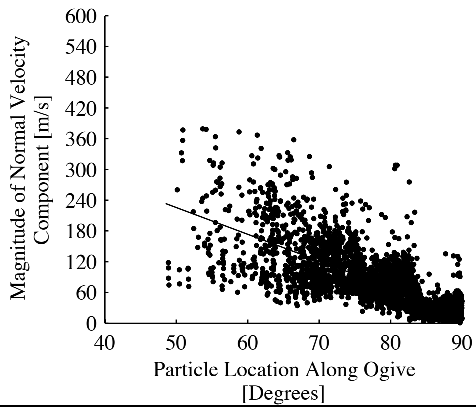

Time Step: 0.38-ms, Depth: -0.2-m, Slope: -5.2, Int: 486.8.

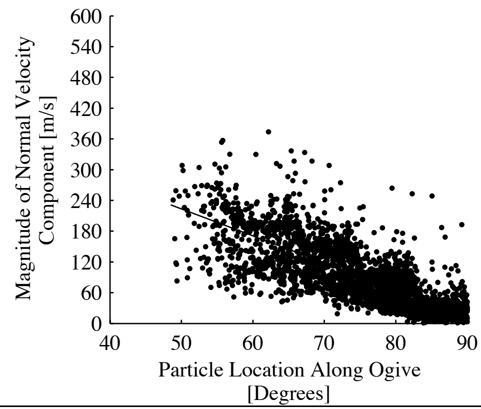

Time Step: 0.46-ms, Veloc: -400-m/s, Slope: -5.3, Int: 486.2.

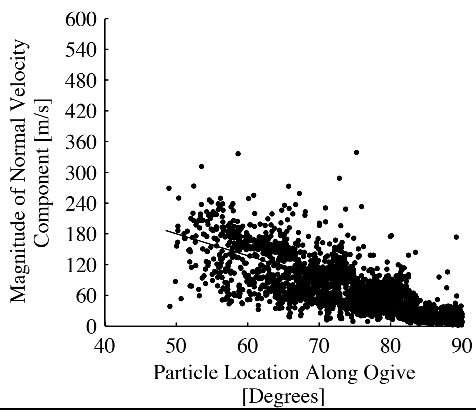

Time Step: 0.65-ms, Depth: -0.3-m, Slope: -4.3, Int: 394.5.

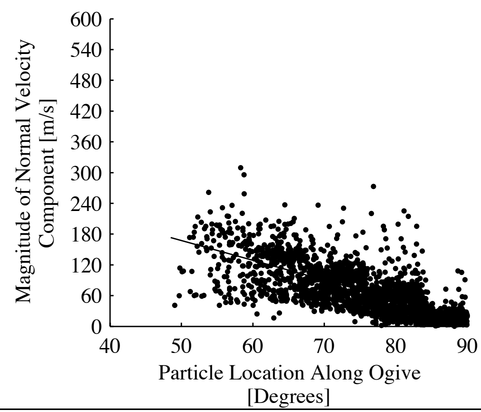

Time Step: 0.68-ms, Veloc: -300-m/s, Slope: -3.9, Int: 360.2.

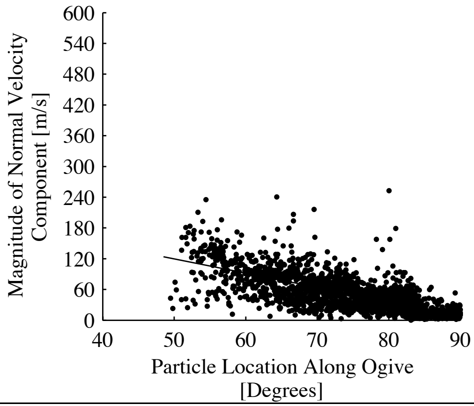

Time Step: 0.90-ms, Veloc: -200-m/s, Slope: -2.8, Int: 258.5.

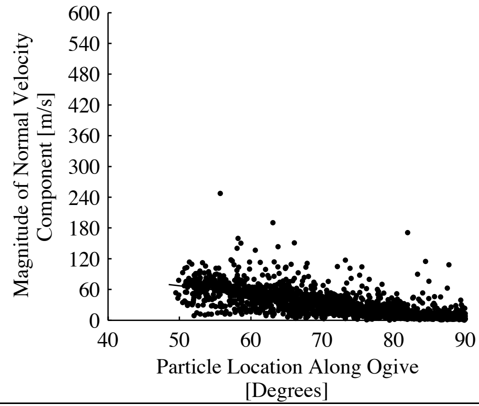

Time Step: 1.11-ms, Veloc: -100-m/s, Slope: -1.6, Int: 149.3.

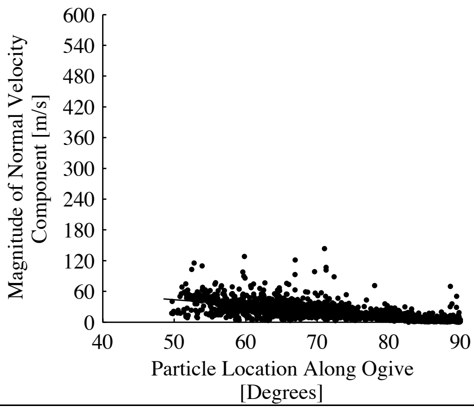

Time Step: 1.17-ms, Depth: -0.4-m, Slope: -1.1, Int: 97.1.

Figure 151. Data Set 6, 600-m/s Striking Velocity, 97-MPa Concrete, 26.9-mm, 2-CRH Projectile

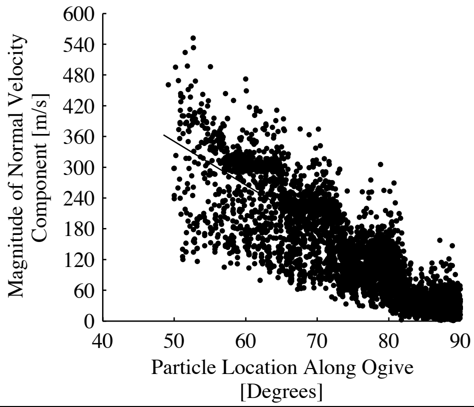

Time Step: 0.15-ms, Depth: -0.1-m, Slope: -8.5, Int: 775.3

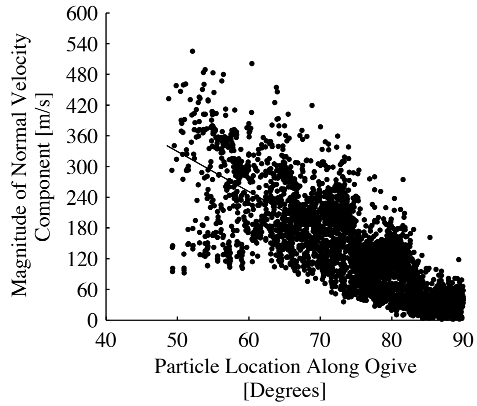

Time Step: 0.21-ms, Veloc: -600-m/s, Slope: -7.8, Int: 720.6

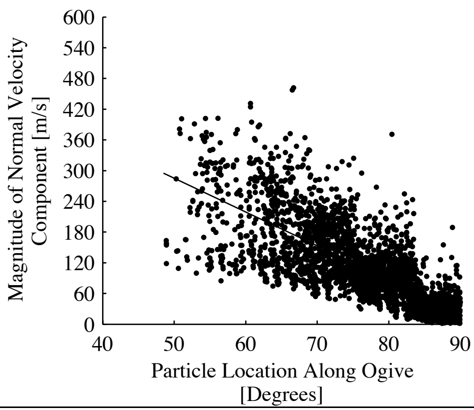

Time Step: 0.32-ms, Depth: -0.2-m, Slope: -6.6, Int: 615.6

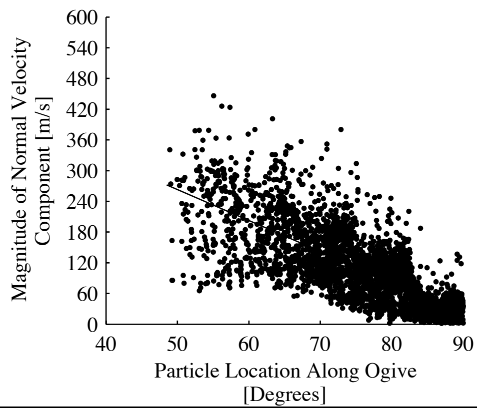

Time Step: 0.42-ms, Veloc: -500-m/s, Slope: -6.1, Int: 565.5

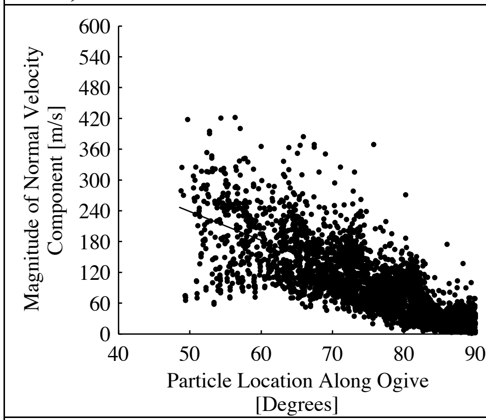

Time Step: 0.51-ms, Depth: -0.3-m, Slope: -5.6, Int: 519.4

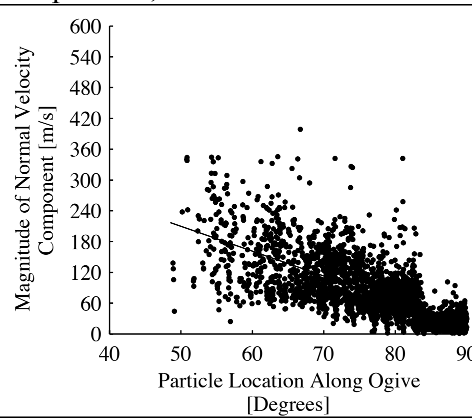

Time Step: 0.63-ms, Veloc: -400-m/s, Slope: -4.9, Int: 452.4

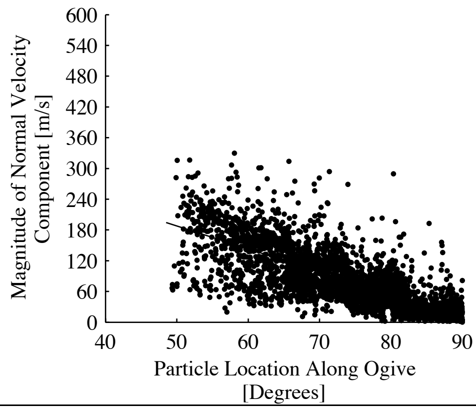

Time Step: 0.77-ms, Depth: -0.4-m, Slope: -4.5, Int: 411.0

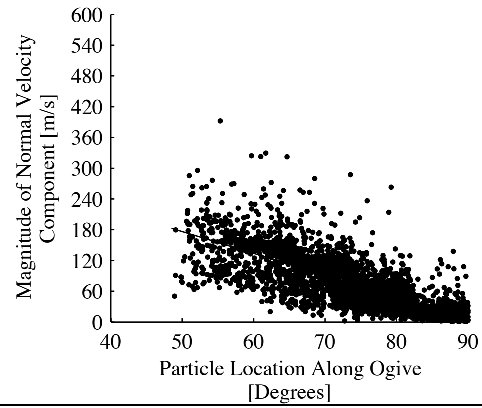

Time Step: 0.84-ms, Veloc: -300-m/s, Slope: -4.3, Int: 389.4

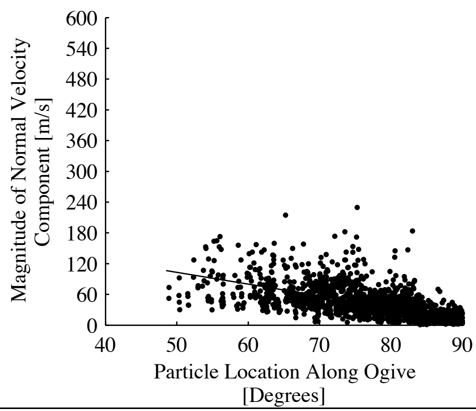

Time Step: 1.06-ms, Veloc: -200-m/s, Slope: -2.3, Int: 217.8

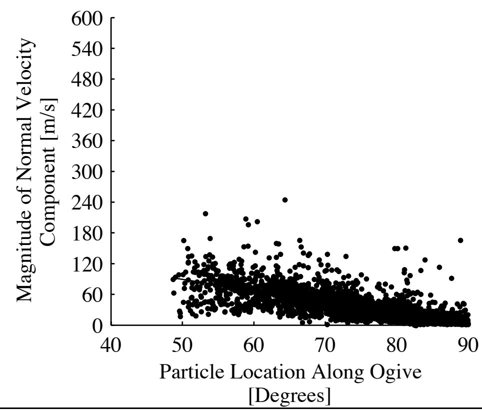

Time Step: 1.19-ms, Depth: -0.5-m, Slope: -2.2, Int: 197.3

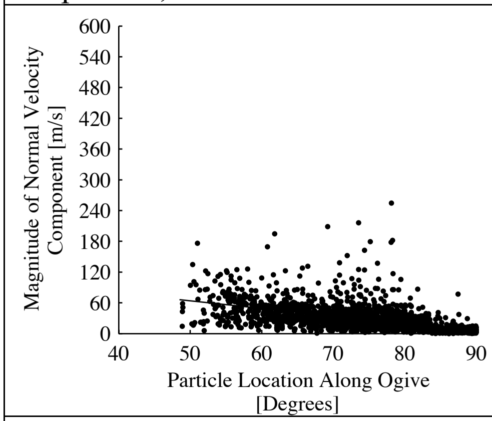

Time Step: 1.27-ms, Veloc: -100-m/s, Slope: -1.5, Int: 138.4

Figure 152. Data Set 6, 700-m/s Striking Velocity, 97-MPa Concrete, 26.9-mm, 2-CRH Projectile

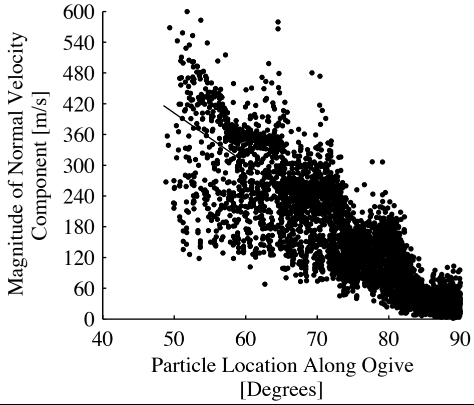

Time Step: 0.13-ms, Depth: -0.1-m, Slope: -9.8, Int: 889.7

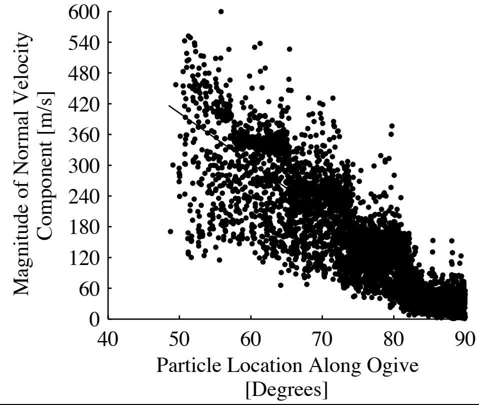

Time Step: 0.19-ms, Veloc: -700-m/s, Slope: -9.8, Int: 890.6

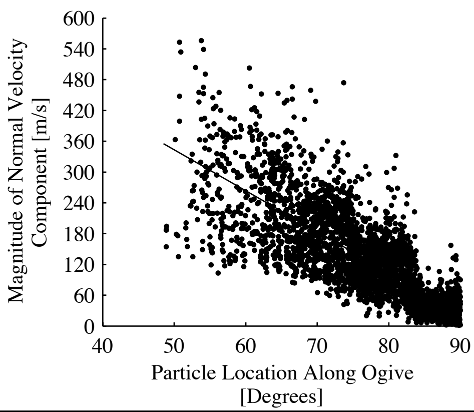

Time Step: 0.27-ms, Depth: -0.2-m, Slope: -8.0, Int: 743.0

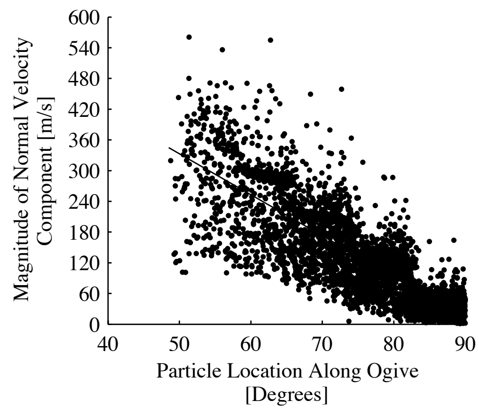

Time Step: 0.39-ms, Veloc: -600-m/s, Slope: -8.0, Int: 733.1

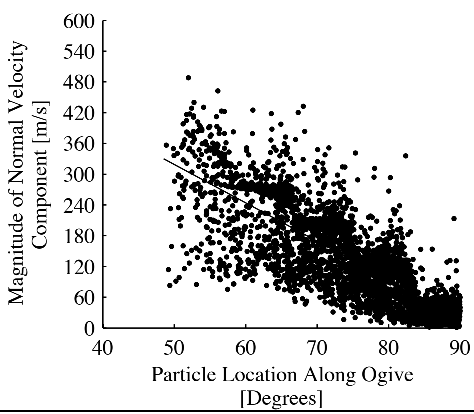

Time Step: 0.43-ms, Depth: -0.30-m, Slope: -7.5, Int: 693.4

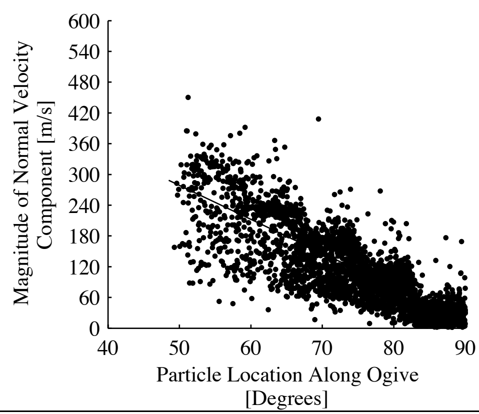

Time Step: 0.59-ms, Veloc: -500-m/s, Slope: -6.6, Int: 609.0

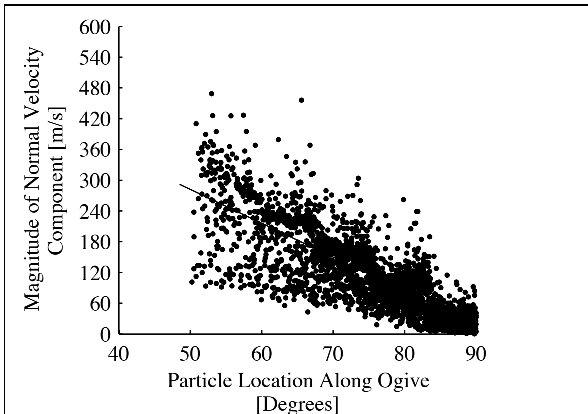

Time Step: 0.62-ms, Depth: -0.4-m, Slope: -6.6, Int: 613.1

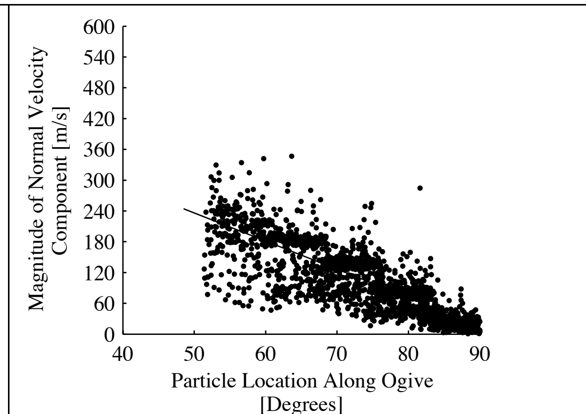

Time Step: 0.79-ms, Veloc: -400-m/s, Slope: -5.4, Int: 503.2

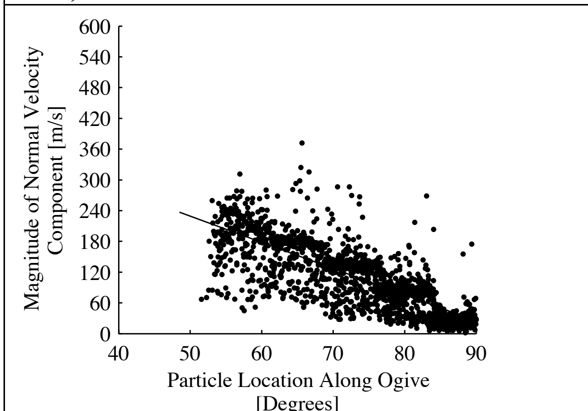

Time Step: 0.85-ms, Depth: -0.5-m, Slope: -5.1, Int: 485.5

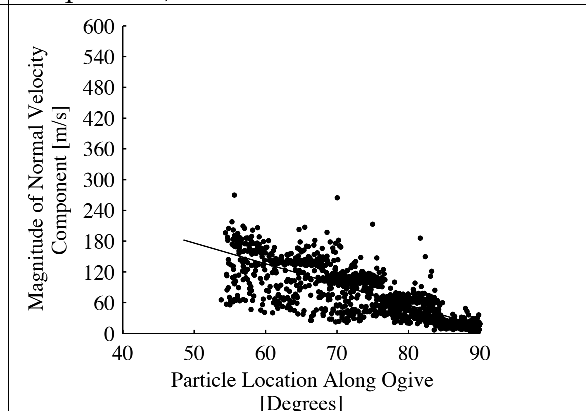

Time Step: 1.01-ms, Veloc: -300-m/s, Slope: -4.4, Int: 411.1

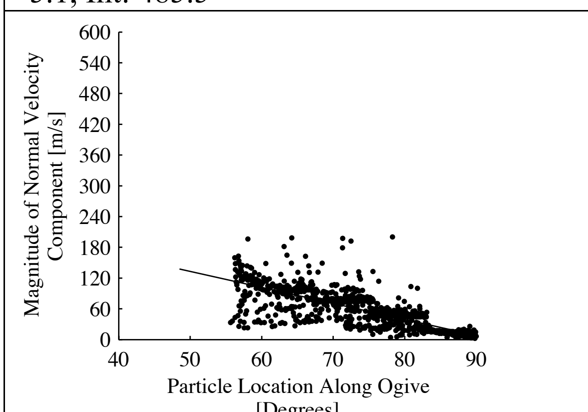

Time Step: 1.19-ms, Depth: -0.6-m, Slope: -3.2, Int: 297.7

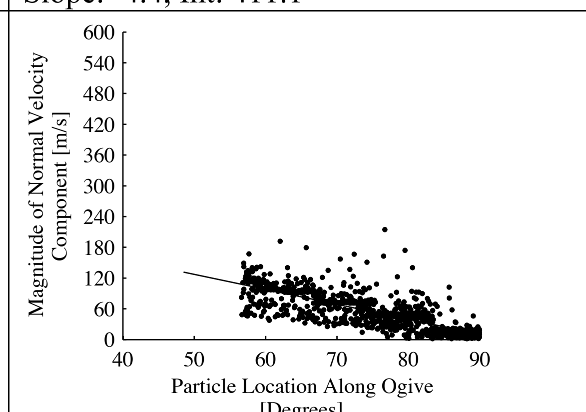

Time Step: 1.22-ms, Veloc: -200-m/s, Slope: -3.1, Int: 285.1

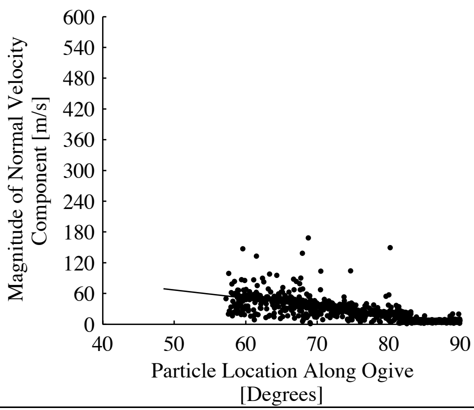

Time Step: 1.45-ms, Veloc: -100-m/s, Slope: -1.6, Int: 149.7	

Figure 153. Data Set 6, 800-m/s Striking Velocity, 97-MPa Concrete, 26.9-mm, 2-CRH Projectile

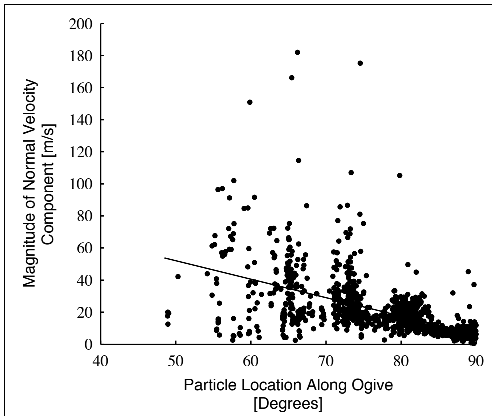

Time Step: 0.34-ms, Veloc: 100-m/s,
Slope: -1.15, Int: 109.6

Figure 154. Data Set 7, 200-m/s Striking Velocity, 157-MPa Concrete, 26.9-mm, 2-CRH Projectile

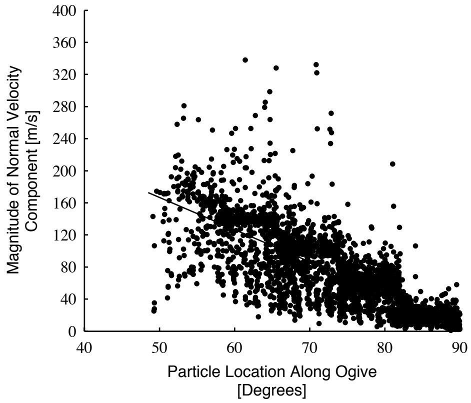

Time Step: 0.25-ms, Veloc: 300-m/s, Slope: --4.0, Int: 367.1

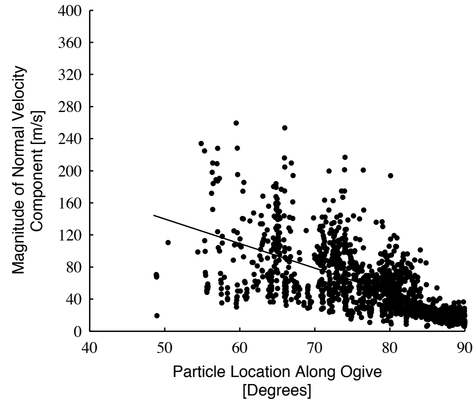

Time Step: 0.29-ms, Depth: -0.10-m, Slope: -3.1, Int: 293.4

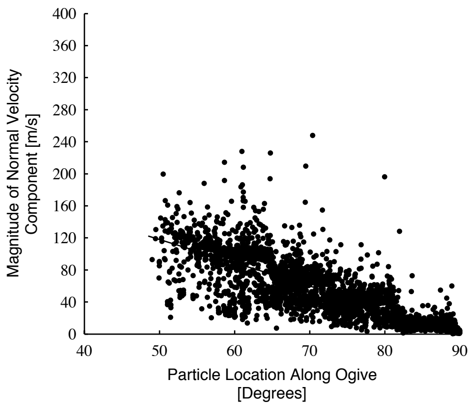

Time Step: 0.40-ms, Veloc: 200-m/s, Slope: -2.9, Int: 263.2

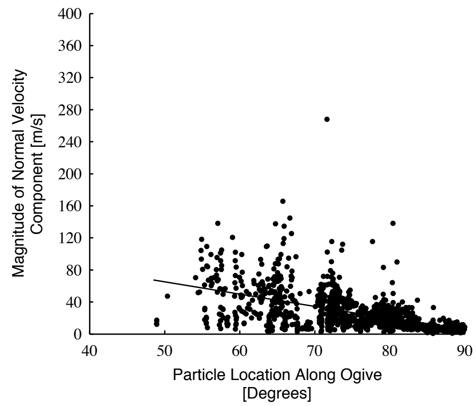

Time Step: 0.56-ms, Veloc: 100-m/s, Slope: -1.5, Int: 142.2

Figure 155. Data Set 7, 400-m/s Striking Velocity, 157-MPa Concrete, 26.9-mm, 2-CRH Projectile

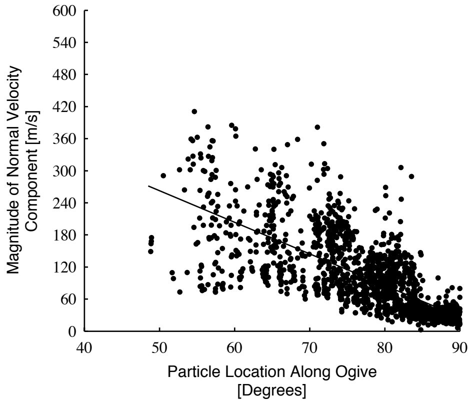

Time Step: 0.18-ms, Depth: -0.1-m,
Slope: -5.9, Int: 558.2

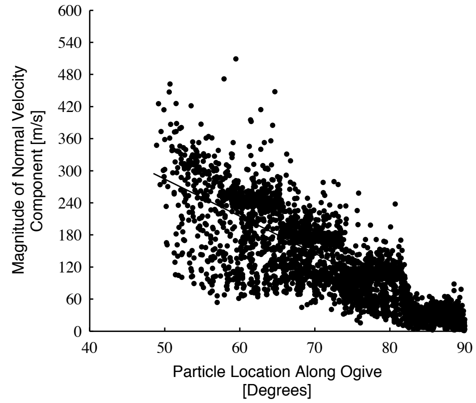

Time Step: 0.19-ms, Veloc: -500-m/s,
Slope: -6.9, Int: 631.8

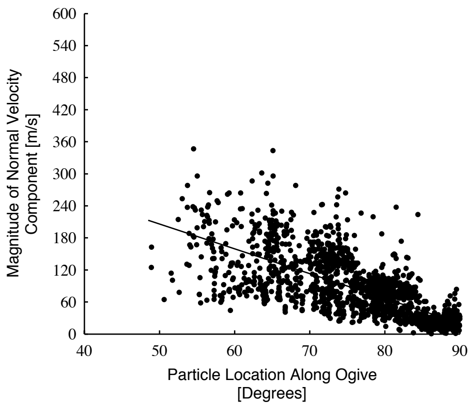

Time Step: 0.34-ms, Veloc: -400-m/s,
Slope: -4.6, Int: 438.1

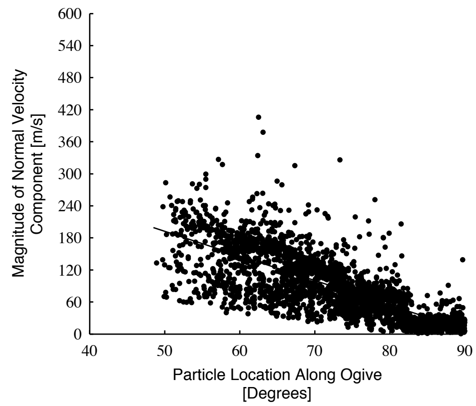

Time Step: 0.41-ms, Depth: -0.2-m,
Slope: -4.6, Int: 422.6

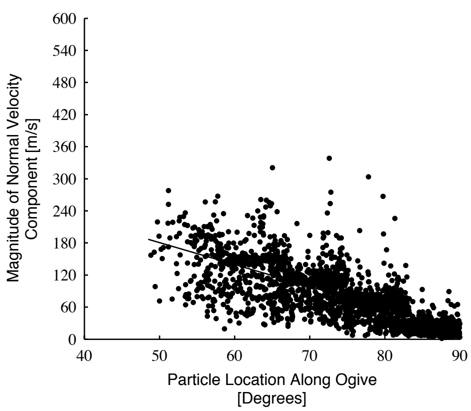

Time Step: 0.47-ms, Veloc: -300-m/s,
Slope: -4.1, Int: 385.9

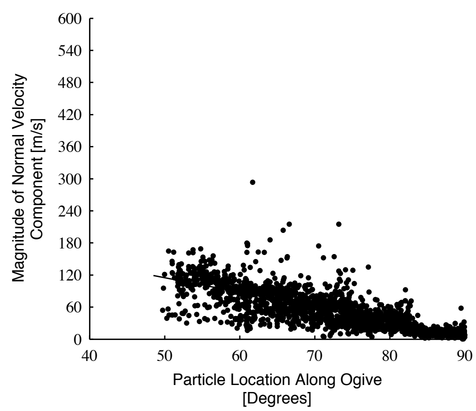

Time Step: 0.62-ms, Veloc: -200-m/s,
Slope: -2.7, Int: 251.2

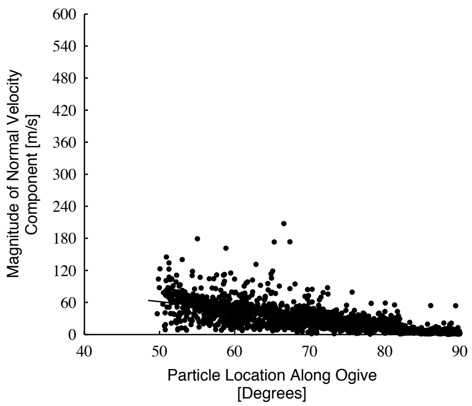

Time Step: 0.78-ms, Veloc: -100-m/s,
Slope: -1.6, Int: 139.6

Figure 156. Data Set 7, 600-m/s Striking Velocity, 157-MPa Concrete, 26.9-mm, 2-CRH Projectile

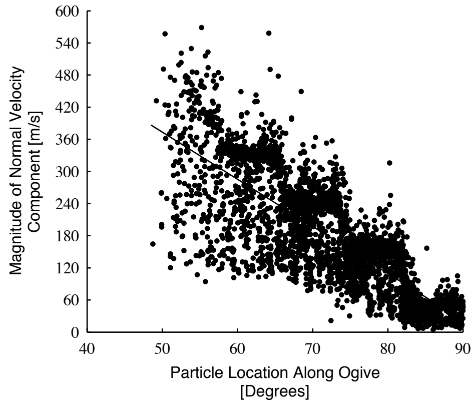

Time Step: 0.13-ms, Depth: -0.10-m,
Slope: -8.8, Int: 813.4

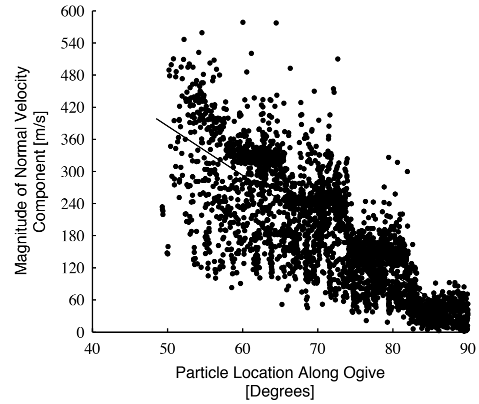

Time Step: 0.16-ms, Veloc: -700-m/s,
Slope: -9.2, Int: 845.9

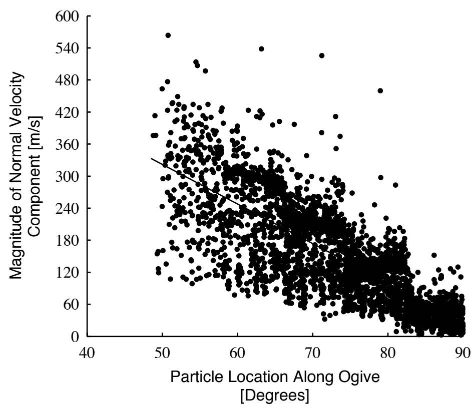

Time Step: 0.28-ms, Veloc: -600-m/s,
Slope: -7.4, Int: 692.7

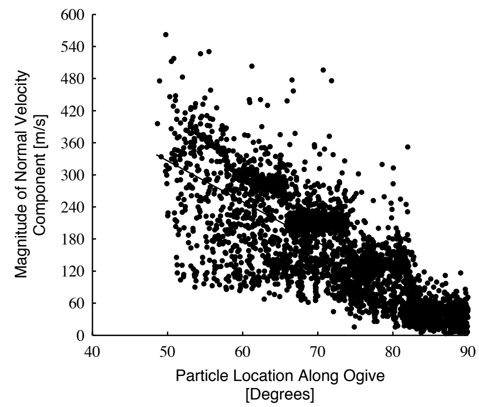

Time Step: 0.28-ms, Depth: -0.2-m,
Slope: -7.6, Int: 707.6

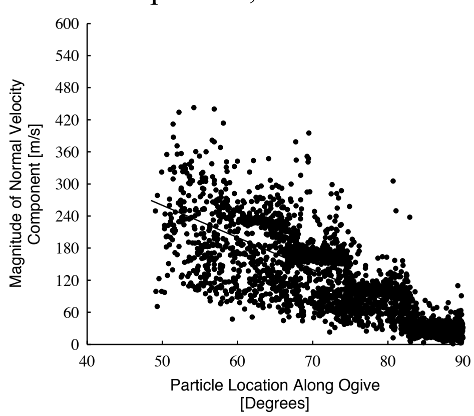

Time Step: 0.42-ms, Veloc: -500-m/s,
Slope: -6.0, Int: 561.4

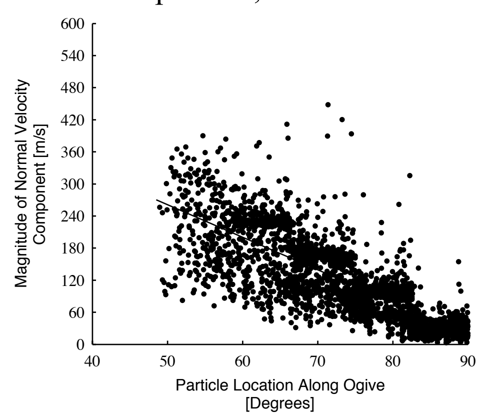

Time Step: 0.45-ms, Depth: -0.3-m,
Slope: -6.1, Int: 566.1

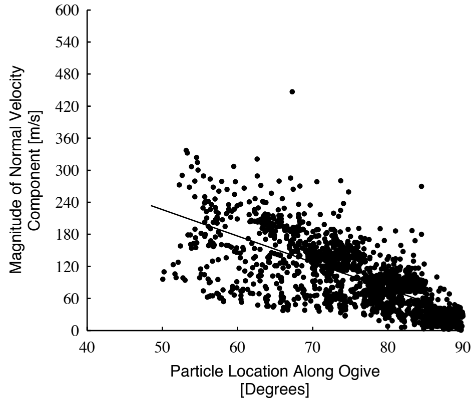

Time Step: 0.54-ms, Veloc: -400-m/s, Slope: -4.9, Int: 473.3

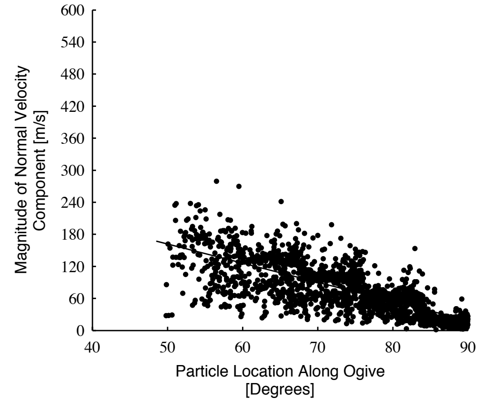

Time Step: 0.70-ms, Veloc: -300-m/s, Slope: -3.6, Int: 341.3

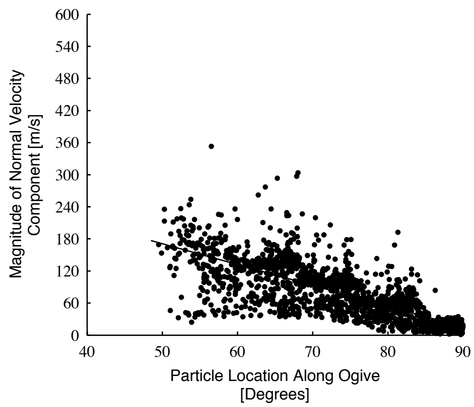

Time Step: 0.72-ms, Depth: -0.4-m, Slope: -3.9, Int: 365.5

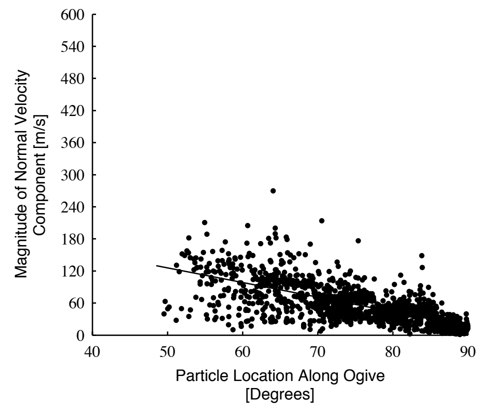

Time Step: 0.83-ms, Veloc: -200-m/s, Slope: -2.7, Int: 262.3

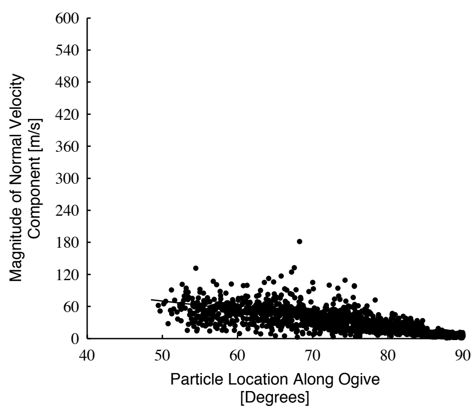

Time Step: 0.99-ms, Veloc: -100-m/s, Slope: -1.6, Int: 150.2

Figure 157. Data Set 7, 800-m/s Striking Velocity, 157-MPa Concrete, 26.9-mm, 2-CRH Projectile

REFERENCES

Air Force Weapons Laboratory (AFWL). (1965). *Deviatoric Effects in High Intensity Stress Waves* (Technical Report AFWL-TR-65-15). Kirtland AFB, NM: McDowell, E.L.

Air Force Armament Laboratory (AFAL). (1987). *Two- and Three-Dimensional Computational Analyses of Projectile-Concrete Impact* (Report AFATL-TR-87-57). Brooklyn Park, MN: Johnson, G. R. and Stryk, R. A.

Bangash, M.Y.H. (2009). *Shock, Impact and Explosion: Structural Analysis and Design*, Heidelberg. Springer Verlag.

Belytschko, T. and Lin, J. I. (1987). "A three-dimensional impact-penetration algorithm with erosion." *International Journal of Impact Engineering*. Vol. 5, No. 1-4, 111-127.

Bishop, R. F., Hill, R. and Mott, N. F. (1945). "The Theory of Indentation and Hardness Tests." *The Proceedings of the Physical Society*, Vol. 57, No. 321,147-159.

Blacker, T. D., and Stephenson, M. B. (1991), "Paving: A new approach to automated quadrilateral mesh generation." *International Journal of Numerical Methods*. Vol. 32, 811–847.

Cargile, J. D., O'Neil, E. F. and Neeley, B. D. (2003). "Very-High-Strength Concretes for Use in Blast- and Penetration-Resistant Structures." *The AMPTIAC Quarterly*, Special Issue, Vol 6, No. 4, 61-67.

Chadwick, P. (1959). "The Quasi-Static Expansion of a Spherical Cavity in Metals and Ideal Soils." *The Quarterly Journal of Mechanics and Applied Mathematics*, Vol. 12-1, 52-71.

Chen, X. W., and Li, Q. M. (2004). "Transition from Nondeformable Projectile Penetration to Semihydrodynamic Penetration." *Journal of Engineering Mechanics*. 123-127.

Forrestal, M. J. (1986). "Penetration into Dry Porous Rock." *International Journal of Solids and Structures*, Vol. 22,1485-1500.

Forrestal, M. J., Altman, B.S., Cargile, J.D., and Hanchak, S. J. (1993). “An Empirical Equation for Penetration Depth of Ogive-nosed Projectiles into Concrete Targets.” *Proceedings of the Sixth International Symposium on Interaction of Nonnuclear Munitions with Structures*, 29-32.

Forrestal, M. J., Altman, B.S., Cargile, J.D., and Hanchak, S. J. (1994). “An Empirical Equation for Penetration Depth of Ogive-nose Projectiles into Concrete Targets.” *International Journal of Impact Engineering*, Vol. 15, No. 4, 395-405.

Forrestal, M. J., Cargile, J. D., and Tzou, R. D. Y. (1993). “Penetration of Concrete Targets.” *American Society of Mechanical Engineers*, AMD-171, 9-16.

Forrestal, M. J., Frew, D. J., Hickerson, J. P., and Rohwer, T.A. (2003). “Penetration of Concrete Targets with Deceleration-time Measurements.” *International Journal of Impact Engineering*. Vol. 28, 479-497.

Forrestal, M. J., Longcope, D. B., and Norwood, F. R. (1981). “A Model to Estimate Forces on Conical Penetrators into Dry Porous Rock.” *Journal of Applied Mechanics*, Vol. 48-1, 25-29.

Forrestal, M. J. and Longcope, D.B. (1982). “Closed-form Solutions for Forces on Conical-Nosed Penetrators into Geological Targets with Constant Shear Strength.” *Mechanics of Materials*, Vol. 1-4, 285-295.

Forrestal, M. J. and Luk, V.K. (1992). “Penetration into Soil Targets” *International Journal of Impact Engineering*, Vol. 12-3, 427-444.

Forrestal, M. J., Norwood, F. R., and Longcope, D. B. (1981). “Penetration into Targets Described by Locked Hydrostats and Shear Strength.” *International Journal of Solids and Structures*, Vol. 17-9, 915-924.

Forrestal, M. J., Okajima, K. and Luk, V.K. (1988). “Penetration of 6061-T651 Aluminum Targets with Rigid Long Rods.” *ASME Journal of Applied Mechanics*, Vol. 55-4, 755-760.

Forrestal, M. J., Tzou, D. Y. (1997). “A Spherical Cavity-Expansion Penetration Model For Concrete Targets.” *International Journal of Solids and Structures*, Vol 34, No. 31/32, 4127-4146.

Forrestal, M. J., Tzou, D. Y., Askari, E. and Longcope, D. B. (1995). “Penetration into Ductile Metal Targets with Rigid Spherical-Nose Rods.” *International Journal of Impact Engineering*, Vol. 16, No. 5/6, 699-710.

Frew, D.J., Forrestal, M.J., and Cargile, J.D. (2006). "The Effect of Concrete Target Diameter on Projectile Deceleration and Penetration Depth." *International Journal of Impact Engineering*. Vol. 32, 1584-1594.

Frew, D. J., Hanchak, S. J., Green, M. L., and Forrestal, M. J. (1998). "Penetration of Concrete Targets with Ogive-Nose Steel Rods." *International Journal of Impact Engineering*. Vol. 21, No. 6, 489-497.

Gold, V. M., Vradis, G. C., and Pearson, J. C. (1996). "Constitutive Models for Concrete Penetration Analysis." Journal of Engineering Mechanics. Vol. 122, 230-238

Goodier, J. N. (1965). "On the Mechanics of Indentation and Cratering in Solid Targets of Strain-Hardening Metal by Impact of Hard and Soft Spheres." *Proceedings of the 7th Symposium on Hypervelocity Impact III*, *NY*.

Habel, K. and Gauvreau, P. (2008). "Response of Ultra-High Performance Fiber Reinforced Concrete (UHPFRC) to Impact and Static Loading." *Cement and Concrete Composites*, Vol. 30, 938-946.

Hanagud, S.V. and Ross, B. (1971). "Large Deformation, Deep Penetration Theory for a Compressible Strain-Hardening Target Material." *American Institute of Aeronautics and Astronautics (AIAA) Journal*. Vol. 9, No. 5, 905-911.

He, Tao, Wen, H. and Guo, X. (2011). "A Spherical cavity Expansion Model for Penetration of Ogival-Nosed Projectiles into Concrete Targets with Shear-Dilatancy." *Acta Mech. Sin*. 27-6, 1001-1012.

Hill, R. (1948). "A Theory of Earth Movement Near a Deep Underground Explosion." Memo No. 21-48, Armament Research Establishment, Kent, UK.

Holmquist, T.J., Johnson, G.R., and Cook, W.H. (1993). "A Computational Constitutive Model for Concrete Sugjected to Large Strains, High Strain Rates, and High Pressures." *Fourteenth International Symposium on Ballistics*, Quebec City, Canada.

Hopkins, H. G. (1960). "Dynamic Expansion of Shperical Cavities in Metal." *Progress in Solid Mechanics*, Vol. 1, 82-162.

Hunter, S. C. and Crozier, R.J.M. (1968). "Similarity Solution for the Rapid Uniform Expansion of a Spherical Cavity in a Compressible Elastic-Plastic Solid." *Quarterly Journal of Mechanics and Applied Math*, Vol. 21-4.

Institute for Advanced Technology (IAT), The University of Texas at Austin. (1997) *Application of Cavity Expansion Analysis to Penetration Problems*. (IAT.R 0075). Austin, TX: Satapathy, S.

Johnson, G. R. (1972). *Impact Strength of Materials*. Edward Arnold, London.

Johnson, G. R. (2009). "Model Behavior." *Technology Today*. San Antonio, TX, Southwest Research Institute, 2-5.

Johnson, G.R., Beissel, S.R., Gerlach, C.A., Stryk, R.A., Johnson. A.A., and Holmquist, T. J. (2004) "Advanced Computations for Ballistic Impact Problems." *Proceedings for the Army Science Conference*. Orlando, Fl.

Johnson, G.R., Beissel, S.R., Stryk, R.A. (2000) "A Generalized Particle Algorithm for High Velocity Impact Computations." *Computational Mechanics* 25, 245-256.

Los Alamos National Laboratory. (1994). Constitutive Equations for Annealed Metals Under Compression at High Strain Rates and High Temperatures (LA-12669-MS). Los Alamos, NM: Gray, G.T., Chen, S.R., Wright, W., and Lopez, M.F.

Luk, V. K. and Forrestal, M.J. (1987). "Penetration into Semi-Infinite Reinforced-Concrete Targets with Spherical and Ogival Nose Projectiles." *International Journal of Impact Engineering*. Vol. 6, No. 4, 291-301.

Millard, S. G., Molyneauz, T. C. K., Barnett, S. J. and Goa, X. (2010). "Dynamic Enhancement of Blast-Resistant Ultra High Performance Fibre-Reinforced Concrete under Flexural and Shear Loading." *International Journal of Impact Engineering*. Vol. 37, 405-413.

National Defense Research Committee of the Office of Scientific Research and Development, Division 2. (1950). *Final Report on Concrete Penetration* (NRDC Report No. A-388). Washington, DC: Beth, R. A.

Office of the Chairman of the Joint Chiefs of Staff (OCJCS). (2003). *Joint Tactics, Techniques, and Procedures for Intelligence Support to Targeting* (Joint Publication 2-01.1). Washington, DC.

Office of the Chairman of the Joint Chiefs of Staff (OCJCS). (2007). *Joint Targeting* (Joint Publication 3-60). Washington, DC.

Federal Highway Administration (FHWA). (2011). "Ultra-High Performance Concrete." *TECHNOTE.* McLean, VA.

Rahman, I. A., Zaidi, A.M.A., and Latif, ,Q.B. (2010). "Review on Empirical Studies of Local Impact Effects of Hard Missile on Concrete Structures." *International Journal of Sustainable Construction Engineering and Technology*. 73-97.

Rosenberg, Z. and Dekel, E. (2012). *Terminal Ballistics*. New York, Springer.

Sandia National Laboratory (SNL), (1966). *Dynamic Penetration of Selected Projectiles into Particulate Media*, (SC-RR-66-376). Albuquerque, NM: Thompson, L. J.

Sandia National Laboratory (SNL). (1997). *Penetration Equations*. Albuquerque, NM: Young, C. W.

Sandia National Laboratory (SNL). (2010). *Ballistic Penetration Test Results for Ductal and Ultra-High Performance Concrete Samples* (SAND2010-2222). Albuquerque, NM: Thornhill, T. F., and Reinhart, W. D.

Sandia National Laboratory (SNL). (2014). CUBIT 14.1 User Documentation. Retrieved from https://cubit.sandia.gov/public/documentation.html

Satapathy, S. (2001). "Dynamic spherical cavity expansion in brittle ceramics." *International Journal of Solids and Structures*. 38, 5833-5845.

Schwer, L. E. (2009). "Strain Rate Induced Strength Enhancement in Concrete: Much ado about Nothing?" *7th European LS-Dyna Conference*.

Shiqiao, Gao, Lei, Jin, Haipeng, Liu, Xinjian, Liang, and Li, Han. (2007). "A Normal Cavity-Expansion (NCE) Model based on the Normal Curve Surface (NCS) Coordinate System." *International Journal of Applied Mathematics*. Vol. 37-2. IJAM_37_2_02.

Silling, S.A., Forrestal, M.J. (2007). "Mass Loss from Abrasion on Ogive-Nose Steel Projectiles that Penetrate Concrete Targets." *International Journal of Impact Engineering*, Vol 34, 1814-1820.

Soils and Pavements Laboratory (SPL). U.S. Army Engineer Waterways Experiment Station. (1975). *Evaluation of Empirical and Analytical Procedures used for Predicting the Rigid Body Motion of an Earth Penetrator* (S-75-15). Vicksburg, MS: Hadala, P. F.

Southwest Research Institute (SWRI). (2000). Probabilistic Sensitivity Analysis of the Holmquist-Johnson-Cook Material Model for Concrete (SWRI 18-02947). San Antonio, TX: Thacker, B. H.

Stivaros, P. C. and Philippacopoulos, A. J. (2011). "Structural Evaluation of Reinforced Concrete Bunkers in High Speed Balancing Facilities." *ACI Special Publication*. SP281-05, 1-18.

Swedish Defence Research Agency. (2003) *A note on empirical formulas for the prediction of concrete penetration* (FOI-R-0968-SE). Tumba: Hansson, H. A.

Tate, A. (1977). “A Possible Explanation for the Hydrodynamic Transition in High Speed Impact*.” International Journal of Mechanical Science*. Vol. 19, 121-123.

Tate, A. (1986). “Long Rod Penetration Models-Part I. A Flow Field Model for High Speed Long Rod Penetration.” *International Journal of Mechanical Science*. Vol. 28, No. 8, 535-548.

Tham, C. Y. (2005). “Reinforced Concrete Perforation and Penetration Simulation using AUTODYN-3D.” *Finite Elements in Analysis and Design*. Vol. 41, 1401-1410.

Tham, C. Y. (2006). “Numerical and Empirical Approach in Predicting the Penetration of a Concrete Target by an Ogive-Nosed Projectile.” *Finite Elements in Analysis and Design*. Vol. 42, 1258-1268.

Unosson, M., and Nilsson, L. (2006). “Projectile Penetration and Perforation of High Performance Concrete: Experimental Results and Macroscopic Modeling.” *International Journal of Impact Engineering*. Vol. 32, 1068-1085.

U.S. Army Armament Research, Development and Engineering Center (USAARDEC). (1997). *Analysis of the Penetration of Concrete* (Technical Report ARWEC-TR-97010), Picatinny Arsenal, NJ: Gold, V. M.

U.S. Army Ballistic Research Laboratory (USABRL). (1980). Impact Dynamics: Theory and Experiment (ARBRL-TR-02271). Aberdeen, MD: Zukas, J. A.

U.S. Army Engineer Research and Development Center (USAERDC). (1999). *Tensile properties of very-high-strength concrete for penetration-resistant structures*. Vicksburg, MS: O’Neil, E.F., Neeley, B.D., and Cargile, J.D.

U.S. Army Engineer Research and Development Center (USAERDC). (2006). *Low-Velocity-Probe Penetration Experiments*, CEERD-GM-I, Vicksburg, MS: Guillet, M. D., Cargile, D. J., Williams, E. M., Johnson, J. B., and Jones, K.F.

U.S. Army Engineer Research and Development Center (USAERDC). (2010). *The Advanced Fundamental Concrete (AFC) Model*. (TR10-51) Vicksburg, MS: Adley, M. D., Frank, A. O., Danielson, K. T., Akers, S. A. and O’Daniel, J.

U.S. Army Engineer Waterways Experiment Station (USAEWES). (1975). *Development of a Projectile Penetration Theory. Report 1. Penetration Theory for Shallow to Moderate Depths* (Technical Report S-75-9). Vicksburg, MS: Bernard, R. S. and Hanagud, S. V.

U.S. Army Engineer Waterways Experiment Station (USAEWES). (1976). *Development of a Projectile Penetration Theory. Report 2. Deep Penetration Theory for Homogeneous and Layered Targets* (Technical Report S-75-9). Vicksburg, MS: Bernard, R.S.

US Naval Weapons Laboratory (USNWL). (1966) *Development of a Scaling Law and Techniques to Investigate Penetration in Concrete*. (NWL Report No. 2057). Dahlgren, VA: Canfield, J.A. and Clator, I.G.

Wang, Z., Li, Y., Shen, R.F., and Wang, J.G. (2007). "Numerical Study on Craters and Penetration of Concrete Slab by Ogive-Nose Steel Projectile." *Computers and Geotechnics*. Vol 34, 1-9.

Warren, T. L. (2002). "Simulations of the Penetration of Limestone Targets by Ogive-nose 4340 Steel Projectiles." *International Journal of Impact Engineering*. Vol. 27, 475-496.

Young, C. W. (1969). "Depth Prediction for Earth-Penetrating Projectiles." *Journal of Soil Mechanics and Foundations Division. Proceedings of the American Society of Civil Engineers*. 803-817.

Zukas, J. A. (2004). *Introduction to Hydrocodes. Studies in Applied Mechanics, 49*. Baltimore, Elsevier.

BIOGRAPHY

Robert Sobeski graduated from Pittston Area Senior High School, Pittston, PA in 1984. He enlisted in the Army in 1985 and was assigned to the 3rd Armored Division in Friedberg, Germany. He was accepted into the United States Military Academy at West Point in 1988 and graduated with a B.S. in Engineering Physics in 1992. As a lieutenant he supervised the renovation and construction of numerous structures to include a schoolhouse in San Luis Talpa, El Salvador and a 140-ft single-span bridge in Jacmel, Haiti. He received a M.S. in Engineering Management from the University of Missouri, Rolla in 1996 and a M.S. in Nuclear Engineering from the Massachusetts Institute of Technology in 2001. He served as an instructor at the United States Military Academy from 2001 to 2003 and then as an Assistant Professor from 2003 to 2004. From 2004 to 2009, Bob worked as program manager for the Defense Threat Reduction Agency in the Research and Development Enterprise. Prior to attending George Mason, Bob was assigned as the Deputy Division Chief of the Stockpile Services Division of the National Nuclear Security Administration. He received his Ph.D. in Civil and Infrastructure Engineering from George Mason University in 2014. He is currently assigned as the Chief, Nuclear Effects Branch, Physical Vulnerability Division, of the Defense Intelligence Agency.